Alma Mater Studiorum - University of Bologna

DOCTORATE OF RESEARCH IN INDUSTRIAL CHEMISTRY

XXI CYCLE

Scientific Sector: CHIM/04

DEVELOPMENT AND CHARACTERIZATION OF NON-OXIDE CERAMIC COMPOSITES FOR MECHANICAL AND TRIBOLOGICAL APPLICATIONS

A Doctoral Thesis by

Laura Silvestroni

Coordinator:

Prof. Luigi Angiolini

Supervisor:

Prof. Giuseppe Palombarini

Supervisors at ISTEC-CNR:

Dr. Diletta Sciti

Dr. Stefano Guicciardi

Final exam 2009

A mio babbo,
che aveva un'inventiva stravagante
e continua a prendersi cura di me

TABLE OF CONTENTS

ABSTRACT

Keywords: carbides, borides, silicides, densification, microstructure, mechanical properties.

The main reasons for the attention focused on ceramics as possible structural materials are their wear resistance and the ability to operate with limited oxidation and ablation at temperatures above 2000°C. Hence, this work is devoted to the study of two classes of materials which can satisfy these requirements: silicon carbide -based ceramics (SiC) for wear applications and borides and carbides of transition metals for ultra-high temperatures applications (UHTCs).

SiC-based materials: Silicon carbide is a hard ceramic, which finds applications in many industrial sectors, from heat production, to automotive engineering and metals processing.

In view of new fields of uses, SiC-based ceramics were produced with addition of 10-30 vol% of $MoSi_2$, in order to obtain electro conductive ceramics.

$MoSi_2$, indeed, is an intermetallic compound which possesses high temperature oxidation resistance, high electrical conductivity ($21 \cdot 10^{-6}$ Ω·cm), relatively low density (6.31 g/cm^3), high melting point (2030°C) and high stiffness (440 GPa).

The SiC-based ceramics were hot pressed at 1900°C with addition of Al_2O_3-Y_2O_3 or Y_2O_3-AlN as sintering additives. The microstructure of the composites and of the reference materials, SiC and $MoSi_2$, were studied by means of conventional analytical techniques, such as X-ray diffraction (XRD), scanning electron microscopy (SEM) and energy dispersive spectroscopy (SEM-EDS). The composites showed a homogeneous microstructure, with good dispersion of the secondary phases and low residual porosity.

The following thermo-mechanical properties of the SiC-based materials were measured: Vickers hardness (HV), Young's modulus (E), fracture toughness (K_{Ic}) and room to high temperature flexural strength (σ). The mechanical properties of the

composites were compared to those of two monolithic SiC and $MoSi_2$ materials and resulted in a higher stiffness, fracture toughness and slightly higher flexural resistance. Tribological tests were also performed in two configurations disco-on-pin and slider-on cylinder, aiming at studying the wear behaviour of SiC-$MoSi_2$ composites with Al_2O_3 as counterfacing materials. The tests pointed out that the addition of $MoSi_2$ was detrimental owing to a lower hardness in comparison with the pure SiC matrix.
On the contrary, electrical measurements revealed that the addition of 30 vol% of $MoSi_2$, rendered the composite electroconductive, lowering the electrical resistance of three orders of magnitude.

Ultra High Temperature Ceramics: Carbides, borides and nitrides of transition metals (Ti, Zr, Hf, Ta, Nb, Mo) possess very high melting points and interesting engineering properties, such as high hardness (20-25 GPa), high stiffness (400-500 GPa), flexural strengths which remain unaltered from room temperature to 1500°C and excellent corrosion resistance in aggressive environment. All these properties place the UHTCs as potential candidates for the development of manoeuvrable hypersonic flight vehicles with sharp leading edges.
To this scope Zr- and Hf- carbide and boride materials were produced with addition of 5-20 vol% of $MoSi_2$. This secondary phase enabled the achievement of full dense composites at temperature lower than 2000°C and without the application of pressure.
Besides the conventional microstructure analyses XRD and SEM-EDS, transmission electron microscopy (TEM) was employed to explore the microstructure on a small length scale to disclose the effective densification mechanisms. A thorough literature analysis revealed that neither detailed TEM work nor reports on densification mechanisms are available for this class of materials, which however are essential to optimize the sintering aids utilized and the processing parameters applied.
Microstructural analyses, along with thermodynamics and crystallographic considerations, led to disclose of the effective role of $MoSi_2$ during sintering of Zr- and Hf- carbides and borides.
Among the investigated mechanical properties (HV, E, K_{Ic}, σ from room temperature to 1500°C), the high temperature flexural strength was improved due to the protective and sealing effect of a silica-based glassy phase, especially for the borides.

Nanoindentation tests were also performed on HfC-$MoSi_2$ composites in order to extract hardness and elastic modulus of the single phases.

Finally, arc jet tests on HfC- and HfB_2-based composites confirmed the excellent oxidation behaviour of these materials under temperature exceeding 2000°C; no cracking or spallation occurred and the modified layer was only 80-90 μm thick.

LIST OF PUBLICATIONS RELATED TO THIS THESIS

1 D. Sciti, L. Silvestroni, A. Balbo, S. Guicciardi, G. Pezzetti, "High–strength and –toughness electroconductive SiC-based composites", Advanced Engineering Materials 8 No. 10 (2006) 997-1001.

2 D. Sciti, A. Bellosi, "High density pressureless sintered HfC-based composites", Journal of the American Ceramic Society 89 Issue 9 (2006) 2668-2670.

3 S. Guicciardi, L. Silvestroni, G. Pezzotti, D. Sciti, "Depth-sensing indentation hardness characterization of HfC-based composites", Advanced Engineering Materials 9 No. 5 (2007) 389-392.

4 L. Silvestroni, D. Sciti, "Effects of $MoSi_2$ additions on the properties of Hf- and Zr-B_2 composites produced by pressureless sintering", Scirpta Materialia 57 (2007) 165-168.

5 L. Silvestroni, D. Sciti, A. Bellosi, "Microstructure and properties of pressureless sintered HfB_2-based composites with additions of ZrB_2 or HfC", Advanced Engineering Materials, 9, No 10 (2007) 915-920.

6 S. Guicciardi, L. Silvestroni, C. Melandri, D. Sciti, G. Pezzotti, "Nanoindentation characterization of HfC-based composites", International Journal of Surface and Engineering 1, N. 2/3 (2007) 198-212.

7 D. Sciti, L. Silvestroni, A. Bellosi, "Properties of Pressureless Sintered (Hf, Zr) Borides and Carbides with Additions of $MoSi_2$", Proceedings of the 31th International Conference on Advanced Ceramics and Composites, January 2007 Cocoa Beach, Florida.

8 R. Savino, M. De Stefano Fumo, L. Silvestroni, D. Sciti: Arc-jet testing on $HfB_2$and HfC -based Ultra-High-Temperature-Ceramic Materials, Journal of the European Ceramic Society 28 (2008) 1899–1907.

9 D. Sciti, L. Silvestroni, "Microstructure and properties of pressureless sintered ZrC-based materials", Journal of Materials Research 26 No. 7 (2008) 1882-1889.

10 S. Guicciardi, C. Melandri, L. Silvestroni, D. Sciti, "Indentation grid analysis of nanoindentation bulk and *in situ* properties of ceramic phases", Journal of Materials Science 43 No. 12 (2008) 4348-4352.

11 L. Silvestroni, D. Sciti, J. Kling, S. Lauterbach, H-J. Kleebe, "Sintering Mechanisms of Zirconium and Hafnium Carbides doped with $MoSi_2$", accepted at Journal of American Ceramic Society.

12 L. Silvestroni, D. Sciti, S. Lauterbach, H-J. Kleebe, "Transmission electron microscopy on Zr- and Hf-borides doped with $MoSi_2$: mechanisms of densification", submitted to the Journal of American Ceramic Society.

AIM OF THE WORK

The possibility to obtain new materials which possess good thermo-mechanical properties and wear resistance is a common demand in many fields of technological research and in industrial sectors.

The availability of materials with improved performances implies a better and more efficient functioning of many technological systems thus leading to new applications, new processes and to improved uses of the disposable sources.

In the last decades, much effort has been done in the field of advanced ceramics thanks to the broad spectrum of possible applications and to the uniqueness of their properties. In this branch, silicon carbide-based materials constitute a class of very promising structural materials for engineering application such as components operating at high temperature or in aggressive environment, engine parts, heat exchanger and wear resistant materials.

Besides SiC-based materials, a new class of materials with interesting engineering properties is arising always more interest in the scientific community. These materials, labelled Ultra High Temperature Ceramics (UHTC), can withstand temperature above 1600°C in aggressive environment. In addition to high melting points, UHTCs possess extremely high melting temperatures and a unique combination of chemical stability, high electrical and thermal conductivities and resistance to erosion and corrosion that make them suitable for extreme environments associated to hypersonic flights, atmospheric re-entry and rocket propulsion.

This work is composed by two sections: the first deals with silicon carbide-based materials, the second with ultra high temperature ceramics. The materials were produced from commercial powders, the pellets were sintered by hot pressing or pressureless sintering and finally they were characterized by microstrucutral and thermo-mechanical analysis.

The purposes of this work were therefore:

- part I: to develop electroconductive SiC-based electroconductive materials with improved mechanical properties and good wear behaviour;
- part II: to obtain ceramics with a controlled microstructure which show good mechanical properties even at temperature of 1500°C and oxidation resistant.

An outline of the performed activity is reported below.

Literature review	Introduction to advanced ceramic materials	Chapter 1
	Analysis techniques and testing methods	Chapter 2
SECTION I	**SiC-based ceramics**	
Literature review	Features and utilizations	Chapter 3
	Secondary phase	Chapter 4
Experimental procedure	Materials production	Chapter 5
	Results and discussion	Chapter 6
	Conclusions I	Chapter 7
SECTION II	**UHTCs materials**	
Literature review	Features and utilizations	Chapter 8
Experimental procedure	Materials production	Chapter 9
	Results and discussion	Chapter 10, 11
	Ternary composites	Chapter 12
	Conclusions II	Chapter 13

The majority of this work was carried out at the Institute of Science and Technology for Ceramics – National Research Council (Istec-CNR) of Faenza.

Part of the wear analyses on SiC-based materials was performed at the Department for Metals Science, Electrochemical and Chemical Techniques of the Faculty of Industrial Chemistry of Bologna.

TEM analyses on UHTCs were performed at the Department of Materials Science at the Technnische Univestität Darmstadt, Germany.

Arc-jet tests on UHTCs were performed at the Department of Aerospace Engineering of the University of Napoli.

CHAPTER 1

ADVANCED CERAMIC MATERIALS

1.1 INTRODUCTION

Until recently, materials for advanced structural applications have been largely restricted to advanced metallic alloys. However it now appears that for certain applications, mainly those involving high temperatures, metallic materials have reached the limit for their potential development. In combustion engines and other energy generating equipment, the desirability of higher operating temperatures has driven the development of Ni-, Co- and Fe-based alloys to extreme levels of sophistication in microstructural and structural design. However, such development is necessarily limited by the melting point of these materials. For further development, ceramics offer one of the few avenues to a significant increase in service temperatures. Their low density, chemical inertness and high hardness offer additional potential for extending performances limits beyond those offered by metallic materials. Hitherto, the widespread use of ceramics has been inhibited by their brittleness and poor reliability of strength. To overcome these problems, considerable progress has been made during the past two decades in the compositional and microstructural design of ceramics. The application of the composite principle has been the most important advance in this field, for example, the combination of two or more constituent phases with appropriate microstructural morphology in a material brings to a combination of improved properties.[1]

The definition of ceramics given by Warren[1] is the following:

Ceramics can be defined as chemically stable, inorganic, crystalline, non-metallic compounds or mixture of such compounds.[1]

The bonds set by the above definition are flexible. A large number of compounds with high melting point, notably the carbides, nitrides, borides and silicides of the transition

metals are borderline ceramics. They often exhibit metallic character being electrically conducting and having poor chemical resistance. They are nevertheless of interest as matrix in ceramic composites. Some examples of ceramics and currently used composites are listed with the most significant properties in Tab. 1.I.

Tab. 1.I: Materials and properties of some ceramics of industrial interest.

Material	**δ**	**Tm**	**E**	**ν**	**Th. cond**	**α**	**ρ**	**K_{Ic}**	**HV**	**Wear resistance**
	g/cm^3	**°C**	**GPa**		**W/mK**	**K^{-1} 0-10^3°C**	**Wm (25°C)**	**MPam$^{1/2}$**	**GPa**	**$K_{Ic}^{3/4}H^{1/2}$**
Al_2O_3	3.99	2050	390	0.23	6.0	8.0	$>10^{15}$	3-5	19	10-14.5
SiC	3.2	2500	440	0.15	40	4.5	~1	3.4	26	12-15
Si_3N_4	3.2	1900	300	0.22	15	3	-	4-6	16	10-15
B_4C	2.5	2450	440	0.18	15	5.5	0.5	3.7	45	17.9
BN h ⊥	2.3	3000	45	-	21	7.5	10^{11}	-	5	-
AlN	3.3	2300	320	0.25	50	6	10^{12}	2.7	13	7.6
TiB_2	4.5	2980	570	0.11	25	5.5	10^{-5}	5-7	30	21
TiC	4.9	3070	450	0.18	30	8.5	10^{-4}	4	30	15.5
TiN	5.4	3090	-	-	30	8.5	10^{-5}	-	20	-
$MoSi_2$	6.3	2100	440	0.17	20	8.5	10^{-5}	5	13	11.8
ZrO_2 t	6.1	2400	-	-	2	12	-	5-10	12	11.5-20
ZrO_2 m	5.6	-	240	0.3	-	15	-	1	-	-
mullite	2.8	1850	150	0.24	5	5.5	-	2	15	6.5

The chemical bonds of ceramic is generally hybrid of covalent and ionic, the proportions of which vary from compound to compound. The characteristic properties resulting from such bonding are, for example, high melting point, high chemical stability, high elastic modulus and low atomic mobility, the latter leading to high hardness and creep resistance but also to brittleness.

1.2 GENERAL PROPERTIES OF ADVANCED CERAMIC MATERIALS

Ceramics can be classified into different groups depending on chemical composition, microstructure and application.[2] From the application point of view, the main difference has to be done between traditional and advanced ceramics.

The traditional ceramics include tableware, pottery, sanitary, ware, tiles, bricks and clinker.

The advanced ceramics include functional ceramics and structural ceramics. The former have been developed and are primarily used for non-mechanical properties such as

thermal insulation, electrical resistance/conductivity, etc. whereas the latter have been developed for application able to bear various forms of mechanical loading, for example high temperature strength and conditions of wear and erosion.

Some fields of application of advanced ceramics are listed in Tab. 1.II.

Tab. 1.II: Fields of application of some advanced ceramics.

Field	Required properties	Materials	Examples
Engine manufacturing	Wear resistance, heat and electrical insulation, low density, resistance to corrosion, high temperature strength	Al_2O_3, ZrO_2,SiC, Si_3N_4	Thermal insulation of combustion chambers, valve seats, spark plugs, turbochargers, gas turbine
Industrial processing engineering	Resistance to corrosion, wear resistance	Al_2O_3, SiC, C (graphite), ZrO_2	Chemical devices, drawing die, slide rings, thread guides, rolls for paper industry
High temperature techniques	Resistance to corrosion, thermal and electrical insulation, high temperature strength	Si_3N_4, SiC, Al_2O_3, C, BN, $MoSi_2$, ZrB_2	Heat exchangers, crucibles, heating conductors, protective tubes for thermocouples, loading devices for materials testing, burner units
Machining of materials	Resistance to corrosion, wear resistance	Al_2O_3, Si_3N_4,SiC, B_4C, TiC, TiN, BN, diamond	Cutting tools, grinding wheels, sandblast nozzles
Medical devices	Resistance to corrosion, physiological compatibility	Al_2O_3, ZrO_2	Bone replacement (hip joints), dental ceramics
Electrical engineering electronics	Electrical insulation, heat conductivity	Al_2O_3, AlN	Substrates for integrated circuits, insulations

The advanced ceramics can be further distinguished among:

- silicate ceramics,
- oxide ceramics,
- non-oxide ceramics.

This classification is a mixture of chemical composition (oxide/non-oxide) and atomic structure (glassy-amorphic/crystalline). The main feature of silicate ceramics is the glassy-amorphic phase with a pronounced pore structure. The main content is SiO_2 with addition of Al_2O_3, MgO, BeO, ZrO_2 and other oxides.

Oxides ceramics are distinguished from silicate ceramics by the dominance of a crystalline phase with only a small content of glassy phase. The most important oxides are: Al_2O_3, BeO, MgO, ThO_2, TiO_2, UO_2, ZrO_2.

The non-oxides ceramics comprise:

- ✓ elements carbon in the form of graphite and diamond,
- ✓ nitrides AlN, BN, Si_3N_4, TiN
- ✓ carbides B_4C, SiC, TiC, WC, ZrC, HfC, TaC
- ✓ borides TiB_2, ZrB_2, HfB_2
- ✓ silicides $MoSi_2$, $TaSi_2$
- ✓ sialons Si_3N_4 with Al_2O_3
- ✓ syalons Si_3N_4 with Al_2O_3 e Y_2O_3.

1.3 PRODUCTION OF ADVANCED CERAMICS

Advanced ceramic materials are characterized by high and specific level of mechanical and functional performances. The achievement of such performances requires a step of design in which the microstructural and functional characteristics and the cost of production have to be taken into consideration. In the case of the advanced ceramic materials, a deep knowledge of the relationships between process, microstructure, and functional properties is necessary. The whole processing has to be optimized in each steps in such a way as to obtain the desired properties.

The processing of ceramics is developed in several stages:

- ✓ choice of raw materials
- ✓ powder treatment
- ✓ moulding
- ✓ thermal treatment
- ✓ finishing

Each of these phase is critical, as each of them can be source of flaws or imperfections in the materials which sum each others up and hinder the achievement of the desired properties.

1.3.1 Starting materials

The raw material are of great importance to get high quality ceramics. The correct evaluation of the appropriate starting powders is critical because, as it is the starting point of the industrial process, it will determine the features of the final product. For

high performances materials strict characteristics are requested. An example of requirements for a typical high performances ceramic is reported in Tab. 1.III.

The purity of starting powder is of essential importance for high temperature behaviour, because impurities may segregate at grain boundary, provoke creep and sliding of amorphous phases and lower the mechanical properties at high temperature. The dimensions are relevant too for the final density of a compact: they should have an optimal size distributions in order to fill the voids and leave the least porosity as possible during the densification. Besides, particles with a high specific surface possess a high free Gibbs energy which is thermodynamically favourable and brings to the decrease of the specific surface area through the densification. Then, finer powders allows the decrease of time and temperature necessary for sintering, thus hindering the grain coarsening.

Tab. 1.III: Characteristics and requirements of starting powders for high performances prodoucts.

Particles dimensions	Small
Particle size distributions	Tight
Particles shapes	(usually) regular and spherical
Agglomerates	As low as possible
Specific surface	High
Reactivity	High
Chemistry	
composition	Homogeneous
impurities	Absent
stoichiometry	Full
phases	Stable

1.3.2 Synthesis and powder processing

The addition of organic or inorganic additives to the starting powder is often necessary as a function of the following processes and of the desired quality in the final products.

The additives can be organic binder, necessary to favour the transition from a powder to a semi manufactured which withstands to handling, lubricants, which favour moulding and pressing operations, plasticizers, which allow the development of plastic deformations, dispersants, that increase the stability of colloidal suspensions, antistatic agents, antifoam agents or inorganic additives which favour the densification.[3]

1.3.3 Moulding

During the moulding stage, powders opportunely treated, are consolidated through different techniques in a green compact. This hand-manufactured is characterized by a high degree of porosity that depends on the kind of the utilized powder, on the underwent treatment and on the particular moulding technique, it generally goes from 50 to 70% of the theoretical density. Through this process the ceramic component is preformed depending on the final application to whose is destined. The objective of this process, beyond giving a shape to the component, is to obtain a high degree of density in the green compact, without cracking and with a homogenous distribution of the porosity. The handmade deriving from the performing is quite brittle and has to be handled with care, nevertheless it has to be transportable and it has to guarantee the workability. For a lot of applications, it might be necessary indeed to obtain ceramic with particular and complex shapes which require the machining of the green before being subjected to the following sintering treatment.

Many shapes can be obtained with various techniques briefly explained in the following.

- Pressing
  - *Uniaxial pressing:* the compacting occurs in a stiff die through the application of a unidirectional pressure. It can be a dry or damp process depending on the amount of humidity lower or higher than 4%. Often binder are added to improve the adhesion of the particles and lubricant to increase the sliding of the particles and so optimizing the packaging. Powders with a high fluency are those obtained through spry drying. Further improvement in this step can be achieved when the die is subjected to ultrasonic pulse during the filling. In this way porosity and big defects can be removed with subsequent increase in the homogeneity.
  - *Cold isostatic pressing:* it consists of the application of pressure in a uniform way in each direction. The pre-compacted powder is placed in a rubber die, immersed in a fluid (glycerine, hydraulic oil, water,…) into a pressure chamber. The fluid transfers the pressure to every part of the die in a uniform way. The deformation of the die is followed by a

compacting of the powder. Also in this case moulding additives, such as lubricant and binder, are used. By this techniques high pressure (more than 500 MPa) can be achieved; by cold isostatic pressing more complex shapes can be obtained then by uniaxial pressing.

- Slip casting

  A ceramic suspension is poured in a porous chalk die, when the suspended particles sediment and the die absorbs the liquid phase, a final solid component is obtained. To improve the sedimentation of the particle this process can be carried out under pressure or in vacuum, otherwise the sedimentation is accelerate through centrifuge of the die and ultrasounds.

- Tape casting

  A fluid mixture composed of ceramic powder, organic or aqueous additives (solvent, binder, plasticizer,…) is poured on a tape, generally celluloid made, while it flows. Thanks to the presence of two doctor-blades, a film of controlled thickness, varying from 200 to 1.3 mm, can be obtained. By this method it is possible to get a variety of supports or multilayered ceramics.

- Injection moulding

  This technology is a variation of polymers moulding processes. A ceramic powder, opportunely mixed with organic binders, assume a paste aspect. When this compound is heated to temperature above the softening temperature of the binders, is injected into the cavities of the die, where it is cooled and solidifies. A debonding treatment is necessary to remove the binders.

- Extrusion

  The extrusion process derives from the metallurgical processes. A mixture of ceramic powder and polymeric additives is rendered homogeneous into a cylinder in vacuum which removes air and bubbles from the mixture, then it is driven into the extrusion chamber through a Archimedes screw and extruded in the desired shape.

- Electrophoresis

  This technique exploits the properties of very fine particles in solution which becomes electrically charged by adsorption of ions on the surface. Under the action of an electric field, the particles migrate to the electrode-die of opposed charge, they set in and increase the component thickness which will be then sintered.

1.3.4 Sintering mechanisms

Because of the high melting point of oxide and non-oxide ceramics, the processing of ceramics requires a heat treatment, during which a powder is consolidated in a dense compact which possesses desired properties and shape. Even if the main objective is the compacting and the elimination of the pores from the green, the control on microstructure is a crucial problem. Studies on sintering deal with the understanding of the process variables as temperature, holding time, particles dimensions and shapes and sintering environment which all contribute to the final microstructure. All the properties of the ceramics, as mechanical and electrical properties, are strongly influenced by the sintering treatment.

The sintering process can be seen as a coordinate variation of the shape of all the grains of a compact powder activated by matter transport mechanisms which allow to fill interparticle voids. The centre of the grains moves the ones along the others thus reducing their dimensions and removing the porosity in the material. In Fig. 1.1 is schematized this principle which gives a full density material with the smallest specific interfacial area.

Fig. 1.1: 2D and 3D ideal changes in shape of the grains during sintering.

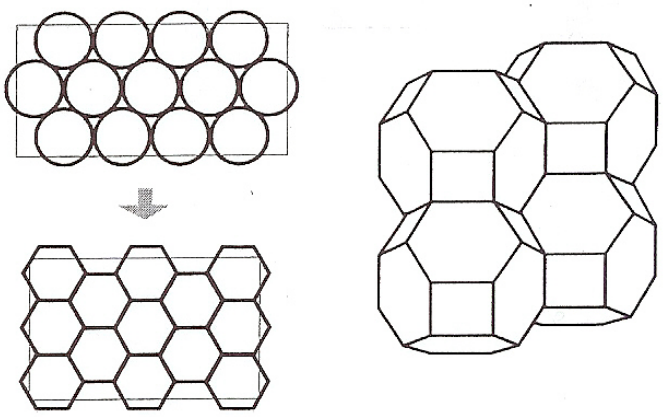

The sintering process brings to a compact material, by the reinforcement of adjacent particles bonds and the removal of porosity. To activate the mass transfer mechanisms (diffusion or creep) and a energy source which sustains the transport (heat, thermal gradient) are needed. The driving force is represented by the diminishing of the Gibbs free energy linked to the decrease of the total volume of the component.

When an atom is transferred from the boundary to a pore, this last shrinks because is partially filled: the free energy decreases as the interfacial surface among the grains later decreases. This mechanism can be expressed by the equation (1):[4]

$$dG_F = \gamma_s\, dA_s + \gamma_b\, dA_b + p\, dV \qquad (1)$$

where:

dA_s: variation of the total area of the pores;

dA_b: variation of the total surfacial area of the grain boundaries;

γ_s and γ_b: specific surfacial area of the pores and of the grains respectively:

p: external applied pressure;

dV: volume variation due to shrinkage.

Three different sintering processes can be outlined depending on composition and the amount of the secondary phases which form during densification. These are: solid state sintering, liquid phase sintering and vitrification.

❖ Solid state sintering: the preformed green is thermally treated at temperature ranging from 0.7 to 0.9 of the melting point. Any liquid phase is present and the solid state atomic diffusion produces necks between the particles and progressively eliminates the porosity. A sketch of the solid state sintering process is reported in Fig. 1.2.

Fig. 1.2: Densification phenomena among grains during solid state sintering.

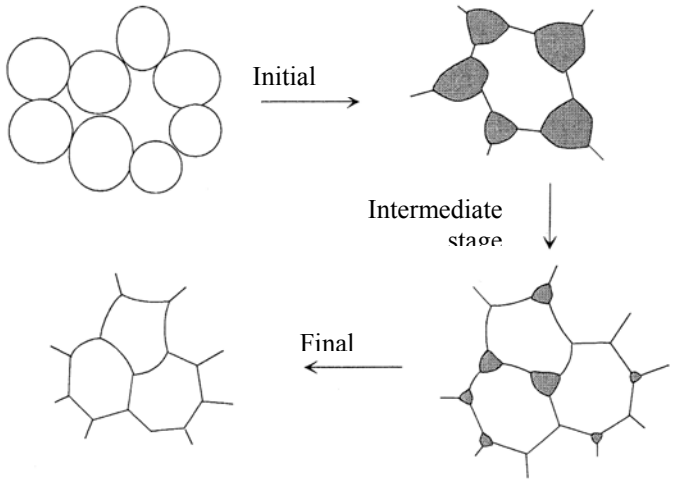

❖ Liquid phase sintering: is classically defined as sintering involving a particulate solid and coexisting liquid during the sintering process. The liquid can result from melting of one component or formation of an eutectic due to the interaction of two or more components. The liquid may be transient or persistent during sintering depending on the solubility relationships. The fundamental requests for a good matter transport and so a good densification are the presence of a liquid phase at the sintering temperature, a good wettability of the solid and a good solubility of the solid into the liquid. Three different stages can be distinguished as shown in Fig. 1.3: rearrangement, solution-reprecipitation, skeleton sintering. The mechanisms of liquid phase sintering have been extensively discussed by Kingery.[5] Classically, the following sequence of sintering stages is thought to be prevailing.

- **Particle rearrangement -** Densification results from particle rearrangement under the influence of capillary forces and the filling of pores by the liquid phase. Due to this mechanism, during the early stage of sintering a much faster densification occurs than in solid state sintering. Parameters like volume fraction of the liquid, solubility, green density, temperature, wetting, etc., strongly affect this step.
- **Solution-reprecipitation - C**onsequences of the solution-reprecipitation processes are microstructural development, shape accommodation and grain growth. Due to the chemical potential gradient generated by capillary forces, smaller grains dissolve in the liquid and through diffusion, the mass is transported to the larger grains where it re-precipitates. This process is known as Ostwald ripening.[6] The process alters the grains shape, which re-accommodate, reduce the porosity and hence shrinkage and densification take place.
- **Solid-state or skeleton sintering** - The last stage is referred to as solid state controlled sintering. The overall shrinkage and densification is very sluggish due to the rigidity of the solid skeleton that inhibits further rearrangement, although microstructural coarsening continues by grain boundary diffusion.

  Ceramics sintered by liquid phase sintering have as advantage, the possibility to be near-net shaped, but on the other side, show low creep resistance at high temperature, because of the softening of amorphous grain boundary phases.

Fig: 1.3: Scheme of the different stage of the liquid phase sintering which shows the microstructural evolution of a green compact.

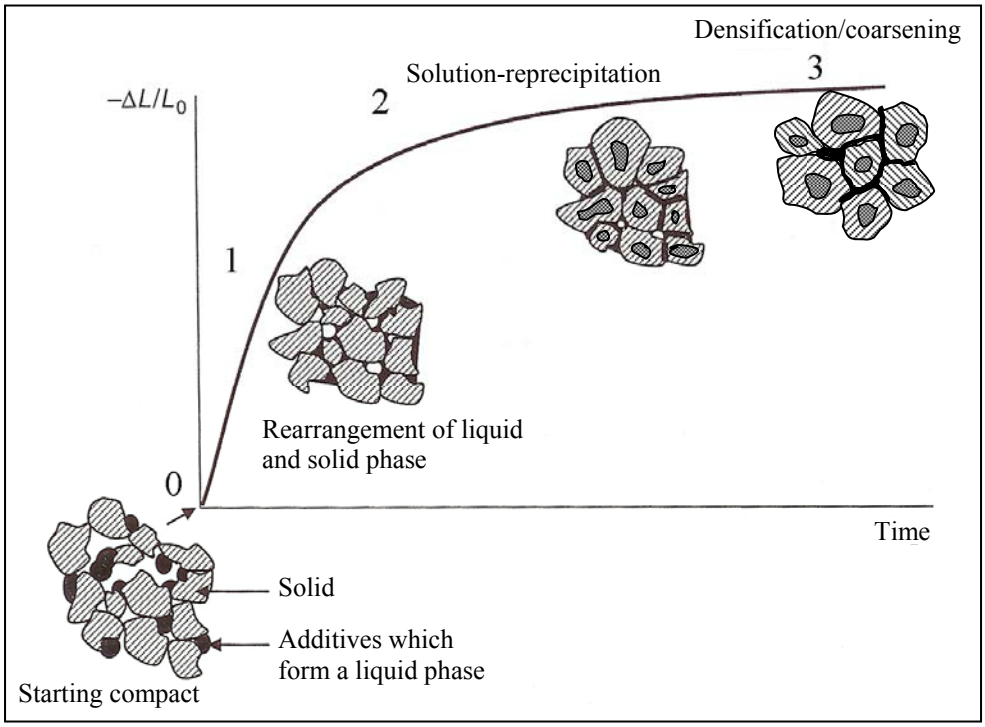

❖ Vitrification/glazing: during the sintering the porosity is filled by a liquid mixture, about 25 vol%, that vitrifies when under cooled. This method is more used in traditional ceramics, for advanced ceramics is avoided as it brings unhomogeneity and most of all to poor mechanical properties.

1.3.5 Sintering technologies

Several sintering technologies will be briefly described.

❖ *Traditional sintering:* a green component is subject to a thermal cycle and a holding time in a determinate temperature. It can be performed in air, under vacuum or in controlled environment. In this study, a graphite furnace (ASTRO Thermal Technology Inc, see Fig. 1.4) is mainly utilized which can achieve a maximum temperature of 2100°C and the heating is through graphite heating elements.

Fig. 1.4: The furnace ASTRO Thermal Technology Inc.

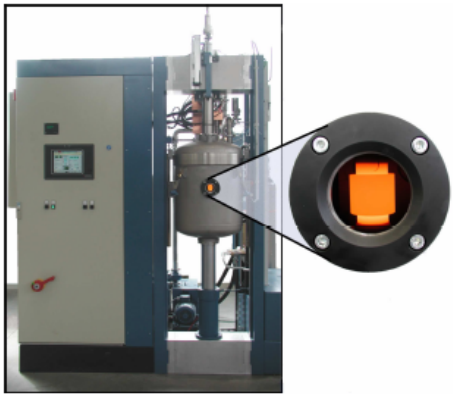

- *Reactive sintering:* Synthesis and sintering of the product occur at the same time during the heating treatment. For example in the case of silicon nitride, a preformed green of silicon is placed in a furnace and react with flowing nitrogen at temperature around 1200°C. Nitrogen penetrates in the porous structure and gives rise to silicon nitride. Consolidation and densification take place at the same time.
- *Hot pressing:* while the temperature increases, a uniaxial pressure is applied to a pre-compacted powder in order to accelerate the densification. The process occurs under vacuum or in a controlled environment. This techniques allows to record the shrinkage of the material as a function of time and temperature, by the relative movement of the rams. By this way the sintering process can be controlled and the process parameters can be modified during the hot pressing. The collected data are utilized for kinetic studies. An example of a hot pressing, principle of functioning and apparatus, is reported in Fig. 1.5.
- *Hot isostatic pressing:* during the heating of the component a uniform pressure is applied in all the directions. The inner pressurization is obtained by gases as nitrogen or argon, which act on the powder previously sealed under vacuum with a metallic or glassy sheath which is impermeable to the same gas.
- *Self-propagating high-temperature synthesis:* it's a particular case of the previous method. An electric arc is switched on through a powder mixture in air or in a controlled environment which triggers an exothermic chain reaction propagating at velocity of 0.1-20 cm/sec and self-sustaining. Temperatures of 3500°C can be

achieved. This techniques is quite economical thanks to its fastness and the absence of a continuously fed furnace.

Fig. 1.5: Hot pressing: a) complete apparatus, b) chamber and rams.

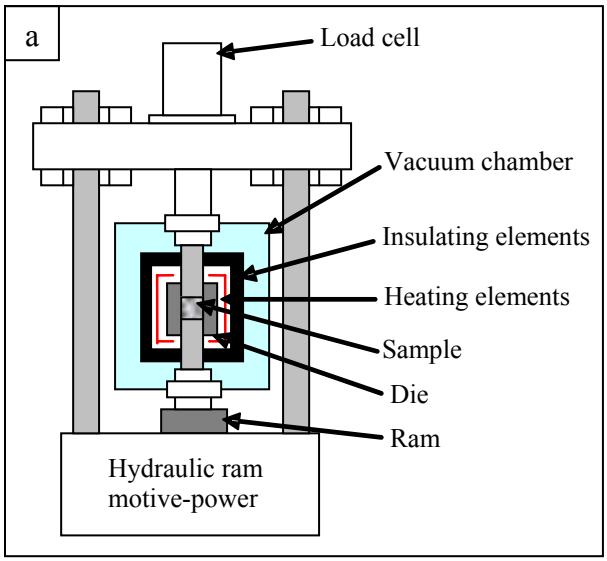

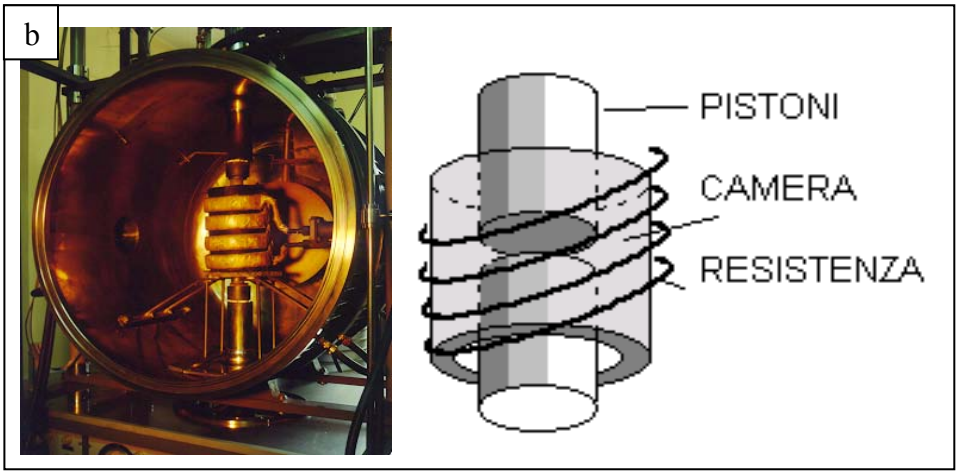

- *Explosive compacting:* a green compact is placed in a cylindrical crucible externally covered with an explosive charge. The detonation is lightened at one of the extremity of the crucible, this generates a shock wave, which propagates along the axis of the cylinder thus radially compressing the material. The main drawback is the high amounts of defects and cracks in the final product.
- *Microwave sintering:* thanks to the high dielectric constant of ceramic materials, the sample is heated from inside, in spite of furnish heat from outside. The precompacted sample is invested by a radiation of suitable wave length which produces a thermal flow and the densification occurs at higher speed than in the

previous cases. This technique allows high heating rates, but it's difficult to achieve a high degree of uniformity in the sample. It was observed indeed that high microwave frequencies tend to preferably heat the external part of the compact. A solution to this problem is to utilize multi-frequency microwave generators which lead to higher homogeneity during heating.

- *Spark plasma sintering:* a direct current passes through the precompacted powder in a graphite crucible at 5000-20000 A, depending on the sample dimensions, with an applied pressure of 10-100 MPa. By this technique it is possible to obtain very hig heating rate of the order of 600°C/min or even higher. The sintering mechanisms involved in this process are still a matter of discussion but the most diffused opinion is that the plasma formed around the particles notably increase the densification rates and the diffusive processes in such a way that the densification requires holding time of few minutes and lower temperatures with respect to conventional techniques.[7-10] A drawn of the apparatus is reported in Fig. 1.6.

Fig. 1.6: Spark plasma sintering apparatus.

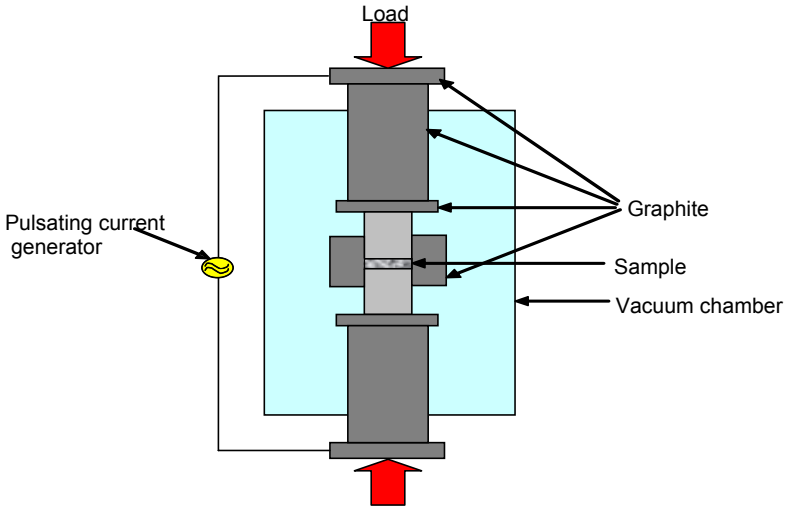

1.3.6 Finishing

Even if modern sintering techniques allow to obtain near net shape products with no need of further machining, in most cases the processing furnishes materials which posses slightly irregular shapes or need surface finishing. A good state of finishing can be obtained through a series of techniques as machining with diamond tools, which is expensive and takes long times, laser machining or electron discharge machining, if

the material is conductive. This last techniques, EDM, exploits discharge phenomena between an electrode (cathode) and the same rough material (anode) divided by a thin layer containing a dielectric fluid. This stage of machining is long, complex and expensive and can notably influence the final performances of the component. As a matter of fact, cutting operations or machining of sintered materials often generate surface flaws which have to be taken into account before the employ.

1.4 SiC-BASED CERAMICS

Silicon-carbide-based ceramics are promising materials for applications in gas turbine components, heat exchangers, and wear-resistant components. Most of these applications require good strength and toughness, high thermal conductivity and good environmental stability at high temperature.

Silicon carbide was first synthesized in 1891 by Acheson by passing an electric current through a mixture of carbon powder and clay. The material was originally thought to be a mixture of carbon and corundum (aluminum oxide) and trademarked *Carborundum*. Acheson soon determined that it was actually silicon carbide. The product was an immediate commercial success as an abrasive.[11] The Acheson process is still the major production process. In the US, over 115,000 metric tons of silicon carbide were produced in 1994 with a value estimated at $40 million, much of which was for abrasives and metallurgical uses.[12]

Although silicon carbide can fulfill requirements of high strength, one major problem is that SiC hardly densifies without additives, because of the covalent nature of Si-C bonding and the low self-diffusion coefficient. Solid state sintering at temperature around 2100°C was a routine process to densify silicon carbide. The pressureless consolidation of this material was pioneered by Prochazka, who found that small additions of boron and carbon drastically improve the shrinkage kinetics of SiC.[13] Following the basic developments, a variety of sintering additives were studied during the past decades, including boron and B-compounds, aluminium and Al-compounds and Be-compounds, all being used in combination with carbon. An innovative approach to pressureless sintering of silicon carbide was initiated in the early 1980 with addition of

oxides to promote the densification of SiC via a liquid phase. Wide variety of rare-earth oxides were investigated in combination with alumina and/or boron compounds to densify SiC and dense and fine materials were obtained without excessively high processing temperatures.[14-16] Materials with improved sinterability and room-temperature strength around 700 MPa were obtained by careful optimization of the processing, sintering additives and sintering cycles.[16] However, the major problems encountered with this class of liquid-phase sintered materials are the low fracture toughness and the degradation of strength at high temperature. The relatively low toughness (3 $MPa \cdot m^{0.5}$)[16] is caused by a fine equiaxed microstructure, which does not provide any crack deflection or crack bridging phenomena. On the other hand, the high-temperature strength is degraded by the softening of residual secondary phases deriving from the sintering aids.

During the past 30 years, many different aspects have been explored, such as the fundamental properties of SiC, powder production, porous and dense SiC and amorphous thin films for applications in electronics. It was found that SiC possesses a unique combination of properties, such as high strength at ambient and high temperatures, good thermal shock resistance due to a low coefficient of thermal expansion, relatively good resistance to oxidation compared to other high-temperature structural materials, high wear resistance and high thermal conductivity. In addition, the density of SiC is only about 40% of superalloys. This combination of properties makes it possible for SiC to replace metallic components that are conventionally used as structural materials.

Since some aspects of the production of dense SiC-based materials are still critical, considerable efforts are continuously addressed to find and optimize sintering aids and processing.

1.5 ULTRA HIGH TEMPERATURE CERAMICS

The need for high temperature materials that can maintain mechanical strength and operate with limited oxidation at temperatures >2000°C have driven the development of a variety of ceramics and ceramic composites. These refractory materials have come to

be known as Ultra High Temperature Ceramics (UHTCs).[17] The earliest work on UHTCs began in the 1960's by ManLabs under a research program funded by the Air Force Materials Research Lab (AFML). Compared to the other refractory compounds such as carbides and nitrides, ManLabs determined that intermetallic diboride compounds offer the highest degree of oxidation resistance. In comparison to carbides and nitrides, diborides also have high thermal conductivity which gives them good thermal shock resistance. Through further studies, HfB_2 and ZrB_2 were chosen as the most promising candidates for use in high temperature applications. It was shown that all UHTCs are characterized by very strong bonding which gives them high temperature structural stability. It also makes them very difficult to fabricate and, so far, only limited research has involved these materials despite their potentialities. Conventional hot pressing of pure UHTCs typically yields porous materials with poor mechanical properties. But the addition of sintering additives helps the densification thus obtaining materials with strengths higher than 500 MPa. Work by ManLabs demonstrated that SiC additions to UHTC powders improved densification and increased oxidation resistance of the composites. High temperature oxidation testing was conducted in both furnace studies as well as in simulated re-entry environments (arc jet) and gave excellent results.

After the ManLabs work, further research on UHTCs slowed until the early 1990's when NASA Ames renewed efforts. Work there resulted in two hypersonic flight experiments, SHARP-B1 and SHARP-B2 that proved the successful application of monolithic high temperature ceramic composites on sharp leading edges. Since then, NASA Glenn has also started conducting research to further improve UHTC oxidation resistance. Current work by the Navy is also seeking to provide a better understanding of the oxidation of not only ZrB_2 and HfB_2 but HfC, ZrC and HfN as well. Clearly, the potential applications for UHTCs span a wide number of needs arising from future military, industrial and space based projects. While continued work has provided valuable insight on the performance of UHTCs, consistent ongoing research efforts are required if future applications are to be realized.

References

1 R. Warren, "Ceramic-matrix composites", BLACKIE, USA: Chapman & Hall, New York.

2 D. Munz, T. Fett, "Ceramics- Mechanical properties, Failure behaviour, Materials Selection", Eds: R. Hull, R. M. Osgood, H. Sakaki, A. Zunger, Materials Science, Springer (1999) 3.

3 A. Bellosi, rapporto interno n.87270 CNR IRTEC Faenza.

4 A. Bellosi, rapporto interno n. 03/90 CNR IRTEC, Faenza.

5 W. D. Kingery, H. K. Bowen, D. R. Uhlmann "Introduction to Ceramics", 2nd Edition, New York, John Wiley, Academic Press, (1960).

6 W. Ostwald, "Lehrbuch der Allgemeinen Chemie", vol. 2, part 1. Leipzig, Germany, (1896).

7 J. R. Groza, A. Zavaliangos, Mat. Sci. Eng., A287 (2000) 171-177.

8 D. S. Parrera, M. Tokita and S. Morica, J. Eur. Ceram. Soc., 4 (1998) 401-404.

9 L. Gao, H. Z. Wang, J. S. Hong, H. Miyamoto, K. Miyamoto, Y. Nishikawa, S. D. D. L. Torre, J. Eur. Ceram. Soc., 19 (1999) 609-613.

10 L. Gao, H. Wang, H. Kawaoka, T. Sekino and K. Niihara, J. Eur. Ceram. Soc., 22 (2000) 2149-2152.

11 Parche, M. C., "Fact about Silicon Carbide", The Carborundum Company, Niagara Falls, NY 1961.

12 Ault, N. N., and Crowe, J. T., Silicon Carbide, Ceramic Bulletin, 5, (1991)70.

13 S. Prochazka, Proceedings of the Conference on Ceramic for High Performance Applications (Hyannis, MA, 1973) Ed. By J. J. Burke, A. E. Gorum, R. M. Katz. Brook Hill Publishing Co., (1975) 77-13.

14 F. K Van Dijen and E. Mayer, J. Europ. Ceram Soc. 16 (1996) 413.

15 E. W. Dressler and R. Riedel, Int. J. Refractory Metals and Hard Materials, 15 (1997) 13.

16 L. K. Falk, J. Europ. Ceram. Soc.17 (1997) 983.

17 M. J. Gash, D. T. Ellerby, S. M. Johnson, "Ultra High Temperature ceramic composites" in "Handbook of Ceramic Composites", ed by Narottam P. Bansal, NASA Glen Research Center, USA, (2005) Kluwer Academic Publishers, Boston.

CHAPTER 2

ANALYSIS TECHNIQUES

2.1 MICROSTRUCTURAL CHARACTERIZATION

Microstructure can be defined as the whole compositional, crystallographic, morphological and texitural characteristics of the phases constituting a material. Studying microstructure means analyzing chemical composition, crystallographic phases, quantity, spatial distribution and mean grain size of the constituting phases, and the presence of flaws into a material.

The analytical techniques that will be performed in the present work are X-Ray Diffraction (XRD), Scanning Electron Microscopy (SEM) and Transmission Electron Microscopy (TEM). A description of the principle is given in the following sections for each technique.

2.1.1 X-ray powder diffraction

X-ray scattering techniques are a family of non-destructive analytical techniques which reveal information about the crystallographic structure, chemical composition, and physical properties of materials and thin films. These techniques are based on observing the scattered intensity of an X-ray beam hitting a sample as a function of incident and scattered angle, polarization, and wavelength or energy.[1]

X-rays are electromagnetic radiation with a wavelength of about 1 Å (10^{-10} m), which is about the same size of an atom. They occur in that portion of the electromagnetic spectrum between gamma-rays and the ultraviolet. The discovery of X-rays in 1895 enabled scientists to probe crystalline structure at the atomic level. X-ray diffraction has been in use in two main areas, for the fingerprint characterization of crystalline materials and the determination of their structure. Each crystalline solid has its unique characteristic X-ray powder pattern which may be used as a "fingerprint" for its identification. Once the material has been identified, X-ray crystallography may be

used to determine its structure, i.e. how the atoms pack together in the crystalline state, what the interatomic distance and angle are, etc. X-ray diffraction is one of the most important characterization tools used in solid state chemistry and materials science. We can determine the size and the shape of the unit cell for any compound most easily using the diffraction of X-rays. Here the background of the technique.

The distance between two crystallographic planes (d) of polycrystalline materials have dimensions comparable to the wavelength of X-rays and as a consequence the interaction between electromagnetic radiation and atoms can give rise to interference phenomena. The crystallographic plane reflects the incident radiation and the θ angle of constructive interference is determined (Fig. 2.1).

Fig. 2.1: Reflection of x-rays from two planes of atoms in a solid.

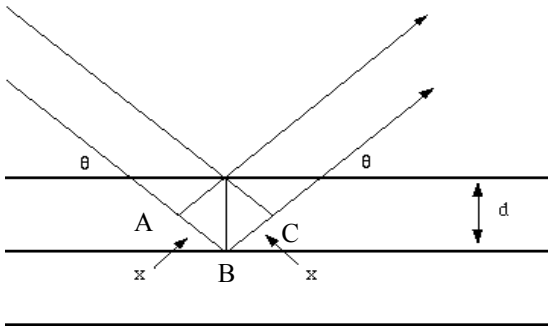

The path difference between two waves is (1) :

$$AB + BC = 2\,d\sin\theta \qquad (1)$$

When $AB+BC=n\lambda$, where n integer, the reflected waves are in phase and a constructive interference occurs . A luminous reflection is observed when θ angle satisfy Bragg law (2):

$$n\,\lambda = 2\,d\sin\theta \qquad (2)$$

From x-ray diffraction pattern, strong intensities can be seen for a number of values of n; from each of these lines we can calculate the value of d, the interplanar spacing between the atoms in the crystal.

The X-ray diffraction experiment requires X-ray source, the sample under investigation and a detector to collect the diffracted X-rays. In Fig 2.2 is reported a scheme of a powder X-ray diffractometer.

Fig. 2.2: Schematic of an X-ray powder diffractometer.

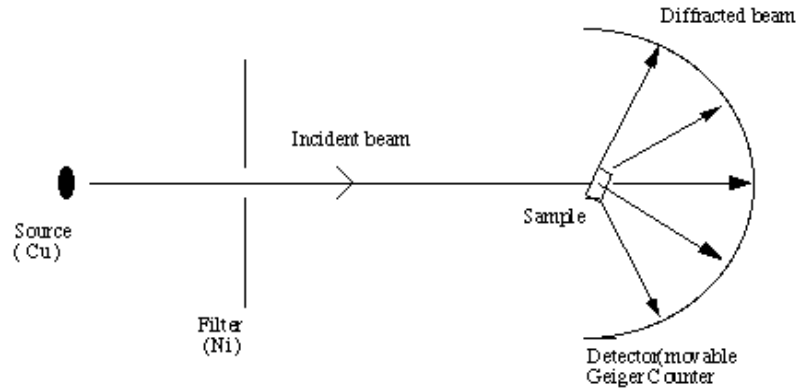

The most commonly used X-ray radiation is that emitted by copper, whose characteristic wavelength for the K radiation is 1.5418 Å. When the incident beam hits a powder sample, diffraction occurs in every possible orientation of 2θ. The diffracted beam may be detected by using a moveable detector, such as a Geiger counter, which is connected to a chart recorder. In normal use, the counter is set to scan over a range of 2θ values at a constant angular velocity. Routinely, a 2θ range of 5 to 70 degrees is sufficient to cover the most useful part of the powder pattern. The scanning speed of the counter is usually 2θ of 1 degrees min^{-1} and therefore, about 30 minutes are needed to obtain a trace.

By the X-ray powder method it is also possible to determine mean grain size of the crystallites composing the microcrystalline powder, lattice constants, induced stress in samples which underwent particular strain and preferential orientation of the grains. All these applications make the X-ray diffraction one of the most important technique in materials science.[1]

2.1.2 Scanning electron microscope

The Scanning Electron Microscope (SEM) is a microscope that uses electrons rather than light to form an image. There are many advantages in using the SEM instead of a light microscope. The SEM has a large depth of field, which allows a large amount of the sample to be in focus at the same time. Preparation of the samples is relatively easy since most SEMs only require the sample to be conductive. A sputter coater is necessary if the sample is not conductive: it is used gold to observe the morphology of the sample or carbon to investigate the composition and the present phases. The

combination of higher magnification, larger depth of focus, greater resolution, and ease of sample observation, makes the SEM one of the most heavily used instruments in materials science. The basic theory of SEM functioning is explained.[2]

A beam of electrons is generated in the electron gun, located at the top of the column, (in Fig. 2.3).

Fig. 2.3: Beam's path through the column.

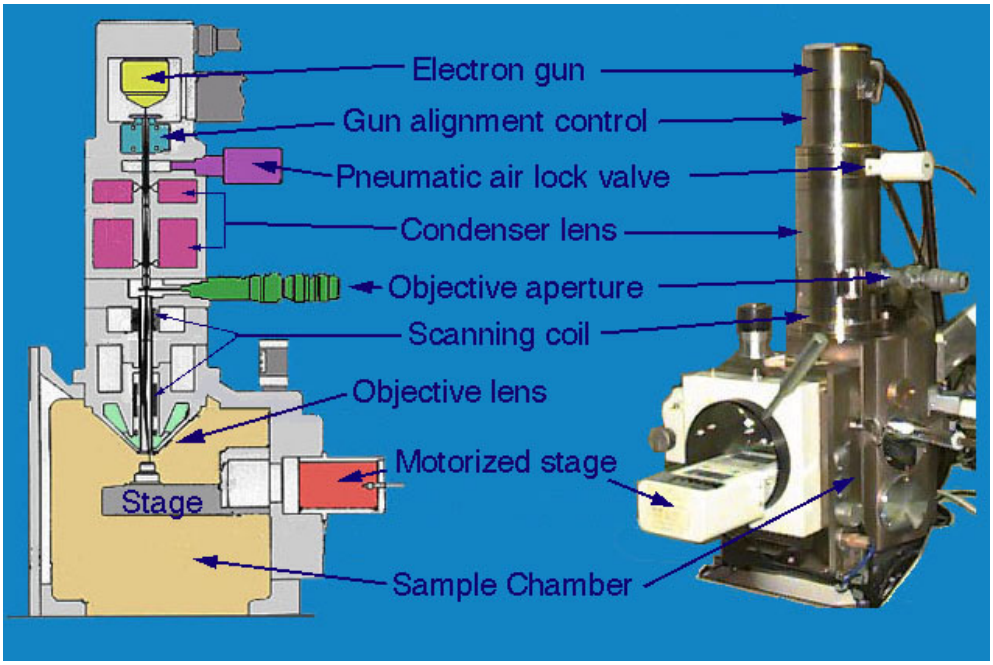

The most common filament is the tungsten hairpin gun. This filament is a loop of tungsten which functions as the cathode. A voltage is applied to the loop, causing it to heat up. The anode, which is positive with respect to the filament, forms powerful attractive forces for electrons. This causes electrons to accelerate toward the anode. Some accelerate right by the anode and on down the column, to the sample. Other types of filaments are lanthanum hexaboride (LaB_6) filaments and field emission guns.

The electron beam hits the sample, provoking the expulsion of electrons from the sample. These electrons are collected by a secondary detector or a backscattered detector, converted to a voltage, and amplified. The amplified voltage is applied to the grid of the CRT and causes the intensity of the spot of light to change. The image consists of thousands of spots of varying intensity on the face of a CRT that correspond to the topography of the sample.

While all these signals are present in the SEM, not all of them are detected and used for information. The most commonly used signals are the secondary electrons, the backscattered electrons and X-rays.

A schematic of the interaction between sample and incident electron beam is shown in Fig. 2.4.

Fig. 2.4: Electron beam/specimen interaction.

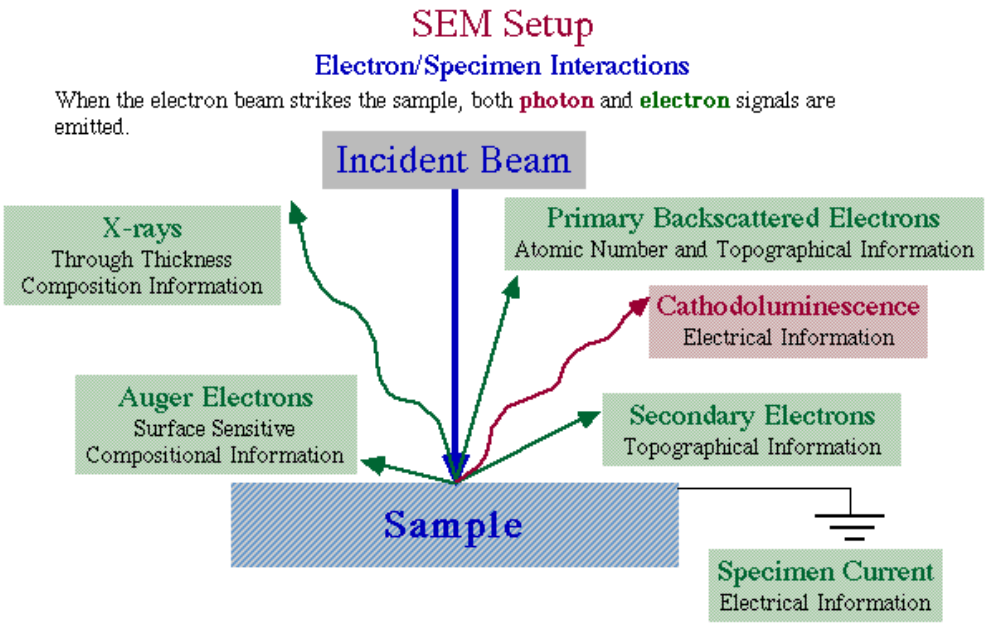

Secondary electrons are specimen electrons that obtain energy by inelastic collisions with beam electrons. They are defined as electrons emitted from the specimen with energy less than 50 eV.

Secondary electrons are predominantly produced by the interactions between energetic beam electrons and weakly bonded conduction-band electrons in metals or the valence electrons of insulators and semiconductors. There is a great difference between the amount of energy contained by beam electrons compared to the specimen electrons and because of this, only a small amount of kinetic energy can be transferred to the secondary electrons.

Elastic scattering occurs between the negative electron and the positive nucleus. This is essentially Rutherford scattering. Sometimes the angle is such that the electron comes back out of the sample. These are backscattered electrons.

During inelastic scattering, energy is transferred to the electrons surrounding the atoms and the kinetic energy of the energetic electron involved decreases. A single inelastic event can transfer a various amount of energy from the beam electron ranging from a fraction to many keV. The main processes include phonon excitation, plasmon excitation, secondary electron excitation, continuum X-ray generation, and ionization of inner shells. In all processes of inelastic scattering, energy is lost, though different processes lose energy at varying rates.

During utilization, a good vacuum level inside the column must always be insured for several reasons. If the sample is in a gas filled environment, an electron beam cannot be generated or maintained because of a high instability in the beam. Gases could react with the electron source, causing it to burn out, or could produce random discharges and lead to instability in the beam. The transmission of the beam through the electron optic column would be also hindered by the presence of other molecules. These molecules, which could come from the sample or the microscope itself, could form compounds and condense on the sample. This would lower the contrast and obscure details in the image.

The spatial resolution of the SEM depends on the size of the electron spot, which in turn depends on both the wavelength of the electrons and the electron-optical system which produces the scanning beam. The resolution is also limited by the size of the interaction volume, or the extent to which the material interacts with the electron beam. The spot size and the interaction volume are both large compared to the distances between atoms, so the resolution of the SEM is not high enough to image individual atoms, as it is possible in the shorter wavelength (i.e. higher energy) transmission electron microscope. The SEM has compensating advantages, though, including the ability to image a comparatively large area of the specimen, the ability to image bulk materials (not just thin films or foils) and the variety of analytical modes available for measuring the composition and properties of the specimen. Depending on the instrument, the resolution can fall somewhere between less than 1 nm and 20 nm. The world's highest SEM resolution is obtained by the Hitachi S-5500. Resolution is 0.4 nm at 30kV and 1.6 nm at 1kV. In general, SEM images are easier to interpret than TEM images.

2.1.3 Transmission electron microscope

It is well established that Transmission Electron Microscopy (TEM) is a very helpful and powerful technique to characterize microstructures of materials in detail. It should be emphasized that this technique allows the gathering of a wide variety of different information with respect to microstructure and/or composition with high spatial resolution. The main areas of information covered by TEM investigations are:[3,4]

- conventional imaging;
- electron diffraction;
- chemical microanalysis-EDX, EELS;
- high-resolution imaging;
- magnetic structure imaging-Lorentz microscopy.

Apart from diffraction data, obtained by either selected area (SAD) or convergent beam electron diffraction (CBED) techniques, which allow phase identification as well as space group determination or residual stress analysis, one of the major contributions of TEM to materials science is the enlarged understanding of materials performance.[5-8] This is based on the correlation between microstructural features observed during TEM inspection and bulk material properties. In order to tailor materials to meet specific requirements such as high temperature performances, the relationship between processing, microstructure, and mechanical behaviour has to be known.

However, it should be underlined that the information obtained by TEM with respect to the overall ceramic microstructure is the final result of a number of processing steps involved, each of which plays an important role during microstructure development.

2.1.3.1 Components

A TEM is composed of several parts, which include a vacuum system in which the electrons travel, an electron emission source for generation of the electron stream, a series of electromagnetic lenses, as well as electrostatic plates. The latter two allow the operator to guide and manipulate the beam as required. Also required is a device to allow the insertion into, motion within, and removal of specimens from the beam path. Imaging devices are subsequently used to create an image from the electrons that exit the system. A schematic of a transmission electron microscope is reported in Fig. 2.5.

Vacuum system - In order to allow for uninterrupted passage of electrons, the TEM must be evacuated to low pressures, typically on the order of 10^{-4} to 10^{-8} kPa. The need for this is twofold, firstly the allowance for the voltage difference between the cathode and the ground without generating an arc, and secondly to reduce the collision frequency of electrons with gas atoms to negligible levels, this effect is characterised by the mean free path. As the TEM, unlike a CRT, is a system where components must be replaced, specimens inserted and, particularly on older TEMs, film cartridges must be replenished, the ability to re-evacuate a TEM on a regular basis is required. As such, TEMs are equipped with extensive pumping systems and are not permanently vacuum sealed. Poor vacuum in a TEM can cause several problems, from deposition of gas inside the TEM onto the specimen as it is being viewed through a process known as electron beam induced deposition, or in more severe cases damage to the cathode from a electrical discharge. Vacuum problems owing to specimen sublimation are limited by the use of a cold trap to adsorb sublimated gases in the vicinity of the specimen.

Fig. 2.5: Layout of components in a basic TEM. The electron source of the TEM is at the top, where the lensing system (4,7,8) focuses the beam on the specimen and then projects it onto the viewing screen (10). The beam control is on the right (13,14)

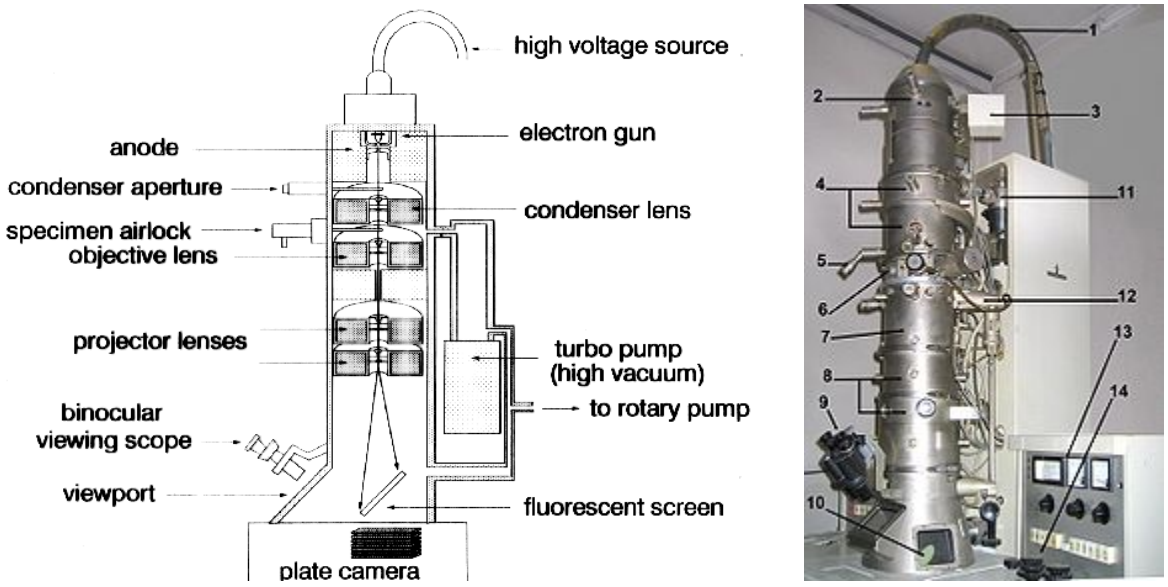

Electrons - Theoretically, the maximum resolution, d, that one can obtain with a light microscope has been limited by the wavelength of the photons that are being used to probe the sample, λ and the numerical aperture of the system, NA, according to (3):

$$d = \frac{\lambda}{2\,n\,\sin\alpha} \approx \frac{\lambda}{2\,\mathrm{NA}} \tag{3}$$

In optics, the numerical aperture (NA) of an optical system is a dimensionless number that characterizes the range of angles over which the system can accept or emit light.

In the early twentieth century, scientists theorised ways of getting around the limitations of the relatively large wavelength of visible light (wavelengths of 400–700 nm) by using electrons. Like all matter, electrons have both wave and particle properties (as theorized by Louis-Victor de Broglie), and their wave-like properties mean that a beam of electrons can be made to behave like a beam of electromagnetic radiation. The wavelength of electrons is found to be given by equating the de Broglie equation to the kinetic energy of an electron. An additional correction, (4), must be introduced to account for relativistic effects, as in a TEM an electron's velocity approaches the speed of light.

$$\lambda_e \approx \frac{h}{\sqrt{2m_0E(1+\frac{E}{2m_0c^2})}} \tag{4}$$

Electrons generated by thermionic emission from a filament, or alternatively by field emission are accelerated by an electric potential (characteristic voltage) and focused by electrostatic and electromagnetic lenses onto the sample. The transmitted beam contains information about electron density, phase and periodicity; this beam is used to form the image.

Source formation - From the top down, the TEM consists of an emission source, which may be a tungsten filament, or a LaB_6 source, see Fig. 2.6. For tungsten, this will be of the form of either a hairpin-style filament, or a small spike-shaped filament. LaB_6 sources utilize small single crystals.

Fig. 2.6: Electron source: a) LaB_6 filament and b) hairpin style tungsten filament.

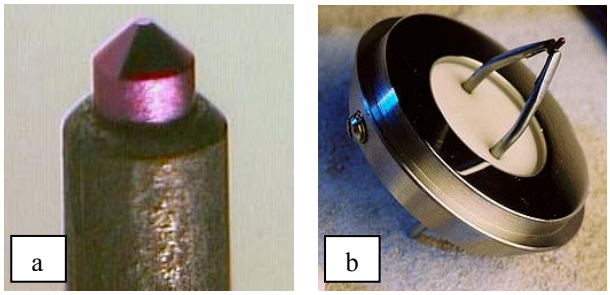

By connecting this gun to an HV source (typically ~120 kV for many applications) and giving sufficient current, the gun will begin to emit electrons into the vacuum either by thermionic effect or field emission. Once extracted, the upper lenses of the TEM allow for the formation of the electron probe to the desired size and location for later interaction with the sample.

Manipulation of the electron beam is performed using two physical effects. Firstly, the interaction of electrons with a magnetic field will cause electrons to move according to the right hand rule, thus allowing for electromagnets to manipulate the electron beam. The use of magnetic fields allows for the formation of a magnetic lens of variable focusing power. Additionally, electrostatic fields can cause the electrons to be deflected through a constant angle. Coupling of two deflections in opposing directions with a small intermediate gap allows for the formation of a shift in the beam path, this being used in TEM for beam shifting, subsequently this is extremely important to STEM (Scanning-TEM). From these two effects, as well as the use of an electron imaging system, sufficient control over the beam path is possible for TEM operation. Additionally, the optical configuration of a TEM can be rapidly changed, unlike that for an optical microscope, as lenses in the beam path can be enabled, have their strength changed, or be disabled entirely simply via rapid electrical switching, the speed of which is only limited by the magnetic hysteresis of the lenses.

Optics - The lenses of a TEM allow for beam convergence, with the angle of convergence as a variable parameter, giving the TEM the ability to change magnification simply by modifying the amount of current that flows through the coil, quadrupole or hexapole lenses. The quadrupole lens is an arrangement of electromagnetic coils at the vertices of the square, enabling the generation of a lensing

magnetic fields, the hexapole configuration simply enhances the lens symmetry by using six, rather than four coils.

Typically a TEM consists of three stages of lensing. The stages are the condensor lenses, the objective lenses, and the projector lenses. The condensor lenses are responsible for primary beam formation, whilst the objective lenses focus the beam down onto the sample itself. The projector lenses are used to expand the beam onto the phosphor screen or other imaging device, such as film. The magnification of the TEM is due to the ratio of the distances between the specimen and the objective lens' image plane. Additional quad- or hexapole lenses allow for the correction of asymmetrical beam distortions, known as astigmatism. It is noted that TEM optical configurations differ significantly with implementation, with manufacturers using custom lens configurations, such as in spherical aberration corrected instruments, or TEMs utilising energy filtering to correct electron chromatic aberration.

Display - Imaging systems in a TEM consist of a phosphor screen, which may be made of fine (10-100 um) particulate zinc sulphide, for direct observation by the operator. Optionally, an image recording system such as film based or doped YAG screen coupled CCDs.

Specimen stage - The specimen stage design allows for the external insertion of a TEM sample into the vacuum, ideally with minimal disruption to the vacuum inside the TEM. To allow for the transport of samples between multiple TEMs, a common standard of sample "grid" design is a 3 mm diameter brass ring, with a thickness of 100 um and an inner diameter of approximately 2.5 mm into which the sample is placed. The TEM stage and holder pair are designed to accommodate such specimens, although a wide variety of designs of stages and holder exist.

Once inserted into a TEM, the sample has often to be manipulated to present the region of interest to the beam, sometimes, such as in single grain diffraction, in a specific orientation. To accommodate this, the TEM stage includes a mechanism for the translation (XYZ) and often rotation of the sample. Thus a TEM stage may provide four degrees of freedom for the motion of the specimen. Additional degrees of freedom can be provided by specialised holder designs. The design criteria of TEM stages are complex, owing to the simultaneous requirements of mechanical and electron-optical constraints and have thus generated many unique implementations.

Two main designs for stages in a TEM exist, the top entry and the side-entry version.[12] Each design must accommodate the matching holder to allow for specimen insertion without either damaging delicate TEM optics nor allowing gas into the TEM vacuum.

Insertion procedures for side entry TEM holders typically involve the rotation of the sample to trigger micro switches that initiate different pump cycles to minimise vacuum leakage into the chamber.

2.1.3.2 Imaging

Imaging methods in TEM utilize the information contained in the electron waves exiting from the sample to form an image. The projector lenses allow for the correct positioning of this electron wave distribution onto the viewing system. The observed intensity of the image, I, assuming sufficiently high quality of imaging device, can be approximated as proportional to the time-average amplitude of the electron wavefunctions, where the wave which form the exit beam is denoted by Ψ, according to (5):

$$I(x) = \frac{k}{t_1 - t_0} \int_{t_0}^{t_1} \Psi\Psi^* dt \tag{5}$$

Different imaging methods therefore attempt to modify the electron waves exiting the sample in a form that is useful to obtain information with regards to the sample, or beam itself. From the previous equation, it can be deduced that the observed image depends not only on the amplitude of beam, but also on the phase of the electrons, although phase effects may often be ignored at lower magnifications. At higher resolutions, phase effects dominate the image, complicating analysis as well as modifying the preferred operating conditions. For example, typically to improve the contrast in the image, the TEM may be operated at a slight defocus to enhance contrast, owing to convolution by the contrast transfer function due to the TEM optics.

Contrast Formation - Contrast formation in the TEM greatly depends on the mode of operation. Complex imaging techniques which utilize the unique ability to change lens strength or to deactivate a lens allows for many operating modes. These modes may be used to discern information that is of particular interest.

The most common mode of operation for a TEM is the Bright Field imaging mode. In this mode the contrast formation, when considered classically, is formed directly by blocking electrons deflected away from the optical axis of the microscope by placing the aperture to allow only unscattered electrons through (Fig. 2.7a). This produces a variation in the electron intensity that reveals information on the crystal structure, and can be viewed on a fluorescent screen, or recorded on photographic film or captured electronically. This technique is particularly sensitive to extended crystal lattice defects in an otherwise ordered crystal. As the local distortion of the crystal around the defect changes the angle of the crystal plane, the intensity of the scattering will vary around the defect. As the image is formed by the distortion of the crystal planes around the defect, the contrast in these images does not normally coincide exactly with the defect, but is slightly to one side.

It is also possible to produce an image from electrons deflected by a particular crystal plane. By either moving the aperture to the position of the deflected electrons, or tilting the electron beam so that the deflected electrons pass through the centered aperture, an image can be formed by only deflected electrons, known as a *Dark Field imaging* (Fig. 2.7b).

Fig. 2.7: Beam path in a) bright field and b) dark field imaging.

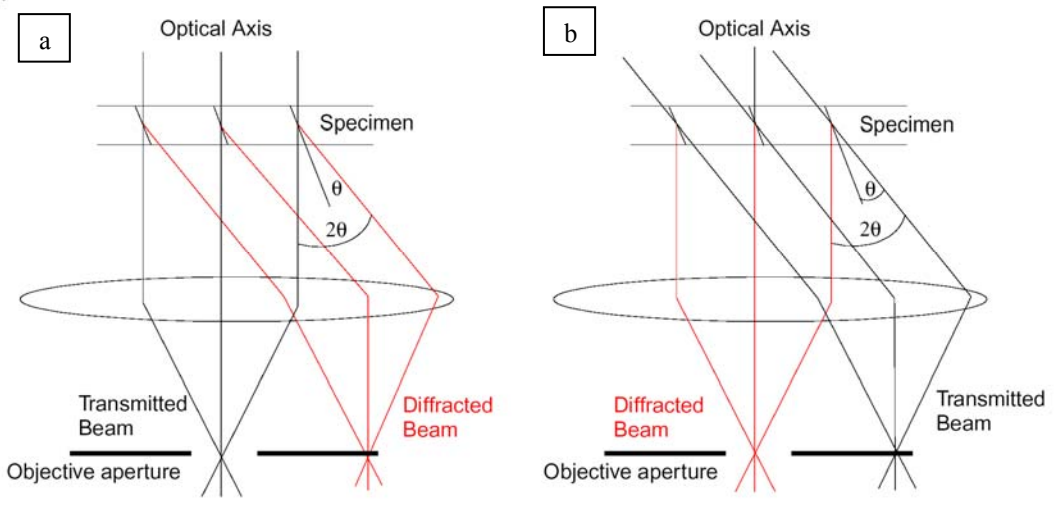

Modern TEMs are often equipped with specimen holders that allow the user to tilt the specimen to a range of angles in order to obtain specific diffraction conditions, and

apertures placed above the specimen allowing the user to select electrons that would otherwise be diffracted.

Applications for this method include the identification of lattice defects in crystals. By carefully selecting the orientation of the sample, it is possible not just to determine the position of defects but also to determine the type of defect present. If the sample is orientated so that one particular plane is only slightly tilted away from the strongest diffracting angle (known as the Bragg angle), any distortion of the crystal plane that locally tilts the plane to the Bragg angle will produce particularly strong contrast variations. However, defects that produce only displacement of atoms that do not tilt the crystal to the Bragg angle (i.e. displacements parallel to the crystal plane) will not produce strong contrast.

Electron Energy Loss - Utilizing the advanced technique of EELS, for TEMs appropriately equipped electrons can be rejected based upon their voltage (which is their energy due to their constant charge), using magnetic sector based devices known as EELS spectrometers. These devices allow for the selection of particular energy values, which can be associated with the way the electron has interacted with the sample. For example different elements in a sample result in different electron energies in the beam after the sample. This normally results in chromatic aberration, however this effect can, for example, be used to generate an image which provides information on elemental composition, based upon the atomic absorption of electrons during electron-electron interaction.

Phase Contrast - Crystal structure can also be investigated by High Resolution Transmission Electron Microscopy (HRTEM), also known as phase contrast. When utilizing a Field emission source, the images are formed due to differences in phase of electron waves, which is caused by specimen interaction. Image formation is given by the complex modulus of the incoming electron beams. As such, the image is not only dependent on the number of electrons hitting the screen, making direct interpretation of phase contrast images more complex. However this effect can be used to advantage, as it can be manipulated to provide more information about the sample, such as in complex phase retrieval techniques.

Resolution of the HRTEM is limited by spherical and chromatic aberration, but a new generation of aberration correctors has been able to overcome spherical

aberration.[9] Software correction of spherical aberration has allowed the production of images with sufficient resolution to show carbon atoms in diamond separated by only 0.89 Å and atoms in silicon at 0.78 Å at magnifications of 50 million times. Improved resolution has also allowed the imaging of lighter atoms that scatter electrons less efficiently. The ability to determine the positions of atoms within materials has made the HRTEM an indispensable tool for nanotechnology research and development in many fields, including heterogeneous catalysis and the development of semiconductor devices for electronics and photonics.

Diffraction - As previously stated, by adjusting the magnetic lenses such that the back focal plane of the lens is placed on the imaging apparatus a diffraction pattern can be generated, see Fig. 2.8.

Fig. 2.8: Beam path during image formation (on the left) and diffraction pattern formation (on the right).

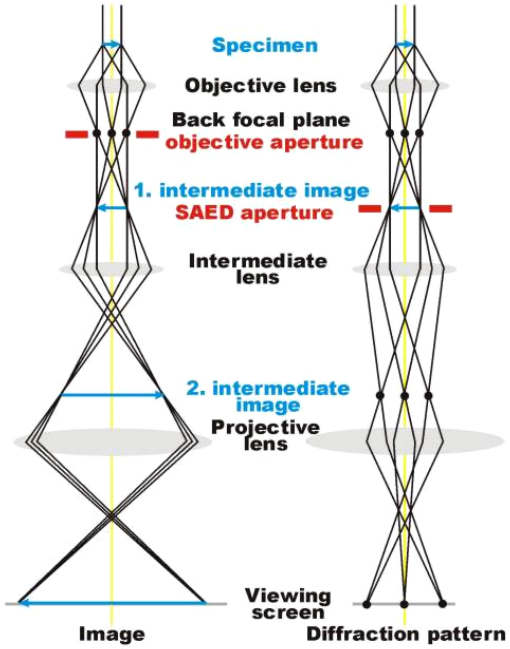

For thin crystalline samples, this produces an image that consists of a series of dots in the case of a single crystal (Fig. 2.9a), or a series of rings in the case of a polycrystalline material (Fig. 2.9b). For the single crystal case the diffraction pattern is dependent upon the orientation of the specimen. This image provides the investigator with information about the space group symmetries in the crystal and the crystal's

orientation to the beam path. This is typically done without utilizing any information but the position at which the diffraction spots appear and the observed image symmetries.

Fig. 2.9: Selected area electron diffraction on a) single grain and on b) nano-crystalline material and c) convergent beam electron diffraction on one grain.

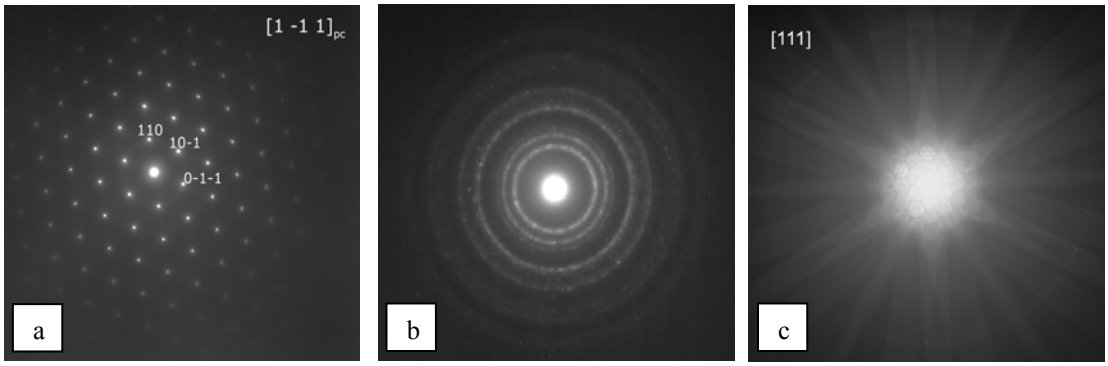

Analysis of diffraction patterns beyond point-position can be complex, as the image is sensitive to a number of factors such as specimen thickness and orientation, objective lens defocus, spherical and chromatic aberration. Although quantitative interpretation of the contrast shown in lattice images is possible, it is inherently complicated and can require extensive computer simulation and analysis, such as multislice analysis.[10]

More complex diffraction behavior is also possible, with phenomena such as Kikuchi lines or convergent beam electron diffraction (CBED) providing additional information, beyond structural data, such as sample thickness (Fig. 2.9c).

Three dimensional imaging - As TEM specimen holders typically allow for the rotation of a sample by a desired angle, multiple views of the same specimen can be obtained by rotating the angle of the sample along an axis perpendicular to the beam. By taking multiple images of a single TEM sample at differing angles, typically in 1 degree increments, a set of images known as a "tilt series" can be collected. Under purely absorption contrast conditions, this set of images can be used to construct a three dimensional representation of the sample.

As TEM samples cannot typically be viewed at a full 180 degrees rotation, the observed images typically suffer from a "missing wedge" of data. Mechanical

techniques, such as multi-axis tilting, as well as numerical techniques exist to limit the impact of this missing data on the observed specimen morphology.

2.1.3.3 Specimens preparation

The TEM is used heavily in material science, metallurgy and the biological sciences. In each case the specimens must be very thin, but able to withstand the high vacuum present inside the instrument.

Sample preparation in TEM can be a complex procedure. TEM specimens are typically hundreds of nanometres thick, as the electron beam interacts readily with the sample, an effect that increases roughly with atomic number. High quality samples will have a thickness that is comparable to the mean free path of the electrons that travel through the samples, which may be only a few tens of nanometres. Preparation of TEM specimens is specific to the material under analysis and the desired information to obtain from the specimen. As such, many generic techniques have been used for the preparation of the required thin sections.

To withstand the instrument vacuum, biological specimens are typically held at liquid nitrogen temperatures after embedding in vitreous ice, or fixated using either a negative staining material such as uranyl acetate or by plastic embedding.

In material science and metallurgy the specimens tend to be naturally resistant to vacuum, but still must be prepared as a thin foil, or etched so some portion of the specimen is thin enough for the beam to penetrate. Constraints on the thickness of the material may be limited by the scattering cross-section of the atoms from which the material is comprised. Materials that have dimensions small enough to be electron transparent, such as powders or nanotubes, can be quickly produced by the deposition of a dilute sample containing the specimen onto support grids or films.

Different sample procedures are adopted depending on the inner features of the sample, for example microtome method is used for tissue sectioning, biological samples utilize stain to enhance contrast, certain metallic specimens may be prepared by chemical etching. For bulk materials, as those examined in the present work, the conventional method foresees the mechanical grinding, followed by Ar-milling.

Mechanical milling - Mechanical polishing may be used to prepare samples. Polishing needs to be done to a high quality, to ensure constant sample thickness

across the region of interest. A diamond, or cubic boron nitride polishing compound may be used in the final stages of polishing to remove any scratches that may cause contrast fluctuations due to varying sample thickness. Even after careful mechanical milling, additional fine methods such as ion etching may be required to perform final stage thinning.

Ion etching - Ion etching is a sputtering process that can remove very fine quantities of material. This is used to perform a finishing polish of specimens polished by other means. Ion etching uses an inert gas passed through an electric field to generate a plasma stream that is directed to the sample surface. Acceleration energies for gases such as argon are typically a few kilovolts. The sample may be rotated to promote even polishing of the sample surface. The sputtering rate of such methods are on the order of tens of microns per hour, limiting the method to only extremely fine polishing.

More recently, Focussed Ion Beam (FIB) methods have been used to prepare samples (Fig. 2.10).

Fig. 2.10: Sequence of the preparation of a thin TEM sample by FIB. The thin membrane shown here is suitable for TEM examination; however, at ~200-nm thick, it would not be suitable for high-resolution TEM without further milling.

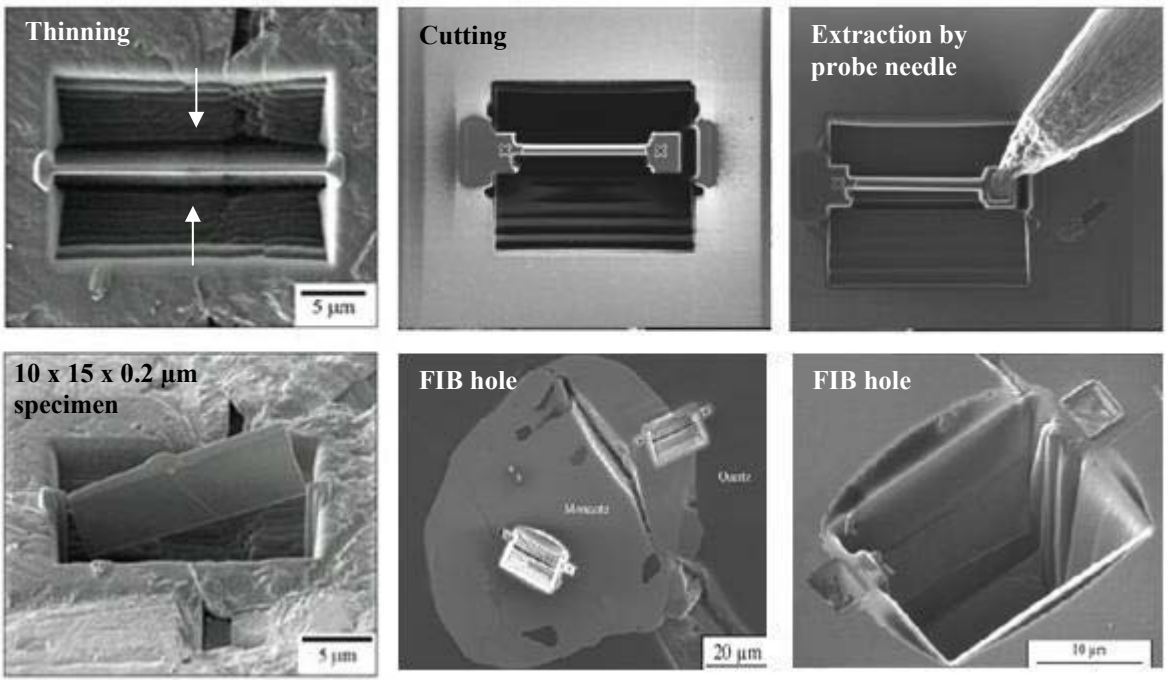

FIB is a relatively new technique to prepare thin samples for TEM examination from larger specimens. Because FIB can be used to micro-machine samples very precisely, it is possible to mill very thin membranes from a specific area of interest in a sample by scanning the surface with a finely focused ion beam. Further, by generating secondary electrons, it enables the observation of the cut surface. The Ga ions strike the specimen and sputter atoms from the surface.

Unlike inert gas ion sputtering, FIB makes use of significantly more energetic gallium ions and may alter the composition or structure of the material through gallium implantation.[11]

2.1.3.4 Modifications

The capabilities of the TEM can be further extended by additional stages and detectors, sometimes incorporated on the same microscope. An *electron cryomicroscope* is a TEM with a specimen holder capable of maintaining the specimen at liquid nitrogen or liquid helium temperatures. This allows imaging specimens prepared in vitreous ice, the preferred preparation technique for imaging individual molecules or macromolecular assemblies.

A TEM can be modified into a scanning transmission electron microscope (STEM) by the addition of a system that scans the beam across the sample to form the image, combined with suitable detectors.

An analytical TEM is one equipped with detectors that can determine the elemental composition of the specimen by analyzing its X-ray spectrum or the energy-loss spectrum of the transmitted electrons.

The importance of the TEM technique in the ceramic field is bond to the detailed characterization of the ceramic microstructures with high spatial resolution. The TEM technique can be applied, in addition to spectroscopic methods, in most of the relevant steps involved during ceramic processing such as:

- Powder processing; organometallic doping(powder surface chemistry);
- Microstructure development during densification (transient crystalline phases);
- Crystallization of polymer derived ceramics (micro/nanocomposites);
- Secondary phase crystallization (phase change upon post-sintering heat treatment);

- As-sintered microstructures (amorphous intergranular films);
- Microstructural changes under service conditions (formation of new glass).

Transmission and analytical electron microscopy is hence shown to be a very helpful characterization tool which allows us to expand our understanding of the development of ceramic microstructures. This technique can be applied in order to investigate the formation process of complex ceramic microstructures and, based on the understanding of microstructure formation, used to influence materials processing. This enables the direct influence of materials fabrication with respect to tailoring ceramic microstructures for potential application requirements.

Nevertheless, there are a number of drawbacks to the TEM technique. Many materials require extensive sample preparation to produce a sample thin enough to be electron transparent, which makes TEM analysis a relatively time consuming process with a low throughput of samples. The structure of the sample may also be changed during the preparation process. Also the field of view is relatively small, raising the possibility that the region analyzed may not be characteristic of the whole sample. There is potential that the sample may be damaged by the electron beam, too, particularly in the case of biological materials.

2.2 MECHANICAL AND TRIBOLOGICAL CHARACTERIZATION

Having good mechanical properties makes a structural ceramic a suitable material for application under heavy mechanical and stress conditions. Here a description of experimental methods for hardness testing, Young's modulus, fracture toughness, flexural strength at room and at high temperature, nanoindentation and wear measurements is furnished.

2.2.1 Hardness

Hardness describes the resistance of a material to plastic deformation (dislocation flows), usually by penetration. However, the term hardness may also refer to resistance to bending, scratching, abrasion or cutting. Hardness is defined as the resistance of a material to the penetration of a hard penetrator of specific geometry and charged in a defined way (CEN ENV 843, 1992).

Hardness is influenced by different factors:

- interatomic bound,
- type and quantity of dislocation needed for the plastic deformation,
- microstructural parameters, namely mean grain size, porosity and composition.

Hardness is not an intrinsic material property dictated by precise definitions in terms of fundamental units of mass, length and time, but it's rather the result of a defined measurement procedure.

Hardness is usually dependent from yield stress σ_y, following the empirical relationship:[12]

$$H = 3\sigma_y \quad (6)$$

Beyond plastic deformation, a sample under penetration can arise cleavage or brittle fracture following different mechanisms.

Dynamical or static methods of measurement are used. In the first case, hardness is calculated on the basis of the load-penetration graph acquired during the fall of a penetrator with increasing load; nevertheless dynamical method are not standardized yet and require sophisticated instrumentations.

The usual static method to obtain a hardness value is to measure the depth or area of an indentation left by an indenter of a specific shape, with an applied specific force for a certain time. There are three principal standard test methods for expressing the relationship between hardness and the size of the impression, these being Brinell, Vickers, and Rockwell. For practical and calibration reasons, each of these methods is divided into a range of scales, defined by a combination of applied load and indenter geometry. A drawn of this technique is shown in Fig. 2.11.

Fig. 2.11: Vickers hardness indentation.

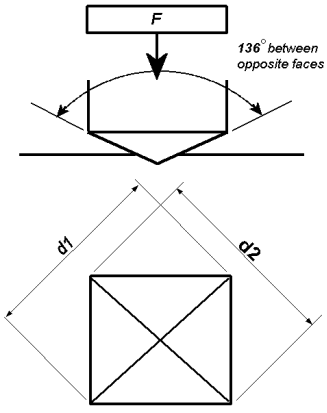

The term microhardness test usually refers to static indentations made with loads not exceeding 1 kgf. The indenter is either the Vickers diamond pyramid or the Knoop elongated diamond pyramid.

In a macro or micro indentation test, a hard tip whose mechanical properties are known (frequently made of a very hard material like diamond) is pressed into a sample whose properties are unknown. The load placed on the indenter tip is increased as the tip penetrates further into the specimen and soon reaches a user-defined value. At this point, the load may be held constant for a period or removed. The area of the residual indentation in the sample is measured and the hardness, *HV*, is defined as the maximum load *F* (kgf), divided by the residual indentation area, d^2 (mm), or (7):

$$HV = \frac{2F\sin\frac{136^\circ}{2}}{d^2} \qquad HV = 1.854\frac{F}{d^2} \text{ approximately} \tag{7}$$

For most techniques, the projected area may be measured directly using light microscopy. As can be deduced from this equation, a given load will make a smaller indent in a "hard" material than in a "soft" one.

The advantages of the Vickers hardness test are that extremely accurate readings can be taken, and just one type of indenter is used for all types of materials and surface treatments.

Indentation technique is limited due to large and varied tip shapes, with indenter rigs which do not have very good spatial resolution. Comparison across experiments, typically done in different laboratories, is difficult and often meaningless.

The tested surface generally requires a metallographic finishing; the smaller is the load used, the higher is the required surface finishing. Precision microscopes are used to measure the indentations; these usually have a magnification of around x500 and measure to an accuracy of $\pm$0.5 micrometres. It should, however, be underlined that considerable care and experience are necessary to obtain this accuracy.

2.2.2 Elastic Modulus

Young's Modulus of Elasticity, E, is defined as the ratio of the stress (force per unit area) to the corresponding strain (deformation) in a material under tension or compression. Elastic modulus is called Young's modulus after Thomas Young

published the concept back in 1807. An elastic modulus (E) can be determined for any solid material and represents its stiffness, (8):[12]

$$E = \frac{stress}{strain} \tag{8}$$

Shear Modulus of Elasticity, G, is similar to the ratio of the stress to the strain in a material subjected to shear stress.

Poisson's Ratio, ν, is the ratio of transverse strain to the corresponding axial strain on a material stressed along one axis.

A material is elastic if it is able to return to its original shape or size immediately after being stretched or squeezed. Almost all materials are elastic to some degree as long as the applied load does not cause it to deform permanently. Thus, the "flexibility" of any object or structure depends on its elastic modulus and geometric shape. The modulus of elasticity for a material is basically the slope of its stress-strain plot within the elastic range (as shown in Fig. 2.12). The initial straight-line portion of the curve is the elastic range. If the material is loaded to any value of stress in this part of the curve, it will return to its original shape. Thus, the modulus of elasticity is the slope of this part of the curve. It is important to remember that a measure of a material's modulus of elasticity is not a measure of strength. Strength is the stress needed to break or rupture a material (as illustrated in Fig. 2.12), whereas elasticity is a measure of the difficulty to initially deform a material.

Fig. 2.12: Stress-strain plot showing the elastic range.

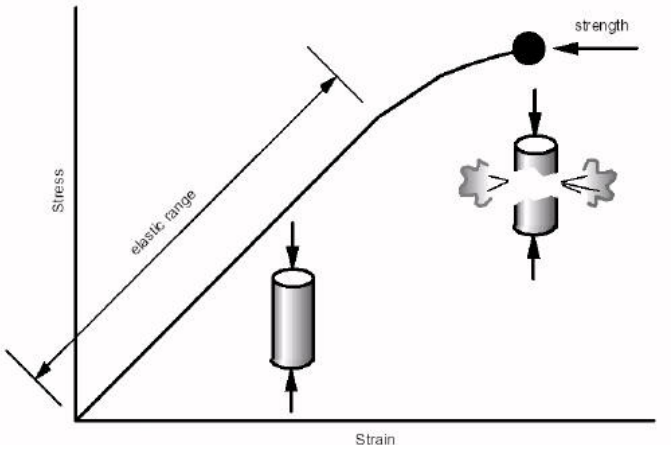

Methods of testing elastic modulus are divided into two groups: static and dynamical.

With static methods, a known load is imposed to the sample by dynamometers and the induced deformations are measured by strain gauges (small metal coil, whose electrical resistivity changes while the section of the sample changes).

This method is not recommended for very stiff materials, as for ceramics, because it is necessary to apply very high loads to arise an appreciable signal; for this reason dynamical methods are preferred. These includes:

- ultrasounds, in which the time of distance of an ultrasonic impulse trough a material of known geometry is measured,
- resonance frequencies, in which the sample is undergone to a scanning of frequencies and the resonance frequency is measured.

In this work resonance frequencies method is mostly used.

Elastic longitudinal, transversal and torsion oscillations can be generated in materials by defined stimulation. If the generated wavelength corresponds to specific dimensions of the specimen, resonance effects will occur and particularly large oscillation amplitudes will be observed. These natural frequencies allow to determine the Young's modulus providing geometry and the density of the test bar. The natural frequency of the test piece can be determined from the recorded oscillation. In the case of known weight and form factor, the elastic modulus of a prismatic bar can be calculated following the equation (9):

$$E = 0.946\left(\frac{mf^2}{b}\right)\left(\frac{l}{h}\right)^3\left[1 + 6.585\left(\frac{h}{l}\right)^2\right]10^{-9} \qquad (9)$$

where m: mass (g); f: frequency (Hz); b: width, (mm); l: lenght (mm); h: thickness, (mm);.

The results of these calculations show a good repeatability of the measured frequency for test specimens whose geometry ratio length/ thickness is larger than 6.

2.2.3 Nanoindentation

Indentation tests are perhaps the most commonly applied means of testing mechanical properties of materials. The technique has its origins in the Mohs scale of

mineral hardness, in which materials are ranked according to what they can scratch and are, in turn, scratched by. The characterization of solids in this way takes place on an essentially discrete scale, so much effort has been expended in order to develop techniques for evaluating material hardness over a continuous range. Hence, the adoption of the Meyer, Knoop, Brinell, Rockwell, and Vickers hardness tests. More recently (ca. 1975), the nanoindentation technique has been established as the primary tool for investigating the hardness in small volumes of a material.

Nanoindentation improves on the previously described macro and micro indentation tests by indenting on the nanoscale with a very precise tip shape, high spatial resolutions to place the indents, and by providing real-time load-displacement (into the surface) data while the indentation is in progress.

In nanoindentation small loads and tip sizes are used, so the indentation area may only be a few square micrometres or nanometres. This presents problems in determining the hardness, as the contact area is not easily found. Atomic force microscopy or scanning electron microscopy techniques may be utilized to image the indentation, but can be quite cumbersome. Instead, an indenter with a geometry known to high precision (usually a Berkovich tip, which has a three-sided pyramid geometry) is employed. During the course of the instrumented indentation process, a record of the load and *depth* is made, and then the contact area of the indent is determined using the known geometry of the indentation tip. These values can be plotted on a graph to create a *load-displacement curve* (such as the one shown in Fig. 2.13). These curves can be used to extract mechanical properties of the material.[13,14]

Fig. 2.13: a) Schematic of the section of an indentation where the parameters involved in the measurements are indicated. b) Schematic of a load-displacement curve recorded during a nanoindentation test, where the corresponding parameters from a) are marked by the same colour. ε=0.75 is a constant depending on the tip geometry.

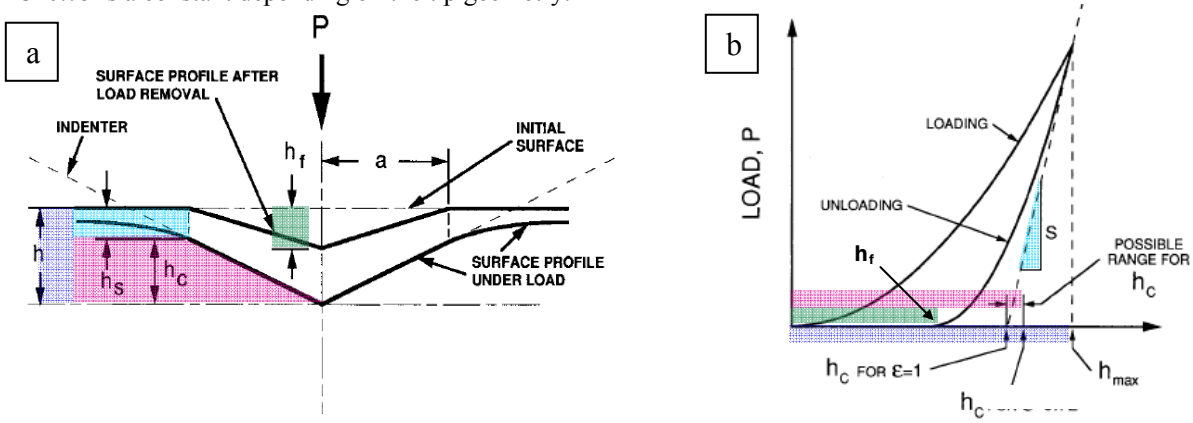

- Modulus of elasticity: The slope of the curve, dP/dh, upon unloading is indicative of the stiffness S of the contact. This value generally includes a contribution from both the material being tested *and* the response of the test device itself. For a diamond indenter tip, E_i is 1140 GPa and ν_i is 0.07. Poisson's ratio varies between 0 and 0.5 for most materials, though it can be negative, and, for hard ceramics like those discussed in the present work, is typically in the range 0.11-0.16.

- Hardness: There are two different types of hardness that can be obtained from a nanoindenter: one is as in traditional indentation tests where one attains a single hardness value per experiment (single load-penetration curve); the other is based on the hardness as the material is being indented resulting in hardness as a function of depth. This last is only available in MTS indenters, the so called "continuous stiffness" option.

The hardness is given by the equation relating the maximum load to the contact area. The area can be measured after the indentation by in-situ atomic force microscopy, 'after-the event' optical or electron microscopy. An example indent image, from which the area may be determined, is shown in Fig. 2.14.

Fig. 2.14: An AFM image of an indent left by a Berkovich tip in a Zr-Cu-Al metallic glass; the plastic flow of the material around the indenter is apparent.

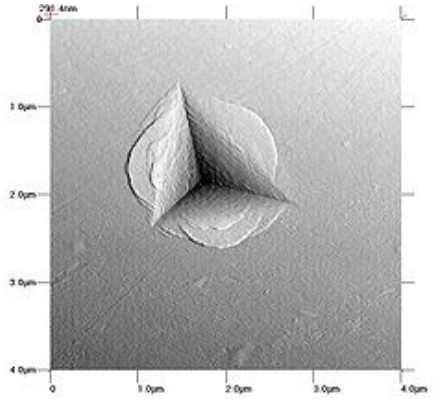

However, in nanoindentation the area of interest is the contact area, i.e. the projected area at the contact under the maximum load. Nanoindenters normally use an *area function* based on the geometry of the tip and calibrated on standard fused silica specimens. Nevertheless, there is some controversy over the use of *area functions* to estimate the contact areas versus direct measurement, especially in presence of pile-up around the indentation marks as it happens in many metallic materials. An area function $A(h)$ typically describes the projected area of an indent as a polynomial

function of the indenter depth *h*. Exclusive application of an area function in absence of adequate knowledge of material response can lead to misinterpretation of resulting data. Cross-checking of areas microscopically is to be encouraged especially if pile-up is suspected to take place.

The construction of a depth-sensing indentation system is made possible by the inclusion of very sensitive displacement and load sensing systems. Load transducers must be capable of measuring forces in the μN range and displacement sensors are very frequently capable of sub-nanometre resolution. Environmental isolation is crucial to the operation of the instrument. Vibrations transmitted to the device, fluctuations in atmospheric temperature and pressure, and thermal fluctuations of the components during the course of an experiment can cause significant errors.

Conventional nanoindentation methods for the calculation of modulus of elasticity and hardness, based on the unloading curve, are limited to linearly elastic materials, even if recently developed energy-based methods claim to be able to measure hardness and Young's modulus independently on the effective contact area.[15] It is possible to measure the pile-up contact area using computerized image analysis of Atomic Force Microscope (AFM) images of the indentations. This process also depends on the linear isotropic elastic recovery for the indent reconstruction. Problems associated with the "pile-up" or "sink-in" of the material on the edges of the indent during the indentation process remain a problem that is still under investigation.

2.2.4 Fracture toughness

Vickers hardness indentations as a means to measure the K_{Ic} have become quite popular due to the simplicity of the method. In this method, a diamond indenter is penetrated into the surface of the specimen to be tested. Upon removal of the indenter, the lengths of the cracks that depart from the corners of the indent are measured, and the Vickers hardness *H* in GPa of the material is calculated.[16] A number of empirical and semi-empirical relationships have been proposed relating K_{Ic} to the crack length, and in general the expression take the form as given below (10,11):[17,18]

$$K_{Ic} = 0.16\, H_v a^{1/2} (c/a)^{-3/2} \quad (10)$$

$$K_{Ic} = 0.016\, (E/H_v)^{0.5} P (c)^{-3/2} \quad (11)$$

where *Hv* is Vickers hardness (load 10 kgf), *E* is Young's modulus, *P* is the applied load (10 kgf), *c* is the crack length from the centre of the indentation, *2a* is the diagonal of the Vickers indentation, as shown in Fig. 2.15. It should be emphasised that the K_{Ic} values measured by this technique are usually not as precise as those from other macroscopic tests like the single edge-notched beam (SENB) tests.[16]

Fig. 2.15: Measurements in Vickers' indentation.

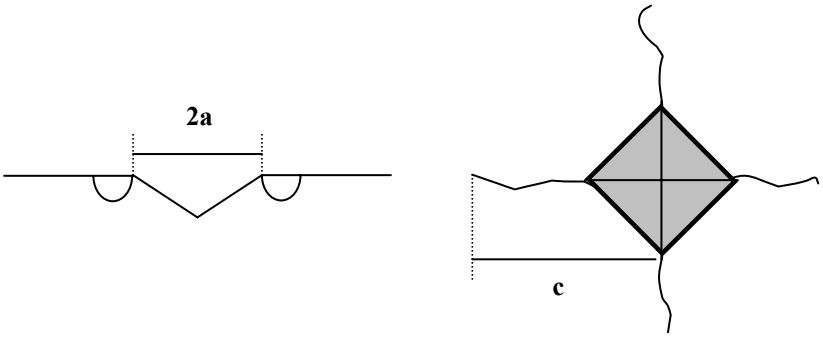

According to this method, notches are usually produced by very sharp diamond blades. The preparation is critical for determining the K_{Ic} of brittle materials like ceramics. Measured values, indeed, decrease with the width of the notch, even if below a critical value of the width of the notch, K_{Ic} seems to remain constant, equal to the plain strain fracture toughness, that could be obtained with real cracks. Unfortunately, critical radius of the notch may depend on material, that's why Claussen et al.[19] recommend that the radius of the notch is below 25 μm for a good determination of K_{Ic}. Problems of reproducibility and measurement of the starting notch can be overcome using Barker's[20,21] specimen in which an inverse V notched is introduced in a round or rectangular bar, a method called Chevron-Notched Bar (CNB). When the load is applied, the crack starts to propagate from the tip of the triangular notch. Depending on the sample geometry, the crack propagation is initially stable at increasing load. At a certain critical value of load, the crack achieves an instability point and then spreads catastrophically. The instability point depend on the sample geometry. It is possible to calculate the dimensions of the notch at the instable propagation without measuring it. Another advantage of the CNB method is that the notch advances atomically sharp without problem of curvature radius at the tip. Munz et al.[22] determined the relationships which allow to calculate K_{Ic} starting from the maximum load (P_{max}) measured in a four-point bending test of a chevron-notched sample of known geometry. These relationship are reported in Fig. 2.16.

Fig. 2.16: Chevron notched beam model and Munz's relationships. [22]

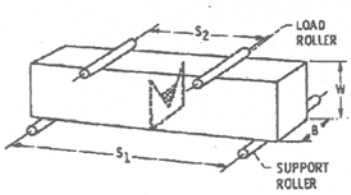

$$K_{Ic} = \frac{P_{max}}{B\sqrt{W}} y^*$$

$$y^* = \left(3{,}08 + 5\alpha_0 + 8{,}33\alpha_0^2\right)\frac{(S_1 - S_2)}{W}\left(1 + 0{,}007\sqrt{\frac{S_1 S_2}{W^2}}\right)\left(\frac{\alpha_1 - \alpha_0}{1 - \alpha_0}\right)$$

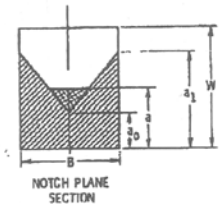

$$\alpha_0 = \frac{a_0}{W}$$

$$\alpha_1 = \frac{a_1}{W}$$

2.2.5 Flexural strength

Tensile testing of ceramics is not only time consuming, but it is also expensive to fabricate the specimens. Therefore, the easier-to-handle transverse bending or flexure test is commonly used for determining the strength of ceramics. In this case, the specimen is loaded up to failure in either three- or four-point bending geometry. The maximum stress or stress at fracture is commonly referred to as fracture strength. For rectangular cross sections, the fracture strength in four-point bending is given by (12):

$$\sigma_{4P} = \frac{3}{2} \cdot \frac{F(l_o - l_i)}{b h^2} \qquad (12)$$

where F is the force, lo is the length between two outer supports, l_i is the length between two inner supports, b and h are the breadth and height of the specimen, respectively. The flexural strength of a sintered body is strongly dependent on such factors as size, shape, density, and distribution of residual pores, agglomerates, surface flaws, inclusions and their distribution, grain size and grain boundary properties.

Pores are usually quite deleterious to the strength of ceramics not only because they reduce the cross-sectional area over which the load is applied, but also because they act as stress concentrators. Typically, the strength and the porosity have been related by the following empirical relationship (13):[16]

$$\sigma_P = \sigma_0 e^{-BP} \qquad (13)$$

where P, σ_p and σ_0 are, respectively, the volume fraction of the pores and the strength of the specimen with and without porosity, respectively. B is a constant and depends on the distribution and morphology of the pores.

Agglomerates and large grains cause degradation in strength. During sintering, the rapid densification regions containing agglomerates can induce stresses within the surrounding compact facilitating the formation of voids and cracks. Anisotropic large grains often produce mismatch in thermal expansion and elastic modulus and act as flaws in a homogeneous matrix.

Surface flaws can also degrade the mechanical performance to a greater extent. They can be a result of post-fabrication machining operations, or accidental damage to the surface during use. During high temperature testing, grain boundary can result in lower flexural strength. According to the Griffith criterion,[23] the fracture stress is expected to decrease with increasing flaw size. Empirically, the strength of ceramics (σ) shows an inverse correlation with the average grain size (G). In general, the σ vs $G^{1/2}$ relationship for ceramic materials shows two branches: one branch at larger grain sizes showing a strong grain size dependence of the strength (Orowan branch), and another branch at smaller grain sizes where extrinsic factors, such as, surface finish, preferred orientation, pores and inclusions dictate the strength of the ceramics (Petch or Hall-Petch branch).[24] Carniglia[25] suggested that microplasticity was the failure mechanism for the fine-grain branch whereas, for large grains, Griffith flaw failure operates with the critical flaw dimensions being close to the grain size. So, invoking the Orowan-Petch relationship, one expects the strength to be proportional to $G^{1/2}$ for larger grain size.[24] In the present investigation, Orowan branch behaviour is ruled out as the grain sizes lie between 1-5 μm.

Apart from the above-mentioned factors, residual stresses, subcritical crack growth, elastic anisotropy and temperature influence the flexural strength of ceramics.[24]

Strengthening can occur by the introduction of a compressive surface layer that inhibits surface cracks to propagate. Similar strengthening can occur when a protective, usually oxide, layer forms on the surface, which tends to blunt and partially heal pre-existing flaws or surface cracks leading to higher strength values. On the contrary, during high temperature testing, surface pits or etching of the surfaces occur that can result in a drop in strength. At high temperature, ceramics containing

amorphous intergranular phases exhibit a drop in strength value which is usually related to the softening of glassy and secondary phases.

2.2.6 Wear

In materials science, wear is the erosion of material from a solid surface by the action of another substance. The definition of wear does not include loss of dimension from plastic deformation, although wear has occurred despite no material removal. This definition also fails to include impact wear, where there is no sliding motion, cavitation, where the counterbody is a fluid, and corrosion, where the damage is due to chemical rather than mechanical action.

Aspects of the working environment which affect wear include:

- loads, such as unidirectional sliding, reciprocating, rolling, and impact loads,
- speed,
- temperature,
- type of counterbody, solid, liquid or gas,
- type of contact, single phase or multiphase, in which the phases involved can be liquid plus solid particles plus gas bubbles.

In the results of standard wear tests, such as those formulated by the respective subcommittees of ASTM Committee G-2, the loss of material during wear is expressed in terms of volume. The volume loss gives a truer picture than weight loss, particularly when comparing the wear resistance properties of materials with large differences in density. The study of the processes of wear is part of the discipline of tribology.

The study of tribology involves the measurement of friction, wear and the study of the mechanisms occurring during friction. These properties are not peculiar of a material, but rather are characteristic of the tribological system. In order to test the behaviour of a component, it is of primary importance to identify the mechanisms responsible of deterioration of a component during employment and reproduce the same conditions in laboratory tests.

The working life of an engineering component is over when dimensional losses exceed the specified tolerance limits. Wear, along with other aging processes such as fatigue, creep and corrosion, causes progressive degradation of materials with time,

leading to failure of material at an advanced age. Under normal operating parameters, the property changes during usage normally occur in three different stages as follows:

1. Primary or early stage or run-in period, where rate of change can be high.
2. Secondary or mid-age process where a steady rate of aging process is maintained, most of the useful or working life of the component is comprised in this stage.
3. Tertiary or old-age stage, where a high rate of aging leads to rapid failure.

With increasing severity of environmental conditions such as higher temperatures, strain rates, stress and sliding velocities, the secondary stage is shortened and the primary stage tends to merge with the tertiary stage, thus drastically reducing the working life. Surface engineering processes are used to minimize wear and extend working life of material.[26,27]

Depending on the geometry of the contact, there are five principal wear processes:

- Adhesive wear
- Abrasive wear
- Surface fatigue
- Fretting wear
- Erosion wear

Adhesive wear - Adhesive wear is also known as scoring, galling, or seizing. It occurs when two solid surfaces slide over one another under pressure. Surface projections, or asperities, are plastically deformed and eventually welded together by the high local pressure. As sliding continues, these bonds are broken, producing cavities on the surface, projections on the second surface, and frequently tiny, abrasive particles, all of which contribute to future wear of surfaces. A sketch of this mechanism is reported in Fig. 2.17.[28]

Fig. 2.17: Process of material transfer due to adhesive wear.

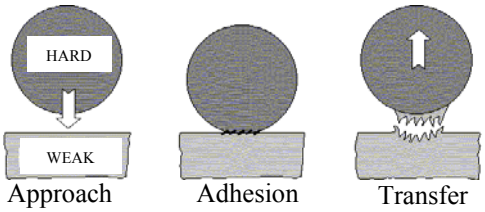

Abrasive wear - When material is removed by contact with hard particles, abrasive wear occurs (Fig. 2.18). The particles either may be present at the surface of a second material (two-body wear) or may exist as loose particles between two surfaces (three-body wear). Abrasive wear can be measured as loss of mass by the Taber Abrasion Test according to ISO 9352 or ASTM D 1044.[29]

Fig. 2.18: Sketch of the mechanisms of abrasive wear.

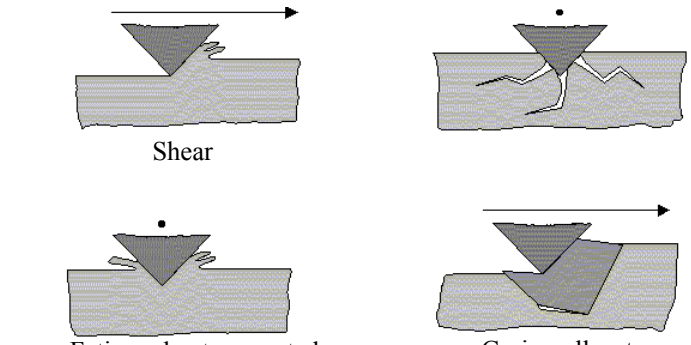

Surface fatigue - Surface fatigue is a process by which the surface of a material is weakened by cyclic loading, which is one type of general material fatigue.

Wear in this conditions is determined by mechanisms of opening of the crack, propagation and growth of the crack and failure. The eroded surface contains a high amount of plastic deformation compared to the surface which has not underwent erosion (Fig. 2.19). This deformation and the following modification of the microstructure affect the wear process in a great extent.

Fig. 2.19: Layers of surface deformation in a material which underwent shear stress.

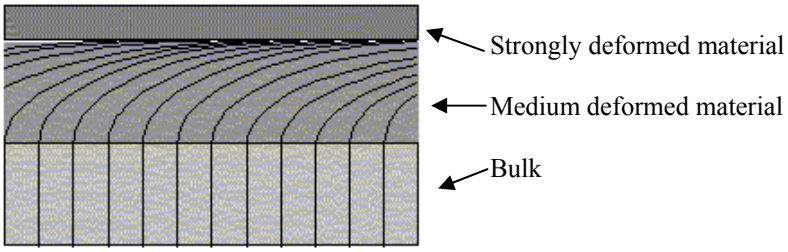

Fretting wear - Fretting wear is the repeated cyclical rubbing between two surfaces, over a period of time which will remove material from one or both surfaces in contact. It occurs typically in bearings, although most bearings have their surfaces hardened to resist the problem. Another problem occurs when cracks in either surface are created, known as fretting fatigue. It is the most serious of the two phenomena, because it can lead to catastrophic failure of the bearing. An associated problem takes place when the small particles removed by wear are oxidised in air. The oxides are usually harder than the underlying metal, so wear accelerates as the harder particles abrade the metal surfaces further (Fig. 2.20). Fretting corrosion acts in the same way, especially when water is present. Unprotected bearings on large structures like bridges can suffer serious degradation in behaviour, especially when salt is used during winter to deice the highways carried by the bridges.

Fig. 2.20: Sketch of the mechanisms of wear during fretting.

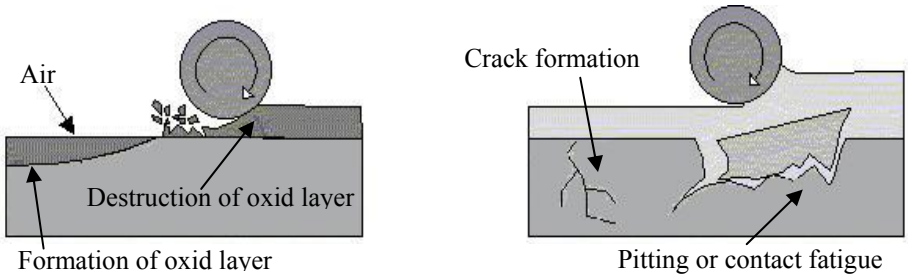

Erosion wear – It is caused by impact of solid particles or liquids on the surface of a materials. This kind of wear can take place in gas-turbines or pumps for mineral suspensions. The properties of the eroding particles are of great importance and become fundamental parameters during the control of erosion wear.

Erosion wear implies several mechanisms mainly controlled by the material constituting the particle, by the impact angle, by the speed of impact and by the dimensions of the particles. If a particle is hard and solid, it is possible to fall into the abrasive wear. When the eroding element is liquid, the wear is the result of repeated impact solicitations. The most known mechanisms of erosion wear are represented in Fig. 2.21, where different configuration can be observed.

The angle of impact is the angle between the eroded surface and the trajectory of the particle before the impact. A small angle favours abrasive wear, because the

particles tend to slide along the eroded surface after the impact. A high angle is typical of erosion wear.

Fig. 2.21: Sketch of the mechanisms of erosion wear. a) abrasion due to low impact angle, b) surface fatigue due to low speed and high impact angle, c) brittle fracture or plastic deformation due to medium speed and high impact angle, d) surface melting at high impact speed, e) macroscopic erosion, f) degradation of crystal lattice due to atomic impact.

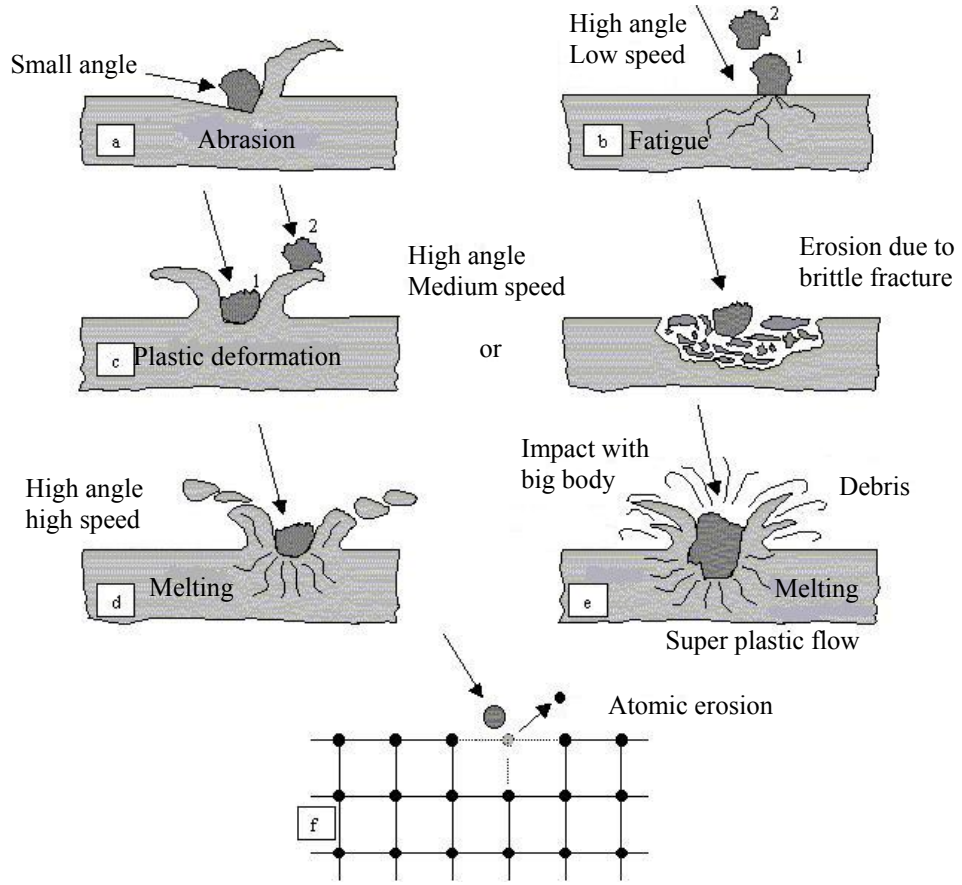

The speed of the particles is also an important parameter. If it is very low, the stresses are not sufficient to have plastic deformation. At very high impact speed melting of the collided surface can occur.

The dimension and shape of the particles is of considerable relevance and many erosive wear are due to particles with dimensions in the range 5-500 μm. If the colliding particles are spherical or blunt, due to high plastic deformation, thin layers of eroded material are formed on the surface. If the particles are sharp, shear mechanisms or brittle fragmentation are favoured. On the other side, brittle materials suffer of fracture under the surface.

Like solids, liquids can also cause large erosion damages if the impact speed is sufficiently high. Example of this problem can be found on planes crossing clouds or on blades of steam turbine.[30]

2.3 ELECTRICAL CHARACTERIZATION

2.3.1 Electrical resistivity

The method for the determination of electrical resistivity ρ (Ω·cm) is based on the measurement of the electrical resistance of samples having geometrical shapes of known dimensions. If we know the dimensions of the sample, we can go back to the exact value of resistivity by mean of the relationship (14):

$$\rho = RS/l \quad (14)$$

where R is the measured resistance, S is the transversal section of the specimen, l is its length.

Firstly, it is important to determine if the material is a conductor, a semiconductor or an insulator.[31]

For elements with high resistivity it is possible to omit eddy resistance introduced by link cable, so the resistance can be measured following the classical method with two terminals: by applying a certain current, the drop potential is measured at the tip of the sample and from the ratio voltage/current it is possible to obtain he resistance. This is only an apparently simple measure, actually it is affected by complication which can bring to coarse errors.

Being an insulating material, it is necessary to distribute the electrical field uniformly on the two plane and parallel faces between which the measure is conducted. A non uniform contact should bring to a higher resistance value. To overcome this hurdle, two conductive rubber electrodes can be used, rubber fits harshness surfaces creating a more uniform contact.

Resistivity measurements of conductive or low resistive elements are carried out by a four- probe DC method, inducing a current in bar specimens and measuring the drop potential between two intermediate points at fixed distance. In this way link cable eddy currents are eliminated. In this configuration the inner resistance of the voltmeter is many order of magnitude higher than the current in measure, it means that the necessary

current for the voltmeter is enough low compared with the current circulating in the sample that can be neglected.

Tests are carried out paying attention that the sample won't dissipate more than 100-150 mW, in order not to cause self-heating of the same sample by Joule effect during the test. Afterwards, the choice of one specific method to measure the current is chosen from time to time as compromise among the different demands: too low currents give lower drop of potential and not stable lecture, too high currents provoke self-heating of the sample.

References

1 G. Celotti, in “Fisica e tecnologia”, Vol. III, 1980, pp. 3-30.

2 G. I.Goldstein, D. E. Newbury, P. Echlin, D. C. Joy, C. Fiori, E. Lifshin, “Scanning electron microscopy and x-ray microanalysis”, New York, 1981.

3 H. J. Kleebe, W. Braue, H. Schmidt, G. Pezzottic, G. Ziegler, J. Europ. Ceram. Soc. 16 (1996) 339-351.

4 H. J. Kleebe, G. Pezzotti, J. Ceram. Soc. Jap., 107 (1999) 801-813.

5 P.Greil, J.Weiss, J. Mater. Sci., 17 (1982). 1571-8.

6 G. Van Tendelo, L. Anders, G. Thomas, Acta Met., 31 (1983) 1619-25.

7 Bonnell, D. A., Tien, T.-Y. & Rtlhle, M., J. Am. Ceram. Sot., 70 (1987) 460-5.

8 Riihle, M., Ma, L. T., Wunderlich, W., Evans, A. G., Physica B, 150 (1988) 8698.

9 Crewe, Albert V; Isaacson, M., Johnson, D., Rev. Sci. Inst. 40 (1969) 241–246.

10 Porter, K and Blum, J. "A study in Microtomy for Electron Microscopy". The anatomical record 4 (1953) 117.

11 Baram, M., Kaplan, W.D, J. of Microscopy 232 (2008) 395-05.

12 S. Guicciardi, “Appunti di caratterizzazione meccanica, Corso di perfezionamento in Chimica e Tecnologia dei Materiali”, CNR-IRTEC, (1996-1997).

13 W.C. Oliver and G.M. Pharr, J. Mater. Res. 19 (2004) 3.

14 Meza J.M., M. C. Farias, R. M. Souza, J. Cruz, J. Mater. Res. 10 (2007) 437-447.

15 Y. T. Cheng, C. M. Cheng, Mat. Sci. & Eng. Reports, 44 (2004) 91-149.

16 M. Barsoum, ‘Fundamentals of Ceramics’, McGraw-Hill, Singapore (1997).

17 A.G. Evans, E.A. Charles, J. Am, Ceram. Soc. 59 (1976) 371.

18 G.R. Antis, P. Chantikul, B.R. Lawn, D.B. Marshall, J. Am, Ceram. Soc. 64 (1981) 359.

19 N. Claussen, R. Pabst, C.P. Lahmann, Proc. Br., J. Am, Ceram. Soc. 25 (1975) 139.

20 L.M. Barker, “Engieering Fracture Mechanisms”, 9 (1977) 361.

21 L.M. Barker, “Fracture Mechanics of Ceramics”, 3, Plenum, NY, 1978, 483.

22 D. Munz, R.T. Bubsey, J.L. Shannon jr., J. Am, Ceram. Soc. 63 (1980) 300.

23 A. A. Griffith, Phil. Trans. R. Acad., A221 (1920) 163.

24 R. W. Rice, ‘Mechanical Properties of Ceramics and Composites’, Marce Dekker, New York (2000) p.127.

25 S. C. Carniglia, J. Am. Ceram. Soc., 55 (1972) 243.

26 Chattopadhyay, R. (2001). Surface Wear - Analysis, Treatment, and Prevention. OH, USA: ASM-International.

27 Chattopadhyay, R. (2004). Advanced Thermally Assisted Surface Engineering Processes. MA, USA: Kluwer Academic Publishers.

28 G.W.Staichowiak, A.W.Batchelor, Engineering tribology, Elsevier Applied Science Publishers, Londra e New York; pp 613-616.

29 G.W.Staichowiak, A.W.Batchelor, Engineering tribology, Elsevier Applied Science Publishers, Londra e New York; pp 557-562.

30 G.W.Staichowiak, A.W.Batchelor, Engineering tribology, Elsevier Applied Science Publishers, Londra e New York; pp 586-591.

31 Paul Tipler. Physics for Scientists and Engineers: Electricity, Magnetism, Light, and Elementary Modern Physics (5th ed.), W. H. Freeman (2004).

SECTION I

SiC-BASED CERAMICS

CHAPTER 3

SILICON CARBIDE-BASED MATERIALS

3.1 INTRODUCTION

Since the early days of civilisation, there has been an increasing need for advanced ceramic materials and it has continuously increased due to the rapid advancement in technology. The main reasons for the attention focused on ceramics as possible structural materials are their heat resistance and wear resistance. As a matter of fact, however, few ceramics are capable of maintaining their strength at temperatures which prohibit the use of metals, the exceptions being covalent materials like Si_3N_4 and SiC, etc. The development of silicon carbide ceramics during the last two decades is one example for the progress that has been made. Applications of SiC compacts as structural materials can be divided into two categories:

- abrasion and corrosion resistant components,
- heat resistant components.

It was found that SiC sintered bodies possess superior strength at high temperatures, and they were seen as promising heat resistant structural material. Their characteristics include high temperature properties like creep resistance, bending strength, high hardness, heat resistance and corrosion resistance. These properties enable SiC to be the prime material for structural components such as high temperature furnace components (heating elements, core tubes, refractory bricks, etc.).[1] These applications, however, do not require high density sintered bodies. The developments of SiC compacts as structural components with high density were initially begun with the objective of application to gas turbine engines.

Si–C bonds have a high degree of covalency (87 %),[2] and this is the source of the intrinsically high strength of SiC sintered bodies. SiC is fundamentally a brittle material, its low fracture toughness presents difficulties in application as a structural material. But SiC sintered bodies belong to the few materials, which can be used at extremely high temperatures (e.g. 1300°C and above). However, due to the highly

covalent bond characteristics, it is difficult to densify these materials to full density without sintering additives.[1] Addition of suitable sintering additives leads to dense, fine-grained microstructures and, hence, high strength of the sintered body, but generally it may also result in the formation of secondary phases at the grain boundaries that frequently cause loss of high strength due to softening of these phases.

Three representative technologies have been developed for sintering of SiC namely, hot pressing with a sintering aid, pressureless or gas pressure sintering with a sintering aid, and reaction sintering. Among these techniques, pressureless sintering is considered to be the most important from an industrial standpoint because it allows the manufacture of large or complex-shaped pieces, offers good mass productivity at low costs, and can produce products with superior performance. Several additives or combinations of them, such as Al_4C_3, Al_2O_3-Y_2O_3, Al_2O_3-Y_2O_3-CaO and AlN-Y_2O_3 have been investigated for SiC in order to improve the thermomechanical behaviour.

Typically LPS-SiC ceramics consist of highly refractory SiC grains bonded by a less refractory vitreous phase. Therefore the high temperature behaviour depends primarily on the composition, distribution, and crystallinity of the intergranular phase.

In order to improve the high temperature performance of the intergranular phase, additive systems containing different rare-earth sesquioxides have been used in the case of Si_3N_4 and SiAlON materials.[3-8] This new approach was motivated by the relatively poor refractoriness of the glass phases formed with conventional sintering additives, particularly the aluminium containing ones.

A literature review of the physico-chemical properties, sintering and microstructural evolution and mechanical properties is presented in the following paragraphs.

3.2 CHIMICAL-PHISICAL FEATURES

3.2.1. Crystal Structure

Silicon carbide shows many different crystal structures.[1,2] All of them are characterised by the fact that any given atom is always tetrahedrally bonded with four heteroatoms. The nearest-neighbour bonding distance is approximately 1.89 Å. All structures can be considered as polytypes consisting of differently packed layers of atoms. According to Ramsdell,[9] the notation of these polytype consists of one number describing the

number of layers (A, B or C-layer) associated with the unit cell, and a letter indicating the crystal system (cubic (C), hexagonal (H) or rhombohedral (R)), as shown in Fig. 3.1. The cubic 3C polytype is designated as β-SiC and all other polytypes are referred to as α-SiC. The stacking order of the closely-packed plane (the (111) plane in cubic crystals and the (0001) plane in hexagonal crystals) is shown in Fig. 3.2 by the stacking sequence (ABC). The stacking of β-SiC in the (111) direction is ...ABCABC..., while that of the hexagonal (2H) variety in the direction of the c-axis is ...ABAB.... The 2H polytype is not stable above 1400°C and transforms to different polytypes depending on the temperature.[10] At 1600°C or above, the stacking sequence changes to ...ABCACB... or ...ABCB... mainly due to stacking transformation, leading to α-SiC polytypes denoted as 6H and 4H respectively.[10]

Fig. 3.1: Crystallographic structures of polytypes: 3C, 2H, 4H, 6H, 15R.

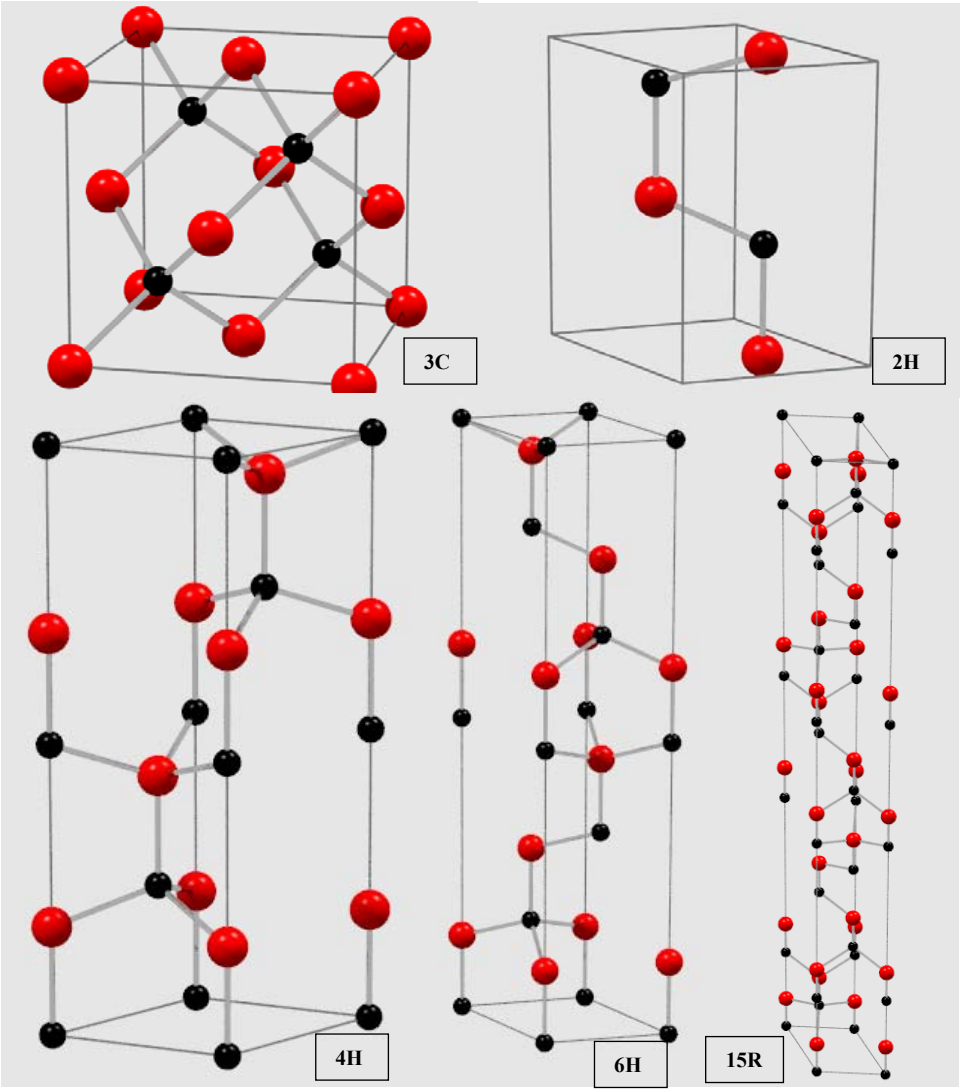

Figure 3.2: Structure of cubic and hexagonal SiC that crystallises in the zinc blende structure and faulted wurtzite structures, respectively.

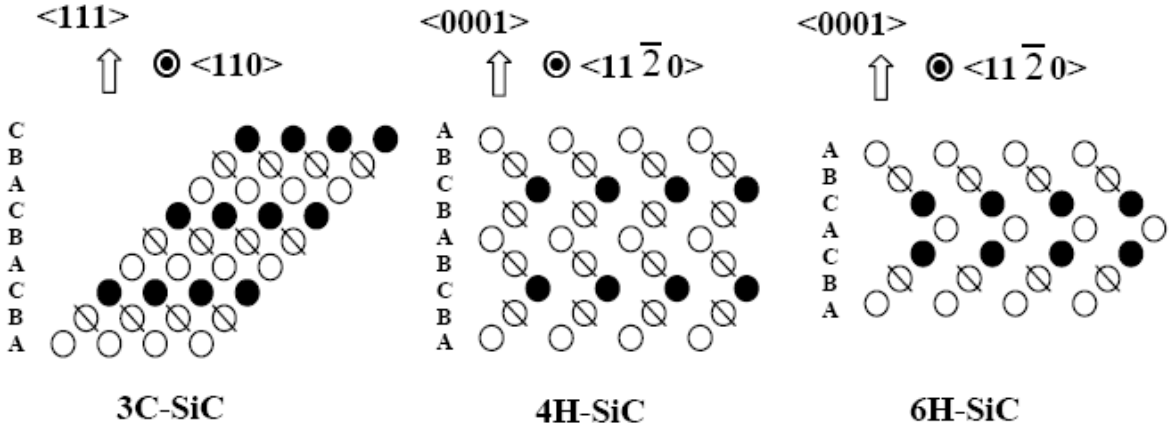

3.2.2 Stability and transformations

Silicon carbide is a crystalline compound in which carbon and silicon are bounded with covalent bounds whose energy is around 318 kJ/mol.[11]

The Si-C phase diagram is shown in Fig. 3.3. Silicon carbide is the only solid intermediate in the Si-C system that crystallizes both in the cubic and in the hexagonal form with a lot of polytypes. Silicon carbide doesn't show any solid solution with Si or C but it has a certain non-stoichiometry in the composition due to carbon vacancies which has been reported by Prochazka.[12] SiC decomposes in a peritettic point forming liquid silicon and solid carbon at around 2545°C with an atomic percentage of liquid silicon of 27%.[13]

Since SiC has been firstly synthesised it has always interested crystallographers for its wide variety of crystallographic structures in which it can be present without changing the stoichiometry. The phenomena by which a material shows different dispositions of one-dimensional layers of identical planes of atoms is called polytypism and the deriving structures are called polytypes. It is important to know the conditions of stability in that way to forecast and prevent undesired transformations during processing. Some important electrical properties depend on the specific polytype and in the case of structural applications polytypic transformations, which occur during sintering, can determine variations in mechanical properties of the material.[14]

Fig. 3.3: Silicon carbide phase diagram.

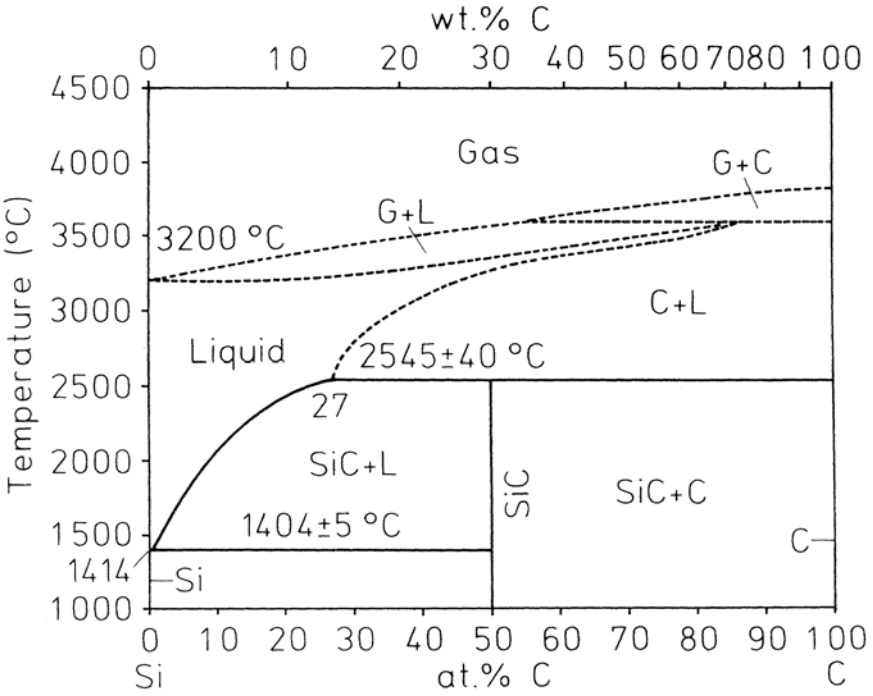

A great number of experiments were conducted in order to identify the stability regions of SiC polytypes. The performed studies and the developed theories are based on kinetic and thermodynamical considerations. These studies had a big impulse especially because of the possibility to exploit the interesting electronic properties of silicon carbide, which changes depending on the polytype, and bounded to the necessity to obtain crystals made of one single polytype. In any cases the stability of a polytype depends on the temperature and on the grain growth rate. Kippenberg suggested a stability diagram in Fig. 3.4 of the different polytypes drawn out from experiments on single crystals growth.[15,16]

Fig. 3.4: SiC polytype stability diagram as a function of the temperature.

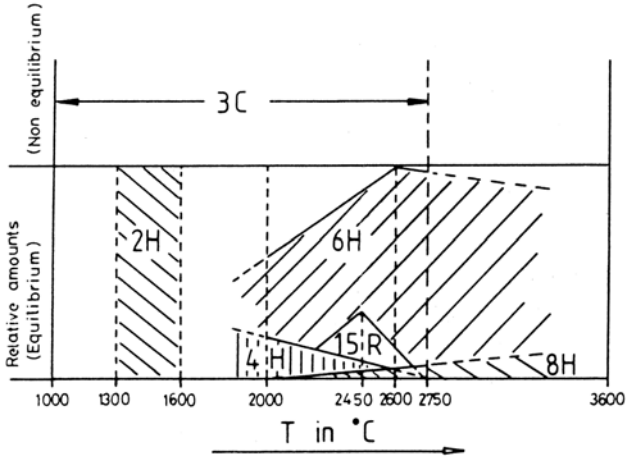

It is usually observed that the 3C (β-SiC) cubic polytype is formed at mild temperature and at high temperature turns into α-SiC. It could be thought that these two polytypes are the two stable phases at low and high temperature respectively, nevertheless β-SiC has been observed even at high temperature and quantum-mechanical calculations evidenced that other polytypes should be more stable at lower temperature, this indicating that β-SiC is a metastable phase.[17-19]

β-SiC is the polytype which forms first in the processes of crystal growth, even if the cubic phase is not the lowest energy structure at temperature above 1873°C.[16] The reasons for this metastable form consist in the high symmetry and multiplicity of the 3C lattice which allows the rearrangement of the tetrahedrons in a lower local energy configuration, further lowered by electron-donor impurities.[20] These factors kinetically favour the nucleation and growth of the 3C form. Once the 3C phase is formed other polytypes can be observed (α-phases): 2H, 4H, 6H, 15R. Many of the hexagonal polytypic structures derive from this transformation. In the temperature range 1673-1873°C none of these transformations takes place.

The most common transformation is 3C → 6H,

but others are possible: 3C→4H, 3C → 2H, 3C → 15R, 4H → 6H, etc.

Among the suggested mechanisms for the solid state transformations, periodic slip and diffusional rearrangement are supposed to occur. The first case hypothesizes that the transformation is the result of the partial sliding of the dislocations on the basal plane with periodicity in the stacking direction, caused by the rotation of these dislocations on other dislocations with Bourger's vector parallel to the c axes.[21] In the case of diffusional rearrangement, nucleation and stacking fault expansion occur on the basal plane. The defects expand for thermal effects, actived by defect/matrix interface.

Heuer et al.[22-25] demonstrated that transformation processes and α-phase growth during annealing treatment of polycrystalline SiC occur through a rapid growth of composite grains constituted by a layer of α-SiC in a β-SiC matrix. This growth is faster than the development of the grains at the interface with β-grain. The study on the energy evidenced a high anisotropy of the interface energy between α and β-SiC: the interface $\{111\}_\beta \| (0001)_\alpha$ energy is much lower than any interface and this favors the development in this preferential direction.

The β→α transformation during sintering or during annealing processes is often associated to the formation of plate and elongated grains, that is an anisotropic growth, which offers the possibility to a in situ reinforcement and, as a consequence, to an increased fracture toughness.[26-30]

A crucial point is the purity of the sample. Some transformation can be associated to the presence of specific impurities either in the material or in the atmosphere. The reverse transformation 6H→3C occurs by heating 6H SiC in nitrogen atmosphere. This transformation is the opposite of what is commonly observed during high temperature sintering of silicon carbide in N_2. In nitrogen atmosphere the transformation β → α is hindered or slowed down.

The presence of aluminium or boron in the starting materials or in the liquid phase favors a series of polytypic transformations, such as 6H→4H→2H or 3C→4H and the microstructure shows elongated and plate grains characterized by a high aspect ratio, where aspect ratio is the ratio between length and width of the grains.[31] The degree of transformation is more evident when the amount of Al or B is high.

Electron-donor species, as nitrogen or phosphorus, stabilize tetrahedral layer in the cubic structure, whilst electron-acceptor species, as aluminium or boron, stabilize the hexagonal structure.

Also the pressure plays an important role. During the sintering of β-SiC, the 3C→6H transformation occurs at temperatures increaseing with the pressure. At temperature above 2500°C and with applied pressure higher than 4.5 GPa the reverse transformation (6H→3C) occurs.[32]

During sintering at temperature below 1900°C and at pressure of 30 MPa, the transformation β → α is inhibited.

One of the aspect to evaluate is that we often deal with starting powder containing traces of different polytypes, so experimental systems show a notable complexity and during sintering much more interactions can occur. Although extensive studies on phase transformation were conducted, the mechanisms which take place during the polytypic transformation are still unclear because the achieved results are often contradictory. These systems are very complex because of the sintering conditions and the various parameters which in turn take part to the transformation.

3.3 SYNTHESIS

Silicon carbide is most frequently synthesized on industrial scale by the Acheson method.[33] In this technique, two solid electrodes are connected with graphite powder, a mixture of silica and coke is packed in the surrounding area, and the whole assembly is electrically heated at 2700°C for producing SiC mainly by the reaction (1):

$$SiO_2+3C \rightarrow SiC+2CO \quad (1)$$

SiC crystal blocks from the reaction are then ground, refined and classified to produce SiC powders. The SiC grades thus prepared are characterised as α-SiC having a relatively coarse grained structure with a mean particle size of 5 μm. This requires a further refining process to produce submicron grain powders suitable for sintering.[34] β-SiC is also produced by the Acheson method at lower temperature (1500-1800°C) or by vapour-phase reactions.[35-37]

This last method foresees the reaction of SiH_4 [35] or $SiCl_4$ with hydrocarbons such as CH_4 and C_3H_8 [31] or the thermal decomposition of CH_3SiCl_3, $(CH_3)_4Si$,[32] or polycarbosilane.[37] The steps leading to the production of SiC by vapour-phase method can be summarised as follows (2-5):

$$SiH_4 + CH_4 \xrightarrow{plasma} SiC + 4\ H_2 \quad (2)$$

$$CH_3\ SiCl_3 \xrightarrow{1400^\circ C} SiC + 3\ HCl \quad (3)$$

$$Si(CH_3)_4 \xrightarrow{950\text{-}1400^\circ C} SiC + 3\ CH_4 \quad (4)$$

$$(CH_3)_2SiCl_2 \xrightarrow{1200^\circ C} SiC + CH_4 + 2HCl \quad (5)$$

Particle size and stoichiometry are controlled by varying reaction temperature, gas concentration and gas flow rate.

Other methods include the direct reaction of silicon and carbon[34] and the gas evaporation method,[38] in which the raw material surface is heated and melted using an arc discharge in a mixed gas (consisting of an inert gas and H_2 or N_2) to form ultrafine SiC particles.

A new synthesis process has been recently developed to produce small, high purity, non-agglomerated powders of SiC.[39,40] In this process, the ceramic powder is synthesised by rapid heating (plasma heating) a reactant gas (silane, SiH_4, mixed with methane, CH_4, or ethylene,C_2H_4). The characteristics of the powders are controlled by the cell pressure, the reactants, their flow rates and flow ratios and the temperature

distribution within the reaction zone. Luce *et al.*[41] further studied the same process by using laser heating and by varying the reaction conditions (laser power, flow rates and ratio of reacting gases). The powder synthesised by this technique is a mixture of amorphous and crystalline powder.

3.4 SINTERING

The high degree of covalence implies a difficult sintering of SiC-bodies by simple heating of powder compacts. As a result, many different sintering techniques have been developed. Among these, pressureless sintering, hot-pressing and reaction sintering are the most important ones and, depending on the impurities or the sintering additives, a solid state or a liquid phase sintering is activated.

3.4.1 Solid state sintering

Silicon carbide is produced on industrial scale by solid state sintering. The most utilized additives are boron and carbon. The effectiveness of these two elements was firstly reported by Prochazka.[42] The amount of B, in metallic form or as B_4C, necessary to obtain fully dense materials is about 0.3 wt%. Boron or carbon by alone are not able to activate any sintering mechanisms of SiC, but an amount above 0.25 wt% of free carbon must be present.

It is supposed that carbon, during sintering removes the SiO_2 present on SiC particles as surface oxide with formation of volatile species following:

$$SiO_2 + C \rightarrow SiO(g) + CO(g) \quad (6)$$

From this reaction, the required amount of C depends on the amount of SiO_2 to be removed. However, higher C content hinders the densification of SiC, according to Motzfeld.[43] The reaction of removal of silica is quite sluggish and it was suggested by Tanaka a slow heating in the range 1000-1500°C or even an isothermal stage to complete the reaction and allow the leak of the volatile species.[44]

The function of B in the mechanisms of densification is not completely understood, but it is hypothesized that its selective segregation at the grain boundaries decreases the interface energy, hence the combined action of B and C should increase the driving force for the densification. It is also suggested that B introduces C-

vacancies in SiC lattice increasing the diffusivity of Si and C.[45] It was also observed that boron acts as grain inhibitor.[42]

Besides B and C, another additive utilized for SiC sintering in solid state is Al, in the element form or as Al_4C_3. Al possesses a higher solubility in SiC than B and it is supposed to activate diffusive processes leading, however, to lower densities.[46]

Summarizing, the solid state sintering requires temperature ranging from 2100 and 2200°C in vacuum or Ar, and an eventual application of pressure in the final stage. This process has several advantages:

- the mechanical properties retain the same values from room to high temperature, due to the absence of grain boundaries phases that would soften and make the material to collapse;
- high oxidation resistance;
- high resistance to corrosion owing to clean grain boundaries.

However several drawbacks are also evident:

- high technological costs, due to the high temperatures and pressures required for the densification;
- poor microstructural control, as the sintered material has 20-50 μm-sized grains and the flaws population can be remarkable;
- low fracture toughness of the final material, ~2-2.5 $MPam^{1/2}$, due to the absence of toughening mechanisms;
- low flexural strength values, owing to the coarse microstructure deriving from the extreme processing parameters.

3.4.2 Liquid phase sintering

Liquid phase sintering has been extensively applied in order to obtain dense SiC ceramics. This innovative approach to the sintering of SiC was initiated in the early 1980s.[47] The major inspiration for this densification strategy came from the sintering procedures of Si_3N_4 with Al_2O_3-Y_2O_3 additives.[48-50] Adopting this combination of additives, superior self-reinforced SiC was successfully fabricated.[51,52] Various sintering parameters and types of additives were utilised for the optimisation of the properties. The advantage of liquid phase was that SiC could be sintered to high densities (>95% th. density) at temperatures well below 2000°C.[53] The addition of

Al_2O_3-Y_2O_3 in ratio 6:4 promotes the formation of a liquid phase whose composition depends on the amount of SiO_2 present in the starting SiC powders, and on other impurities. Once the liquid is formed, it helps the mass transfer mechanisms, unless the matrix is soluble in the liquid. Its function is, indeed, to favour the rapid SiC particle rearrangement and lead to densification through dissolution and repercipitation mechanisms.

The most relevant factors affecting the liquid phase sintering are the specific surface of SiC particles, the sintering atmosphere, the amount and composition of the liquid phase, the presence of a protective bed and the time and temperature of sintering.

Firstly, the higher is the specific surface of the particles, the faster is the densification as the driving force is the minimization of the total surface energy.[54]

Concerning the sintering atmosphere, N_2 hinders the densification, as a temperature of 2100°C is required compared to 1900°C under Ar.[55,56]

The utilization of additives implies the presence of grain boundaries phases, which can negatively affect some properties, such as creep resistance and electrical conductivity. However, an adequate thermal treatment after sintering could totally remove the boundary phases, favouring the re-crystallization at the triple points.[57]

The major problem during sintering in presence of oxide additives is the formation of volatile composites occurring after reaction between SiC and the same additives.[58,59] SiC could react with the surfacial SiO_2 following the decomposition reaction:

$$SiC + 2\ SiO_2 \rightarrow 3\ SiO(g) + CO(g) \quad (7)$$

which provoke weight loss of the order of 1.5-2 %. On the contrary, in presence of additives, such as Al_2O_3, the weight loss is more consistent, around 5-11%, according to:

$$SiC + Al_2O_3 \rightarrow Al_2O(g) + SiO(g) + CO(g) \quad (8)$$

The analogous reaction for Y_2O_3 is still ambiguous and controversial.

If the weight loss exceeds values of 5%, the deriving microstructure is inhomogeneous with considerable amount of residual porosity. Further, the carbo-reduction of the additives implies a decrease of the volume of the liquid phase and hence the sintering rate is decreased.

These inconveniences can be overcame, through a protective powder bed containing the additives, which tend to evaporate. Besides constituting a physic barrier t the leakage of volatile species, the powder bed is a source of SiO, Al_2O and CO in the pellet, increasing their partial pressure and hindering the decomposition of SiC.[60]

Due to the lower temperatures required by liquid phase sintered SiC, the final composites present a higher flexural strength and an increased fracture toughness thanks to the change from transgranular to intergranular fracture, both because the mean grain size is reduced and the abnormal grain growth is limited.

The most widespread sintering additive system is composed by Al_2O_3-Y_2O_3 which forms a eutectic between Al_2O_3 and YAG (yttrium allumina garnet), 3 Y_2O_3· 5 Al_2O_3, at 1780°C and favours the densification.[61] On the contrary, the other liquids resulting from the other eutectics are not equally effective, probably due to the wettability of SiC by these liquids. The presence of SiO_2 sensibly influences the temperature of formation of liquid phase as depicted in the ternary phase diagram of Fig. 3.5, where is shown that the lowest temperature of formation of liquid phase is around 1400°C.

Fig. 3.5: Ternary phase diagram among SiO_2-Y_2O_3-Al_2O_3.[61]

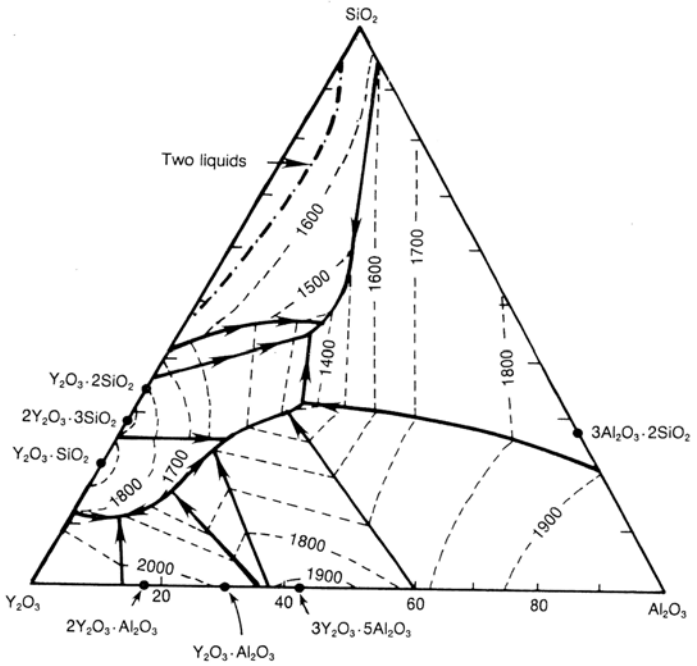

The sintering of SiC occurs through the mechanisms of Ostwald ripening, as confirmed by the core-rim structure observed in the sintered material by Sigl and Kleebe.[62] The final microstructure also depends on the typology of the starting powder and on the temperature and sintering time.[63] If β-SiC phase is hot pressed, the obtained microstructure is fine and regular, due to the low sintering temperature and the shorter sintering time compared to the pressureless sintering. These processing parameters hinder the β to α transformation. If SiC is pressureless, then the temperatures are higher and the holding time lower, allowing the plytypism change. A schematic of this transformation is shown in Fig. 3.6.

Fig. 3.6: Schematic microstructure development of β-SiC during liquid phase sintering sintering.

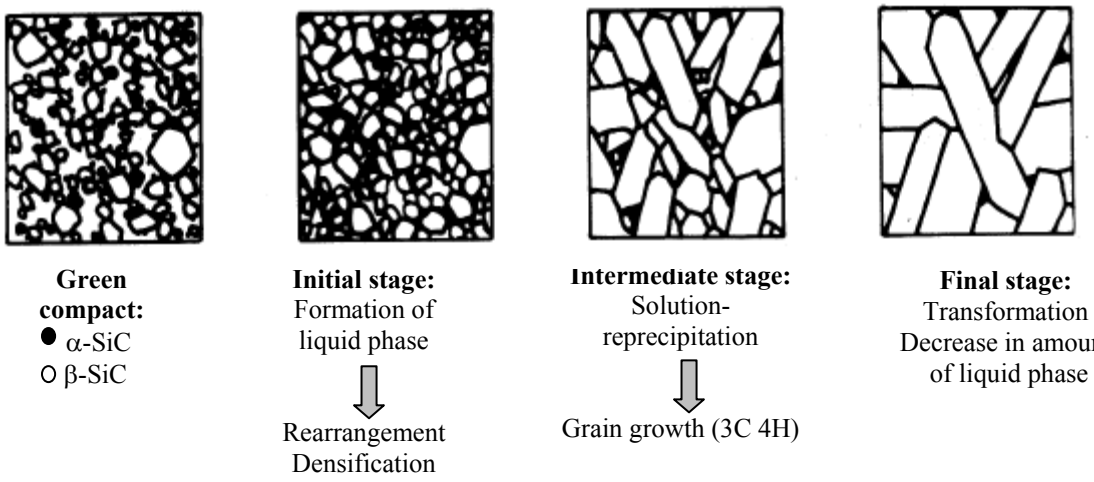

An alternative to the Al_2O_3-Y_2O_3 system, utilizes the liquid phase produced by Al_2O_3 and C,[64] with formation of Al_2OC which can form through different paths:

$$SiC + Al_2O_3 + Al_4C_3 \rightarrow SiC + 3\ Al_2OC \quad (9)$$

$$SiC + Al_2O_3 + 4\ Al + 3\ C \rightarrow SiC + 3\ Al_2OC \quad (10)$$

$$SiC + SiO_2 + Al_4C_3 \rightarrow 2\ SiC + 2\ Al_2OC \quad (11)$$

The occurrence of liquid start from 1850°C (see Fig. 3.7) and the densification is much faster than with addition of B and C.

Silicon carbide sintered with Al_2OC is considered a very promising material from the mechanical point of view, even though the elastic modulus decreases with increasing the amount of the oxycarbide and hence high amount of this phase are not suitable for structural applications.[64]

Other additives systems are MgO-Al_2O_3, SiAlON and rare-earths metal oxides with Al_2O_3 or AlN.[65-67]

The use of AlN drives to materials with interesting mechanical properties and is used in combination with Y_2O_3. This system, in contrast with Al_2O_3-Y_2O_3, does not require any protective bed powder during pressureless sintering.[68]

Fig. 3.7: Pseudo binary phase diagram between Al_2O_3-Al_4C_3.[64]

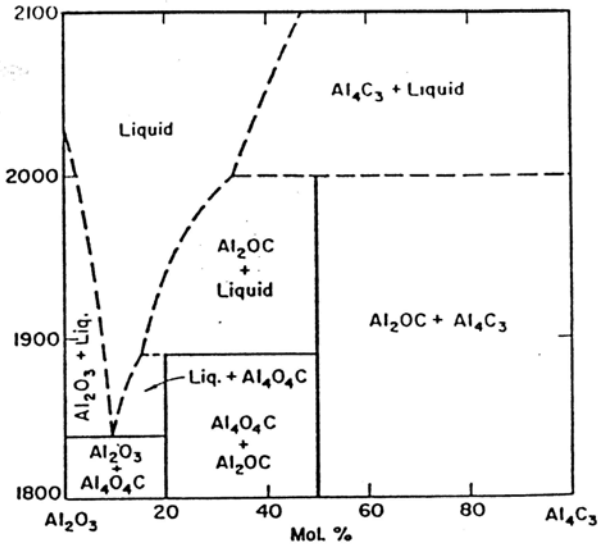

Figure 3.8: Pseudobinary phase diagram of AlN-Y_2O_3.[66]

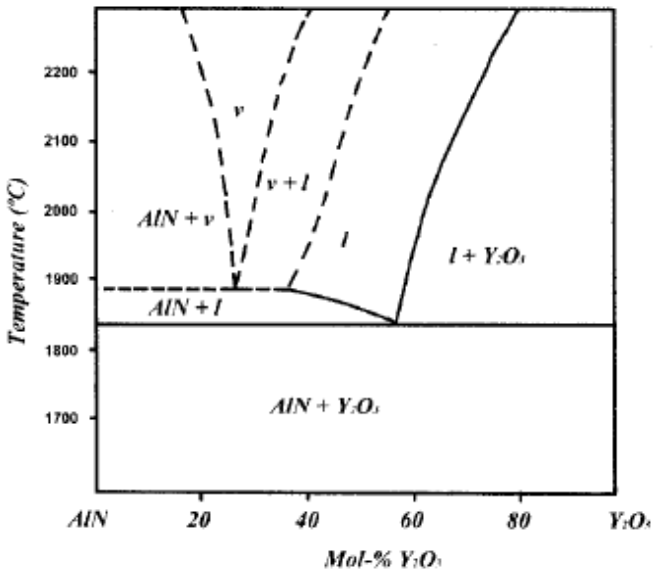

The reaction of decomposition of AlN according to

$$2\,AlN \rightarrow 2Al + N_2 \quad (12)$$

is easily suppressed by N_2 atmosphere during sintering. It has been observed by Biswas et al.[66] that the most effective composition, which leads to the highest density at lower temperature, does not coincide with the composition of the eutectic (40 mol% AlN – 60 mol% Y_2O_3, see Fig. 3.8), but with an amount of AlN equal to 60 mol% at 1920°C. High pressures hinder the achievement of high density material, due to an increased viscosity following the dissolution of nitrogen which decreases the matter transfer activity.[69,70]

In the literature, Al_2O_3 is combined with Nd_2O_3, Yb_2O_3, La_2O_3, or Er_2O_3 to form other sintering additives systems.[71,72] These materials are hot pressed at around 1800°C and the respective amount of the oxide is chosen in correspondence of the eutectic. The microstructures obtained exhibit similar features with homogeneous secondary phase distribution and small grain size. For SiC sintered with such additives hardness of 18-21 GPa, room temperature flexural strength of 600 MPa and fracture toughness up to 5.5 $MPam^{1/2}$ are reported.

Summarizing, the liquid phase sintering offers several advantages compared to the solid state sintering, such as:

- lower technological costs;
- higher microstructure control
- high mechanical resistance, as at room temperature the values obtained by LPS are 50-80% higher than those obtained by solid state sintering
- possibility to induce microstructural modifications upon thermal treatments which induce in crease in the fracture toughness and high temperature resistence and could eventually remove the grain boundaries phases favouring their recristallyzation at the triple points.

But, unavoidably there are also negative aspects, as:

- lower oxidation and corrosion resistance, since the grain boundaries phases accentuate the chemical reactions; however the operating temperature in oxidizine environment exceed 1200°C;
- collapse of the mechanical properties above 1000°C for many as-sintered systems, due to the grain boundaries softening.

3.5 MECHANICAL PROPERTIES

3.5.1 Strength

The strength of SiC sintered bodies depends on a number of factors including the impurities amount, size distribution of microstructural defects, mechanical testing method, strain rate, temperature and, in some cases, the orientation of the test specimen relative to the original material.[73] It was reported that surface flaws drastically lower the strength, which, in turn, increases with increasing density of the sintered body. A study on the influence of the mechanical testing method revealed that the values of strength measured in tension were lower than those obtained in bending, because a larger volume of material was tested. Although bending strength was independent from the orientation of the tested specimen, higher values were obtained in the direction parallel to the applied pressure during hot pressed SiC.[73] Inclusions play a significant role in determining the strength of fully dense material, as these inclusions are the crack initiating regions. The temperature dependence of the strength of hot pressed SiC containing B additions had been measured by Prochazka and Charies.[74] Edington *et al.*[73] also reported on the variation of bend strength with temperature in hot pressed SiC (Fig. 3.9).

Figure 3.9: The variation of bending strength with temperature in hot pressed SiC.[73]

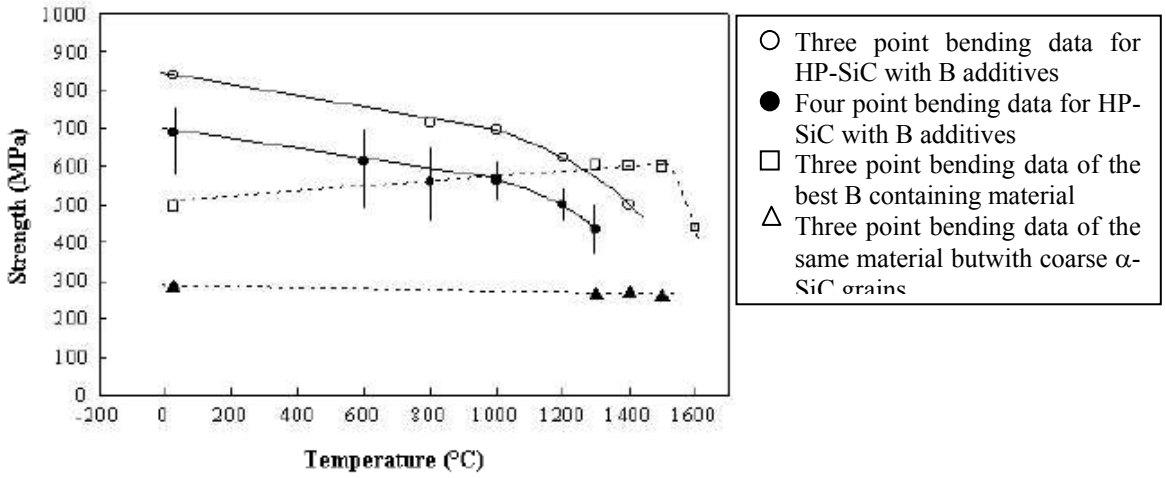

Dutta[75,76] studied the strength behaviour from room temperature to 1370°C. It was found that surface oxidation was responsible for the decrease. Additions of boron and carbon were found to have negligible effect on the room temperature flexural strength

of α-SiC. Similarly, the bending strength was lower at 1400°C than at room temperature in the case of both 2 wt% and 15 wt% Al_2O_3-added SiC.[77]

However, bending strength showed a tendency to increase with sintering time for both 2 wt% and 15 wt% Al_2O_3. Jun *et al.*[78] reported the effects of additions of AlN, TiN additives to SiC and of the sintering atmosphere on the flexural strength. When sintering is carried out in N_2/Ar atmosphere, SiC with improved flexural strength is obtained due to a higher sintered density and finer grain size. AlN addition also shows a similar influence on the flexural strength. The bending strength increases with the amount of sintering aids at room temperature. A maximum average 3-point bending strength of 953 MPa was obtained in a sample sintered in N_2/Ar with 16 wt% sintering aids. This value was much higher as compared to conventional Ar-sintered SiC.[78] Keppeler *et al.*[79] investigated the high temperature bending strength and concluded that globular LPS-SiC material showed an increase of strength in the temperature range between 1000°C to 1200°C due to healing of flaws and surface cracks by a glassy phase formed by oxidation. Superior strength will be eventually achieved by proper microstructural design and minimising the size of defects through improved manufacturing processes.

3.5.2 Fracture toughness

The K_{Ic} value of SiC was shown[74] to increase with decreasing grain size, the and optimum fracture toughness was obtained for grain sizes less than 10 μm. Schwetz and Lipp[80] determined the value of K_{Ic} at room temperature and at 1200°C using the SENB (Single Edge Notched Beam) method for SiC sintered with the additive systems B+C and Al+C. The results showed that the room temperature K_{Ic} values of both materials were identical. However, with increasing temperature, the fracture toughness also increased, and this was much more pronounced in the B+C system. Grathwohl *et al.*[81] investigated similar system and found that all materials exhibited a moderate resistance against fatigue at 1300°C. The fracture mode was found to be clearly different for B+C and Al+C additive systems. Suzuki and Sasaki[82] reported the K_{Ic} values of sintered SiC with 2 wt% and 15 wt% Al_2O_3 and found that K_{Ic} increased with sintering time. After 24 h of sintering, the sintered SiC with 15 wt% Al_2O_3 revealed a K_{Ic} of 5.7 $MPa \cdot m^{1/2}$ which was twice the fracture toughness of B-doped

sintered -SiC (2-3 MPa·m$^{1/2}$).[83] This value was also higher than K_{Ic} of 3-4 MPa·m$^{1/2}$ for an Al_2O_3-fluxed hot pressed SiC.[83] The K_{Ic} values strongly depend on the aspect ratio of the grains. Higher aspect ratio increases the K_{Ic} value owing to the resulting microstructure with interlocking plate-like grains.

Improved fracture behaviour of novel SiC ceramics having rod-like whiskers grains was observed by Kodama and Miyoshi.87 They concluded that the fracture toughness of these ceramics was higher than that of ordinary SiC and its maximum value was 7.3 MPa·m$^{1/2}$. Grains pullout, grains bridging and crack deflection were considered to be the main operative mechanisms that led to improved fracture toughness. Based on these toughening mechanisms, Lee and Kim[84] and Cao *et al.*[85] improved the fracture toughness of β-SiC ceramics with Al-B-C additives. Lee and Kim[84] also showed that with α-SiC starting powder, the fracture toughness increased slightly upon annealing whereas in the case of β-SiC powder, it increased significantly due to crack bridging and crack deflection by the plate-like grains. Keppeler *et al.*[79] also observed a similar mechanism in a material liquid phase sintered from 99 wt% β-SiC and 1 wt% α-SiC, although they considered that pullout of platelets was not a toughening mechanism as platelet grains with an orientation normal to the crack propagation were broken without any debonding.

3.6 APPLICATIONS OF SiC-BASED CERAMICS

Thanks to the unique combination of properties just presented, as high melting point (2730°C), extremely high hardness (25 GPa), flexural strength around 900 MPa, low density (3.22 g/cm^3) and low coefficient of thermal expansion (4·10^{-6}/K) which does not significatively changes with changing of polytypes, SiC-based ceramics find employ in several industrial sectors. Example of structural components made in silicon carbide are reported in Fig. 3.10.

Semiconductor - Pure α-SiC is an intrinsic semiconductor with band gaps of 3.28 eV (4H) and 3.03 eV (6H) respectively. Historically it was used in early radio as a detector.

Lightning arrestors - The earliest electrical application of SiC was in lightning arresters in electric power systems. These devices must exhibit high resistance until

the voltage across them reaches a certain threshold, VT, at which point their resistance must drop to a lower level and maintain this level until the applied voltage drops below VT. It was recognized that SiC had such a voltage-dependent resistance, and so columns of SiC pellets were connected between high-voltage power lines and the earth. When a lightning strikes the line raises the line voltage sufficiently, the SiC column will conduct, allowing strike current to pass harmlessly to the earth instead of along the power line. Such SiC columns proved to conduct significantly at normal power-line operating voltages and thus had to be placed in series with a spark gap. This spark gap is ionized and rendered conductive when lightning raises the voltage of the power line conductor, thus effectively connecting the SiC column between the power conductor and the earth. Spark gaps used in lightning arrestors are unreliable, either failing to strike an arc when needed or failing to turn off afterwards, in the latter case due to material failure or contamination by dust or salt. Use of SiC columns was originally intended as a way to eliminate the need for the spark gap in a lightning arrester. Gapped SiC lightning arresters were used as lightning-protection tool and sold under General Electrics and Westinghouse brand names, among others. The gapped SiC arrester has been largely displaced by no-gap varistors that use columns of zinc oxide pellets.

Fig. 3.10: Examples of SiC-based structural components.

Circuit elements - Silicon carbide is used for blue leds, ultrafast, high-voltage Schottky diodes and high temperature thyristors for high-power switching. A paper by Jayan Baliga[86] demonstrated the potential of SiC as a power device material. Another problem is that SiC itself breaks down at high electric fields due to the formation of extended stacking faults, but this problem may have been resolved relatively recently.[87]

High-temperature applications - Thanks to its high thermal conductivity, SiC is also used as substrate for other semiconductor materials such as gallium nitride. Due to its wide band gap, SiC-based parts are capable of operating at high temperature, which, together with good thermal conductivity of SiC, makes SiC devices good candidates for elevated temperature applications. SiC devices also possess increased tolerance to radiation damage, making SiC a desirable material for defense and aerospace applications. Although diamond has an even higher band gap, SiC-based devices are easier to manufacture because is more convenient to grow an insulating layer of silicon dioxide on the surface of a silicon carbide wafer than it is on diamond. Pure SiC is a poor electrical conductor. Addition of suitable dopants significantly enhances its conductivity. Typically, such material has a negative temperature coefficient between room temperature and about 900°C, and positive temperature coefficient at higher temperatures, making it suitable material for high temperature heating elements.

Ultraviolet detector - Silicon carbide is also used as an ultraviolet detector. Nikola Tesla, around the turn of the 20th century, performed a variety of experiments with carborundum.[88]

Astronomy - Silicon carbide's hardness and rigidity make it a desirable mirror material for astronomical work, although its properties also make manufacturing and designing such mirrors quite difficult. While rare on Earth, silicon carbide is remarkably common in space. It is a common form of stardust found around carbon-rich stars, and examples of this stardust have been found in pristine condition in primitive meteorites. Silicon carbide found in space and in meteorites is almost exclusively the beta-polymorph. Silicon carbide may be a major component of the mantles of as-yet hypothetical carbon planets.

Abrasive - In the arts, silicon carbide is a popular abrasive in modern lapidary due to the durability and low cost of the material. In manufacturing, it is used for its hardness in abrasive machining processes such as grinding, honing, water-jet cutting and sandblasting. Particles of silicon carbide are laminated to paper to create sandpapers and the grip tape on skateboards.

Disc brakes - Silicon-infiltrated carbon-carbon composite is used for high performance "ceramic" brake discs as it is able to withstand extreme temperatures. The silicon reacts with the graphite in the carbon-carbon composite to become carbon fiber reinforced silicon carbide (C/SiC). These discs are used on some road going sports cars, including the Porsche Carrera GT, the Bugatti Veyron, Bentleys, Ferraris, Lamborghinis, and some specific high performance Audis.

Heating element - References to silicon carbide heating elements exist from the early 20th century when they were produced by Acheson's Carborundum Co. in the U.S. and EKL in Berlin. Silicon carbide offered increased operating temperatures compared with metallic heaters, although the operating temperature was initially limited by the water-cooled terminals, which brought the electric current to the silicon carbide hot zone. Operating temperature and efficiency were later increased by the use of separate low resistance silicon carbide "cold ends". Silicon carbide elements are used today in the melting of non-ferrous metals and glasses, heat treatment of metals, float glass production, production of ceramics and electronics components, etc.

Nuclear fuel - Silicon carbide is often used as a layer of tristructural-isotropic (TRISO) coating for the nuclear fuel elements of high temperature gas cooled reactors or very high temperature reactors.

Jewelry - As a gemstone used in jewelry, silicon carbide is called Moissanite after the jewel's discoverer Dr. Henri Moissan. Moissanite is similar to diamond in several important respects: it is transparent and hard (9 on the Mohs scale compared to 10 for diamond), with a refractive index between 2.65 and 2.69 (compared to 2.42 for diamond). Moissanite is somewhat harder than common cubic zirconia. Unlike diamond, Moissanite is strongly birefringent. This quality is desirable in some optical applications, but not in gemstones. For this reason, Moissanite jewels are cut along the optic axis of the crystal to minimize birefringent effects. It is lighter (density 3.22 g/cm^3 vs. 3.56 g/cm^3), and much more resistant to heat. This results in a stone of

higher lustre, sharper facets and good resilience. Loose moissanite stones may be placed directly into ring moulds; unlike diamond, which burns at 800 °C, moissanite remains undamaged by temperatures up to twice the 900 °C melting point of 18k gold. Moissanite has become popular as a diamond substitute, and may be misidentified as diamond, since its thermal conductivity is much closer to that of diamond than any other diamond substitutes. It can be distinguished from diamond by its birefringence and a very slight green, yellow, or gray fluorescence under ultraviolet light.

Steel - Silicon carbide, dissolved in a basic oxygen furnace for steel, acts as a fuel and provides energy which increases the scrap to hot metal ratio. It can also be used to raise tap temperatures and adjust the carbon content. 90% silicon carbide is used by the steel industry as ladle deoxidizer, source of silicon and carbon in the ladle, electric furnace slag deoxidizer and as synthetic slag additive. It is less expensive than ferrosilicon and in combination with carbon, produces cleaner steel due to low level of trace elements, it has a low gas content, it does not lower the temperature of steel and it has an abundant world wide supply.

Armor - Like other hard ceramics, namely alumina and boron carbide, silicon carbide is used in composite armor (e.g. Chobham armor), and in ceramic plates in bulletproof vests. Dragon Skin, which is produced by Pinnacle Armor, utilizes disks of silicon carbide.

Catalyst support - The natural resistance to oxidation exhibited by silicon carbide, as well as the discovery of new ways to synthesize the higher surface area beta polytipe, has led to significant interest in its use as a heterogeneous catalyst support. The beta cubic form has already been employed for several years as a catalyst support for the oxidation of C4 hydrocarbons, such as n-butane, to maleic anhydride.

Cutting tools - This material proved to be exceptionally strong. In 1985, the first commercial cutting tools made from alumina and silicon carbide whisker-reinforced composite were introduced by the Advanced Composite Materials Corporation (ACMC) and Greenleaf Corporation.

Other applications foresee silicon carbide in diesel particulate filters, thin filament pyrometry to measure gas temperatures, ceramic membrane for industrial processes.

References

1 K. Yamada and M. Mohri, 'Silicon Carbide Ceramics', Vol.1, ed. S. S. Miya and Y. Inomata, Elsevier, Barking, U.K. (1991) 13

2 Popper, 'Special Ceramics', ed. P. Popper, The Brit. Ceram. Res. Assoc., Stoke-on-Trent, U.K. (1960) 209.

3 N. Camucu, D. P. Thompson and H. Mandal, J. Eur. Ceram. Soc., 17 (1997) 599.

4 M. K. Cinibulk and G. Thomas, J. Am. Ceram. Soc., 75 (1992) 2037.

5 Z. Shen, P. Käll and M. Nygren, J. Mater. Res., 14 (1999) 1462.

6 A. Rosenflanz and I. W. Chen, J. Eur. Ceram. Soc., 19 (1999) 2325.

7 K. Hirao, K. Watari, M. Toriyama and S. Kanzaki, J. Am. Ceram. Soc., 84 (2001) 353.

8 Y. Menke, V. Peltier-Baron and S. Hampshire, J. Non-Cryst. Solids, 276 (2000) 145.

9 L. S. Ramsdell, Am. Mineral., 32 (1947) 64.

10 T. Tagai, S. Sueno and R. Sadanaga, Mineral J., 6 (1971) 240.

11 J.E. Huheey, E. A. Keiter and R. L. Keiter, Inorganic Chemistry, HarperCollins College Publisher, (1993), New York, NY

12 S. Prochazka, "Why is it difficult to sinter covalent substancese?", General Electric Corp. Res. And Dev. Center Technical Information Series, Report n. 81CRD025, 1989, Schenectady, NY.

13 R. T. Dollof, WADD, Tech Rep., Wrigth, 60-143.

14 R. Telle, "Boride and carbide ceramics", in Materials Science and Technology – Structure and properties of ceramic"s Vol. 11 Ed R.W. Cahn, P. Haasen, E. J. Kramer, VCH Weinheim, Germany, (1994) 163-266.

15 W. F. Kippenberg, Philips Res. Rep., 18 (1963) 161-274.

16 N. W. Jepps and T. F. Page, Progress in crystal growth and characterization of polytype structure, Vol. 7, ed P. Krishna, Pergamon Press, Oxford, U.K. (1983).

17 C. Cheng, R.J Needs, V. Heine and N. Churcher, Europhysy. Lett., 3, (1987) 475-479.

18 C. Cheng, R.J Needs and V. Heine, J. Phys. C., 21, (1988) 1049-1063.

19 V. Heine and C. Cheng, "Geometry and thermodynamic: common problems of quasi-crystals, liquid crystal and incommensurate insulator", ed. J.C. Toledano, Plenum press, New York, NY, 1990.

20 V. Heine, C. Cheng and R. J. Needs, J. Am. Ceram. Soc., 10, (1991) 2630-2633.

21 J. A. Powell and H. A. Will, J. Appl. Phys., 43, (1972) 1400-1407.

22 A. H. Heuer, G. A. Fryburg, L. U. Ogbuji, T. E Mitchell and S. Shinozaki, J. Am. Ceram. Soc., 9-10 (1978) 406-412.

23 T. E Mitchell, L. U. Ogbuji and A. H. Heuer, J. Am. Ceram. Soc., 9-10 (1978) 412-413.

24 T. E Mitchell, L. U. Ogbuji and A. H. Heuer, J. Am. Ceram. Soc., 2 (1981) 91-99.

25 L. U. Ogbuji, T. E Mitchell, A. H. Heuer and S. Shinozaki, J. Am. Ceram. Soc., 2 (1981) 100-104.

26 N. P. Padture, J. Am. Ceram. Soc., 77 (1994) 519–23.

27 Y. W. Kim, M. Mitomo, and H. Hirotsuru, J. Am. Ceram. Soc., 78 (1995) 3145–3148.

28 J. J. Cao, W. J. MoberlyChan, L. C. De Jonghe, C. J. Gilbert, and R. O. Ritchie, J. Am. Ceram. Soc., 79, (1996) 461–69.

29 D. Sciti, S. Guicciardi, A. Bellosi, J. Eur. Ceram. Soc., 21 (2001) 621-632

30 G.D. Zhan, R.J. Xie, M. Mitomo and Y. W. Kim, J. Am. Ceram. Soc., 84 (2001) 945-950.

31 X. F. Zhang, Q. Yang and L. C. De Jonghe, Acta Mater., 51 (2003) 3849-3860.

32 S. Sugiyama and M. Togaya, J. Am. Ceram. Soc., 84 (2001) 3013-3013.

33 E. G. Acheson, Chem. News, 68 (1893) 179.

34 P. Matje and K. A. Schwetz, "Ceram. Trans., Ceramic Powder Science II", A, Vol.1, ed. G. L. Messing, E. R. Fuller, Jr. and H. Hausner, The Am. Ceram. Soc., Westerville, Ohio (1988) 460.

35 Y. Okaba, J. Hojo and A. Kato, J. Chem. Soc. Japan, 88 (1980) 188.

36 Y. Okaba, J. Hojo and A. Kato, J. Less-Common Met., 68 (1979) 29.

37 G. C. Wei, C. R. Kennedy and L. A. Harris, Am. Ceram. Soc. Bull., 63 (1984) 1054.

38 Y. Ando et al., J. Cryst. Growth, 52 (1981) 178.

39 W. R. Cannon, S. C. Danforth, J. H. Flint, J. S. Haggerty and R. A. Marra, J. Am. Ceram. Soc., 65 (1982) 324.

40 W. R. Cannon, S. C. Danforth, J. S. Haggerty and R. A. Marra, J. Am. Ceram. Soc., 65 (1982) 330.

41 M. Luce, O. Croix, C. Robert and M. Cauchetier, "Ceram. Trans., Ceramic Powder Science III", Vol.12, ed. G. L. Messing, S. Hirano and H. Hausner, The Am. Ceram. Soc., Westerville, Ohio (1990) p.267.

42 S. Prochazka, 'Mass Transport Phenomena in Ceramics', ed. A. R. Cooper and A. H. Heuer, Vol.9, Plenum Press, New York (1975) p.421.

43 K. Motsfeld, Int. Conf. ENGEINEERING CERAMICS '92, ed. M. Haviar, Reproprint Bratislava, (1993).

44 H. Tanaka, Silicon Carbide Ceramics, ed. by S, Smiya and Y. Inomata, Japanese original 1988, English translation Elsevier Science Publ. (19919, Vol. 1, pp. 213-238.

45 C. Greskovich and J.H. Rosolowski, J. Am. Ceram. Soc. 59, (1976) 336-343.

46 W. Bröcker, H. Landfermann and H. Hausner, Powder Metall. Int., 11 (1979) 83.

47 T. Sakai and N. Hirosaki, J. Am. Ceram. Soc., 68 (1985) C-191.

48 N. P. Padture and B. R. Lawn, J. Am. Ceram. Soc., 77 (1992) 2518.

49 M. A. Mulla and V. D. Kristic, J. Mater. Sci., 29 (1994) 934.

50 M. A. Mulla and V. D. Kristic, Acta Metall., 42 (1994) 303.

51 N. P. Padture, J. Am. Ceram. Soc., 77 (1994) 519.

52 Y. W. Kim, M. Mitomo and H. Hirotsuru, J. Am. Ceram. Soc., 78 (1995) 3145.

53 M. A. Mulla and V. D. Kristic, Am. Ceram. Soc. Bull., 70 (1991) 439.

54 H. Hausner, 'Energy and Ceramics', Mater. Sci. Monographs, Vol.6, ed. P. Vincenzini, Elsevier Scientific Publ. Co., Amsterdam (1980) p.582.

55 K. Takatori, N. Ogawa, M. Shimada and M. Koizumi, "Energy and Ceramics", Mater. Sci. Monographs, Vol.6, ed. P. Vincenzini, Elsevier Scientific Publ. Co., Amsterdam (1980) p.525.

56 T. Sakai and T. Aikawa, J. Am. Ceram. Soc., 71 (1988) C-7.

57 D. Sciti, S. Guicciardi, A. Bellosi, J. Eur. Ceram. Soc., 21 (2001) 621-632.

58 T. Grande, H. Sommerset, E. hagen, K. Wiik and M. A. Einarsrud, J. Am. Ceram. Soc. 80 (1997) 1047-1052.

59 S. Baud and F. Thevenot, "Effect of powder bed composition on liquid phase sintered silicon carbide", 9th Cimtec-World Ceramics Congress – Part B, ed. P. Vincenzini, Techna Srl, (1999) 805-812.

60 E. J. Winn and W. J. Clegg, J. Am. Ceram. Soc., 82 (1999) 3466-3470.

61 W. Dressler and R. Riedel, Int. J. Refract. Met. Hard Mat. 15 (1997) 13-47.

62 L. S. Sigl. H.J. Kleebe, J. Am. Ceram. Soc. 76 (1993) 773.

63 Y. W. Kim, M. Mitomo and H. Hirotsuru, J. Am. Ceram. Soc. 80 (1997) 99-105.

64 T. B. Jackson, Silicon carbide, (1987) 227.

65 M. Nader, F. Aldinger and M. J. Hoffman, J. Mater. Sci., 34 (1999) 1197-1204.

66 K. Biswas, G. Rixecker, I. Wiedmann, G. S. Upadhyaya and F. Aldinger, Mater. Chem. Phys. 67 (2001) 180-191.

67 V. A. Izhevskyi, L. A. Genova, A. H. A. Bressiani and J. C. Bressiani, Int. J. Refract. Met. Hard Mat., 19 (2001) 409-417.

68 K. Suzuki, Bull. Ceram. Soc. Japan, 21 (1986) 590.

69 C.W. Jang, J. Kim, and S. J. L. Kang, J. Am. Ceram. Soc., 85 (2002) 1281-1284.

70 A. L. Ortiz, T. Bhatia, N. P. Padture, and G. Pezzotti, J. Am. Ceram. Soc., 85 (2002) 1835-1840.

71 Y. Zhou, K. Hirao, M. Toriyama, Y. Yamauchi and S. Kanzaki, J. Am. Ceram. Soc., 84 (2001) 1642-1644.

72 Y. Zhou, K. Hirao, Y. Yamauchi and S. Kanzaki, J. Eur. Ceram. Soc., 22 (2002) 2689-2696.

73 J. W. Edington, D. J. Rowcliffe and J. L. Hawshall, Powder Met. Int., 7 (1975) 82.

74 S. Prochazka and R. J. Charies, Am. Ceram. Soc. Bull., 52 (1973) 885.

75 S. Dutta, J. Mater. Sci., 19 (1984) 1307.

76 S. Dutta, J. Am. Ceram. Soc., 68 (1985) C 269.

77 K. Suzuki and M. Sasaki 'Fundamental Structural Ceramics', ed. S. S Miya and R. C. Bradt, Terra Scientific Publ. Co., Tokyo (1987) 75.

78 H. W. Jun, H. W. Lee, G. H. Kim, H. S. Song and B. H. Kim, Ceram. Engg. and Sci. Proc., 18 (1997) 487.

79 M. Keppeler, H. G. Reichert, J. M. Broadley, G. Thurn, I. Wiedmann and F. Aldinger, J. Eur. Ceram. Soc., 18 (1998) 521.

80 K. A. Schwetz and A. Lipp, 'Science of Ceramics', Vol.10, ed. H. Hausner, Dt. Keram. Ges., Köln (1980) 149.

81 G. Grathwohl, R. Hamminger, H. Iwanek and F. Thümmler, 'Science of Ceramics', Vol.12, ed. P. Vincenzini, Ceramurgica s.r.1., Faenza, Italy (1984) 583.

82 K. Suzuki and M. Sasaki 'Fundamental Structural Ceramics', ed. S. S Miya and R. C. Bradt, Terra Scientific Publ. Co., Tokyo (1987) 78.

83 K. T. Faber and A. G. Evans, J. Am. Ceram. Soc., 66 (1983) C-94.

84 S. K. Lee and C. H. Kim, J. Am. Ceram. Soc., 77 (1994) 1655.

85 J. J. Cao, W. J. MoberlyChan, L. C. DeJonghe, C. J. Gilbert and R. O. Ritchie, J. Am. Ceram. Soc., 79 (1996) 461.

86 M.; Baliga, B.J. Bhatnagar (March 1993). "Comparison of 6H-SiC, 3C-SiC, and Si for power devices". IEEE Transactions on Electron Devices.

87 A. Madar, R. Roland, Nature 430 (2004) 974–975.

88 Hart, Jeffrey A.; Stefanie Ann Lenway, Thomas Murtha. "A History of Electroluminescent Displays".

CHAPTER 4

SECONDARY PHASE

In this study molybdenum disilicide, $MoSi_2$, was selected as secondary phase both for silicon carbide-based materials and for ultra high temperature ceramics materials, thanks to its high melting point, its high stiffness and its ability to improve the oxidation resistance, thanks to the formation of a protective silica layer on the surface.

4.1 INTRODUCTION

Molybdenum disilicide was discovered in 1907,[1] and was considered a high temperature corrosion-protective coating material for ductile metals. The first commercial heating-elements were patented by Kanthal in 1953.[2]

Molybdenum disilicide is a high-melting-point (2030°C) material with excellent oxidation resistance and a moderate density (6.24 g/cm^3), which is in use in high-temperature furnaces because it can withstand prolonged exposure in air. It is a promising candidate material for high temperature structural applications, particularly in aircraft gas turbine engines.[3-6] Current potential applications of $MoSi_2$-based materials include turbine airfoils, combustion chamber components in oxidizing environments, missile nozzles, molten metal lances, industrial gas burners, diesel engine glow plugs and materials for glass processing. In microelectronic devices, thin silicide layers are used as contacts and interconnections because they have low electrical resistance, high thermal stability, high electron-migration resistance, and excellent diffusion-barrier characteristic.[7]

Fig. 4.1 shows the binary Mo-Si equilibrium diagram.[8] Three Mo-Si stoichiometries have been found, which are Mo_3Si (cubic), Mo_5Si_3 (tetragonal), and $MoSi_2$ (tetragonal).

The crystal structure of $MoSi_2$ is C11b type. The lattice parameters are a = 0.3205 nm and c = 0.7845 nm with c/a = 2.45. Molybdenum atoms occupy (0,0,0) and (1/2, 1/2,

1/2) positions and silicon atom positions are (0,0,1/3), (0,0,2/3), (1/2,1/2,1/6), and (1/2,1/2,5/6). The unit cell can be thought of as consisting in three squashed cubic pseudo-cells stacked in the c direction, each pseudo-cell containing an atom at its body centre (Fig. 4.2).

Until recently, it was believed that $MoSi_2$ exhibited the tetragonal C11b structure (low temperature α phase) below 1900°C and the hexagonal C40 structure (high temperature β phase) between 1900°C and its melting temperature of 2030°C. However, recent investigations revealed that the C11b structure (α phase) is maintained up to the melting point, and the previously reported high-temperature C40 phase (β phase) is stabilized by impurities.[9]

Fig. 4.1: Binary Phase Diagram between Mo-Si.

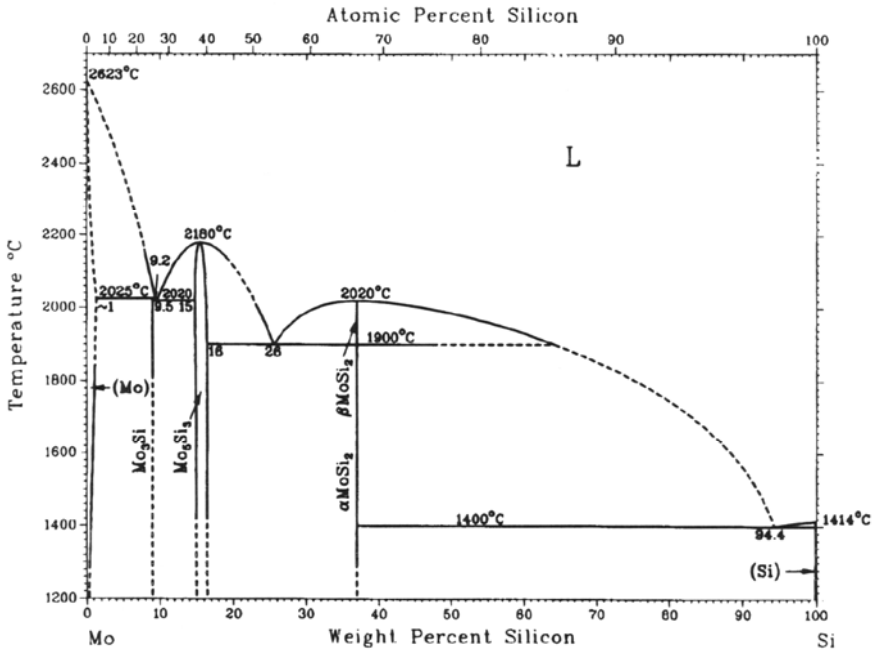

Fig. 4.2: Crystal Structure of $MoSi_2$.

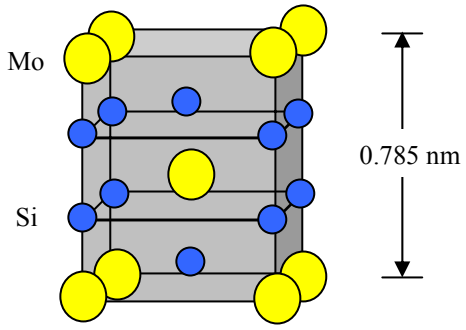

4.2 PHYSICAL PROPERTIES

The properties of $MoSi_2$ make it interesting as a high temperature structural material.[3-6] $MoSi_2$ has a high melting point of 2030°C and superb high temperature oxidation resistance, because it forms a thin coherent, adherent and protective silica layer. In polycrystalline form, $MoSi_2$ exhibits a brittle-to-ductile transition in compression in the vicinity of 1000°C. In some orientations of $MoSi_2$ single crystals, macroscopic ductility is apparent at much lower temperatures. The material is thermodynamically stable with a wide range of structural ceramics, including Si_3N_4, SiC, Al_2O_3, ZrO_2, mullite, TiB_2, and TiC. Hence, there is a significant potential for composite development. It can also be alloyed with other high melting point silicides such as WSi_2 and $NbSi_2$. Due to the metallic nature of its bonding, $MoSi_2$ can be electro-discharge machined, thus making it easier to machine than most structural ceramics. Finally, $MoSi_2$ is an abundant, relatively low cost material which is also environmentally benign.

In terms of engineering properties, $MoSi_2$ has thermal conductivity between that of Si_4N_3 and SiC. High thermal conductivity is very beneficial for increased cooling effectiveness of engine components. The elastic modulus of $MoSi_2$ is close to that of SiC (≅430 GPa).[10] While the high temperature oxidation resistance of $MoSi_2$ is similar to that of SiC, maximum oxidation rates in $MoSi_2$ actually occur at a temperature of 500°C. $MoSi_2$ has a thermal expansion coefficient close to that of Al_2O_3 (≅7.4-8.3 10^{-6}/°K),[11] which is beneficial for minimizing thermal stresses and improving thermal shock resistance. Thermal expansion is also important when designing a composite system. Matching thermal expansion coefficients of matrix and reinforcement is important to minimize the effects of interfacial cracks on subsequent mechanical properties.

The fracture toughness behaviour in both $MoSi_2$ and silicon-based ceramics is similar. They both fracture in a brittle manner resulting in low toughness. The toughness levels of monolithic $MoSi_2$ and silicon-based ceramics are in the same range (~3 $MPa \cdot m^{1/2}$).[12] Thus, it is possible to utilize classical ceramic composite approaches to toughen $MoSi_2$ composites.

Commonly, ceramics are reinforced with other ceramic fibres (continuous and discontinuous), whiskers, or particles, which possess weaker interfacial bonds to permit

crack bridging or deflection processes as dominant toughening mechanisms. Other techniques involve phase transformation toughening and elongated grain structures. In each case, the effects are anyway moderate.

4.3 SINTERING OF $MoSi_2$

Hot pressing has been generally used to consolidate $MoSi_2$ specimens.[13,14] The $MoSi_2$ powder was hot-pressed for 15 minutes from 1500 to 1920°C to obtain a high density (> 97% of the theoretical) and a uniform microstructures. Grain boundaries and secondary phases were clearly visible without etching of the material. Compacts prepared at temperatures from 1500 to 1800°C contained slight porosity along grain boundaries, independent of grain size, with large pores approximately 10 μm in diameter, while the specimen consolidated at 1920°C were fully dense. Small amorphous spherical SiO_2 particles, which are independent of grain size, were observed within the $MoSi_2$ grains and at grain boundaries in all specimens, with a mean grain size of 2 μm. Above approximately 1750°C, volatile SiO(g) and solid Mo_5Si_3 were created from $MoSi_2$ and SiO_2. The increased surface reactivity due to SiO volatilization is a likely mechanism for the observed rapid increase in $MoSi_2$ grain size. Above 1900°C, a $MoSi_2$-Mo_5Si_3 eutectic liquid forms. Increased grain size and lack of porosity in the specimen consolidated at 1920°C are consistent with the effects of liquid-phase sintering.

Hot isostatic pressing (HIP) has also been used to evaluate densification of $MoSi_2$ specimens as a function of temperature, pressure and time.[15-19] Molybdenum disilicide powders have been consolidated by HIP at 207 MPa pressure, in the temperature range of 1200-1400°C for 1 h to 4 h. The higher and the longer are the temperature and the time, the higher are the densities. A relative density of 99% is observed in a specimen consolidated at 1400°C for 4 h. Grain sizes in the $MoSi_2$ specimens vary from 20 to 30 μm over the range of process conditions considered. The grain size increases with temperature (ΔT = 200°C) is of the order of 7 μm and that with time (Δt= 3h) is at most 3 μm. The absence of fine grains in the consolidated specimens suggests that diffusion is probably not the primary densification mechanism. The presence of cusped pores, the observed grain sizes and the low diffusivities of the constituents suggest that the densification is most likely dominated by power law creep (PLC). It has been found that

slow cooling (<5°C/min) under full pressure or slowly released pressure (~2 MPa/min) produces the best material. Rapid cooling or rapid release of pressure at elevated temperatures results in micro cracking in the consolidated material.

Plasma spray processing is a promising near-net shape manufacturing technology, combining melting, blending and consolidation into a single operation.[20] Rapid solidification rate (RSR) processing is an inherent characteristic of plasma spray processing and yields fine-grained and chemically homogeneous microstructures. Low pressure plasma spraying (LPPS) and vacuum plasma spraying (VPS) are important processing methods for fabrication of RSR-processed deposits. The advantages of VPS processing include dense and oxide- free deposits. During VPS processing, the substrate deposit system is exposed to high temperatures (800-900°C) owing to a reduced rate of heat removal and adiabatic recalescence. This causes annealing of the VPS deposit, leading to stress relief, improved interparticle bonding and recrystallization, without any significant grain growth.

Another technique to densify $MoSi_2$ is the vacuum plasma spray.[20,21] $MoSi_2$ powder, with an average particle size of 40 μm and oxygen content of 2400 ppm has been used to generate deposits with a high hardness, indentation fracture toughness and flexural strength. It is observed that annealing increases fracture toughness and flexural strength due to improved inter-particle bonding. Freestanding forms of $MoSi_2$ are annealed at 1100°C in flowing argon for 24 h and furnace cooled. In the as-sprayed deposits, RSR processing, associated with VPS, produces the hexagonal allotrope of $MoSi_2$ (impurities-stabilized β phase), which transforms to the tetragonal structure upon annealing. Elevated-temperature testing has shown that $MoSi_2$ has increased ductility, which may be an advantage in forming of these plasma-processed materials.

4.4 MECHANICAL PROPERTIES

4.4.1 Hardness

A hardness of 9-11 GPa is reported for polycrystalline $MoSi_2$.[22]

Addition of 2 wt% of C to $MoSi_2$, which removes the silica grain boundary phase on $MoSi_2$ particles, improves the Vickers hardness of the monolithic material.[23] In addition, carbon interacts with $MoSi_2$ to form SiC. Microhardness data at room

temperature and at 1000°C for the carbon-containing alloy shows marked improvement over carbon-free $MoSi_2$.

4.4.2 Strength

The major problem which prevents the use of $MoSi_2$ is its high temperature strength. Because its brittle-ductile-transition-temperature (BDTT) at around 1000°C, at low temperature the strength is limited by brittle fracture, while at high temperature is governed by plastic flow. In this respect, and because of its mixed covalent-metallic atomic bonding, $MoSi_2$ is a borderline intermetallic compound. For its effective use as a high temperature structural material, it becomes necessary to toughen the material at lower temperatures while simultaneously improving the strength at higher temperatures.

4.4.3 Fracture toughness

Fracture toughness for $MoSi_2$-based materials is around 3 $MPa{\cdot}m^{1/2}$.[12]

The addition of 2 wt% of C strongly improves the fracture toughness of $MoSi_2$ between 800 and 1400°C, while the fracture toughness of the C-free $MoSi_2$ decreases with increasing temperature as shown in Fig. 4.3.[23] The fracture mode has changed from intergranular (no carbon) to transgranular (with carbon), because of the removal of silica grain boundary phase by reaction with carbon. In pure $MoSi_2$, the viscosity of the grain boundary silica decreases with increasing temperature, resulting in grain boundary sliding with cavitation, thereby decreasing the toughness. On the contrary, the addition of carbon reduces the grain boundary sliding and improves high temperature toughness because of dislocation motion plasticity.

Fig. 4.3: Effect of carbon addition on fracture toughness of $MoSi_2$ at high temperature.

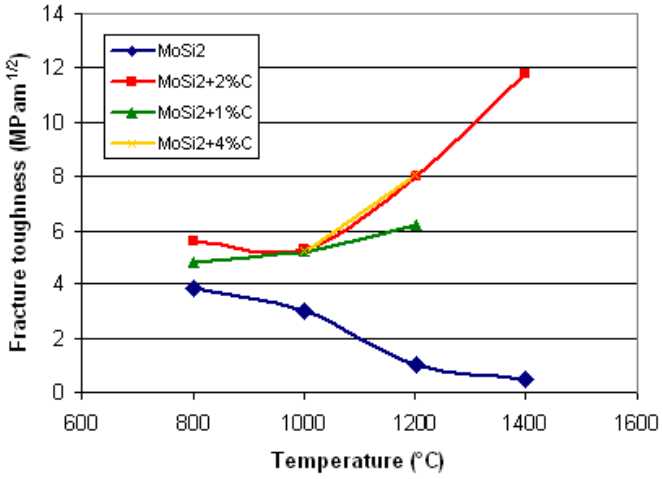

Generally, a second-phase reinforcement to $MoSi_2$, either brittle or ductile, has been proved to improve its mechanical properties. Such reinforcement has resulted in two effects, namely improvement of room temperature fracture toughness, and improvement of high temperature strength and creep properties, without degrading oxidation resistance. This improvement has been attributed to crack-deflection and crack-branching processes, or to the residual stresses at the particle-matrix interfaces. The addition of SiC, refined to about 2-3 μm, gives rise to larger increments in toughness at about 20 vol% SiC. With further increases of SiC volume fraction, the toughness decreases. In this case, it has been observed that the SiC particles fracture. At volume fraction levels greater than 20%, the fractured SiC particles have formed a continuous path, thereby lowering the fracture toughness.

4.5 OXIDATION

One major obstacle for $MoSi_2$ applications is the structural disintegration during low temperature oxidation, which is known as the "pest" effect.[24-26] $MoSi_2$ disintegrates to a powder when subjected to oxidizing environments at 400-600°C. This phenomenon was discovered in 1955 and has been referred to as $MoSi_2$ pesting. It has been suggested that the cause is grain boundary embrittlement produced by short-path diffusion of O_2 and subsequent dissolution into the grain-boundary areas. However, the exact nature of the pest effect is not clearly understood.

There are two possible oxidation reactions for $MoSi_2$.

$$2\ MoSi_2\ (s) + 7\ O_2 \rightarrow 2\ MoO_3\ (s) + SiO_2\ (s) \quad (1)$$

$$5\ MoSi_2\ (s) + 7\ O_2 \rightarrow Mo_5Si_3\ (s) + 7\ SiO_2\ (s) \quad (2)$$

Both reactions are thermodynamically feasible, but reaction (1) is favoured, which results in pesting between 400-600°C. Recent studies on poly- and single-crystalline $MoSi_2$ have shown that the pesting of $MoSi_2$ is associated with a substantial volume expansion, and the disintegrated powdery product contains mainly crystalline MoO_3 whiskers (or platelets), clusters of amorphous SiO_2, and residual $MoSi_2$ crystals. The pest reaction apparently has nucleation and growth stages. The reaction has been found to be highly eterogeneous, only occurring at local areas. An example of component after pest oxidation is reported in Fig. 4.4.

Fig. 4.4: Pest oxidation occurred in a localized area of a sheath of a thermocouple covered of $MoSi_2$.

A schematic drawing illustrating the evolution of reaction products during various stages of volume diffusion is presented in Fig. 4.5.[24] Volume diffusion of oxygen gives rise to the formation of a Si-Mo-O surface oxide, erupted blisters, and eventually loosely bound MoO_3 and SiO_2, which in turn cause massive oxidation and surface recession of the sample.

Polycrystalline $MoSi_2$ is much more susceptible to pest disintegration at 500°C. Both hot-pressed and arc-melted polycrystalline samples have disintegrated into powdery products within a short period of time (10 to 30 h). Pesting also involves grain boundary diffusion of oxygen. Grain boundary diffusion of oxygen causes preferential oxidation of inter-granular interfaces and the formation of protruding MoO_3 whiskers thereon. These would result in the formation of internal tensile stresses, which destroy inter-granular cohesion.

Fig. 4.5: Schematic drawings of the pesting reaction on $MoSi_2$.

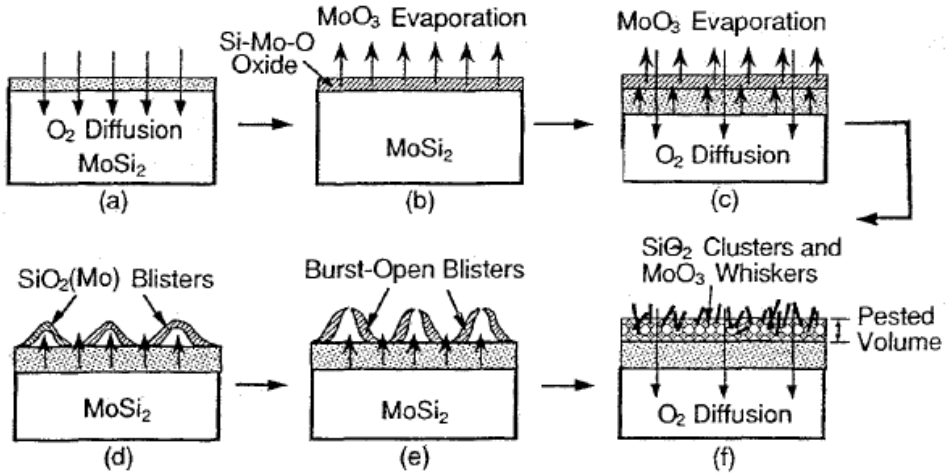

Although $MoSi_2$ has excellent oxidation resistance at temperatures in excess of 1600°C in air, it has a high creep rate above 1200°C, making it unsuitable for high temperature load bearing. Pentamolybdenum trisilicide (Mo_5Si_3) has a high melting point of 2160°C and a more complex unit cell that may lead to better creep resistance. A

major drawback to its application has been the fact that its oxidation resistance is greatly inferior to that of $MoSi_2$. Undoped Mo_5Si_3 exhibits pest oxidation at 800°C. Mass loss occurs in the temperature range of 900 to 1200°C due to volatilization of molybdenum oxide, indicating that the silica scale that forms does not provide a passivating layer. Recently it has been shown that small additions of boron to Mo_5Si_3 significantly improve oxidation resistance.[27] The addition of boron results in protective scale formation and parabolic oxidation kinetics in the temperature range of 1050 to 1300 °C. The oxidation rate of Mo_5Si_3 is decreased by five orders of magnitude at 1200 °C by doping with less than 2 wt% boron. Boron doping eliminates catastrophic pest oxidation at 800 °C. The mechanism for improved oxidation resistance of boron-doped Mo_5Si_3 is viscous sintering of the scale to close pores that form during the initial transient oxidation period due to volatilization of molybdenum oxide. Additionally, the boron forms a multiphase composite material consisting in $Mo_5Si_3B_x$, $Mo_5(SiB)_3$, Mo_3Si, $MoSi_2$, and MoB, with the exact phase composition depending on the level of boron addition. B-Mo_5Si_3 materials have been reported to possess good elevated temperature creep resistance.

4.6 $MoSi_2$ COMPOSITES

The use of $MoSi_2$ as a structural material was suggested in the early 1950s because of its excellent oxidation resistance. However, industrial application of $MoSi_2$ has been limited because of the brittle nature of the material at ambient temperatures, a high creep rate at temperatures above 1200°C, and accelerated oxidation at temperatures between 400 and 500°C. In 1978 it was recognized that $MoSi_2$ was an important matrix material for high temperature structural composites.28 Both refractory and ceramic reinforcements have been used in $MoSi_2$-composites. It was reported in 1985 that niobium wire reinforcement significantly improved the room temperature mechanical properties of the $MoSi_2$-Nb composite.[29] Great improvement in room temperature strength and fracture toughness in SiC whisker-$MoSi_2$ matrix composites was demonstrated in 1985.[30] In 1988 it was established that submicron SiC whisker-$MoSi_2$ matrix composites exhibited mechanical property levels within the range of high temperature engineering applications.[31] It is well known that fracture toughness of

brittle matrices can be improved by the incorporation of a ductile second phase. A key advantage in the use of refractory metal fibres is that they can provide both high-temperature creep resistance and toughness. The ductility of many refractory metal alloys, coupled with very high yield and tensile strengths, gives a large fracture energy and the potential to increase greatly the damage tolerance of a brittle matrix composite. Niobium is a suitable ductile reinforcement for $MoSi_2$ because of its high melting temperature and a thermal expansion coefficient which is close to that of $MoSi_2$. The result is much less matrix cracking upon thermal cycling during processing and in service.[32,33] Studies have demonstrated that such a composite system, indeed, exhibits a substantial increase in toughness compared to the matrix alone. Refractory metals such as W, Mo, and Ta have been used as ductile reinforcements.[34] One important attribute of $MoSi_2$ is that many potential ceramic reinforcements such as SiC, Si_3N_4, Al_2O_3, Y_2O_3, TiC, TiB_2, and ZrB_2 are thermodynamically stable with $MoSi_2$.[3] The reinforcement compatibility becomes important for creep and oxidation resistance. Composites may consist in a $MoSi_2$ matrix reinforced with a ceramic, or a ceramic matrix reinforced with $MoSi_2$. It has been shown that the addition of a ceramic phase to $MoSi_2$ substantially improves the high temperature strength, creep resistance, and room temperature fracture toughness of monolithic $MoSi_2$.

Silicon carbide reinforced $MoSi_2$ shows improved low-temperature fracture toughness and high-temperature strength.[35-38] The creep properties of $MoSi_2$ have also been successfully enhanced by the addition of SiC whiskers and particles. Although creep mechanisms in $MoSi_2$ composites are not clearly understood, the overall process is possibly due to the combined effects of grain boundary sliding and dislocation glide/climb at high applied stresses, while grain boundary sliding dominates at lower stresses. The chemical species SiC and $MoSi_2$ are thermodynamically stable, hence composites based on these materials have excellent microstructural stability. The $MoSi_2$-Si_3N_4 system was studied by Petrovic et al. and selected as promising material for structural applications.[39,40] Additions of Si_3N_4 to a $MoSi_2$ matrix significantly improve the intermediate temperature oxidation resistance of $MoSi_2$ and its elevated temperature mechanical properties. Additions of $MoSi_2$ to a Si_3N_4 matrix allow for the electro-discharge machining of Si_3N_4, and also lead to improved fracture toughness and elevated temperature oxidation resistance. Besides, addition of ZrO_2 particles to a

$MoSi_2$ matrix can produce significant transformation toughening effects in $MoSi_2$ composites.[41] Continuously graded $MoSi_2$-ZrO_2 materials with high density have been fabricated by uniaxial wet-molding, followed by hot pressing or hot isostatic pressing. Hot pressed $MoSi_2$-based composites containing Mo_5Si_3, SiO_2, CaO and TiC as reinforcing second phases have also been investigated in the temperature regime 1000-1300°C.[42] Fabrication of $MoSi_2$ and α- SiAlON or β'-SiAlON composites has also been explored.[43,44]

4.7 APPLICATIONS

$MoSi_2$-based materials find application in many interesting industrial sectors. These applications are driven by the excellent high temperature oxidation/corrosion resistance, in combination with other properties such as electrical conductivity.[4]

Heating elements - $MoSi_2$ materials have been employed for a long time as heating elements for air furnaces. The recent Kanthal Super 1900 heating elements can operate at a temperature of 1900°C in air and oxidizing environments. These Super 1900 elements are actually a solid solution alloy of $MoSi_2$ and WSi_2.

Aerospace gas turbine engines - Pratt & Whitney has been developing advanced materials for a blade outer air seal (BOAS), which is a hot section component of gas turbine engines.[4] In the engine, the BOAS is a stationary part, which is located directly opposite the rotating hot section turbine blades. The BOAS has to maintain a small gap of stable dimensions between itself and the turbine blade. If this gap widens during operation of the turbine, it directly affects the turbine efficiency. Although stationary, the BOAS is exposed to high turbine gas temperatures and significant thermal stresses. It has shown that $MoSi_2$-SiC and $MoSi_2$- Si_3N_4 composites possess significant thermal shock resistance in a simulated jet fuel combustion environment. These materials have survived 250 cycles from room temperature to 1500°C with no failure and they are good candidate for this application.

Diesel engines - The Toyota Central R&D facility in Japan has recently developed Si_3N_4 -30$MoSi_2$ composite diesel engine glow plugs.[4] These glow plugs have two distinct practical advantages over metal glow plugs. First, they are highly resistant to the diesel fuel combustion environment and thus have a long lifetime of approximately

thirteen years. Second, they can be heated at higher heating rates with the result that the diesel engine can be started faster. An inner cylindric composite with an interconnected $MoSi_2$ phase provides the necessary electrical conductivity. An outer, non-conducting sheath of the same $MoSi_2$-Si_3N_4 composition is employed as a cover for the inner conducting composite and has the same thermal expansion coefficient and thermal conductivity. This microstructural tailoring of $MoSi_2$-Si_3N_4 composites allow optimum performances of glow plugs.

Gas burners - Studies have shown that $MoSi_2$ has significant resistance to oxygen-natural gas combustion at high temperatures. After an initial transient period, material stability is achieved through the formation of a stable Mo_5Si_3 layer. Stability occurs under both stoichiometric and fuel-rich combustion conditions. Prototype $MoSi_2$ gas burners have been fabricated by a plasma spray forming process.[45]

Molten metals lances - Some foundry operations require gases to be injected into molten metals. Microlaminate $MoSi_2$-Al_2O_3 composite tubes have been fabricated by plasma spray forming. These tubes have been tested as inert gas lances in molten aluminium alloys at 725°C and in molten copper at 1200°C showing good performances in both molten metals. The $MoSi_2$-Al_2O_3 composite tube is resistant to chemical attack by the molten copper due to the presence of the Al_2O_3 phase, while it exhibits thermal shock resistance and ductile failure due to plastic deformation of the $MoSi_2$ phase.

Glass processing - Recently, it has been shown that $MoSi_2$ is a material that is quite resistant to corrosion by molten glasse.[46] $MoSi_2$ shows excellent corrosion resistance below the glass line due to Mo_5Si_3 formation, and excellent oxidation resistance above the glass line due to SiO_2 formation. While corrosion rates of $MoSi_2$ are somewhat higher at the glass line than below the glass line, it has been reported that anodic protection of the $MoSi_2$ significantly lowers corrosion rates at the glass line. This corrosion resistance of $MoSi_2$ to molten glasses in combination with its elevated temperature mechanical properties has recently led to market a new $MoSi_2$ immersion tube for the injection of gases into molten glass.[4]

References

1 O. Hoenigsschmid, Monatsh. Chem., 28, (1997) 1017

2 Kanthal, Swed. Patent 155,836, (1953).

3 A. K. Vasudevan, J. J. Petrovic, Mat. Sci. Eng. A155, 1992) 1-17.

4 J. J. Petrovic, Ceram. Eng. & Sci. Proceedings, 18, (1997) 3-17

5 J. J. Petrovic and A. K. Vasudevan, Mat. Res. Soc. Symp. Proc., 322 (1994) 3-8.

6 J. J. Petrovic, MRS Bulletin, 8 (1993) 35-40

7 K. S. Kumar and C. T. Liu, "Ordered Intermetallic Alloys, Part II: Silicides, Trialuminides, and Others," JOM, (1993) 28-34.

8 E. A. Brandes and G. B. Brook, "Smithells Metals Reference Book", 7th Ed. (1992) 11-376.

9 W. J. Boettinger, J. H. Perepezko, and P. S. Frankwicz, Mater. Sci. and Eng. A155 (1992) 33-44.

10 P.T.B. Shaffer, Engineered Materials Handbook, Vol. 4, (1991) 804-811, edited by S.J. Schneider, Jr., published by ASM International.

11 M. Miyayama, K. Koumoto, and H. Yanagida, Engineered Materials Handbook, Vol. 4 (1991)748-757, edited by S.J. Schneider, Jr., published by ASM International.

12 Robert K. Wade, John J. Petrovic, J. Am. Ceram. Soc. 75 (1992) 1682–1684.

13 R. K. Wade and J. J. Petrovic, J. Am. Ceram. Soc. 75 (1992) 1682–1684.

14 R. K. Wade and J. J. Petrovic, J. Am. Ceram. Soc. 75 (1992) 3160-3162

15 S. M. L. Sastry, R. Suryanarayanan, and K. L. Jerina, Mater. Sci. Eng. A192/193 (1995)881-890.

16 R. Suryanarayanan, S. M. L. Sastry and K. L. Jerina, Mat. Res. Soc. Symp. Proc. 322 (1994) 191-196.

17 R. Suryanarayanan, S. M. L. Sastry, and K. L. Jerina, Acta Metall. Mater. 42 (1994) 3741-3750.

18 R. Suryanarayanan, S. M. L. Sastry, and K. L. Jerina, Acta Metall. Mater. 42 (1994) 3751-3755.

19 R. Suryanarayanan, S. M. L. Sastry and K. L. Jerina, Scripta Metall. Mater. 28 (1993) 797-802,.

20 R. Towari, H. Herman and S. Sampath, Mat. Sci. Eng. A155 (1992) 95-100.

21 R. G. Castro, R. W. Smith, A. D. Rollett and P. W. Stanek, Mat. Sci. Eng. A155 (1992)101-108.

22 A. Newman, T. Jewett, S. Sampath, C. Berndt, H. Herman, J. Mater. Res. 13 (1998) 2662.

23 S. Maloy, A. H. Heuer, J. J. Lewandowski and J. J. Petrovic, J. Am. Ceram. Soc. 74 (1991) 2704,.

24 T. C. Chou and T. G. Nieh, JOM (1993) 15-22.

25 T. C. Chou and T. G. Nieh, J. Mater. Res. 8 (1993) 214.

26 P. J. Meschter, Met. Trans. A23 (1992) 1763.

27 M.K. Meyer and M. Akinc, J. Am. Ceram. Soc. 79 (1996) 938-944

28 J. Schlichting, High Temp. High Press. 10, (1978) 241.

29 E. Fitzer and W. Remmele, Proc. 5th Int. Conf. On Composite Materials, ICCM-V, Ed. W. C. Harrigan, Jr. J. Strife and A. K. Dhingra, AIME, Warrendale, PA, (1985) 515.

30 F. D. Gac and J. J. Petrovic, J. Am. Ceram. Soc. 68 (1985) C200.

31 D. H. Carter, W. S. Gibbs, and J. J. Petrovic, Proc. 3rd Int. Symp. On Ceramic Materials and Components for Engines, American Ceramic Society, (1989) 977.

32 L. Xiao and R. Abbaschian, Mater. Sci. Eng., A155 (1992) 135-146.

33 D. E. Alman, K. G. Shaw, N. S. Stoloff and K. Rajan, Mater. Sci. Eng., A155, (1992) 85-94.

34 M. J. Maloney and R. J. Hecht, Mater. Sci. Eng., A155 (1992) 19-32.

35 D. H. Carter, W. S. Gibbes and J. J. Petrovic, Proc. 3rd Int. Symp. On Ceramic Materials and Components for Engines, American Ceramic Society, (1989) 977.

36 J. I. Lee, N. L. Hecht and T-I. Mah, J. Am. Ceram. Soc. 81 (1998) 421-424.

37 D. P. Butt, S. A. Maloy, H. H. Kung, D. A. Korzekwa, and J. J. Petrovic, J. Mater. Res. 11(1996) 1-9.

38 A. K. Bhattacharya and J. J. Petrovic, J. Am. Ceram. Soc. 74 (1994) 2700-2703.

39 J. J. Petrovic, M. I. Pena, I. E. Reimanis, M. S. Sandlin, S. D. Conzone, H. H. Kung and D. P. Butt, J. Am. Ceram. Soc. 80 (1997) 3070-3076.

40 J. J. Petrovic, M. I. Pena, and H. H. Kung, J. Am. Ceram. Soc. 80 (1997) 1111-1116.

41 K. Arata, N. Takeuchi, M. Yoshinaka, K. Hirota, and O. Yamaguchi, J. Am. Ceram. Soc. 80 (1997) 2168-70.

42 R. Gibala, A. K. Ghosh, D. C. Van Alken, D. J. Srolovitz, A. Basu, H. Chang, D. P. Mason, and W. Yang, Mater. Sci. Eng. A155 (1992) 147-158.

43 C. M. Huang, C. Y. Yuh, M. Farooque, D. Zhu, Y. Xu and W. M. Kriven, J. Am. Ceram. Soc. 80 (1997) 2837-2843.

44 L. O. Nordberg and T. Ekstrom, J. Am. Ceram. Soc. 78 (1995) 797-800.

45 R. G. Castro, J. R. Hellmann, A. E. Segall, and D. L. Shellman, Mat. Res. Soc. Symp. Proc. 322 (1994) 81-86.

46 S. K. Sundaram and R. F. Speyer, J. Am. Ceram. Soc. 79 (1996) 1851-1856.

CHAPTER 5

SiC - COMPOSITES PRODUCTIONS AND CHARACTERIZATION

5.1 MIXTURES COMPOSITION

In the present dissertation, SiC-based materials with $MoSi_2$ varying from 10 to 30 volume percent are produced and characterized.

The materials were produced starting from these commercial powders, whose morphology is reported in Fig. 5.1:

- **SiC** (Starck BF-12): β-SiC 97% and α-SiC 3%, specific surface area 11.6 m^2/g, ~1.65 wt% SiO_2 (estimated from the amount of oxygen);
- **$MoSi_2$** (Aldrich, Germany): <2 μm, mean particle size 1 μm, specific surface area 1.6 m^2/g, oxygen content 1 wt%;

As sintering aids were used the following powders, see Fig. 5.2:

- **Al_2O_3** (Baikalox, Grade CR30F): α 80%, γ 20%; 3 ppm Fe, 13 ppm Na, 16 ppm Si, 2 ppm Ca, 22 ppm K, (Mg, Ti, Cr, Mn, Ni, Cu, Zn)<1ppm each, d_{50}: 0.4 mm, specific surface area 26 m^2/g.
- **Y_2O_3** (Treibacher industries, AG): 99.999% Y_2O_3, 1 ppm Fe_2O_3, 6 ppm CaO, 1 ppm Na_2O, <20 ppm SiO_2, <20 ppm Al_2O_3, <2 ppm K_2O, specific surface area 2.43 m^2/g, particle size distribution 2-10 μm;
- **AlN** (HC- Starck, Grade C): 0.1% C, 2.0% O, 0.005% Fe; d_{50}: 0.8-1.8; specific surface area 4-8 m^2/g.

Fig. 5.1: SEM images showing the morphology of SiC and $MoSi_2$ powders utilized for the composites production.

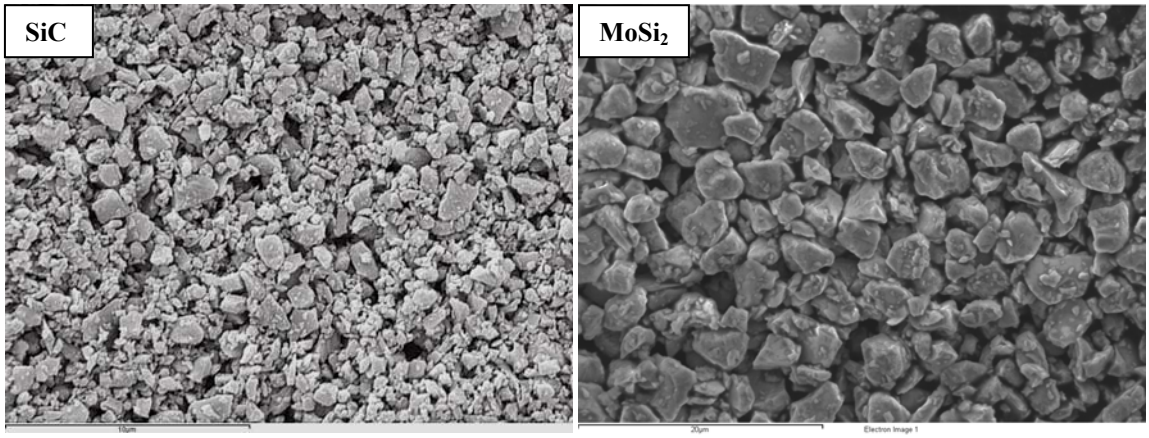

Fig. 5.2: SEM images showing the morphology of powders of the sintering additives utilized for the composites production.

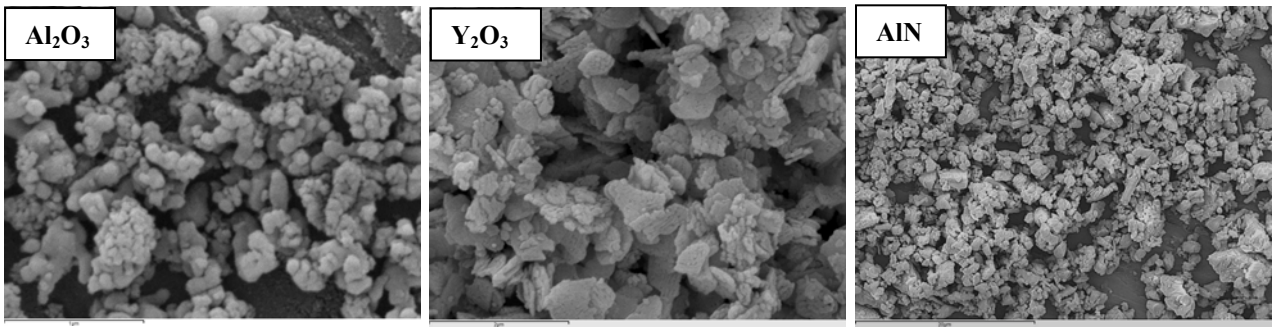

The aim of this work was to hot press silicon carbide with the only addition of molybdenum disilicide, as to obtain electroconductive materials. For this reason the first tests were conducted on the following powder mixture, but, as shown in Tab. 5.I, they retained low relative density.

- 90 SiC + 10 vol% $MoSi_2$ labeled as SM10
- SiC + 10 vol% $MoSi_2$ + 2wt% Y_2O_3 labeled as SYM10

Tab. 5.I: Hot pressing conditions and relative density of the preliminary tests on SiC-based materials.

Sample	HP conditions °C/min/MPa	Relative density %
SM10	1900/10/30	58
SYM10	1900/40/30	86

As a consequence, to ensure the achievement of the full density of the SiC matrix, Al_2O_3 and Y_2O_3 or Y_2O_3 and AlN were used in combination as sintering aids. The respective amount was chosen following the phase diagrams, shown in Fig. 5.3, in the right proportion to form eutectic temperatures.

The following compositions were prepared, when not expressed, the amount is reported in vol% (see Tab. 5.II):

- 90 [SiC + (6 wt% Al_2O_3 + 4 wt% Y_2O_3)] + 10 $MoSi_2$ labeled as SAYM10;
- 70 [SiC + (6 wt% Al_2O_3 + 4 wt% Y_2O_3)] + 30 $MoSi_2$ labeled as SAYM30;
- 70 [SiC+ (60 mol% Y_2O_3 + 40 mol% AlN)] + 30 $MoSi_2$ labeled as SYNM30.

Fig. 5.3: Phase diagram of the additive systems: a) Al_2O_3-Y_2O_3[1] and b) AlN-Y_2O_3.[2]

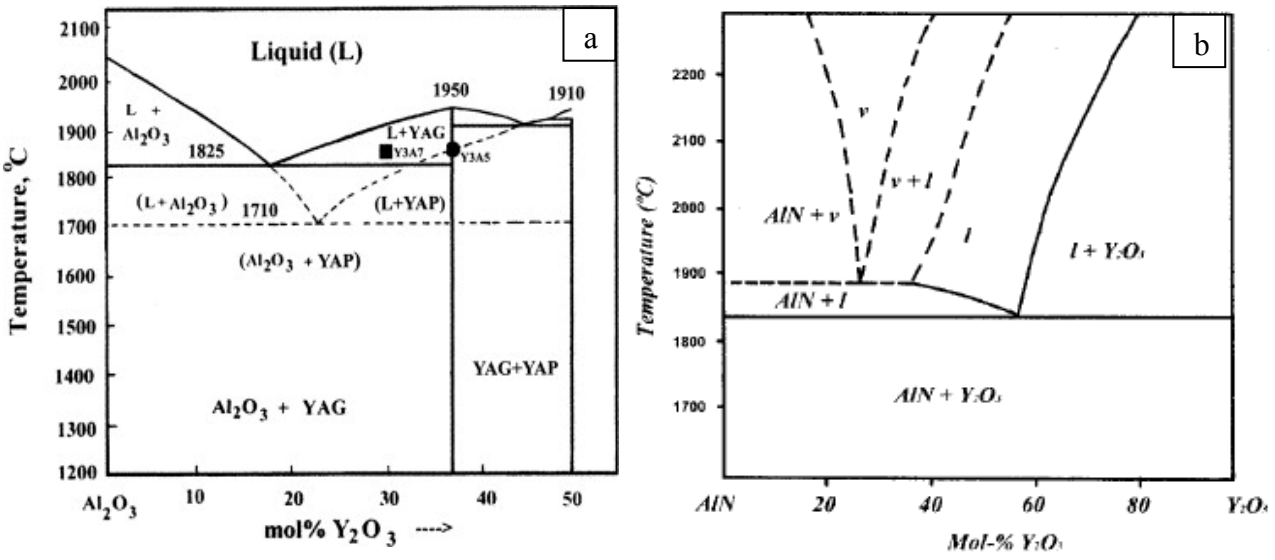

Tab. 5.II: Compositions and theoretical density of the analyzed samples.

Sample label	Composition (vol%)	Theoretical density (g/cm^3)
SAYM0	SiC + 2.6 Al_2O_3 + 5 Y_2O_3	3.296
SAYM10	90 (SAYM0) + 10 $MoSi_2$	3.598
SAYM30	70 (SAYM0) + 30 $MoSi_2$	4.203
SYNM30	70 (SiC + 84.3 Y_2O_3 + 15.7 AlN) + 30 $MoSi_2$	4.258
M	100 $MoSi_2$	6.301

The mechanical properties of these materials were compared to monolithic $MoSi_2$ and SiC matrix material, whose compositions are reported below:

- ❖ SiC+6 wt%Al_2O_3+4 wt%Y_2O_3 labeled as SAYM0;
- ❖ $MoSi_2$ labeled as M.

5.2 POWDER PROCESSING

The right amount of powder of silicon carbide and additives were weighted to obtain one billet for each composition of diameter 4 cm and height 1.2 cm.
The powder mixtures were ball milled for 24 h in absolute ethanol using SiC milling media; the powders were subsequently dried in a rotary evaporator and in a oven at 70°C for 24 hours and finally sieved through a 250 μm screen size.
Once obtained the mixtures, these were directly placed in the hot pressing crucible.

5.3 SINTERING

For hot pressing sintering, powders were placed in a graphite crucible (inner diameter 45 mm, outer diameter 120 mm) and undergone to a definite thermal cycle after a pre-compacting with a 30 MPa load. When the temperature reached 900°C the load was applied. The hot pressing was carried out at 1550-1900°C, 30 MPa and dwelling time of 30-55. Details on the sintering cycle of each sample are reported in the next chapter.

5.4 CHARACTERIZATION

The final density was measured by Archimedes' method on an hydrostatic balance. The theoretical densities are calculate by the rule of mixtures following the equation (1):

$$\rho_{th} = (\Sigma_i \rho_i V_i)/V_{tot} \quad (1)$$

where ρ_i and V_i are density and volumetric fraction of the i-component of the starting powders, respectively.

Crystalline phases were identified by X-ray diffraction (Siemens D500, Germany) using the CuK_α radiation, with 0.04 2θ-step size and 1 second scan step time.

The microstructures were analyzed using scanning electron microscopy (SEM, Cambridge S360) and energy dispersive spectroscopy (EDS, INCA Energy 300, Oxford Instruments, UK). For this purpose, the specimens were polished with diamond paste down to 0.25 μm.

Vickers microhardness (HV1.0) was measured with a load of 9.81 N, using a Zwick 3212 tester shown in Fig. 5.4.

Fig. 5.4: Zwick 3212 tester utilized for microhardness measurements.

Young's modulus (E) was measured by the resonance frequency method on 28 × 8 × 0.8 mm specimens using a Hewlett Packard gain-phase analyzer shown in Fig. 5.5.

Fig. 5.5: Hewlett Packard gain-phase analyzer utilized for Young's modulus measurements.

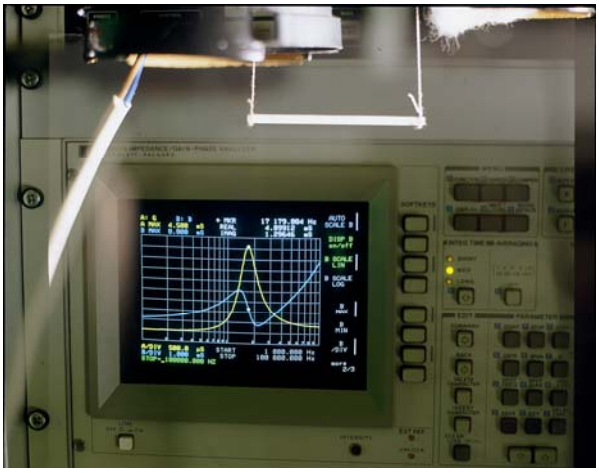

Fracture toughness (K_{Ic}) was evaluated using the chevron-notched beam (CNB) in flexure. The test bars, 25 x 2 x 2.5 mm (length x width x thickness, respectively), were notched with a 0.08 mm diamond saw; the chevron-notch tip depth and average side length were about 0.12 and 0.80 of the bar thickness, respectively. The flexural tests were performed on a semi-articulated silicon carbide four-point jig with a lower span of 20 mm and an upper span of 10 mm on a universal screw-type testing machine (Instron mod. 6025), shown in Fig. 5.6. The specimens were deformed with a crosshead speed of 0.05 mm/min. The "slice model" equation of Munz et al.[3] was used to calculate K_{Ic}.

Fig. 5.6: Instron mod. 6025.

On the same machine and with the same flexural jig, the flexural strength (σ), up to 1300°C in air, was measured on chamfered bars 25 × 2.5 × 2 mm (length × width × thickness, respectively), using a crosshead speed of 0.5 mm/min. For the high-temperature tests, a soaking time of 18 min was set to reach thermal equilibrium. Five specimens were used for each temperature point.

Concerning wear, experimental tests were performed in two different configurations: disc-on-pin (DOP), at Istec-CNR of Faenza, and slider on cylinder (SOC), at the Department of Metals Science, Electrochemist and Chemical Techniques of the University of Bologna.

For the configuration disc-on-pin, unlubricated sliding wear tests were performed on a tribometer Wazau (Berlin, Germany) reported in Fig. 5.7. with the

schematic of the relative sliding. Hemispherical tipped pins were cut and machined with diamond tools from the SiC and the SiC-$MoSi_2$ samples.

The height, diameter and tip radius of the pins were 16 mm, 5 and 2.5 mm, respectively. As mating discs, commercial Al_2O_3 was used. The diameter and the thickness of the discs were 40 and 10 mm, respectively. The discs and pins were tested in as-machined state with a mean surface roughness, R_a, of about 0.13 μm. The following conditions were applied for the wear tests: sliding speed 0.5m/s, applied force 15 N, total sliding distance 10 Km, radius of revolution 16 mm. The torque and the applied load were continuously recorded during the tests by a computer data acquisition program. Ambient temperature and humidity were kept in the range of 22±1 °C and 70±10%, respectively. Before and after each tests, the specimens were ultrasonically cleaned in an acetone bath for 15 min, then dried in an oven at 90°C for 30 min, allowed to cool down at room temperature for 60 min. The same procedure was followed after the test before the mass loss measures.

Fig. 5.7: The Wazau tribometer and the scketch of the relative sliding in the inset.

The disc and pin specific wear were evaluated by dividing the difference in weight before and after the test on the applied load and the sliding distance. For each coupling , three tests were carried out. In order to identify the wear mechanisms, the worn surfaces were analyzed by scanning electron microscopy (SEM, Cambridge S360, Oxford Instruments, UK) and energy dispersive spectroscopy (EDS, INCA energy 300, Oxford instruments, UK).

For the other configuration, the wear tests were performed using a home-made slider-on-cylinder tribometer schematized in Figure 5.8.

Prismatic sliders 5x5x35 mm in size were machined from the ceramic composites, while a cylinder 42 mm in diameter was prepared using massive alumina. The surface finishing grade of the sliding materials was evaluated by means of a stylus profilometer (tip radius 5 μm). The tests were carried out in air, at temperatures of 20-25°C and relative humidity of 35-55%, under different conditions of applied normal load (15, 30 and 50 N) and sliding speed (0.5, 1.0 and 2.0 m/s), for a constant sliding distance of 10 km. Friction resistance and system wear (i.e. cumulative wear undergone by stationary composite and counterfacing rotating alumina) were measured by means of a bending load cell and a displacement transducer, respectively.

Fig. 5.8: Schematic picture of the slider-on-cylinder tribometer. A worn specimen with the entry and exit sides of the sliding contact is shown in the inset.

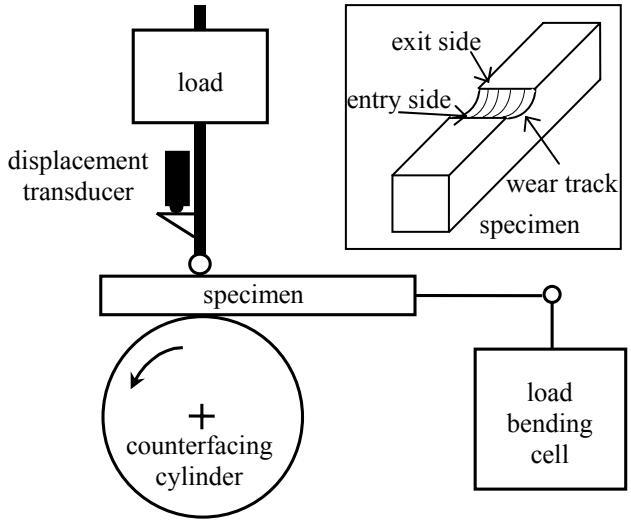

The bulk temperature attained by the slider was measured by a thermocouple joint placed at a distance of about 3 mm from the sliding surfaces. The experiments under most severe testing conditions (50 N at 1 m/s and especially at 2 m/s) usually stopped before the scheduled distance of 10 km was attained, due to excessive friction. The results of these experiments have been taken into consideration only when a sliding distance over 5 km was attained before the safety stop. Normal load, friction resistance, system wear and composite temperature were continuously recorded during the tests as a function of the sliding distance. The composite sliders were carefully cleaned by ultrasounds in acetone before and after each test. The wear rate of the composite was determined by measuring the weight loss that each slider underwent as

a consequence of sliding in contact with alumina. The variations were evaluated using an analytical balance (0.1 mg sensibility). The wear rate of alumina, in turn, was determined by measuring the depth of wear tracks by stylus profilometry. Moreover, wear debris were collected and analyzed by means of XRD and SEM in order to obtain information on the wear mechanisms. XRD was performed using a computer-controlled diffractometer (Philips PW 1720) and CuK_α radiation, with 0.04 2θ step size and 1 second scan step time. Both log(speed) vs. log(load) and adimensional wear maps were drawn interpolating the experimental values of wear rate by means of the Kriging algorithm and Surfer 8.0 software (Golden Software, Inc. 2002). A weighted surface interpolation was carried out as a function of the distance between the experimental points.

For comparison, selected friction and wear tests were carried out also on sintered samples of silicon carbide.

The electrical resistivity measurements were carried out by a four-probe DC method at room temperature, inducing a current in bar specimens of 2 x 2.5 x 25 mm. The current and the voltage were measured at the same time in two different digital high-resolution multimeters. The resistivity values were determined from the electrical resistance measurement, taking into account the distance between the test leads and the cross-sectional area of the samples.

All the measure are carried out in continuous current (DC) at room temperature with the following instrumentation:

- Dual stabilized feeder DC 2x 0-30V, 0-3 A Digimaster mod PS3003DB,
- High resolution digital multimeter Hewlett Packard mod. 3458A (to read the current),
- Digital multimeter Keithley mod. 195 (to read the voltage).

References

1 C.Ullal, Acta Mater. 49 (2001) 2691-2699.

2 A. Jeutter,"Untersichung der Phasenbeziung im System Aluminiumnitrid-Yttriumoxide", Diplomarbeit an Universitat Stuttgart (1993).

3 D.G. Munz, J. L. Shannon Jr., R.T. Bubsey, Int. J. Fracture, 1980,16, R137.

CHAPTER 6

MICROSTRUCTURE AND PROPERTIES

The possibility to obtain complex shapes at low machining costs is of paramount importance at industrial level. Hence, this chapter is devoted to the production and characterization of SiC-based ceramics with the addition of an electroconductive phase, $MoSi_2$, which allows the use of electro-discharge-machining (EDM) when added in a proper amount.

6.1 INTRODUCTION

Silicon-carbide-based ceramics are promising materials for applications in gas turbine components, heat exchangers, and wear-resistant components. Most of these applications require good strength and toughness, high thermal conductivity and good environmental stability at high temperature. Although silicon carbide can fulfil all these requirements, one major problem is that SiC hardly densifies without additives, because of the covalent nature of Si-C bonding and the low self-diffusion coefficient. In the last decade, liquid-phase sintering has been widely studied as a viable process for obtaining dense and fine materials without excessively high temperatures and pressures.[1-6]

Materials with improved sinterability and room-temperature strength (~700 MPa) were obtained by careful optimization of the processing, sintering additives and sintering cycles.[3,7] However, the major problems encountered with this class of liquid-phase sintered materials are the low fracture toughness and the degradation of strength at high temperature. The relatively low toughness (~3 $MPa \cdot m^{1/2}$)[4] is caused by a fine equiaxed microstructure, which does not provide any crack deflection or crack bridging phenomena. On the other hand, the high-temperature strength is degraded by the softening of residual secondary phases deriving from the sintering aids.

Furthermore, SiC-based components must be diamond-machined, due to their low electrical conductivity. Diamond machining is a costly process, which also implies limitations on the complexity of the final component geometry. The addition of electroconductive phases to insulating ceramics in suitable amounts is a straightforward strategy to overcome this problem, since it allows components to be shaped by electro-discharge machining.

All these considerations have led to the attempt to fabricate electroconductive SiC-based materials without a negative effect on its mechanical properties. $MoSi_2$ was selected as the secondary electroconductive phase for a silicon carbide matrix, as $MoSi_2$ has a low electrical resistivity as well as a series of interesting properties, such as the high melting point, high thermal conductivity and excellent oxidation resistance.[8] $MoSi_2$ has been coupled to several ceramic matrixes, such as Si_3N_4, SiC, SiAlON, AlN and it has been found that its addition also causes a significant improvement in the mechanical properties [9-14] and oxidation resistance.[15-16] In this chapter, the microstructure and properties of SiC-based composites containing 10 and 30 vol% of $MoSi_2$ and different sintering aids are presented and compared to those of the reference SiC and $MoSi_2$ monolithic materials.

6.2 SINTERING BEHAVIOUR

As preliminary tests, a mixture of SiC+10 vol% $MoSi_2$ was hot pressed at 1900°C, without any of sintering additive. However, the final relative density was lower than 60%. An improvement of the final relative density, from 60 to 86%, was obtained with the addition of 2 wt% of Y_2O_3. Actually, only the simultaneous addition of alumina and yttria, or aluminum nitride and yttria, allowed to achieve nearly fully dense composites (Tab. 6.I).

Alumina and yttria are the most common sintering additives used for the densification of silicon carbide.[1-7] The Al_2O_3/Y_2O_3 weight ratio (3/2) was the same of the SiC reference material (SAYM0).[4] The densification of these compositions occurred through liquid-phase sintering, owing to the liquid formed by reaction between the sintering aids and the SiO_2 present as oxidation product in the starting SiC and $MoSi_2$ powders. Al_2O_3, SiO_2 and Y_2O_3 have eutectic temperatures in the 1400-1800°C range,

depending on their relative amounts.[17] Analogously, Y_2O_3-AlN, in the molar ratio 6/4, form an eutectic point at around 1840°C.[18]

Tab. 6.I: Sintering conditions, experimental density and microstructural parameters of the hot pressed materials (see also Tab. 5.II).

Sample	Hot pressing (°C/min/MPa)	Exp. ρ (g/cm^3)	Final relative ρ (%)	Residual porosity (%)	SiC m.g.s. (μm)	$MoSi_2$ m.g.s. (μm)
SAYM0	1870/38/30	3.25	~100	<1	0.5	-
SAYM10	1900/55/30	3.51	98.5	1.5	0.7	0.7
SAYM30	1900/30/30	4.05	97.5	1.2	0.7	1.1
SYNM30	1900/22/30	4.11	96.5	<1	0.8	1.1
M	1550/6/30	5.93	~100	<1	/	2.5

Fig. 6.1: Densification curves for a) SAYM0, b) SAYM10, c) SAYM30, d) SYNM30 samples. Relative density is plotted as a function of temperature and dwell time.

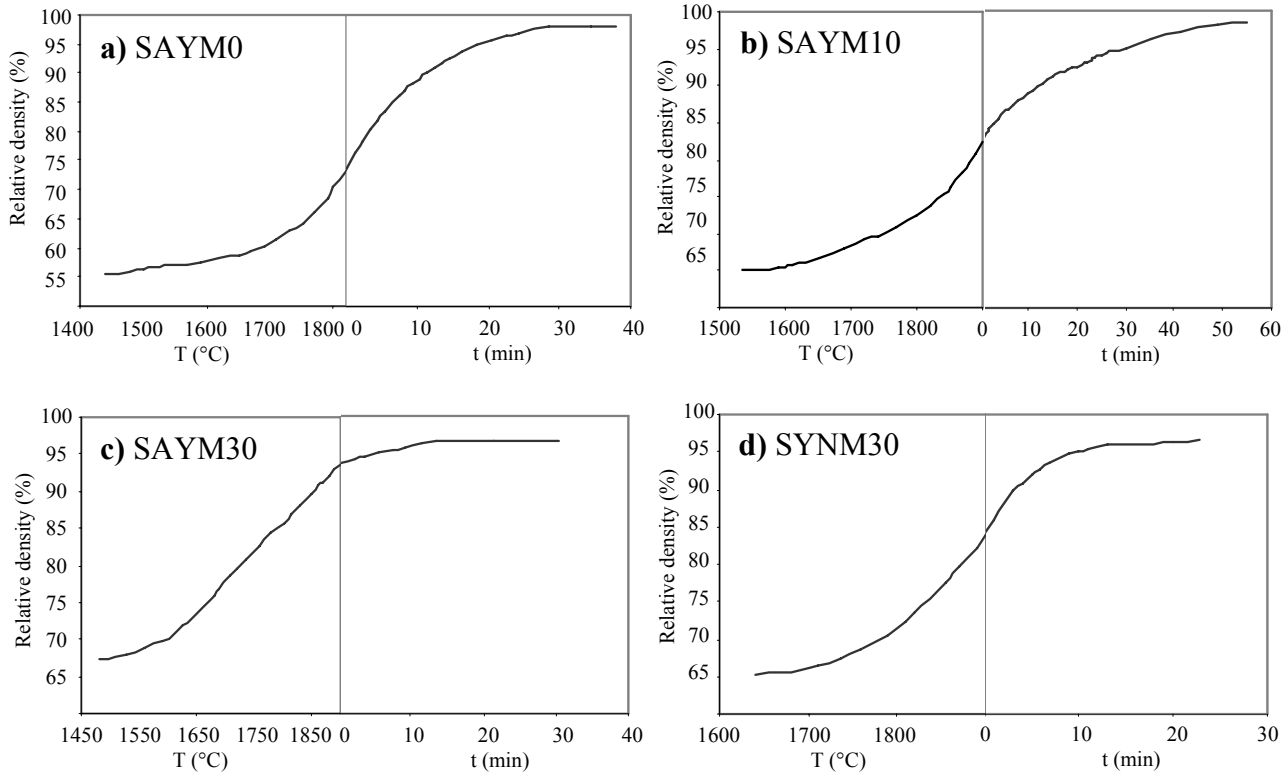

The shrinkage curves recorded during the hot pressing runs, and shown in Fig. 6.1, highlighted that the addition of $MoSi_2$ particles did not significantly alter the densification behavior of the SiC-based composites with respect to the reference SAYM0 material. The starting shrinkage temperatures of SAYM0, SAYM10, SAYM30 and SYNM30 ceramics (1490°C, 1530°C, 1480°C and 1690°C, respectively) were close and in agreement with the eutectic temperatures reported in

the literature.[17] The maximum sintering temperatures and the dwell times needed to obtain the full densification were very similar as well (Tab. 6.I).

Of the three $MoSi_2$-containing samples, the one that moves away from the standard behavior is, as expected, SYNM30, for which a delay in the starting densification temperature was recorded, due to a higher refractoriness of the liquid phase deriving from Y_2O_3-AlN. However, during the isothermal stage the densification was faster compared to the composites with Al_2O_3-Y_2O_3.

It has to be pointed out that the final relative density in Tab. 6.I was calculated on the basis of the starting composition and thus does not consider the eventual presence of SiO_2 coming from SiC and $MoSi_2$ powders or the formation of glassy phases. In other words, a higher final relative density does not always imply a more dense material. A more reliable indication of the residual porosity can be disclosed by image analysis (see Section below).

6.3 MICROSTRUCTURE

A comparison among the XRD patterns of the materials containing Al_2O_3-Y_2O_3 as sintering additives is reported in Fig. 6.2.

The crystalline phases detected by X-ray diffraction in the $MoSi_2$-containing materials, with Al_2O_3-Y_2O_3 as sintering additives, were mainly β-SiC, $MoSi_2$ and traces of crystalline YAG ($3Y_2O_3{\cdot}5Al_2O_3$). Additional peaks with very low intensity were attributed to the Mo_5Si_3 and $Mo_{4.6}Si_3C_{0.6}$ phases, which are commonly formed in SiC-$MoSi_2$ or C-$MoSi_2$ compositions.[11, 19]

The X-ray diffraction pattern of the material containing Y_2O_3-AlN as sintering additives shows the presence of β-SiC, tetragonal $MoSi_2$ and traces of YAG, $Mo_{4.8}Si_3C_{0.6}$ and residual AlN, Fig. 6.3.

All the materials were nearly full dense after the hot pressing routes, (Tab. 6.I). An estimation of the residual porosity by image analysis indicated the SYNM30 composite as the most dense.

The development of microstructure during sintering involved partial solution of the original SiC grains, precipitation around undissolved nuclei and subsequent grain

growth. Compared to silicon nitride, SiC solubility in the melt is lower of about 10%. Intergranular crystalline phases, corresponding to YAG, were observed in amounts around 5 vol%. This value, semi-quantitatively evaluated from the peaks intensities in X-ray diffractograms, was in agreement with calculations based on the starting compositions. Beside these crystalline phases, an amount of amorphous phase was supposed to form in all materials owing to reaction of additives with the silica, despite no confirmation was found in the XRD patterns. By image analysis, the estimated amounts of amorphous Al-silicates is about 4%. Typical microstructural features of the reference hot pressed material are shown in Fig. 6.4.

Fig. 6.2: X-ray diffraction pattern for the SAYM0, SAYM10 AND SAYM30 samples.

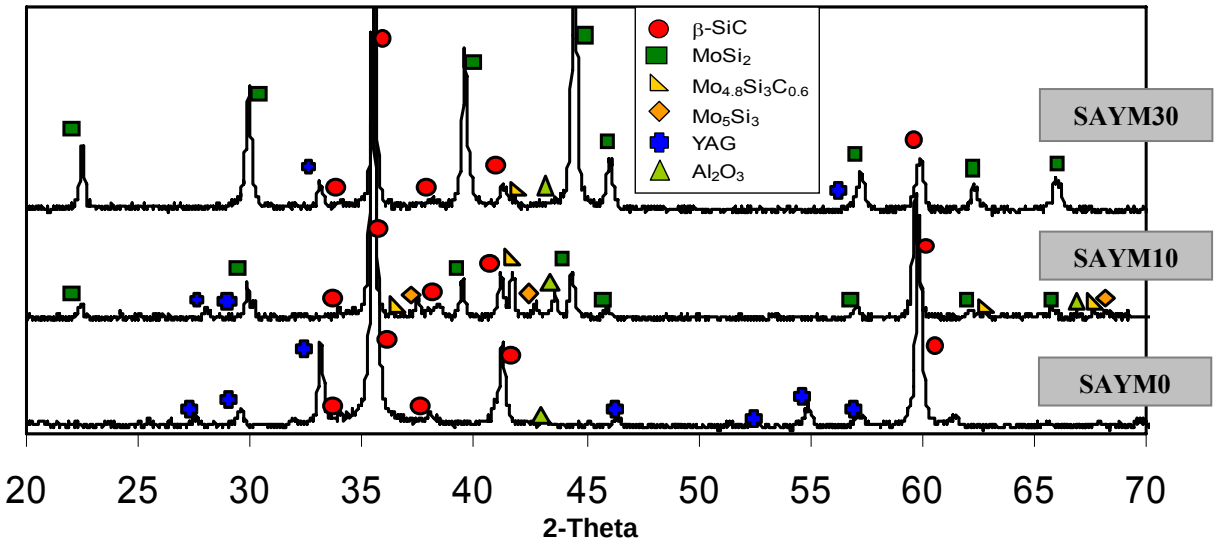

Fig. 6.3: X-ray diffraction pattern for the SYNM30 sample.

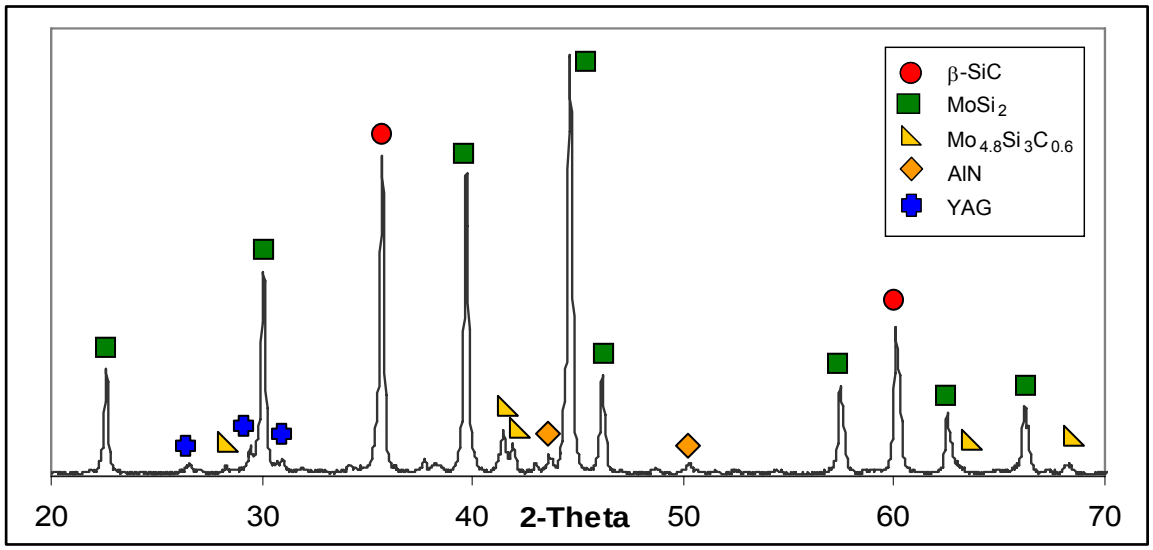

Fig. 6.4: Polished section of the silicon carbide reference material, SAYM0, after plasma etching. a) Lower magnification and b) higher magnification showing the core-rim structure and the grain boundaries phases.

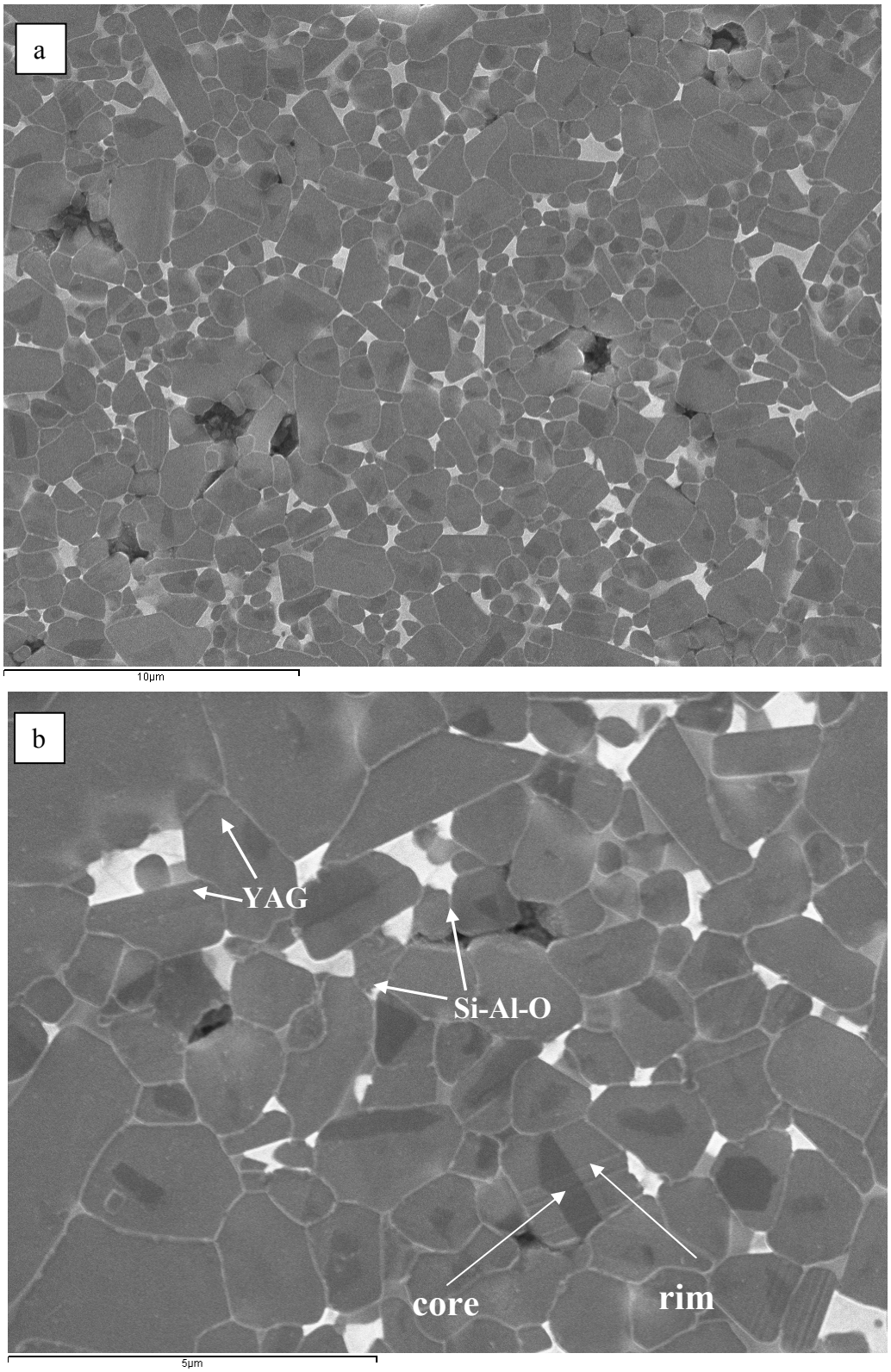

Silicon carbide grains were etched away by a CF_4 plasma, thus the microstructure was delineated by the grain boundary phases. Grain morphology was mainly equiaxed with grain size distribution ranging from 0.1 to 2 μm. Due to the presence of large particles in SiC powder, a small number of larger grains (up to 10 μm) with irregular shape was also observed. Adjacent SiC grains were mainly separated by a thin grain boundary film, which was the residue of liquid phase sintering medium. Intergranular phases appeared mainly at three- and four-grain pockets: these areas were supposed to be crystalline,[20] while the grain boundary phase between SiC grains was presumed to be amorphous.

The etched surfaces of the samples produced with the addition of Al_2O_3+Y_2O_3 revealed a core/rim structure in SiC grains. EDS analyses confirmed variations in the core and rim composition. In the core region, only Si and C could be detected. In the outer rim, traces of Al and O were also observed, in agreement with previous results which claimed the presence of Al, O and Y.[21] This provided evidence that liquid phase sintering of SiC proceeded via a classical solution-reprecipitation mechanism. As the sintering process started, small SiC grains dissolved into the oxide melts until the solubility limit was reached. Then, SiC reprecipitated on favourably oriented facets of large undissolved SiC grains, which acted as nucleation sites. Undissolved grains constituted the core and the precipitating liquid formed the rim. The difference in chemical composition between core and rim suggested that SiC with small amounts of Al and O in solid solution was more stable in contact with a Al-Y-O-Si liquid than pure SiC. Smaller SiC grains with rounded shapes were observed in larger pockets of grain boundary phase, while most of the SiC grains developed a faceted interface with the grain boundary phase. This confirmed that, during densification and grain growth, a reactive Al-Y-O rich liquid phase was present and that surface silica on the starting SiC particles participated in this reaction, as previously observed.[21]

The microstructure of the $MoSi_2$-containing composites is shown in the fracture and polished surfaces of Fig. 6.5. The bright contrast inclusions are $MoSi_2$ particles dispersed in the dark contrasting SiC matrix. The fracture mode (Fig. 6.5a,c,e) was mainly intergranular in the SiC matrix. On the other hand, for $MoSi_2$ particles, the fracture was both intergranular and transgranular. Despite the differences in thermal

expansion coefficient between the two phases, no microcracks were observed at the boundaries between the inclusions and the matrix.

Fig. 6.5: BSE images of fractured and polished surfaces for a) and b) SAYM10, c) and d) SAYM30, e) and f) SYNM30.

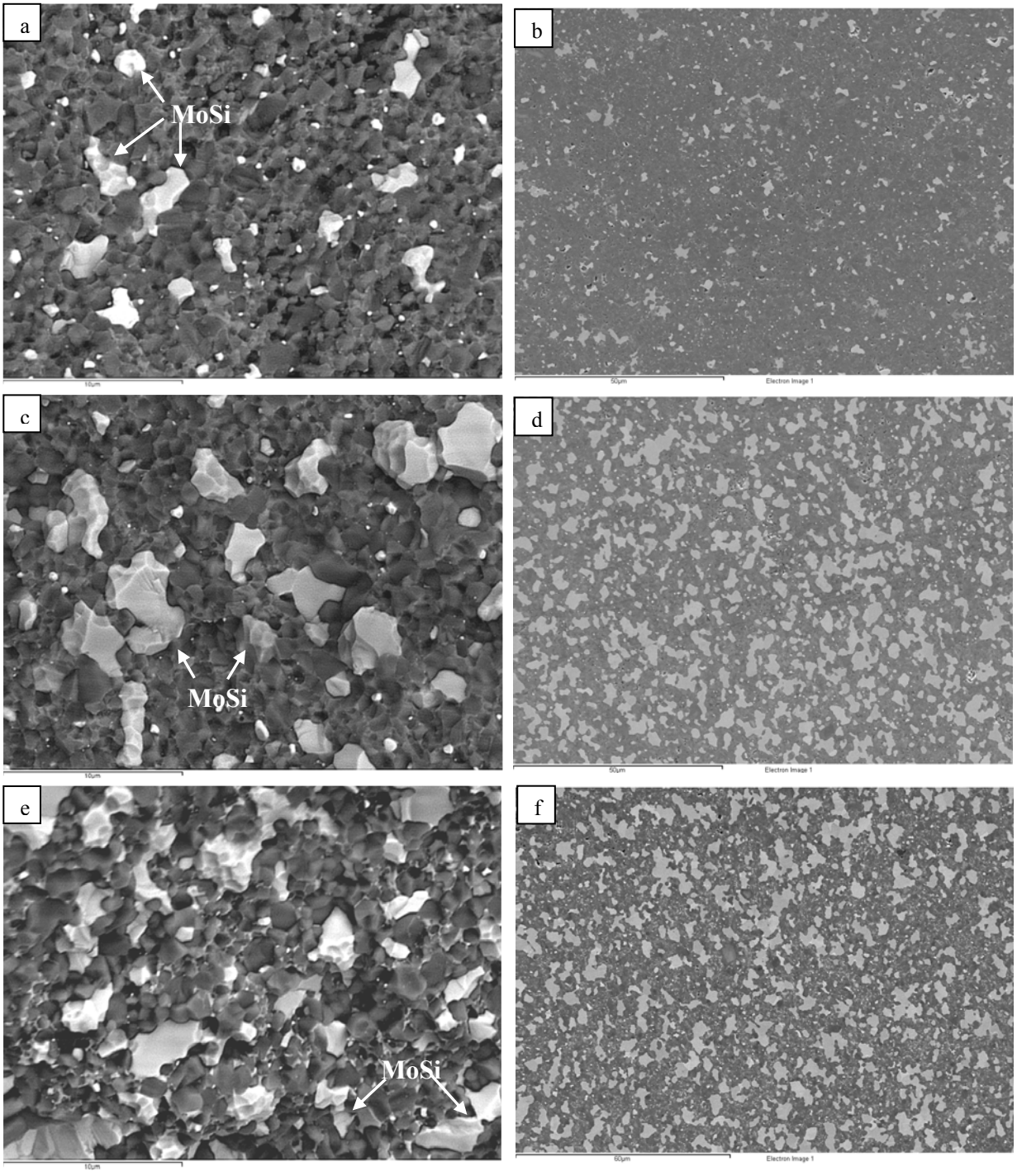

Fig. 6.6: Polished surface for a) SAYM10 and b) SAYM30. In the insets the EDS spectra of the secondary phases: YAG, brighter, and Si-Al-O, darker.

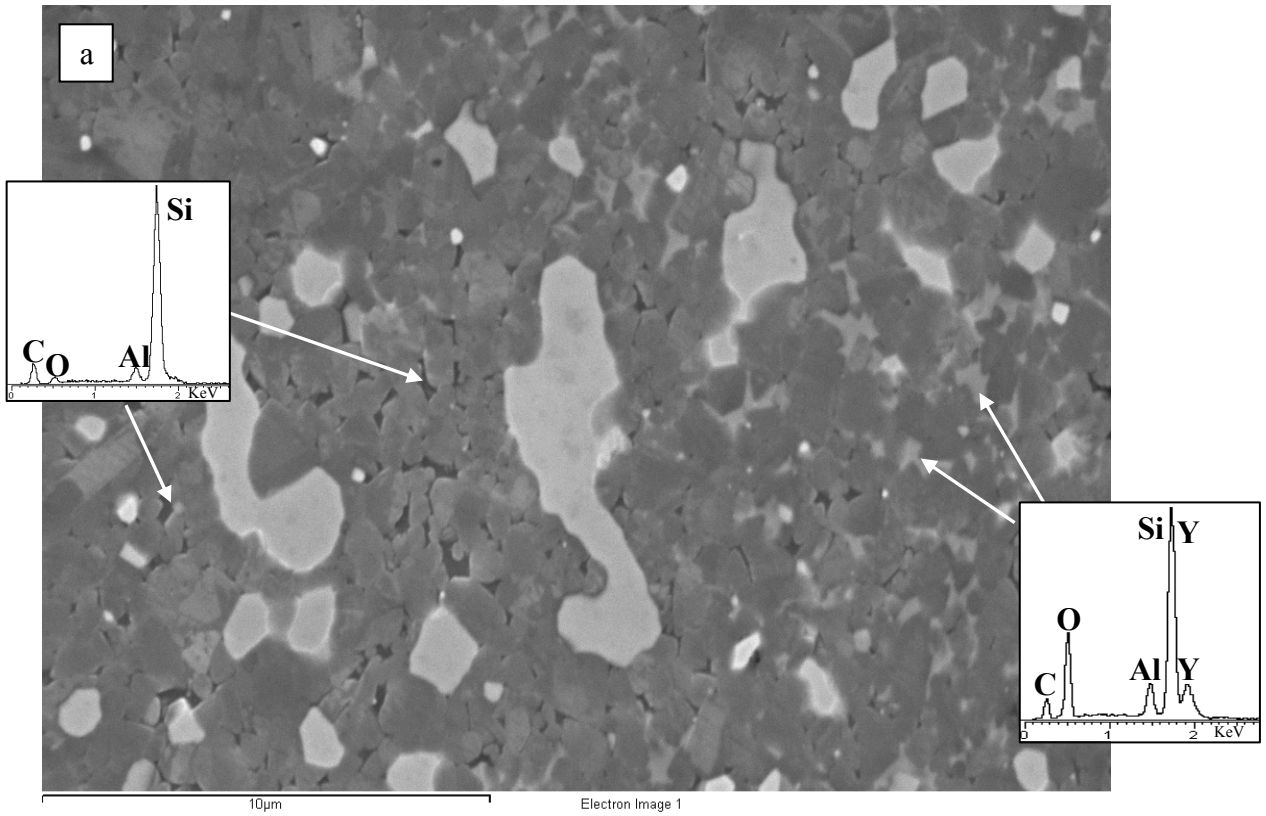

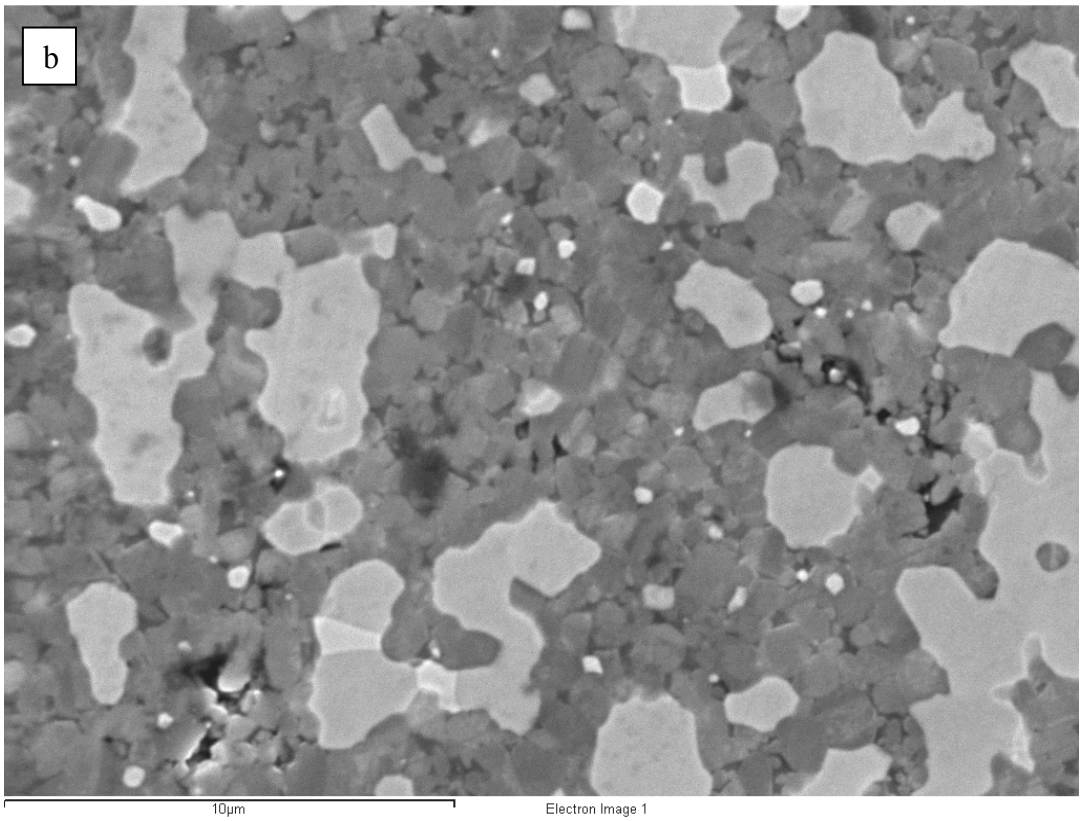

The microstructural features of the SiC matrix, for SAYM10 and SAYM30 samples, resembled those of typical liquid-phase sintered SiC, such as SAYM0, and consisted of preferentially rounded SiC grains separated by intergranular silicate films and of a secondary phase at triple junctions (see Figs. 6.6). The intergranular phase among adjacent SiC grains was based on Si-Al-O or Y-Al-O elements (Fig. 6.6), likewise the baseline SAYM0 material.[4] The SiC mean grain size was in the range of 0.5-1.0 μm.

All the materials containing $MoSi_2$ showed the presence of Mo_5Si_3 which appeared ad brighter phase, Fig. 6.7.

Fig. 6.7: SEM micrograph of SAYM30 sample showing the two Mo-Si-based phases and the corresponding EDS spectra.

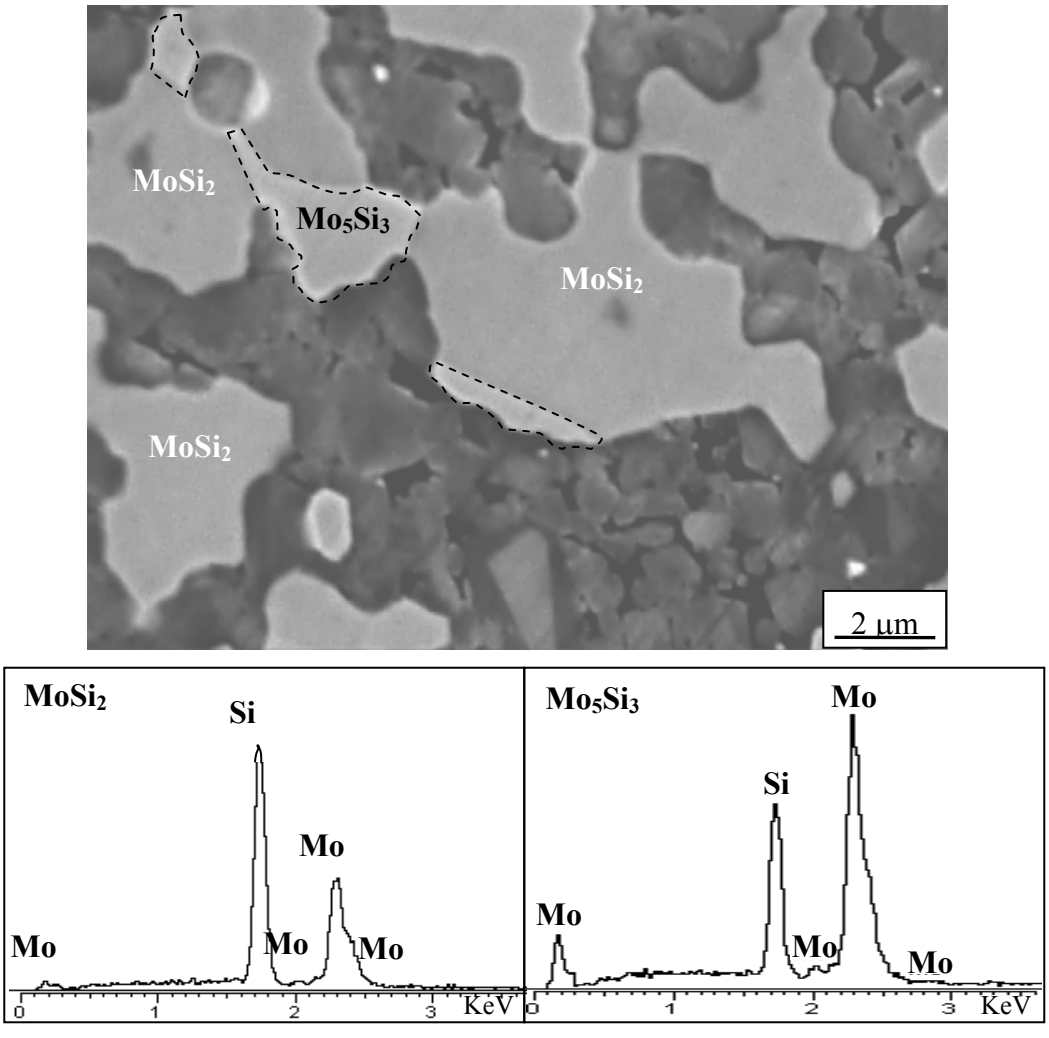

In the SYNM30 sample, some abnormal grain growth occurred, probably due to the presence of nitrogen in the sintering additives which formed a more viscous liquid phase, favouring an inhomogeneous grain growth.[22] In the grain boundary phase, the nitrogen peak was not detected by EDS analysis. In pressureless sintering, the mechanism of volatilization of gaseous species is well known,[22] whilst in pressure-assisted sintering this phenomenon was not noticed yet.

The $MoSi_2$ monolithic material, shown in Fig 6.8, was fully dense, with mean grain size of about 2-3 μm. Pockets of silica, about 5 vol%, were found at the triple grain junctions and derived from silica contamination in the starting powder, as reported by several authors.[8,19] Besides the silica phase, a white phase was detected and assessed to be Mo_5Si_3 by EDS analysis.

Fig. 6.8: Fracture surface of the monolithic $MoSi_2$ sample.

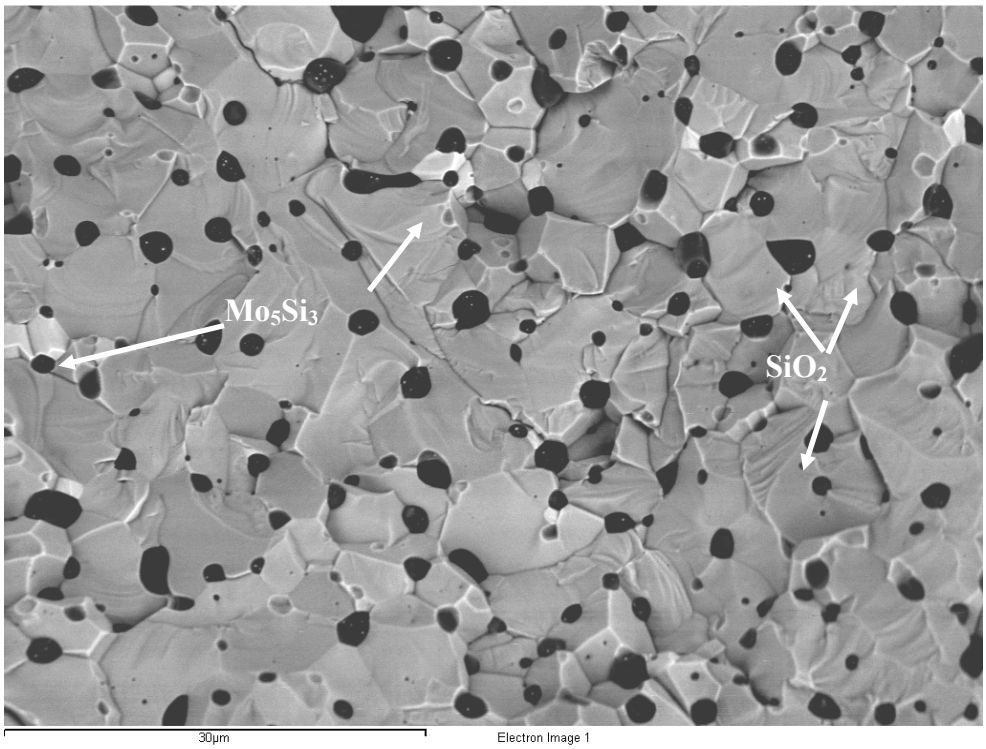

6.4 MECHANICAL PROPERTIES

The measured values of mechanical properties of the composites were compared to those of the reference monolithic SiC (SAYM0) and $MoSi_2$ materials.

The effect of $MoSi_2$ content on the Vickers hardness is presented in Fig. 6.9. The hardness decreased with the increase of the $MoSi_2$ content, as molybdenum disilicide is a relatively softer phase compared to silicon carbide. Starting from the baseline materials, SAYM0 and monolithic $MoSi_2$, the experimental values of SAYM10 and SAYM30 can be compared with the expected bounds,[23] which are presented as dotted lines in the plot of Fig. 6.9. The experimental values found for SAYM10 and SAYM30 compositions can be considered in very good agreement with the theoretical expectations.

Considering the materials with 30 vol% of $MoSi_2$, in SYNM30 composite the hardness was 15% higher than SAYM30 samples thanks to less residual porosity and grains dimensions slightly smaller than SAYM30 (compare Fig. 6.5d,f)

Fig. 6.9: Vickers Hardness as a function of $MoSi_2$ content. Mean values ± standard deviation. Theoretical bounds are represented as dashed lines.

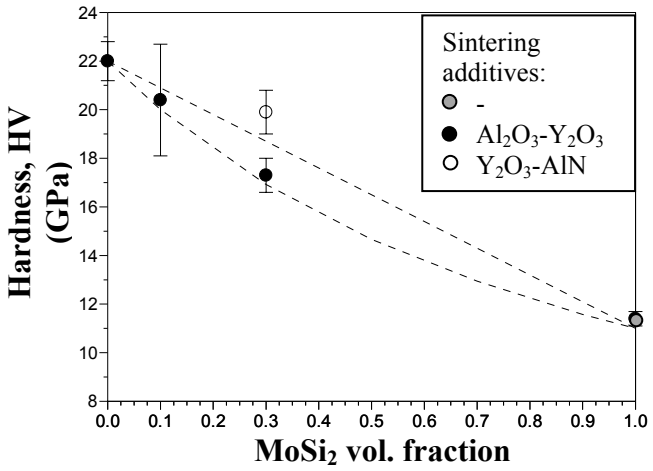

In comparison with the baseline materials (SAYM0 and monolithic $MoSi_2$), there were no significant variations of the Young's modulus in the SAYM10 and SAYM30 composites, see Fig. 6.10. The theoretical bounds for the Young's modulus of SAYM10 and SAYM30 composites can be calculated by means of the relationships proposed by Hashin and Shtrikman.[24] Taking 386 GPa,[4] 355 GPa,[25] 0.19[26] and 0.15[25] as Young's modulus and Poisson coefficient for the SAYM0 and $MoSi_2$, respectively, the lower and upper bounds were found to be nearly coincident (see the broken line in the plot of Fig. 6.10).

Fig. 6.10: Young's modulus as a function of $MoSi_2$ volumetric fraction. Theoretical bounds are represented as broken lines.

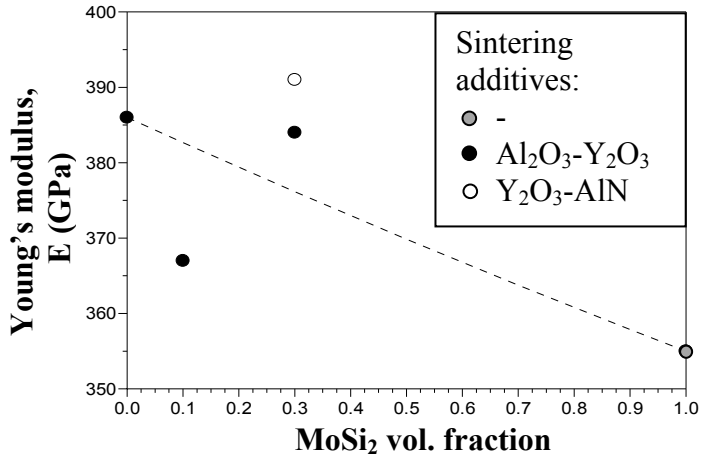

The Young's modulus of SAYM10 was slightly lower than the theoretical bounds, due to the presence of a residual amount of porosity (see Tab. 6.I). For all the materials, the Young's modulus was definitely affected by the presence of amorphous secondary phases deriving from oxygen contamination of the starting $MoSi_2$ powder or deriving from the addition of sintering aids in the case of the SAYM0, SAYM10 and SAYM30 compositions. Higher values of Young's modulus are in fact reported in the literature for SiC and $MoSi_2$ pure phases, about 440 GPa for both of them.[25]

The SYNM30 composite achieved the highest Young's modulus probably thanks to the almost absence of porosity and to a stiffer grain boundary phase.

The influence of $MoSi_2$ addition on the fracture toughness of the SiC-based materials is shown in the graph of Fig.6.11. In the reinforced composite containing 30 vol% of $MoSi_2$, the fracture toughness increased of about 27% in comparison with the reference SiC material. Similar to other $MoSi_2$-reinforced materials,[9-12] one of the toughening mechanisms which were likely to occur in these composites is the residual stresses mechanism,[27] due to the difference in thermal expansion coefficient (CTE) between the reinforcing particles ($9.1 \cdot 10^{-6}$/°C for $MoSi_2$)[25] and the SiC matrix ($5.1 \cdot 10^{-6}$/°C).[25] According to the theoretical model of Taya at al.,[27] when the CTE of the particles is higher than that of the matrix, as in the present case, average compressive stresses arise in the matrix, which cause a toughness enhancement with respect to the stress-free matrix. The toughness increase was also due to the crack deflection mechanism.[28]

Fig.6.11: Fracture toughness as a function of $MoSi_2$ content. Mean values±1 standard deviation.

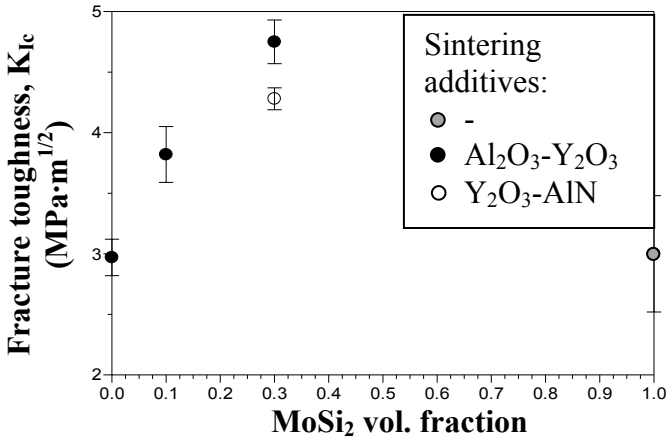

Actually, crack deflection was directly observed by introducing a 98.1 N Vickers indentations into the polished surface of the composite and examining the interaction of the crack front with the microstructure. An example of the crack path in the SAYM30 composition is shown in Fig. 6.12. Analysis of the crack profile evidenced that small $MoSi_2$ particles deflected the crack along the interface with the matrix, whilst the large particles or agglomerates were generally crossed by the crack and did not act as deflecting obstacles. Some intact ligaments formed by SiC grains behind the crack tip were occasionally noted. The presence of intact ligaments may be an indication of toughening mechanisms like crack bridging or crack pinning. However, due to their sporadic occurrence, they are not likely to give any significant contribution to toughening.

Fig. 6.12: Crack path generated by a 98 N Vickers indentation in SAYM30.

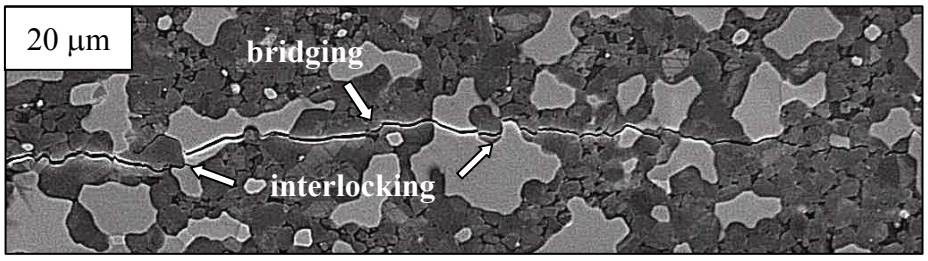

The room-temperature strength values of the SiC-based materials were all higher than 700 MPa. In the graph of Fig. 6.13 the strength is reported as a function of the $MoSi_2$ volumetric fraction for the composites containing Al_2O_3-Y_2O_3 as sintering additives. As in the case of the fracture toughness, an increase of the flexural strength occurred when the content of the secondary phase was 30 vol%. For this composition,

the addition of $MoSi_2$ allowed a simultaneous increase of strength and toughness, compared to the reference material. The flexural strength of the SAYM10 composition was found to be affected by a large dispersion around the mean value.

Fig. 6.13: Room temperature flexural strength as a function of $MoSi_2$ volume content. Mean values±1 standard deviation.

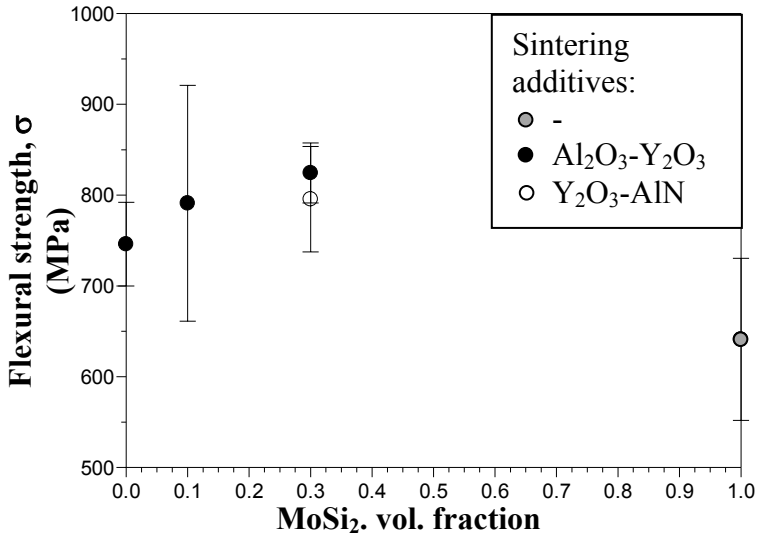

The fracture surfaces of the broken samples were analysed by SEM after strength tests in order to find out the fracture origins. In SAYM10, the largest critical flaws were found to be extended regions with localized porosity, in SAYM30 small agglomerates of Al and in SYNM30 several abnormal grains of the order of 20 μm, Fig. 6.14. $MoSi_2$ seems not to play a role in the formation of such defects thus indicating a good homogeneity in the dispersion of the secondary phase.

Fig. 6.14: Examples of critical flaws observed on the surface fracture of a) SAYM10, b) SAYM30, c) SYNM30 composites.

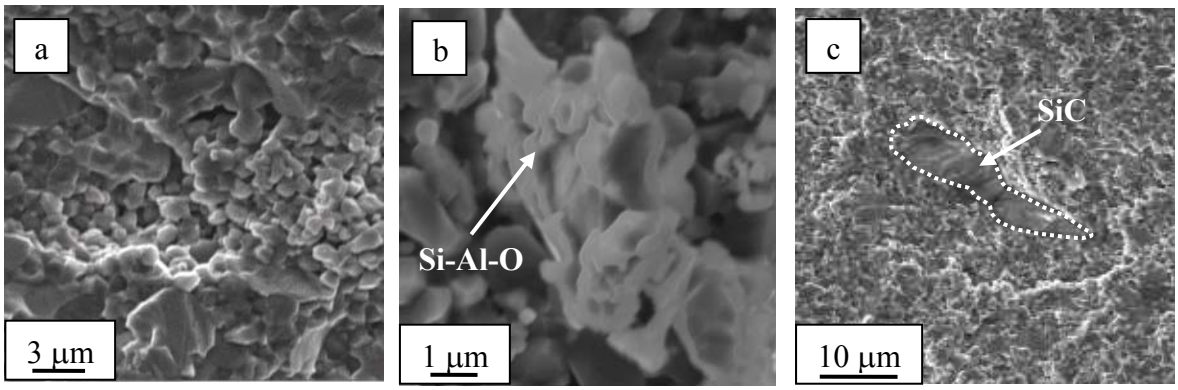

In the high temperature range, the behaviour of the different compositions tested was very similar. In the graph of Fig. 6.15, the flexural strength of SAYM0, SAYM10 and SAYM30 is plotted against the temperature. At 1000°C, a slight decrease was observed for all the compositions and the highest value was still found for SAYM30. At 1300°C the strength notably decreased to values lower than 250 MPa, with SAYM10 as the strongest material. The load-displacement curves of both composites were linear up to fracture at 1000°C, but at 1300°C they deviate from the linearity, as shown in Fig. 6.16. Similar to the SiC reference material, the sudden drop of these composites' strength at 1300°C was thus due to the softening of the amorphous silica-based intergranular phase.[4]

Fig. 6.15: Flexural strength of SAYM0, SAYM10, SAYM30 sample as a function of the temperature. Mean values±1 standard deviation.

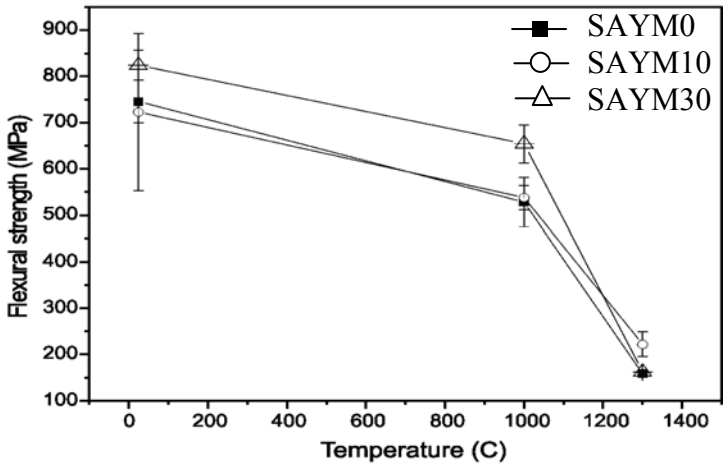

Fig. 6.16: Examples of load-displacement (d) curves for SAYM10 and SAYM30 samples.

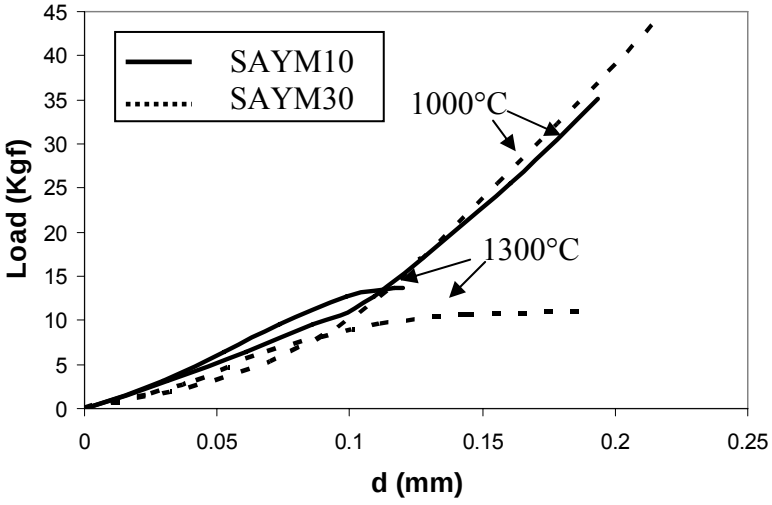

The surface of the bars after high temperature tests appears covered by an amorphous silica layer containing Al, Y and other impurities, Fig. 6.17. Similarly to the specimens tested at 1000°C, this scale was not continuous but localized only in some areas of the surface, next to the flaws, indicating that the viscosity of this layer was quite high.

Fig. 6.17: Fracture surface of a) SAYM10, b) SAYM30 and c) SYNM30 samples after flexural strength at 1300°C.

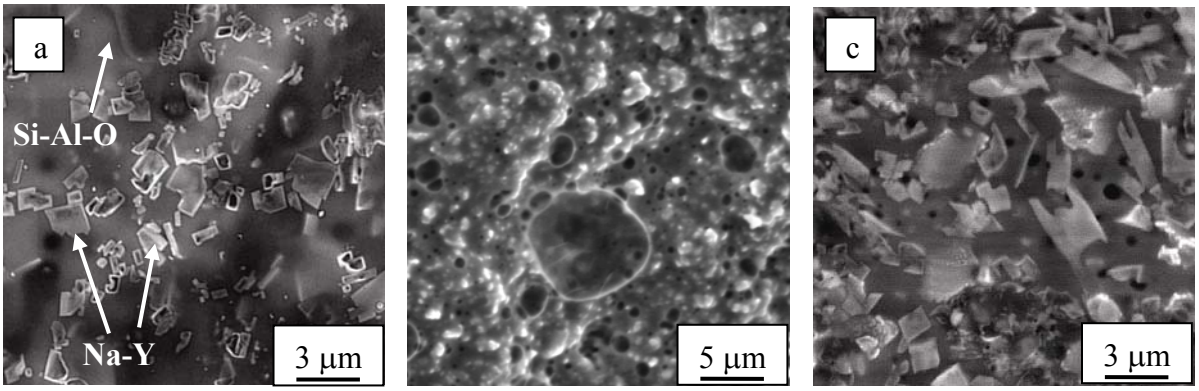

Comparing SAYM30 and SYNM30 (Fig. 6.18), it's evident that all the values were very similar, but at room temperature SAYM30 was stronger, maybe because in the SYNM30 composite an abnormal grain growth occurred (Fig. 6.14c) and these grains, of the order of 20-30 μm, could have acted as critical defects.

At 1000 and 1300°C the strength was higher for SYNM30 than for SAYM30, as the values diminished of 13 and 67% compared to 20 and 80%, respectively, from the room temperature values. This behaviour is due to the higher stiffness and refractoriness of AlN-containing grain boundary phase.

Fig. 6.18: Flexural strength values as a function of the temperature for SAYM30 and SYNM30. Mean values±1 standard deviation.

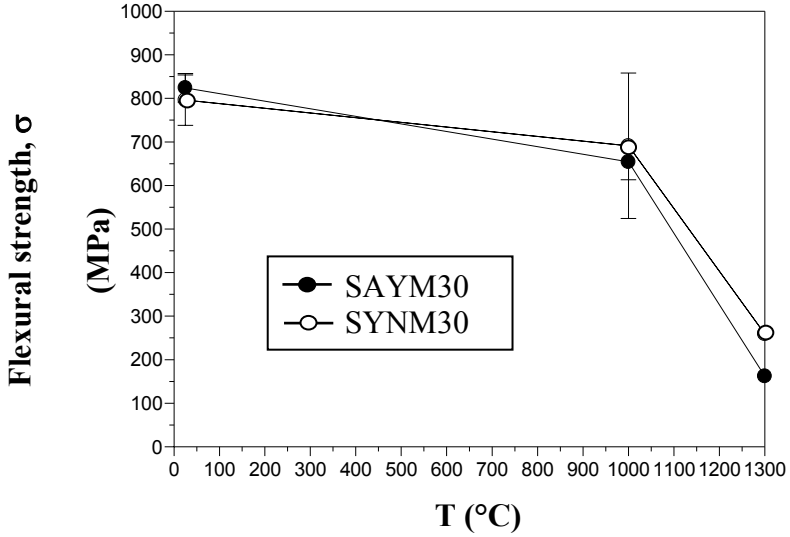

6.5 WEAR BEHAVIOUR

Advanced ceramics are often used as wear-resistant materials, mainly tanks to their hardness. The interesting mechanical properties exhibited by the above presented SiC-$MoSi_2$ composites, compared to the pure SiC matrix, induce to investigate also the wear behaviour.

An extensive tribological characterization was performed on the SiC reference matrix (SAYM0) and the composite containing 30 vol% $MoSi_2$ containing the same sintering additives (SAYM30) in order to:

1. compare the wear behaviour of the SiC matrix to the behaviour of a SiC-$MoSi_2$ composite (disk-on-pin test; Al_2O_3 disc);
2. study the wear behaviour of the SiC-$MoSi_2$ composite SAYM30 in different condition of run distance, speed and applied load (slider-on-cylinder tests; Al_2O_3 cylinder);
3. compare the wear behaviour in two different contact configurations.

6.5.1 Disc on pin tests

In Tab. 6.II the main tribological features of the coupling materials are reported.

In Fig. 6.19 two examples of the friction coefficient behaviour are reported for the two coupling: SAYM0-Al_2O_3 and SAYM30-Al_2O_3. The friction coefficient was calculated in the steady state, which follows the running in state, as the ratio of the shear force on the applied nominal load.

Tab. 6.II: Wear and friction parameters of the coupling SiC/Al_2O_3 e SiC + 30 vol% $MoSi_2$/Al_2O_3. The final data were calculated on 3 tests. Mean values±1 standard deviation.

Coupling (pin/disc)	Friction in steady state	Pin wear ($10^{11}s^2m^{-2}$)	Disc wear ($10^{11}s^2m^{-2}$)
SAYM0/Al_2O_3	0.61±0.06	0.57±0.10	0.19±0.08
SAYM30/Al_2O_3	0.78±0.10	1.10±0.22	0.25±0.13

As can be observed in Tab. 6.II, the SAYM0/Al_2O_3 coupling resulted in a lower friction coefficient than the coupling SAY30M/Al_2O_3. Also the wear rate of the composite was higher, almost doubled, compared to the matrix (see pin wear in Tab.

6.II). Moreover, the same counter facing body, Al_2O_3 disc, resulted in a higher wear when in contact with SAYM30.

Fig.6.19: Friction coefficient trend as a function of time of the two couplings.

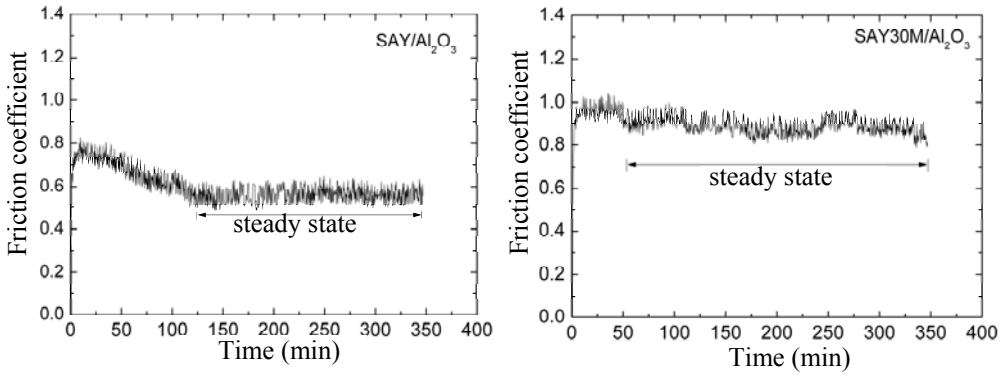

The wear track of SAYM0 pin is shown in Fig. 6.20 and the absence of debris is evident. Light wear was identified as main wear mechanism, as the surface appeared just polished showing microstructural details.

The coupled Al_2O_3 disc is shown in Fig. 6.21. As it can be noticed, the groves due to grinding are still visible, indicating a very low wear. Polished Al_2O_3 grain can be observed, as well as small debris, whose spectra reveals the presence of SiC coming from the pin.

Fig. 6.20: General view (left) and detail (right) of the wear track in the SAYM0 pin.

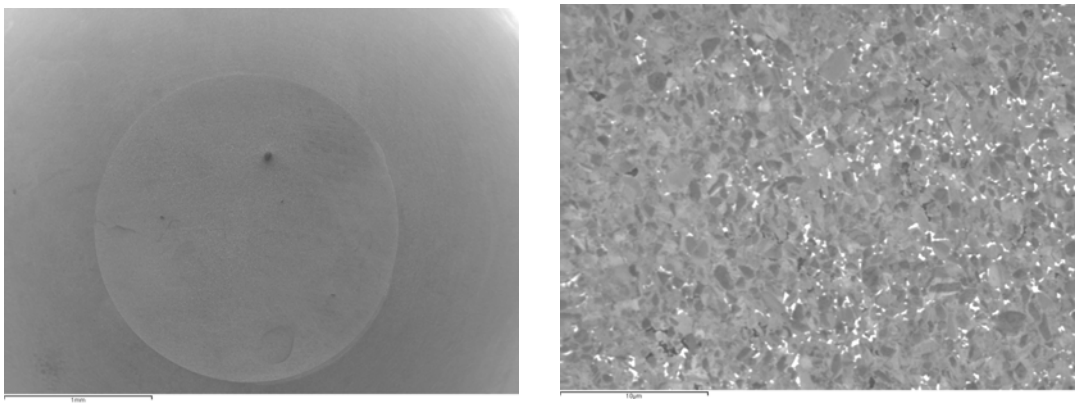

Fig. 6.21: View of the wear track(dark stripe) in the Al_2O_3 disc after coupling with SAYM0. On the right a higher magnification of the track where the smoothed grains are visible and the EDS spectra evidence the presence of SiC debris. Au peaks derive from the coating of the sample.

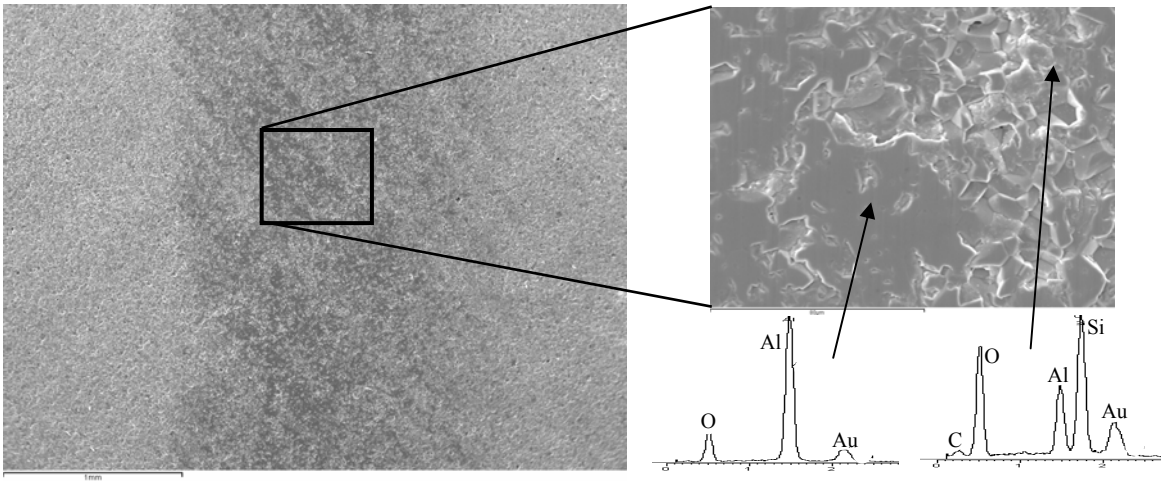

Moving to the coupling SAYM30/Al_2O_3, the pin wear track is shown in Fig. 6.22. Also in this case there were no debris on the track and the details of the microstructure were evidenced by a mild wear which just polished the surface. The counterfacing disc is reported in Fig. 6.23. The microstructure is smoothed and the EDS spectra corresponding to the small debris reveal the presence of Si, which presumably comes from the pin. No trace of Mo was observed.

Fig. 6.22: View of the wear track (left) and detail (right) in the SAYM30 pin after coupling with Al_2O_3. Note the polished microstructure at the tip of the pin revealing a light wear.

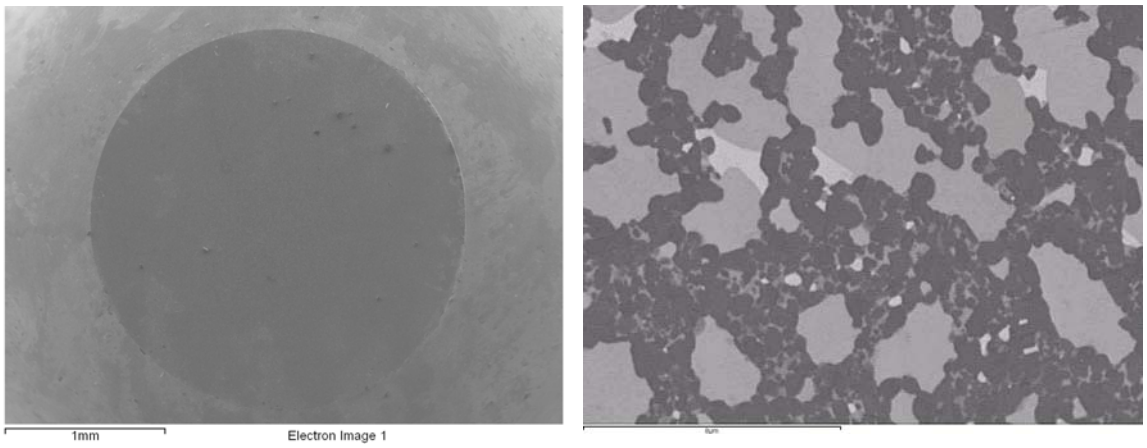

Fig. 6.23: View of the wear track (dark stripe) in the Al_2O_3 disc after coupling with SAYM30. On the right a higher magnification of the track showing smoothed grains and the EDS spectra indicating Si-based debris. C peak derives from the coating of the sample.

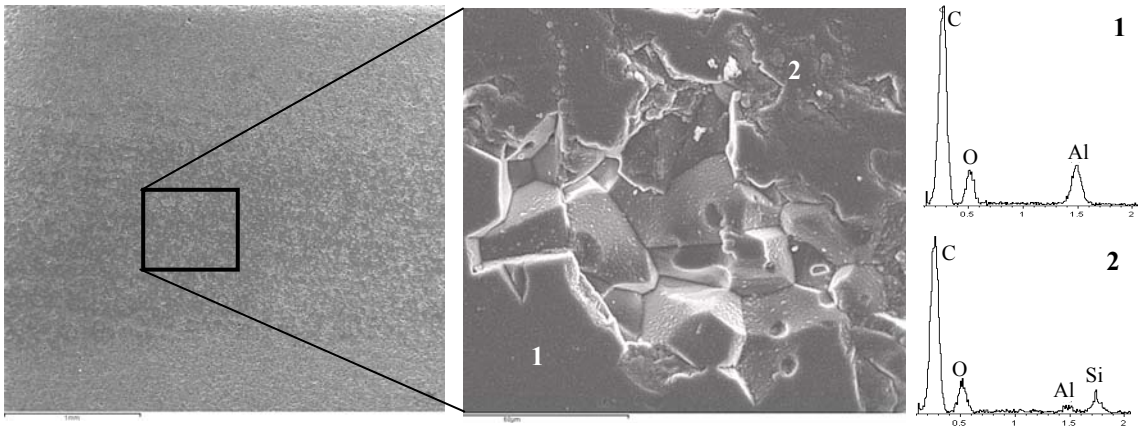

In the light of the tests performed in this configuration, it can be concluded that the friction coefficient and the specific wear of the material containing $MoSi_2$ resulted higher than the pure SiC matrix. It seems, therefore, that for these ceramics wear is more related to hardness than to toughness. The same mild wear mechanisms were observed for both the SiC-based materials.

6.5.2 Slider on cylinder tests

In Tab. 6.III the operating parameters are reported in terms of applied load, speed and distance. In Tab. 6.IV the friction coefficient and the wear rate are reported as a function of each experimental condition. The wear rate was calculated from the weight loss for the slider and from the removed volume for the cylinder. The values reported in Tab. 6.IV are the mean of 4 tests performed in the same conditions.

Tab. 6.III: Experimental conditions of the slider on cylinder tests.

Parameter	Experimental
Distance	**10 km**
Load	**15 N, 30 N, 50 N**
Speed	**0.5 m/s, 1 m/s**

At the beginning of the test, the pressure of contact was of the order of few tens of MPa, but it decreased to few units during the sliding progressing, due to the increasing of the contact surface.

Concerning the data relative to the Al_2O_3 cylinder, it is has to be noted that only the volumetric wear rate was evaluated by measuring the track depth using a profilometer. As a matter of fact, to measure the weight wear rate, it is necessary an analytical balance (±0.001 g) which was not compatible with the size and weight of the cylinder. When the applied load was 15 N, it was not possible to observe a real wear path on the cylinder, as the track appeared just slightly smoothed. It was then concluded that 15 N is the detection threshold of wear for the cylinder, estimated around $4 \cdot 10^{-12}$ $s^2 \cdot m^{-2}$.

Tab. 6.IV: Friction coefficients and wear rates measured in the slider-on-cylinder configuration between SAYM30 slider and Al_2O_3 cylinder. Mean values±1 standard deviation.

Load	Speed	Friction	SLIDER		CYLINDER
N	m/s	μ	Wvol 10^{15} m^2 N^{-1}	Wwt 10^{11} s^2 m^{-2}	Wvol 10^{15} m^2 N^{-1}
15	0.5	0.54 ± 0.05	2.5 ± 0.1	1.0 ± 1.6	< 1*
30		0.61 ± 0.05	2.7 ± 0.2	1.4 ± 0.5	2.0 ± 0.6
50		0.70 ± 0.02	3.5 ± 0.2	1.4 ± 0.3	1.3 ± 0.5
15	1.0	0.59 ± 0.06	3.0 ± 0.2	1.1 ± 0.2	< 0.5*
30		0.70 ± 0.01	7.0 ± 1.6	3.1 ± 0.5	21 ± 3
50		0.67 ± 0.03	98 ± 53	37 ± 21	175 ± 133

*estimation, since the track depth could not be distinguished from the background

The friction coefficient of the coupling SAYM30/Al_2O_3, determined as ratio between the tangential force and the normal applied load, varied depending on the experimental conditions, as shown in the plot of Fig. 6.24.

Fig. 6.24: Mean friction coefficients recorded during the tests at 0.5 e 1 m/s in the slider on cylinder configuration.

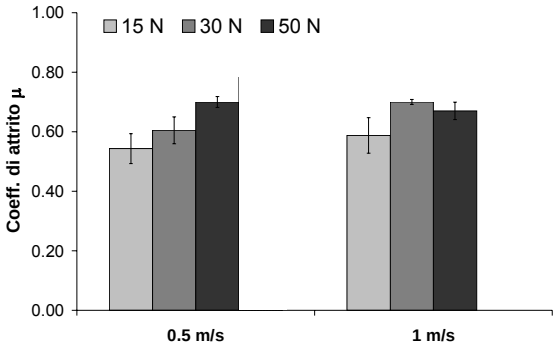

At low speed, the friction increased progressively with increasing the load. During tests at 1 m/s, the obtained values were comparable to those obtained during test at 0.5 m/s. The friction coefficient abruptly increased when 30 N were applied.

In Fig. 6.25 the volumetric wear rates for the slider are reported as a function of the different condition of speed and applied load. It can be stated that the tribological behaviour of this SiC-composite seems to be more sensitive to the sliding speed (and the corresponding increase of temperature), than to the load (Fig. 6.25a). When the load was increased from 15 to 30 N, the wear rate underwent a limited increase at 0.5 m/s but a significant increase at 1 m/s. When the applied load was increased up to 50 N, the wear rate did not change for a sliding speed of 0.5 m/s, but increased of about one order of magnitude at 1 m/s. In this situation, more severe wear mechanisms were observed to occur as a consequence of the higher contact temperatures and the larger amount of debris. Since the debris come from very hard phases (SAYM30: ~18 GPa), they contributed to the slider damage for effect of induced abrasion. Fig. 6.25b shows the volumetric wear rates for the cylinder. As previously mentioned, in mild experimental conditions (15 N, 0.5 m/s) it was not possible to quantify the removed volume of Al_2O_3, hence the reported value just represents an indicative estimate. As for the tests at 15 N at 1/m, the wear rate could be reasonably quoted as $5 \cdot 10^{-16}$ $m^2 \cdot N^{-1}$.

Fig. 6.25: Volumetric wear rate relative to a) SAYM30 slider and b) Al_2O_3 cylinder.

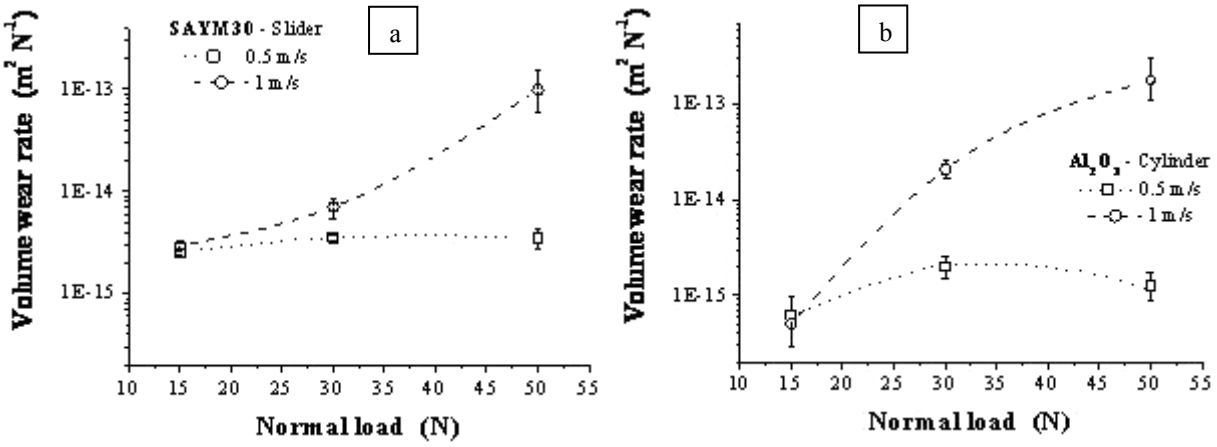

The behaviour of the cylinder wear rate resulted analogous to the behaviour of SAYM30 slider, as, also in this case, at low speed the wear rate did not change significantly with the applied load at 0.5 m/s. On the contrary, during tests carried out at 1 m/s, the wear rate increased almost exponentially with the load.

In Fig. 6.26 the wear rates of slider and cylinder are compared in the same conditions of speed and load. As it can be observed, the wear rates were higher, and more variable, when the speed was 1 m/s. With increasing the severity of the test, the wear

increased both for the slider and the cylinder. According to the ratio between the wear rates of the two antagonist bodies, it can be deduced that at low speed the cylinder wears the slider, whilst at high speed the opposite occurs.

Fig. 6.26: Comparison between the volumetric wear rates of slider and cylinder in the tested conditions: a) tests at 0.5 m/s, b) tests at 1 m/s. The values relative to the cylinder at 15 N are estimations, because the wear was below the detection treshold.

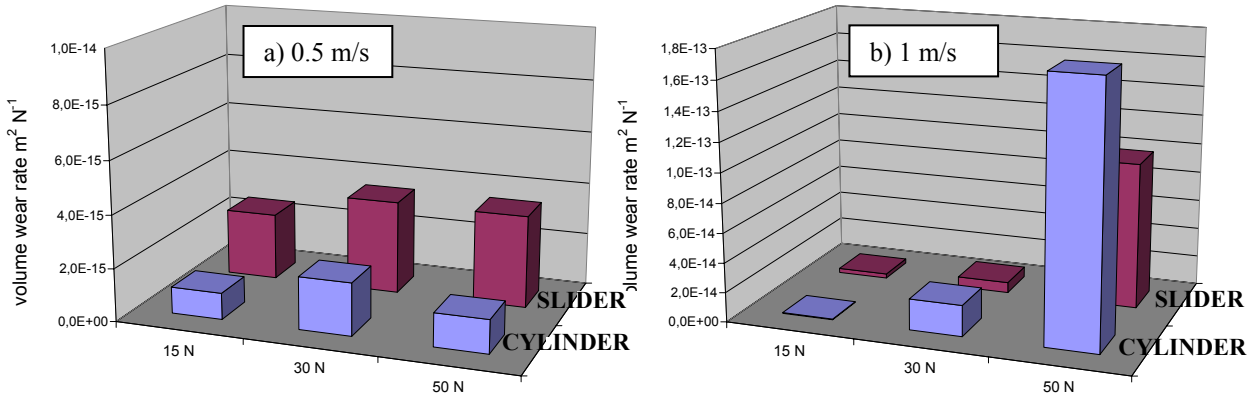

In each coupling, the overall wear curve presented a first small period of running in with increasing friction coefficient, followed by a nearly stationary stage, whose slope was strongly dependent on the experimental conditions. The maximum achieved by the friction coefficient usually corresponds to the final part of the running in stage. During tests at high load and low speed, i.e. 50 N and 0.5 m/s, the wear curves showed very irregular fluctuations, indicating the formation of debris between the two counteracting bodies (an example is shown in Fig. 6.27). This phenomenon seems to have some effects on the friction coefficient, as it can be deduced from the correspondence between the variations in the two curves.

Fig. 6.27: Friction coefficient and system wear during a test at 50 N, 0.5 m/s

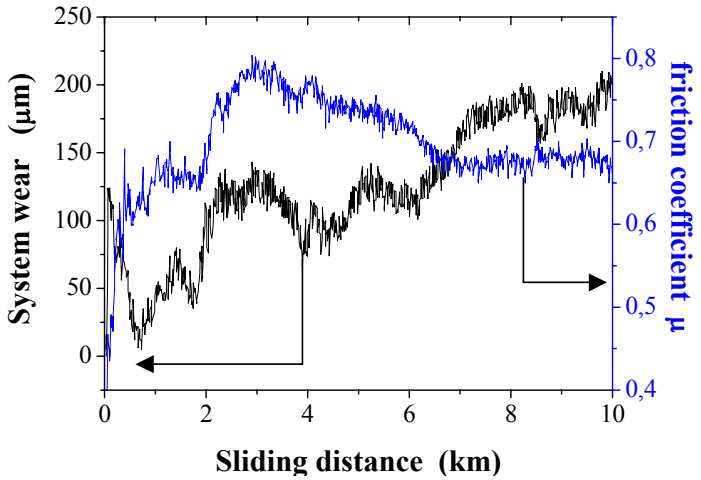

The bulk temperature of the slider increased quickly in the first part of the test, reached a peak at the end of the running in period, and subsequently decreased gradually until it stabilized to a plateau. The temperature trend was quite similar in all the tests, but with differences in the maximum achieved temperature and the distance at which the temperature remained constant. The temperatures were strongly dependent on the experimental conditions: increasing the severity of the parameters, the temperature increased ant the distance of attainment of the maximum temperature decreased. In particular cases, as for the 50 N and 1 m/s tests, during the steady stage, very hot temperatures were achieved which provoked sparks between slider and cylinder, as shown in Fig. 6.28. Due to the high temperature and to the continuous thermal shock, the cylinder was strongly damaged and this damage was reflected in the high wear rate (compare Tab. 6.IV).

The morphological analysis of the wear tracks gives information about the damaging mechanisms triggered during the different experimental conditions. In mild conditions (15 N, 0.5 m/s), only the asperities of the slider were subjected to a small wear, which just smoothed the contacting asperities. At the end of the tests performed at medium load and speed, the tracks on the slider showed the presence of stripes, attributed to the action of isolated hard debris entrapped between the contact surfaces. In more severe conditions, especially with an applied load of 50 N, the wear tracks showed an amount of smeared debris which increased with the sliding speed.

Fig. 6.28: Test at 50 N, 1m/s where the red-hot temperature are noticeable at the contact between slider and cylinder.

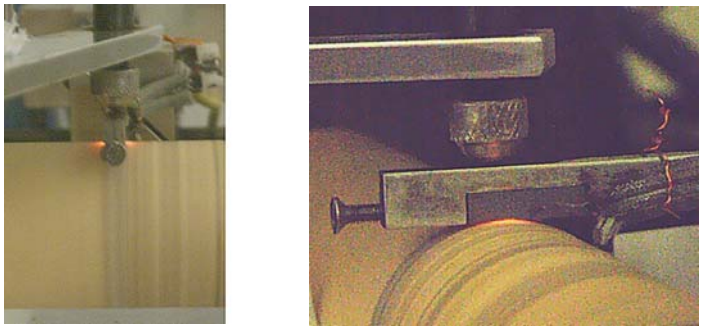

All the tribological tests produced debris. Their amount resulted proportional to the severity of the experimental conditions. In most cases, the colour was yellowish-beige, typical of Al_2O_3. Only for the tests at 50 N at 0.5 and 1 m/s, the debris turned into light grey and dark grey, respectively.

Macroscopically, the debris appeared as compact powder in the form of flakes with dimensions ranging from 20 μm to 1 mm. The presence of SiC and $MoSi_2$ is recognizable since the colour tends to turn into dark, see Fig. 6.29. The morphology and composition of the debris, which take a key part in determining the damaging mechanisms, were studied by SEM-EDS and XRD. These techniques revealed that they were mainly composed by Al_2O_3. The presence of large particles of $MoSi_2$ was also detected among debris agglomerates.

Fig. 6.29: Optical micrographs of debris after tests in different conditions of applied load and speed. Note the darker colour of the debris after the most severe conditions (50 N, 1 m/s).

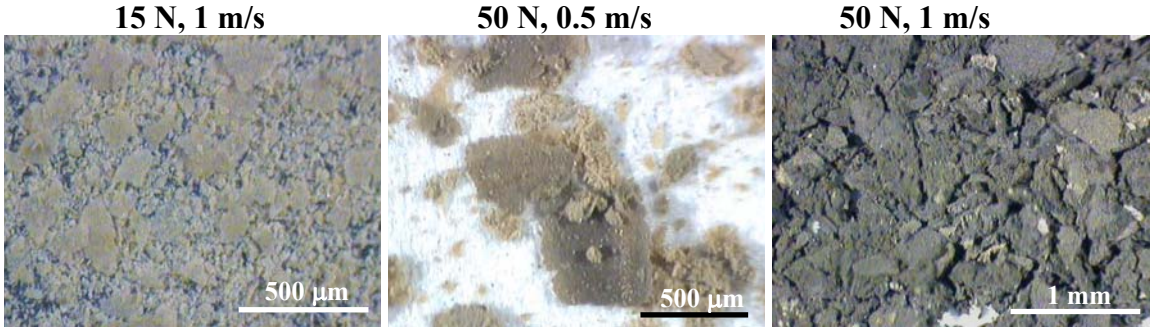

According to the curves recorded during the tests, to the temperatures achieved and the acoustic emissions, it was noticed that the tests performed in the most severe conditions (50 N; 1 m/s) underwent a first running in period, followed by a catastrophic wear of the slider, which occurred when the colour of the track on the cylinder became darker and debris started to be produced in great amount.

To better understand the transition between these two stages, tests at different distances and same load and speed were performed. Some of the tests were interrupted in correspondence of the aspect changes of one of the two body.

These experiment, along with the previous observation, evidenced that:

- in the first 250-300 m, only the surface asperities of the slider are smoothed with no debris or acoustic emission (Fig. 6.30a);
- between 300 and 600 m, the friction produces a strong acoustic emission, the colour of the track turns to dark and then black, debris start forming and permanently accumulating on the entry side of the track.

- between 900 and 1600 m, the dragging of the accumulated debris starts and the transition between running in and catastrophic wear occurs (Fig. 6.30b). The intensity of the acoustic emission diminishes, while on the track of the cylinder peaks of hot temperature are achieved with the appearance of sparks on the slider's sides (~700°C). The slider starts to undergo a strong abrasion and the production of black debris increases. From this period, the wear curve of the system assumes an increasing trend until the attainment of the maximum limit allowed by the tribometer.

Fig. 6.30: a) Optical micrographs showing a smoothed surface of the slider after 100 m sliding. b) Surface of the slider at the transition to catastrophic wear after 1550 m. Note in b) the presence of debris.

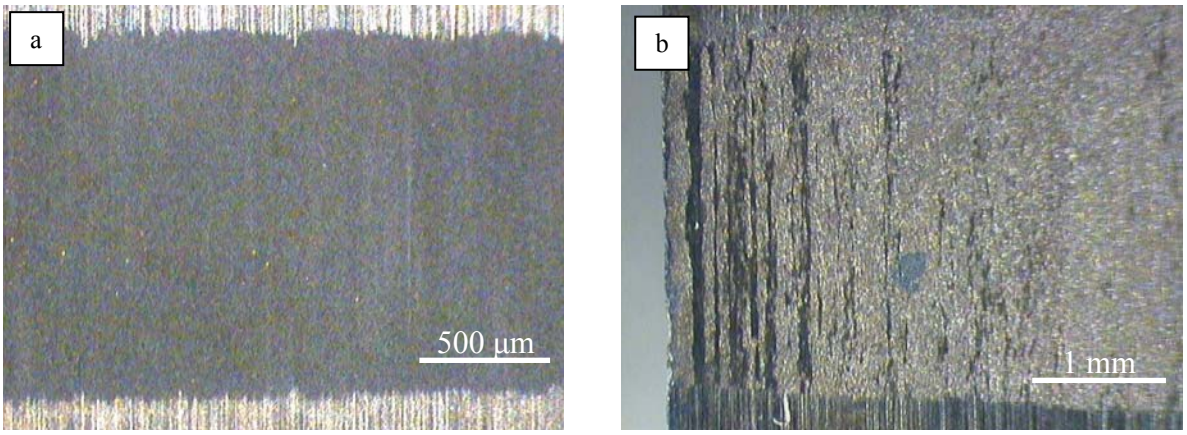

In Fig. 6.31 the volume of removed material from the slider are reported as a function of the sliding distance during a series of interrupted tests at a sliding speed of 1 m/s and with an applied load of 50 N. It can be noticed that the removed volume increases nearly linearly with increasing the sliding distance. Interpolating these data, it was estimated that the volumetric wear rate in the running in was $(4.2\pm0.2)\cdot10^{-15}$ $m^2\cdot N^{-1}$, which is of the same order of magnitude of the wear rate calculated in mild conditions.

Fig. 6.31: Slider removed volume as a function of sliding distance.

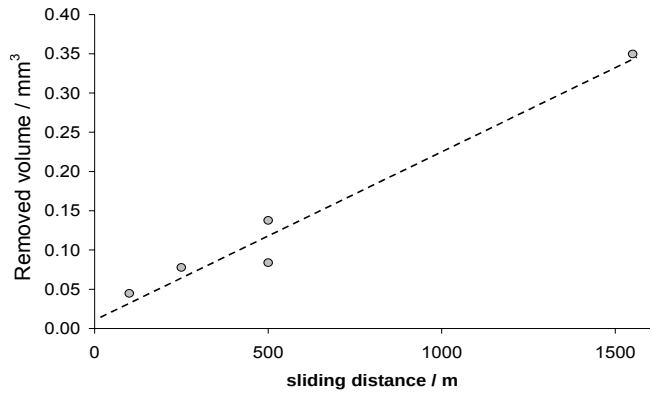

Concluding, the tribological characterizations performed on SiC-$MoSi_2$ composite coupled with Al_2O_3 in the configuration slider on cylinder allowed to individuate the conditions in correspondence of which an abrupt transition from running in to catastrophic wear occurs. Specific activities aiming at the study of running in stage were carried out through interrupted tests, chosen according to the wear curves. Morphological and compositional analysis on wear tracks permitted to individuate the reasons leading to catastrophic wear.

In Tab. 6.V a comparison between the values obtained in the two configurations, disc-on-pin and slider-on-cylinder, in the same experimental conditions (sliding distance=10 km, speed=0.5 m/s, load=15 N) is reported.

Tab. 6.V: Comparison between the values obtained in disc-on-pin and slider-on-cylinder configuration in the same experimental conditions of 10 km, 15 N, 0.5 m/s. Mean values±1 standard deviation.

Measure	Disc-on-pin	Slider-on-cylinder
Friction	0.78±0.10	0.54±0.05
Wear rate SAYM30 ($\mu g \cdot km^{-1} \cdot N^{-1}$)	11.04±2.22	10.0±3.30
Wear rate Al_2O_3 ($\mu g \cdot km^{-1} \cdot N^{-1}$)	2.46±1.33	< 5

Keeping in mind that, at fixed load, the pressure on the pin is about two orders of magnitude higher than on the slider, the friction between the two test is significantly different, ~27%. On the contrary, a very good agreement can be observed between the wear rates of the composite measured in the two contact geometries.

However, due to the complex nature of the wear mechanisms involved, it is rash to directly compare the obtained results. For example, in the configuration disc-on-pin, the eventually formed debris would fall, thus not constituting the third body in the system. On the contrary, in the other configuration it was observed that the debris play a fundamental role in leading to catastrophic damaging.

6.6 ELECTRICAL PROPERTIES

The addition of $MoSi_2$ particles to the SiC matrix caused a gradual decrease of the electrical resistivity of the composites, (Fig. 6.32), due to the increased contiguity of the electroconductive $MoSi_2$ particles. The resistivity of the SAYM30 composition was more than three orders of magnitude lower than that of the SiC reference material (~1.3 Ω·cm).

As AlN is a better electrical insulator than Al_2O_3 (10^{13} and 10^{14} Ω·cm, respectively), SAYM30 was more conductive than SYNM30, even if of the same order of magnitude.

Fig. 6.32: Electrical resistivity as a function of the volumetric fraction of $MoSi_2$.

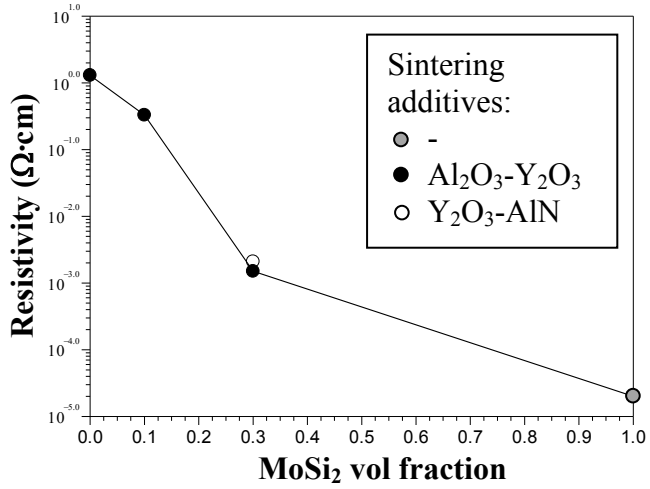

References

1 F. K. Van Dijen and E. Mayer, J. Europ. Ceram Soc. 16 (1996) 413.

2 E. W. Dressler and R. Riedel, Int. J. Refractory Metals and Hard Materials 15 (1997) 13.

3 L. K. Falk, J. Europ. Ceram. Soc. 17 (1997) 983.

4 D. Sciti, A. Bellosi, J. Mat.Sci. 35 (2000) 3849.

5 A. Balbo, D. Dalle Fabbriche, D. Sciti, A. Bellosi, Key Engineering Materials, Vols. 264-268 (Eds: H. Mandal, L.Öveçoğlu), TRANS TECH PUBLICATIONS, Switzerland (2004) 1039.

6 E. Gomez, J. Echeberria, I. Iturriza, F. Castro, J. Europ. Ceram. Soc. 24 (2004) 2895.

7 D. Sciti, A. Balbo, A. Bellosi, Adv. Eng. Mat. 7 (2005) 152.

8 Y.-L. Jang, E. J. Lavernia, J. Mat. Sci. Lett. 29 (1994) 2557.

9 J. J. Petrovic, M. I. Pena, I.E.Reimanis, M. S. Sandlin, S. D. Conzone, H. H. Kung, D. P. Butt, J. Am. Ceram. Soc. 80 (1997) 3070.

10 J.J. Petrovic, R.E. Honnel, J. Mater. Sci. Letts. 9 (1990) 1083.

11 D. Sciti, S. Guicciardi and A. Bellosi, J. Ceram. Proc. Res. 3 (2002) 87.

12 D. Sciti, S. Guicciardi, C. Melandri, A. Bellosi, J. Am. Ceram.Soc. 86 (2003) 1720.

13 A. Newman, S. Sampath, H. Herman, Mat. Sci. Eng. A 261 (1999) 252.

14 L. O. Nordberg and T. Ekström, J. Am. Ceram. Soc. 78 (1995) 797.

15 H. Klemm, K. Tangermann, C. Schubert, W. Hermel, J. Am. Ceram. Soc. 79 (1996) 2429.

16 K.Krnel, D. Sciti, E. Landi, A. Bellosi, Appl. Surf. Sci. 210 (2003) 274.

17 M. A. Mulla, V. K. Kristic, Ceram. Bull. 70 (1991) 439.

18 V. A. Izhevsky, L. A. Genova, A. H. A. Bressiani, J. C. Bressiani, Intern. J. of Refractory Met. and Hard Mater, 19 (2001) 409-417.

19 J.I. Lee, N.L.Hecht, T. –I. Mah, J. Am. Ceram. Soc. 81 (1998) 421.

20 J M. J. Hoffman and M. Nader, Engineering Ceramics'96: Higher reliability Through Processing, edited by G. N. Babini et al. (Kluwer Academic Publisher, The Netherlands, 1977) 133.

21 L. S. SIGL and H.-J. KLEEBE, J. Am.Ceram Soc. 76 (1993) 773.

22 K. Strecker, S. Ribeiro, D. Camargo, R. Silva, J. Vieira, F. Oliveira, Mater. Res. 2 (1999) 249-254.

23 H. S. Kim, Mater. Sci. Eng. A289 (2000) 30.

24 Z. Hashin, Proceedings of the Third International Symposium on Ceramic Microstructure: their Analysis, Significance and Production, John Wiley & Sons Inc.. PUBLISHERS, New York, USA (1968) 313.

25 CRC Materials science and engineering handbook, J. F. Shackelford, W. Alexander, eds., CRC Press, USA, (2001).

26 M. Nakamura, S. Matsumoto, T. Hirano, J. Mat. Sci. 29 (1990) 3309.

27 M. Taya, S. Hayashi, A. S. Kobayashi, H. S. Yoon, J. Am. Ceram. Soc. 73 (1990) 1382.

28 K.T. Faber, A.G. Evans, Acta Metall. 31 (1993) 565.

CHAPTER 7

CONCLUSIONS I

In the field of advanced ceramics the continuous research of innovative composites with improved thermo-mechanical and tribological properties has led to the development of new silicon carbide-based materials, which could be used as components operating under severe wear conditions, high temperatures or in aggressive environment.

Hence, the first part of this thesis deals with the production and characterization of electroconductive SiC-based ceramics. As conducting phase, $MoSi_2$ was chosen in view of its low electrical resistivity, as well as high melting point and excellent oxidation resistance. Electroconductivity enables the possibility to shape components of hard ceramics by electro-discharge machining avoiding the more expensive diamond tools machining.

Chapter 5 describes the processing procedure of SiC-based ceramics doped with 10 and 30 vol% of $MoSi_2$. Despite the use of hot pressing, the addition of sintering additives, like Al_2O_3-Y_2O_3 or Y_2O_3-AlN in amount of 10wt%, resulted to be necessary for the achievement of fully dense materials at temperature of 1900°C.

Chapter 6 presents the microstructure and mechanical properties of the SiC-$MoSi_2$ ceramics, which are compared to those of the reference SiC and $MoSi_2$ pure materials. In additions, in the final sections, tribological characterization and electrical measurements are illustrated.

The microstructures of all the materials resulted dense, homogeneous with low residual porosity; the matrix showed equiaxial grains and mean grain size below 1 μm. The SiC matrix exhibited a core-rim morphology, typical of dissolution-reprecipitation mechanisms, occurring during liquid phase sintering. The inner part, the core, was constituted by the undissolved SiC grains, whilst the outer part, the rim, contained traces of the sintering additives, Al,Si,O. Silica, which is present on the SiC and $MoSi_2$ powders was observed to play a fundamental role in the formation of low-melting liquid phases.

$MoSi_2$ particles did not hinder the densification of the pellets and resulted to be well dispersed in the matrix. Moreover, no cracks were observed between the two constituting phases, despite a significant difference between the corresponding thermal expansion coefficients.

As far as it concerns the mechanical properties, the hardness of the composites decreased with increasing the $MoSi_2$ content, due to the addition of this softer phase, going from 22 GPa for the SiC matrix to around 17 GPa for the material containing 30 vol% of $MoSi_2$.

The Young's modulus was very close to the value of the SiC reference material, because matrix and secondary phase have similar stiffness, this being about 440 GPa. The $MoSi_2$ monolithic materials showed a value of only 355 GPa, due to the high amount of SiO_2 glassy phase, mainly accumulated at the triple point junctions.

For the compositions containing 30 vol% $MoSi_2$, the fracture toughness increased of 27% passing from 2.97 to 4.75 $MPa \cdot m^{1/2}$, thanks to the toughening effect of residual stress provoked by the difference in the thermal expansion coefficient between the two constituting phases. $MoSi_2$ particles did not show any further toughening mechanism, such as crack deflection, crack bridging or crack pinning.

The room-temperature strength passed from 750 MPa of the SiC matrix to 824 MPa for the composition containing 30 vol% of $MoSi_2$, increasing of about 10%. With regard to the high-temperature strength, despite an abrupt collapse at 1300°C of the composite containing 10 vol% of $MoSi_2$, the flexural strength exceeded the matrix value of 38%, increasing from 160 to 220 MPa. The strength degradation experienced by all the composites is related to the softening of the grain boundary phases, deriving from reaction between sintering additives and silica impurities.

Concerning hardness, Young's modulus and high temperature flexural strength, the material containing 30 vol% of $MoSi_2$, hot pressed with Y_2O_3-AlN as sintering additives, gave better results than the analogous composite sintered with the addition of Al_2O_3-Y_2O_3, due to the presence of AlN which is more refractory than Al_2O_3.

Tribological tests conducted in a disc-on-pin configuration, with alumina as counterfacing material, confirmed that the addition of $MoSi_2$ to SiC was detrimental, as the friction coefficient and the wear rate increased compared to the SiC matrix.

The wear behaviour of the SiC-30 vol% $MoSi_2$ was studied in the configuration slider-on-cylinder under different experimental conditions of sliding distance, applied load and sliding speed. Specific tests aiming at individuating the transition from

running in to catastrophic wear evidenced the formation of hard debris as the major cause.

A direct comparison between the results obtained from the two contact configurations (disk-on-pin and slider-on-cylinder) pointed out similar values of wear rates for both the SiC-$MoSi_2$ composite and the Al_2O_3 counterfacing body, despite the different contact geometry. However, much attention has to be paid when comparing two tribological systems, since the wear mechanisms which intervene for the removal of material are strongly dependent on the presence and nature of debris, geometry, temperature, etc.

Finally, another positive effect of $MoSi_2$ addition was disclosed by the electrical conductivity tests. The resistivity dropped from 1.3 to $1.3 \cdot 10^{-3}$ Ω·cm for the materials containing 30 vol% of $MoSi_2$, that is a decrease of three orders of magnitude compared to the SiC matrix. This goal represents a great advance, as these new composites are electro-conductive, thus allowing a cheaper machining by EDM, with respect to the conventional methods which employ diamond tools.

From the work conducted it can be concluded that the addition of $MoSi_2$ to a SiC matrix was generally beneficial for improving sintering, electrical behaviour and most of the mechanical properties at room temperature (flexural strength and fracture toughness). On the contrary it was found to be detrimental for the hardness and the wear behaviour under the specific conditions studied.

SECTION II

UHTCs MATERIALS

CHAPTER 8

UHTC'S MATERIALS: FEATURES AND UTILIZATIONS

8.1 INTRODUCTION

Refractory compounds such as carbides, borides and nitrides are characterized by high melting points, high hardness and good chemical inertness and oxidation resistance.[1–3] These refractory compounds have been broadly termed Ultra High Temperature Ceramics (UHTCs). Works on these materials were initiated to meet the need for high temperature materials that would enable the development of manoeuvrable hypersonic flight vehicles with sharp leading edges.[2] The relatively good oxidation resistance of refractory diboride compounds, compared to other refractory intermetallic compounds (i.e. carbides, nitrides and silicides), has focused many research efforts into detailed investigations of transition metal diborides of groups IV and V (Ti, Zr, Hf, Nb, Ta). Among the transition metal diborides, hafnium diboride (HfB_2) and zirconium diboride (ZrB_2) were identified as the most promising candidates for high temperature applications such as nose caps, sharp leading edges, vanes and similar parts for use in high velocity flight or on future generations of re-entry vehicles.[1,2,4–6]

Strong covalent bonding is responsible for the high melting points, moduli and hardness of the UHTC family of materials.[6,7] High negative free energies of formation also give UHTCs excellent chemical and thermal stability under extreme conditions.[6,7] In comparison to carbides and nitrides, the diborides tend to have higher thermal conductivity, which gives them good thermal shock resistance and makes them ideal for many high temperature thermal applications.[7,8]

Realization of the full potential of UHTCs as future high temperature materials requires a thorough knowledge of their properties and behaviour under diverse conditions of temperature, environment and stress states.[7] A historical review of UHTC research carried out so far and engineering data on UHTCs are provided. Since the most comprehensive research has been focused on compositions containing HfB_2 or ZrB_2 they will be the primary materials discussed. Results from materials containing HfB_2 or ZrB_2 as the principal component with selected additives designed to enhance oxidation

resistance, mechanical properties and thermal stress resistance will also be presented. When available, data on other UHTC compositions will also be discussed.

8.2 CHEMICAL-PHYSICAL FEATURES

8.2.1 Structural stability

Ceramic borides, carbides and nitrides all have very strong chemical bonds that give them high temperature structural stability.[5,7,9]

As a result of the extremely strong bond between carbon atoms, they follow the classical definition of brittle ceramics. They come in three general classes: ionic, covalent and interstitial. None of the ionic carbides have engineering uses because of their extreme brittleness.[10] The two mostly diffused covalent carbides with covalent bonds, SiC and B_4C, both are valuable for their extreme hardness as well as excellent thermal and chemical stability. The largest class of carbides, those of the interstitial type, includes carbides of the metals Hf, Zr, Ti, and Ta. These materials benefit from strong carbon networks and have some of the highest melting points of known materials (see Fig. 8.1).

Fig. 8.1: A comparison of the melting temperatures of the most refractory members of several classes of materials. Several borides, carbides and nitrides have melting temperatures above 3000°C and belong to the class UHTs.

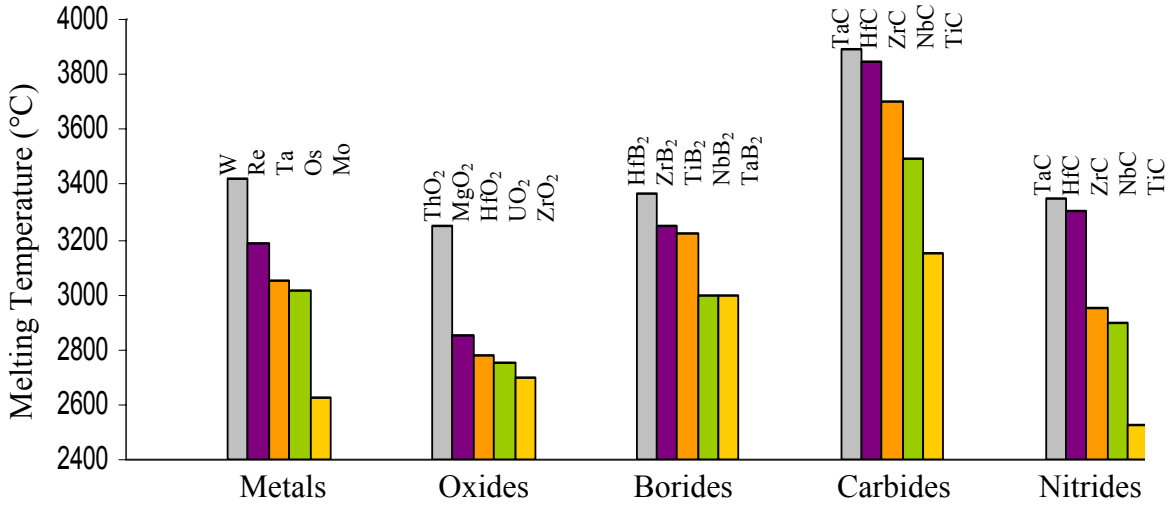

Carbides posses the cubic close packed NaCl-type structure with a fcc B1 symmetry, where the metal-to-metal bond is relatively weak and the metal-to-carbon bond is strong. The only stable composition is the monocarbide with carbon atom in all octahedral sites as stoichiometry. They are nearly completely soluble among each other, as shown in Fig. 8.2. They are also known to have high strengths at elevated

temperatures.[10,11] From this standpoint, carbides offer a tremendous benefit in many engineering applications. Unfortunately, these materials are hard to fabricate because of their refractoriness, and little has been achieved beyond the laboratory scale.[10,11]

Fig. 8.2: mutual solubility of refractory carbides.

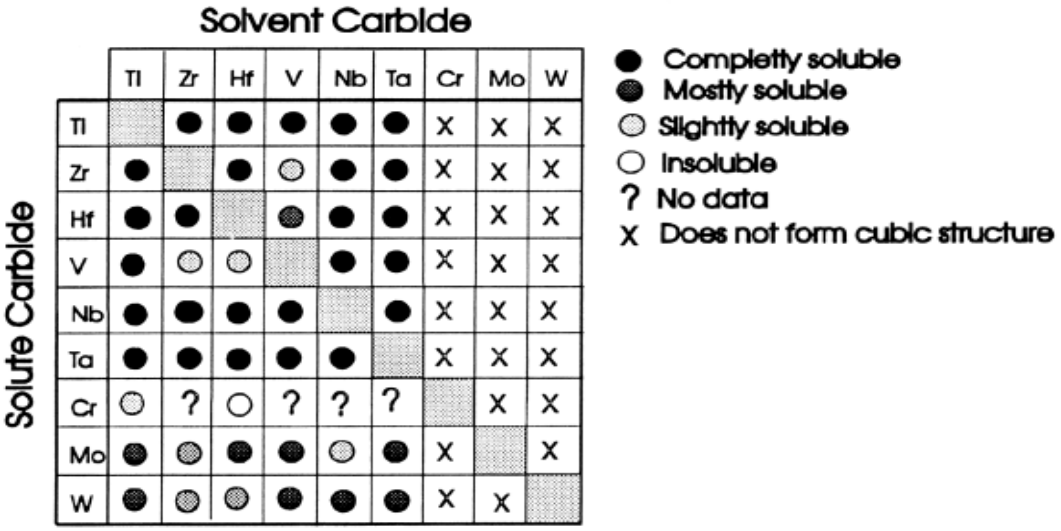

Ceramic nitrides have many of the same properties as carbides since they are difficult to fabricate as well, especially in the pure form, due to strong covalent bonding. Silicon nitride and boron nitride are the primary materials in the family of nitrides to be developed for engineering applications.[9]

Ceramic borides benefit from very strong bonding between boron atoms, although their bonding is not typically as strong as seen in the carbides, thus these materials often have melting points below that of the carbides.[7,10] The unique feature of the electronic nature of the boron bonding in these materials results in having high thermal and electrical conductivities, higher than typically found in carbides and nitrides, as well as low coefficients of thermal expansion, which, combined, give the borides relatively good thermal shock resistance.[7]

Boride ceramics also appear to have improved oxidation resistance over those of carbides and nitrides, the nature of which is discussed in the following section. Table 8.I lists a number of metallic elements that form binary diboride compounds, with the AlB_2 structure, shown in Figure 8.3.[12,13]

Tab. 8.I: Observed phase stability of transition metal diborides of the AlB_2 structure.

Sc	Ti	V	Cr	Mn	Fe	Co	Ni
Y	Zr	Nb	Mo	Tc	Ru	Rh	PD
La	Hf	Ta	W	Re	Os	Ir	Pt

Stable AlB_2 phase
Stable at high temp.
Prepared or detected at high temp.
AlB_2 phase is metastable

Fig. 8.3: A) Atomic projections of the structure showing top down and side view. B) An illustration of metal atom deformation within the structure.[12]

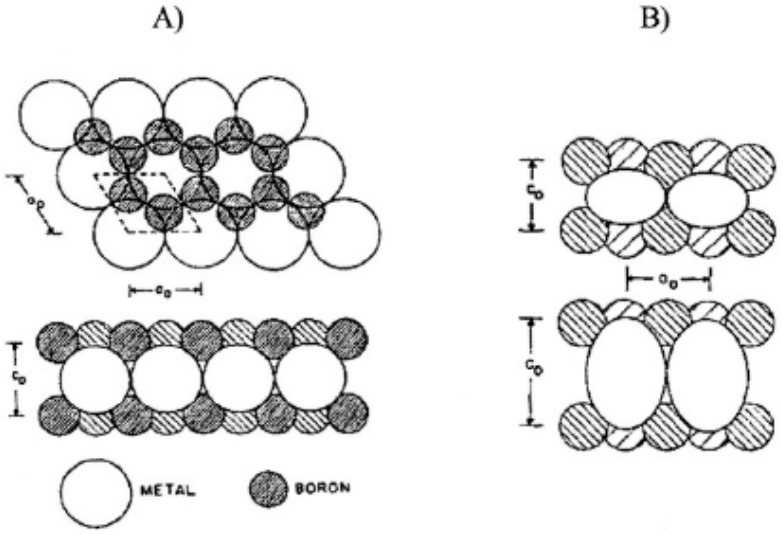

The AlB_2 structure contains graphite-like layers of boron separated by hexagonal close-packed (h.c.p.) layers of metal atoms. The diborides are comprised of rigid covalent boron lattices, such that the boron atoms have a trigonal prismatic metal environment with three close boron neighbours. The metal atoms coordinate twelve boron atoms, six metallic atoms in the same layer and two metal atoms in the two adjacent layers (top and bottom).[12,13] The boron nets have very strong covalent bonds that hinder an increase in the direction, though no such hindrance occurs in the direction, giving borides the ability to accommodate a wide variety of metals.[12]

Spear performed calculations on chemical bonding parameters of borides and deduced that M-B bonding is likely the leading contributor to the structural integrity of AlB_2 type borides, more so than M-M or B-B bonding. Typically, the less distortion there is to the unit cell, the stronger are the bonds that hold it together. As the degree of bonding increases so does the melting point, modulus and hardness, in the diborides as well as for carbide and nitride ceramics.[7,8,10]

Enthalpies of formation for several boride systems were reported by Samsonov and Vinitiskii.[14] From those results it is clear that the stability of diborides decrease in the order $HfB_2>TiB_2>ZrB_2>>TaB_2>NbB_2>VB_2$, with VB_2 the least stable of the diborides, having the lowest energy of formation.

The phase diagram of Zr and Hf carbides and borides are reported in Fig. 8.4.

Fig. 8.4: Phase diagram of a) ZrC, b) HfC, c) ZrB_2 and d) HfB_2.[15]

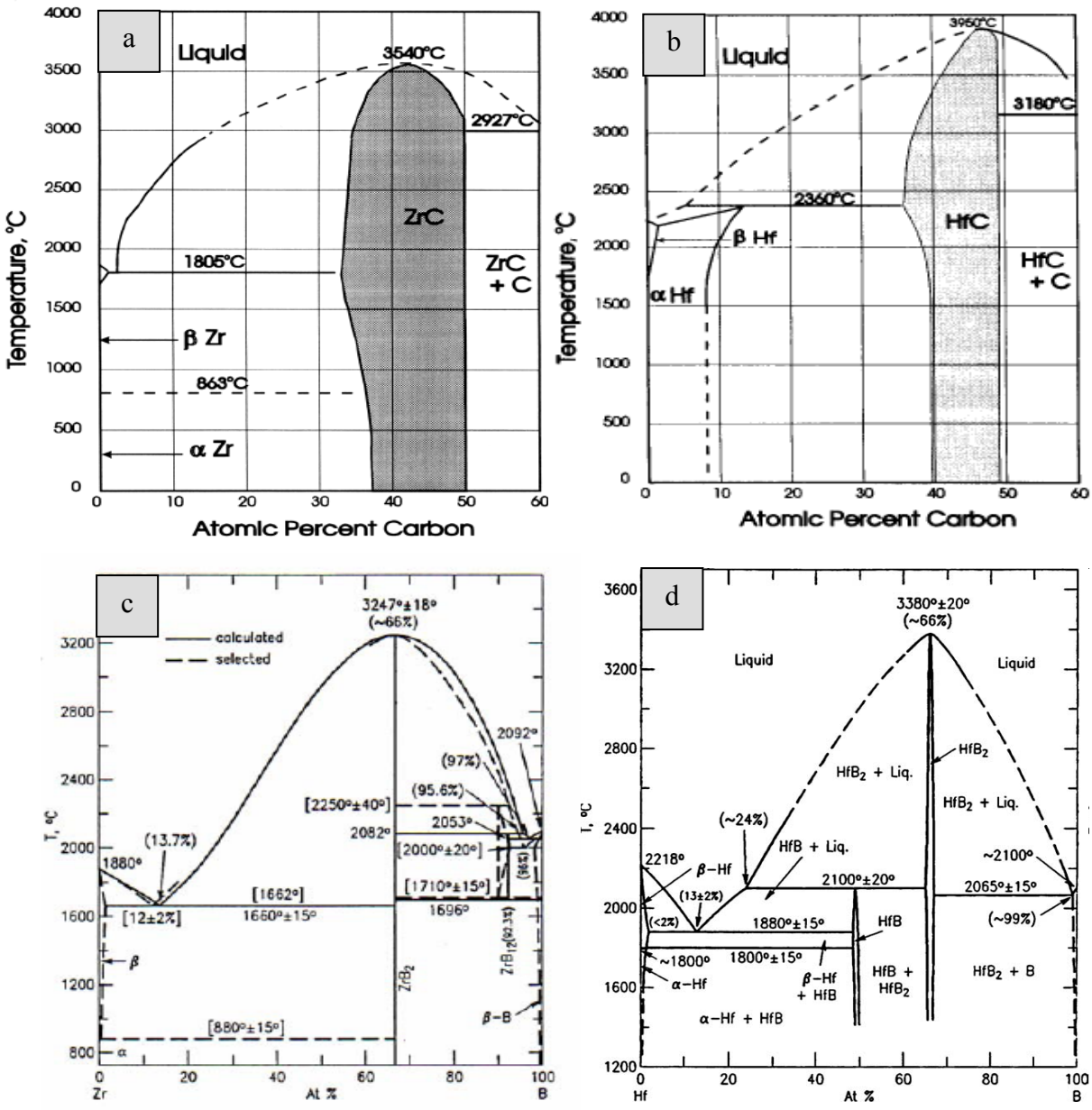

8.2.2 Structure

Following the previous description of the atomic structure of boride, carbide and nitride ceramics, Table 8.II lists physical crystalline structural differences of a variety of UHTCs along with respective density and melting point.[16-20] Note that density increases with increasing mass of the metal atom. Note also the differences in melting points between materials whereby the carbides typically have the highest melting points, above borides or nitrides of the same metal constituent.

Tab. 8.II: Crystal strucure, density and melting point of UHTCs.

Material	Crystal Structure	Lattice Parameters			Density	Melting Pt.
		aÅ	bÅ	cÅ	g/cc	°C
HfB_2	Hexagonal	3.142	–	3.476	11.19	3380
HfC	FCC	4.638	4.638	4.638	12.76	3900
HfN	FCC	4.525	4.525	4.525	13.9	3385
ZrB_2	Hexagonal	3.169	–	3.530	6.10	3245
ZrC	FCC	4.693	4.693	4.693	6.56	3400
ZrN	FCC	4.578	4.578	4.578	7.29	2950
TiB_2	Hexagonal	3.030	–	3.230	4.52	3225
TiC	Cubic	4.327	4.327	4.327	4.94	3100
TiN	FCC	4.242	4.242	4.242	5.39	2950
TaB_2	Hexagonal	3.098	–	3.227	12.54	3040
TaC	Cubic	4.455	4.455	4.455	14.50	3800
TaN	Cubic	4.330	4.330	4.330	14.30	2700
SiC	Polymorphic		Various		3.21	2820

8.2.3 Thermodynamical properties

Some of the thermodynamic properties for a few diborides, including HfB_2 and ZrB_2 are listed in Tables 8.III and 8.IV. The data in these tables are from Pankratz et al.,[20] who reviewed available data in the early 80's and included only the data they deemed to be reliable. Enthalpies of formation are strongly correlated with Gibbs free energies of formation for borides, because the entropy terms are small. This also means that the free energy is relatively insensitive to temperature.[7]

Tab. 8.III: Thermodynamic data for UHTCs.

Material	Enthalpy of formation, ΔH_f (kJ/mol)			Gibbs free energy of formation, ΔG_f (kJ/mol)		
	At 298 K	At 1000 K	At 2000 K	At 298 K	At 1000 K	At 2000 K
HfB_2	−335.98	−334.90	–	−332.20	−324.49	–
ZrB_2	−322.14	−326.65	−340.36	−318.16	−306.34	−279.60
TiB_2	−323.84	−326.59	−347.87	−319.69	−308.34	−347.87
TaB_2	−209.20	−209.77	−208.02	−206.53	−200.18	−191.02

Tab. 8.IV: Heat capacity for UHTCs.

Material	Heat capacity at constant pressure C_p (J/mol*K)		
	At 298 K	At 1000 K	At 2000 K
HfB_2	49.45	81.67	–
ZrB_2	48.37	71.99	82.66
TiB_2	44.28	76.89	94.54
TaB_2	48.12	76.77	96.71

8.3 PROCESSING

8.3.1 Sintering

Fabrication of UHTCs has typically been accomplished by hot pressing in either resistance or induction heated furnaces using graphite dies. Due to the observation of chemical reactions between the graphite dies and the diboride powders, a number of methods have been investigated to produce a diffusion barrier between the powder and the die. ManLabs tested several diffusion barriers including: a) boron nitride wash on a graphite sleeve, b) tungsten foil, c) pyrolytic graphite paper, d) silicon carbide wash and e) pyrolytic graphite paper with an inner BN wash. They found that up to 2100°C the pyrolytic graphite paper with an inner BN wash was most effective, although above 2100°C reaction zones were very evident. ManLabs also investigated the effects of a number of sintering variables on the final billet density and microstructure, including maximum temperature, pressure and heating schedule. They were not able to detect any changes in the final microstructure due to small fluctuations in heating rate or holding time.[2] ManLabs investigations found that changes in pressure from 20–40 MPa produced little or no variation in billet density, but they did observe that, at pressures below 20 MPa, the diboride samples would not densify uniformly.[2]

High-pressure hot pressing technology was also used to fabricate monolithic UHTCs. Hot pressing at temperatures ranging from 1400°C to 1900°C and pressures of 500 MPa to 2 GPa provided a means of preparing fine-grained dense materials without the use of additives. Later on, the influence of pressure on densification was studied by ManLabs on HfB_2 using a fixed pressure of 800 MPa and temperatures from 1400°C to 1900°C with 10 minute holds.[21] Full densification was not achieved at temperatures below 1840°C. Similarly, the influence of pressure was studied at 1790°C with 10 minute holds for a range of pressures from 400 MPa to 1.5 GPa. Full density was achieved at a pressure of 1.5 GPa, very good results were also obtained with a pressure of 800 MPa yielded a sample with 1.4% porosity, and 400 MPa, which resulted in a sample with 6.8% porosity.[21] Pure diborides as well as diborides with several additive systems were investigated in attempts to improve material properties and/or oxidation resistance. Due to the high melting temperatures of the diborides, ManLabs encountered considerable difficulty when consolidating samples of pure HfB_2 or ZrB_2. Without the use of high pressure hot pressing techniques they were unable to produce fully dense billets without significant grain growth or cracking, but the high pressure hot pressing significantly

limited their maximum billet size.[1,2,21] The additives that were investigated were primarily used to increase oxidation resistance (SiC additions) or thermal stress resistance (C additions, added to reduce the materials elastic modulus) and were not originally considered as potentially advantageous to fabrication. However, ManLabs found that with the intentional additives, billet cracking could be eliminated and dense, fine-grained diboride microstructures were achievable (see Fig. 8.5).[4,22]

Fig. 8.5: HfB_2-20vol% SiC produced by ManLabs.

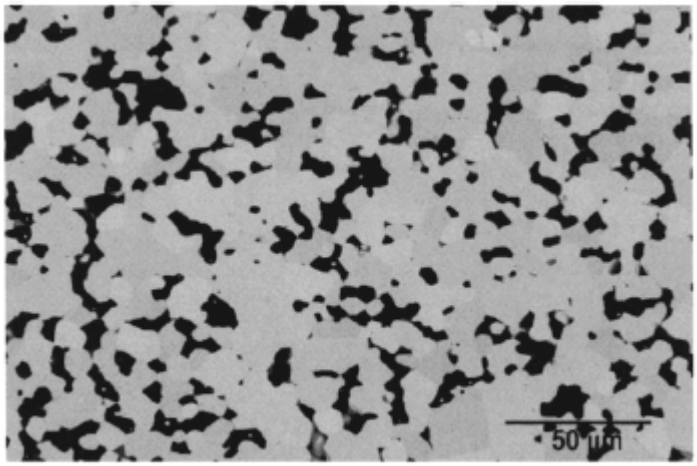

Figure 8.6 shows the influence of SiC additions on the densification behaviour of HfB_2 by comparing the hot pressing characteristics of pure HfB_2 to that of HfB_2-20vol% SiC.[4]

Fig. 8.6: Comparison of hot pressing characteristics of pure HfB_2 and HfB_2-20vol% SiC.

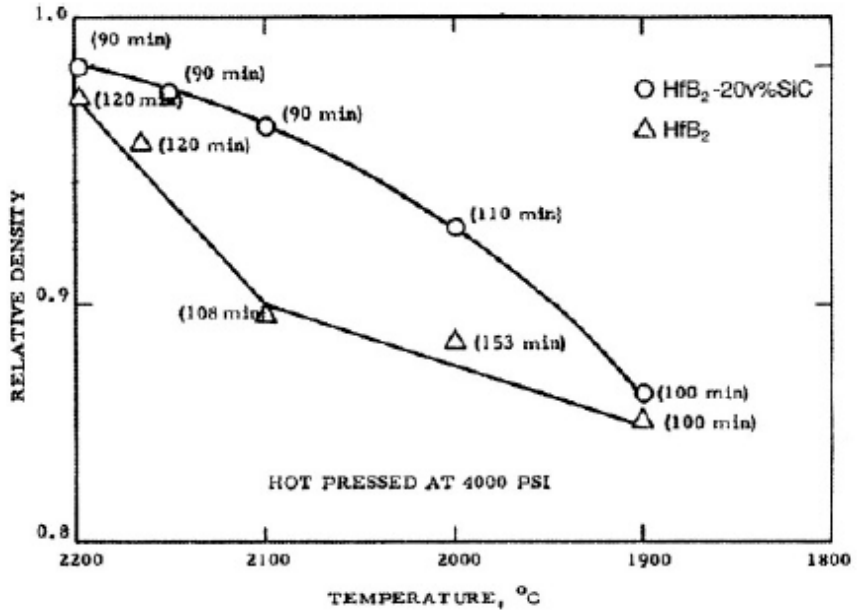

The relative densities of these materials hot pressed at equivalent temperatures clearly show that SiC improves HfB_2 densification by reducing the temperature and time required to achieve a comparable density. Similar trends were observed for the ZrB_2 and ZrB_2/SiC materials. A distinguishing feature of the microstructures of the SiC

containing materials, both ZrB_2 and HfB_2, was their much smaller grain size, compared to hot pressed samples of pure ZrB_2 and HfB_2. ManLabs researchers conjectured that the SiC phase promoted densification by restricting the growth of diboride grains, thus promoting diffusional densification as modeled by Nabarro-Herring, which favours small particle sizes.[4] The presence of chemical impurities was determined by careful microstructural investigation of grain boundaries. Interestingly, ManLabs also found that the SiC additions appear to getter impurities within the materials, and that the reduction in impurity phases was a function of the volume percent of SiC. The minimum remaining impurity phases were observed with the addition of at least 10-15 vol% SiC.[2]

8.3.2 Machining

Due to the hard brittle nature of the UHTC materials, diamond tooling is typically required to machine components. Electron Discharge Machining (EDM) can be used as an alternative to diamond grinding thanks to the high electrical conductivity of these materials. Especially for the borides, this is an advantage over some of the carbide, nitride, and oxide materials that typically have higher resistances, which, in some cases, does not allow them to be machined using EDM. EDM is a non-traditional method of removing material by a series of rapidly recurring electric arcing discharges between an electrode (the cutting tool) and the workpiece, in the presence of an energetic electric field. Consecutive sparks produce a series of micro-craters on the work piece and remove material along the cutting path by melting and vaporization Some of the advantages of EDM include machining of:

- complex, small or odd-shaped angles, intricate contours or cavities that would otherwise be difficult to produce with conventional cutting tools
- extremely hard material to very close tolerances
- very small work pieces where conventional cutting tools may damage the part from excess cutting tool pressure.

But of course EDM include some of the disadvantages, too:

- the inability to machine non-conductive materials
- the slow rate of material removal
- the additional time and cost used for creating electrodes for ram/sinker EDM

It has also to be pointed out that diamond machining introduces less defects in the final material than EDM. The continuous melting and vaporization, occurring during

machining, create micro-cracks, due to thermal gradient, that lead to values of strength 50% lower than diamond machined components.

8.4 MAIN PROPERTIES

8.4.1 Thermal Properties

Typical values for the coefficient of thermal expansion (CTE) and thermal conductivity of some UHTC materials are given in Table 8.V.[5,19,23-25]

Tab. 8. V: Thermal expansion and conductivity of some UHTCs.

	Thermal Expansion	Temp. Range	Thermal Conductivity	Temp.
Material	10^{-6}/K	°C	W/m*K	°C
HfB_2	6.3	20–1027	105	20
	6.8	1027–2027	75	400
	7.6	20–2205	70	800
HfB_2-20v% SiC	–	–	79	100
	–	–	74	500
	–	–	62	1000
HfC	6.6	20–1500	20	20
	–	–	23	400
	–	–	30	800
HfN	~6.5	20–1000	18	20
	–	–	20	400
	–	–	22	800
ZrB_2	5.9	20–1027	–	–
	6.5	1027–2027	–	–
	8.3	20–2205	–	–
ZrB_2-20v% SiC	5–7.8	400–1600	98.7	100
	–	–	84.5	500
	–	–	78	1000
ZrC	6.7	20–1500	–	–
TiB_2	4.6	20–1027	–	–
	5.2	1027–2027	–	–
	8.6	20–2205	–	–
TiC	7.7	20–1500	–	–
TaB_2	8.2	20–1027	16.0	20
	8.4	1027–2027	16.1	1027
	8.4	20–1650	36.2	2027
TaC	6.3	20–1500	–	–
SiC	1.1	20	114	20
	5.0	1000	35.7	1000
	5.5	1500	26.3	1500

In general, the CTE's for these materials increase sufficiently with temperature such that temperature dependent coefficients should be used during design. To illustrate this, a comparison of CTE of pure HfB_2, pure SiC and HfB_2-SiC is shown in Fig. 8.7.[24,25]

As previously indicated, the thermal conductivities of borides are typically high, in comparison to many other ceramics and are a result of both a lattice and an electronic contribution to phonon transport.[7]

Fig. 8.7: Plot of CTE vs temperature for HfB_2, SiC and HfB_2-20v% SiC.

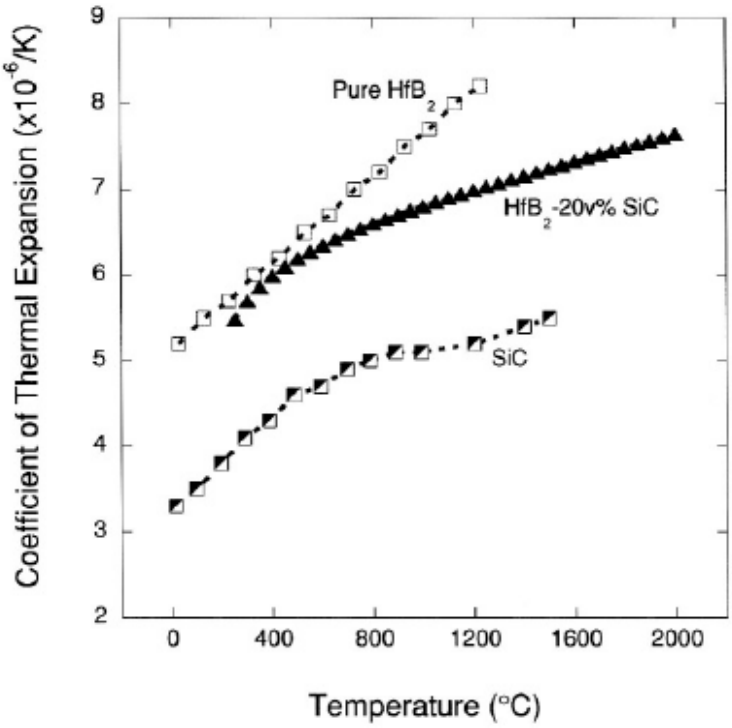

Fig. 8.8: Plot of conductivity vs temperature for several UHTCs.

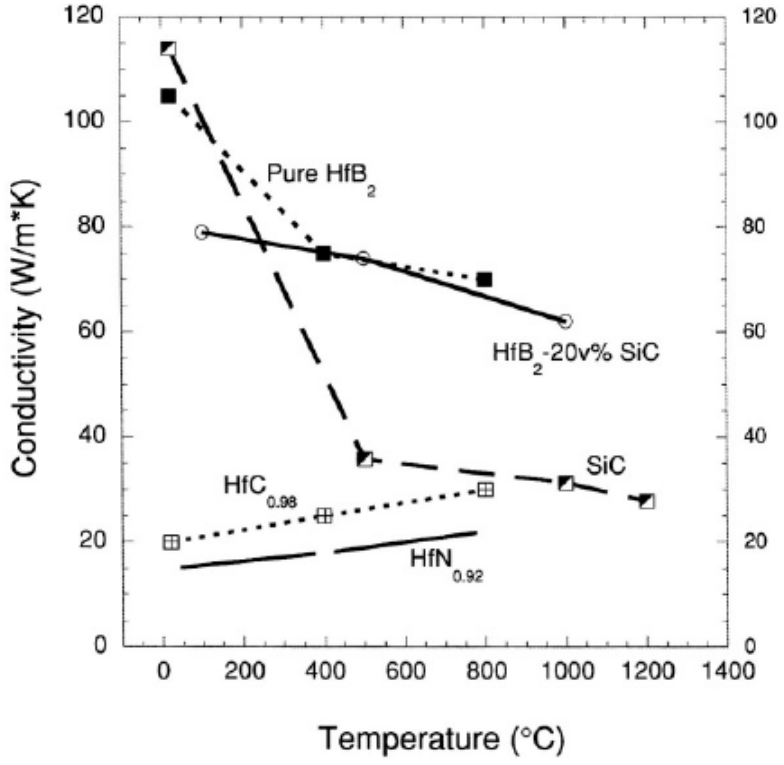

Figure 8.8 illustrates the large difference in conductivities of the borides from the nitride and carbide ceramics of hafnium.[5,24,25] Although the conductivities of the borides initially drop with increasing temperature, they eventually remain still above those for the nitrides and carbides. For a leading edge, high thermal conductivity reduces thermal stresses within the material, by reducing the magnitude of the thermal gradients within the part. High thermal conductivity also allows energy to be conducted away from the tip of the leading edge and reradiated out of surfaces of the component with lower heat fluxes, reducing the surface temperature for a given incident heat flux, compared to an insulating material.

The added benefits of high temperature materials with high conductivity can be seen when comparing a sharp UHTC leading edge to a relatively blunt, low conductivity leading edge such as the conventional reinforced Carbon-Carbon (RCC) thermal protection system, used on the shuttle. Because of the low conductivity of conventional leading edge thermal protection system (TPS) materials, the maximum surface temperature is determined by a balance of the incident heat flux with the energy that is re-radiated out of the leading edge, hence the need for materials with as high an emittance as possible.

Due to the low thermal conductivity of these materials, there is little or no conduction of energy away from the tip of the leading edge. Currently the leading edges of operational space vehicles are relatively blunt, due to limits in the temperature capability of the state of the art materials, which are typically based on SiC and limited to ~1600°C, before active oxidation becomes an issue. As the leading edge radius decreases the surface temperature increases. But the blunt leading edges significantly impact the vehicles performance, which affects overall vehicle safety, as mentioned earlier. Therefore, in order to achieve maximum performance, materials are needed that are both capable of withstanding the re-entry environment at temperatures greater than 2000°C, and have a high thermal conductivity that will direct more energy away from the tip of the leading edge allowing for even further improvements in vehicle performance, i.e. faster velocities at lower altitudes. Fig. 8.9 illustrates how the surface temperature for the sharp UHTC leading edges is determined by an energy balance of incident heat flux, re-radiated energy and energy pulled away from the leading edge tip and re-radiated out the sides of the component where the incident heat flux is lower. In this sharp leading edge design, three dimensional heat transfer plays an important role in understanding

and achieving the full potential of these materials. Thus the need for highly conducting, yet refractory materials is essential in the design of sharp vehicles.

Fig. 8.9: Comparison of the functionality of conduction for blunt and sharp leading edge designs of a hypersonic space vehicle.

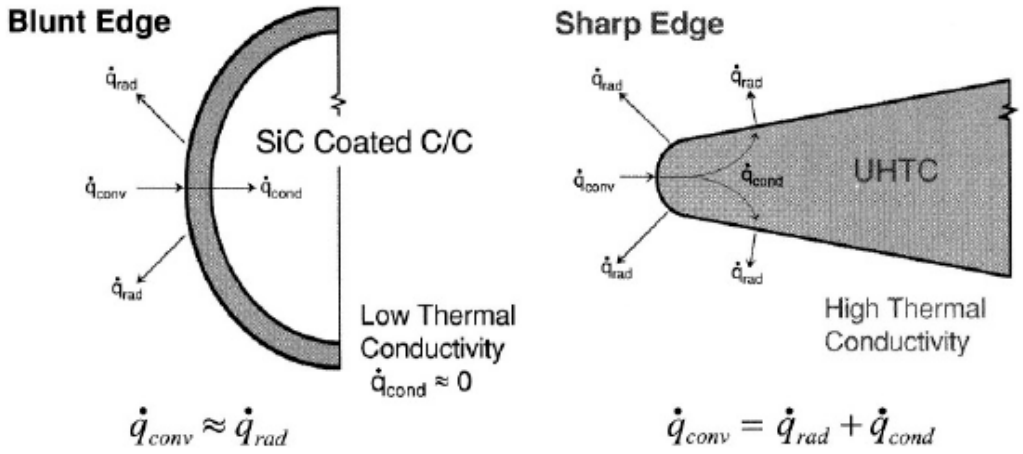

8.4.2 Mechanical Properties

The mechanical properties of a number of UHTC materials, including Hf and Zr borides and carbides with and without SiC additions, are given in Table 8.VI. In general, there is a limited amount of property data for carbides and diborides due to the limited number of studies that have been performed to date.

Generally, large spreads in the reported values found in the literature are common. This is particularly true in older reports which were mostly performed on sintered materials. More recently, testing has been switched to single crystals or polycrystalline materials obtained from the melt or by thin-film deposition. These are believed to yield more accurate and consistent information. Yet, any test must be carefully characterized in order to be meaningful. The following factors influence mechanical testing:[11]

- stoichiometry,
- impurities particularly oxygen, carbon and nitrogen,
- grain size and morphology,
- grain orientation,
- structural defects (vacancies, dislocations),
- presence of different phases.

Transition metal borides and carbides are often processed by sintering with a metal binder such as cobalt and nickel. The mechanical properties of such composites are often quite different from those of single crystal or polycrystalline materials.

Hardness is a complex property which involves elastic and plastic deformation, crack initiation, and the development of new surfaces. It can be defined in terms of bonding energy, covalence level, atomic spacing, and by the parameters of fracture and deformation characteristics.[14] Hardness is dependent on the fabrication process, composition, and the presence of impurities. Table 8.VI shows that all the compounds of Group IV metals are hard, the carbides being the hardest, followed by the borides and the nitrides. The carbides of the IV Group have higher hardness than those of Groups V and VI. This reflects the greater strength of M-C bonds found in these carbides.

Hardness values in these materials are typically relatively high, due to their high degree of covalent bonding. The wide scatter in the data is probably due to differences in processing of these materials resulting in different grain sizes and porosity.[3]

Hardness decreases rapidly with increasing temperature, exception is WC which maintains a high hardness until about 800°C.

Tab. 8.VI: Mechanical properties of selected UHTCs.

	Temp.	Young's Modulus	Flexural Strength		Hardness	
Material	°C	GPa	MPa	Poisson's Ratio	GPa	Ref.
HfB_2	23	530	480	0.12	21.2–28.4	33
	800	485	570	–	–	33
	1400	300	170	–	–	33
	1800	–	280	–	–	33
HfB_2-20v% SiC	23	540	420	–	–	33
	800	530	380	–	–	33
	1400	410	180	–	–	33
	1800	–	280	–	–	33
HfC	23	352	–	–	26.0	25
ZrB_2	23	500	380	0.11	25.3–28.0	20, 33
	800	480	430	–	–	33
	1400	360	150	–	–	33
	1800	–	200	–	–	33
ZrB_2-20v% SiC	23	540	400	–	–	33
	800	500	450	–	–	33
	1400	430	340	–	–	33
	1800	–	270	–	–	33
ZrC	23	348	–	–	27.0	25
TiB_2	23	551	300–370	0.11	25–33	20
TiC	23	451	–	–	30.0	25
TaB_2	23	257	–	–	19–25	20
TaC	23	285	–	–	18.2	25
SiC	23	415	359	0.16	32	32
	1000	392	397	0.157	8.9	32

Similarly, the moduli of HfB_2 and ZrB_2 are high due to the high degree of covalent bonding. Typical modulus values for both HfB_2 and ZrB_2 with and without SiC are around 500 GPa at room temperature. As shown in Fig. 8.10, the modulus of HfB_2

and ZrB_2 with and without SiC additions begins to fall off above 800°C.[14,19,25,26] For Hf and Zr carbides the moduli are lower, about 350 GPa.

Fig. 8.10 Plot of modulus vs temperature for HfB_2 and ZrB_2 with and without SiC additions.

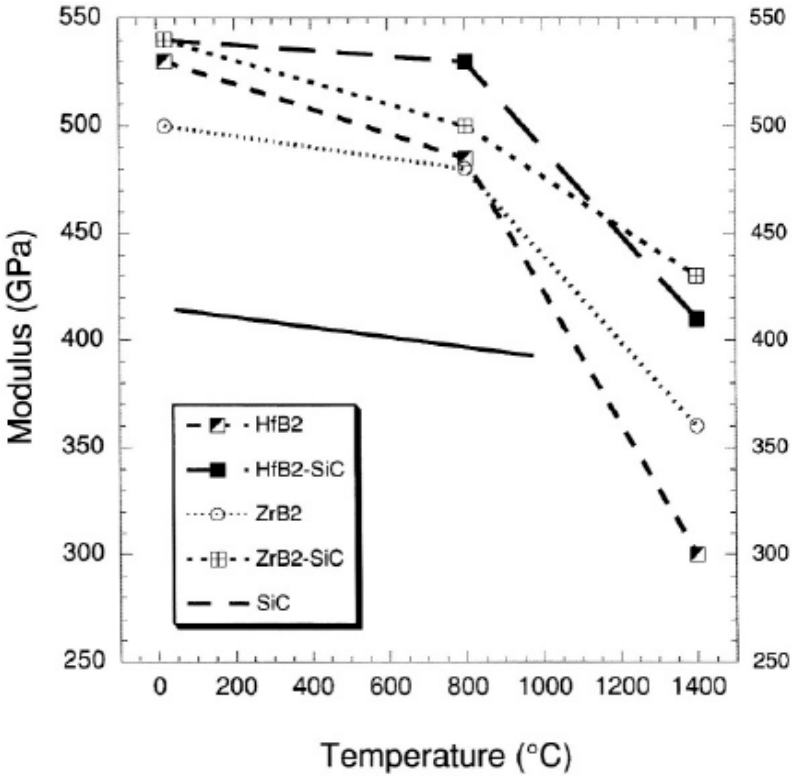

Interstitial borides and carbides are strong materials especially at high temperature. However, like most ceramics, they are intrinsically brittle. For example, metals have a fracture toughness that is generally some forty times greater than conventional ceramics. This brittleness of carbides is related on the atomic level to their strong hybrid ionic-covalent bonds which, as mentioned above, means a relatively weak metal-to-metal bond but a strong metal-to-carbon bond. These strong bonds prevent plastic deformation such as occurs in ductile metals. No plastic deformation means catastrophic brittle failure since applied stresses tend to concentrate at the sites of flaws, such as voids or chemical impurities at grain interfaces. It follows that, if ceramics could be made without such flaws, they would be far more resistant to cracking. In reality, the actual strength of ceramics is only a small fraction of the theoretical strength.

In the testing of tensile properties of brittle materials, it is difficult to obtain perfect grip alignment without bending stresses that tend to give premature fracture. For that reason, tensile testing is not truly representative of the strength of these materials as it is in metals. Transverse bending, particularly the 4-point bending test, is preferred.[16]

The flexural strength of HfB_2 and ZrB_2 can also vary a great deal, mainly due to differences in processing and resulting grain size and other processing defects. In

general, finer grain size results in higher strengths. Researchers at ManLabs noted that impurity phases could be a source of residual stress within materials, further limiting the useful strengths of HfB_2 and ZrB_2.[2] A plot of strength as a function of temperature is shown in Fig. 8.11. Unlike the modulus values at high temperature, strength increases slightly with increased temperature. However, after 800°C strength decreases along with modulus. As shown in the plot, ManLabs data indicate that there is another increase in strength above 1400°C; however these results have not been confirmed.

Due to the difficulties in producing dense carbide-based ceramics and protect by oxidation, analogous data for carbides produced in different ways and tested at different temperatures are lacking.

Fig. 8.11: Plot of strength vs temperature for HfB_2 and ZrB_2 with and without SiC additions.

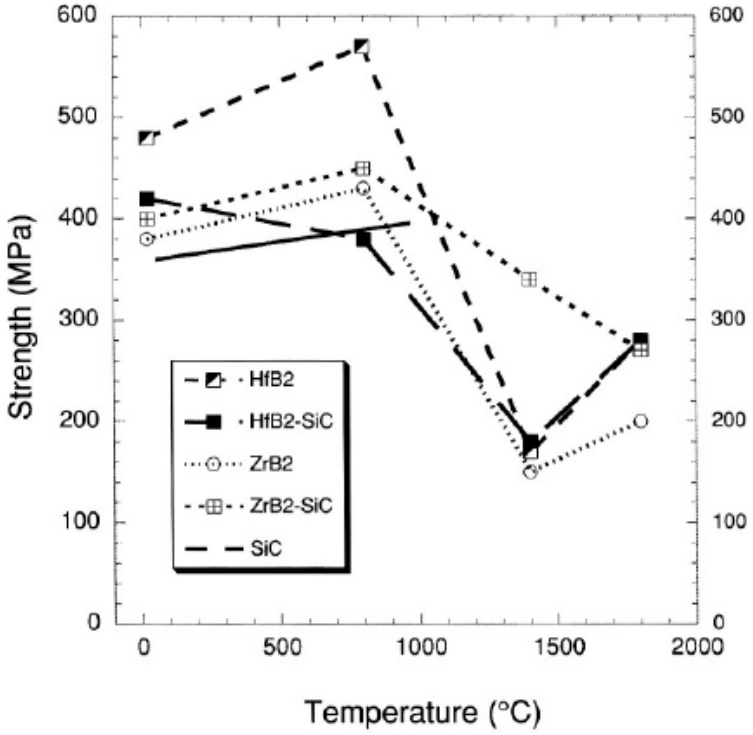

8.4.3 Electrical Properties

Typical electrical properties for some UHTC-type materials including HfB_2 and ZrB_2 are listed in Table 8.VII.[10,14,19,24] The table shows that the diborides have significantly lower resistivity than the associated carbides. As mentioned before, the low resistivity of the borides allows them to be machined using EDM. The ability to use this technique enables the production of complex shapes at reduced costs compared to traditional diamond machining.

Tab. 8. VII: Electrical properties of some UHTCs.

Material	Electrical Resistivity 10^{-6} Ω*cm	Temp. °C	Ref.
HfB_2	11	25	20
HfB_2-20v% SiC	9.6	20	31
	57.8	1000	31
HfB_2-30v% SiC	20.3	20	31
	82.5	1000	31
HfC	109	25	15
ZrB_2	12.1	20	31
	44.0	1000	31
ZrB_2-20v% SiC	10.2	20	31
	54.5	1000	31
ZrC	63	25	25
TiB_2	9	25	20
TiC	68	25	25
TaB_2	33	25	20
TaC	30	25	25

8.4.4 Optical Properties

The optical properties of Zr and Hf carbides and borides are relatively unexplored.[3] Emission coefficients at a wavelength of 0.65 μm (infrared) on unoxidized specimens are generally in the range between 0.5–0.8 at temperatures of 1600°C to 1800°C in vacuum. The emittance can vary drastically from pure material to oxidized material and typically changes with temperature.[24] On oxidized samples, the emittance values obtained for HfB_2-20vol% SiC and ZrB_2-20vol% SiC seem to depend strongly on temperature. Above 1900°C these materials exhibit an emittance near 0.60, characteristic of HfB_2 and ZrB_2.[27] For the oxidized samples below 1900°C the emittance is considerably higher than at the higher temperatures. This is probably the result of the formation of a and/or glass on the surface of the models that would be expected to have a higher emittance. At the higher temperatures, this protective glass layer may have evaporated leaving only HfO_2 or ZrO_2 that would have a lower emittance. In leading edge applications, for re-entry vehicles, a high emittance is desirable, as it would reradiate much of the energy from the surface eliminating some of the energy that otherwise the material/component would have to handle, complicating the design and limiting the conditions under which it could operate.

A summary of some properties of the materials treated in this dissertation is reported in Tab. 8. VIII.

Tab. 8.VIII: Summary of some properties of Hf and Zr borides and carbides composites.

Property	Unit	ZrC	HfC	ZrB_2	HfB_2
Structure		Cubic (NaCl)	Cubic (NaCl)	Hex. (AlB_2)	Hex. (AlB_2)
Lattice parameter	Nm	0.4698	0.4636	3.17, 3.53	3.139, 3.473
Composition		$ZrC_{0.55}$ to $ZrC_{0.99}$	$ZrC_{0.60}$ to $ZrC_{0.99}$	-	-
Molecular weight	g/mol	104.9	190.50	112.82	200.11
Color		Silver gray	Silver gray	Silver gray	Silver gray
X-ray density	g/cm^3	6.59	12.67	6.119	11.212
Melting point	°C	3420	3928	3245	3380
Debye T	K	491	436	910	690
C_p	J/mole·K	37.8	37.4	48.2	49.5
ΔH (at 25°C)	Kj/g-atom metal	-196	-209.6	-322.6	-358.1
Thermal conductivity	W/m·°C	20.5	20.0	60	104
Thermal expansion	10^{-6}/°C	6.7	6.6	5.9	6.3
Electrical resistivity	μΩ·cm	45-78	37-45	15	9
Supercond. Trans.T	K	<1.2	<1.2	-	-
Hall constant	10^{-4} cm·A·s	-9.42	-12.4	-	-
Magn. suscept.	10^{-6} emu/mol	-23	-23	-	-
Vickers hardness	GPa	25.5	26.1	23	28
Young's modulus	GPa	350-440	350-510	489	480
Shear modulus	GPa	172	193	220	228
Bulk modulus	GPa	207	241	215	212
Poisson's ratio		0.191	0.18	0.109	0.12
Fracture tough.	$MPa \cdot m^{1/2}$	3	3.5-3.8	2.3-5.3	3.8-4.15
RT flexural str.	MPa	400	470	900	800
1200 flexural str.	MPa	350	400	600	670
Ox. resistance	°C	800 in air	500 in air		

8.5 HIGH TEMPERATURE TESTING

It is well known that borides of the fourth group possess better oxidation resistance than carbides, thanks to the formation of a protective layer based on B_2O_3. On the contrary, when carbides come in contact with oxygen at high temperature, the formation of CO and porous MO_2 (where M= Hf or Zr) provokes the loss of strength of the materials.

Furnace oxidation studies showed HfB_2 and ZrB_2 to be more oxidation resistant than other diboride materials.[1] Based on these results, ManLabs chose HfB_2 and ZrB_2 from the list of borides, as the best candidates for continued research into high temperature applications. A comparison of oxidation rates of HfB_2 and ZrB_2 with other high temperature ceramics is shown in Fig. 8.12.[6,27-31] At lower temperatures it is apparent that materials such as SiC and Si_3N_4 have lower oxidation rates than either HfB_2, ZrB_2 or their mixture with SiC. But these Si based materials are only applicable in temperature ranges less than ~1700°C. At higher temperatures the materials are either

unstable and dissociate, and/or reach a temperature regime where active oxidation predominates. During active oxidation the protective layer is disrupted by evolution of SiO, exposing the surface below to continued oxidation. Thus, at these ultra high temperatures, materials that are primarily Si-based are currently no longer suitable.

Based on their favourable oxidation resistance, the diborides are one family of materials that make well thinking of some promise for use in ultra high temperature applications. As shown in Fig. 8.12 HfB_2 has a lower oxidation rate than ZrB_2 and that the HfB_2/SiC mixture has improved oxidation resistance compared to pure HfB_2.

Fig. 8.12: Comparison of oxidation rates of several engineering ceramics.

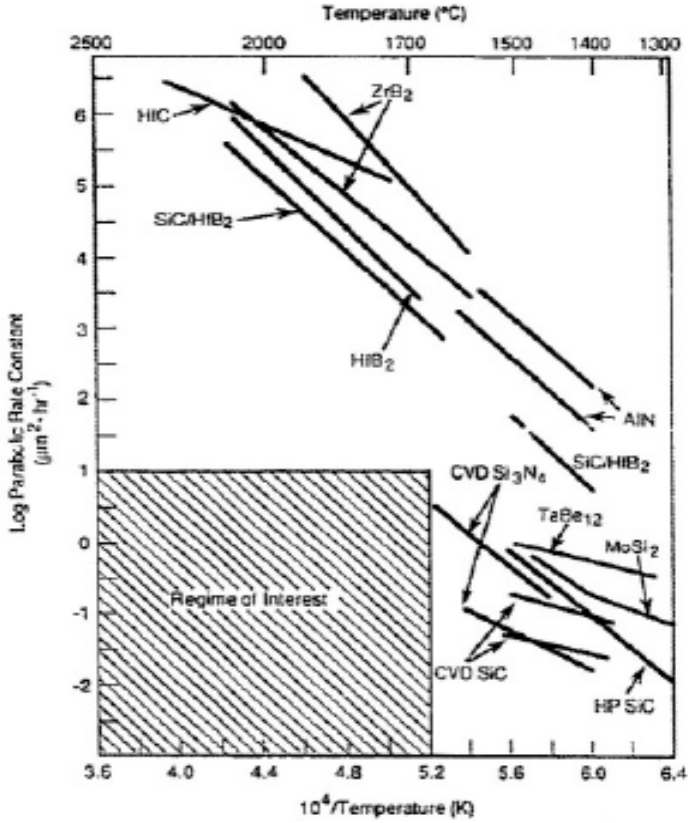

Fig. 8.12 also shows that HfB_2 and HfB_2/SiC have lower oxidation rates than pure HfC. Oxidation studies also showed that metal rich compositions of HfB_2 or ZrB_2 (i.e. $HfB_{1.9}$) were more oxidation resistant and possessed higher thermal stability than boron rich compositions ($HfB_{2.1}$) of the same diboride.[1] To determine the effect of SiC content on diborides oxidation, ManLabs conducted a series of furnace oxidation experiments at 1800°, 1950° and 2100°C on HfB_2 specimens with 10 vol% SiC and ZrB_2 specimens with 50 vol% SiC.[5,10,27,32] Samples were heated in argon to the respective test temperature at which time the dry air was introduced for periods of 30–60 minutes, then argon was reintroduced for cool down. They found that 5 vol% SiC additions provided little improvement in oxidation resistance while samples containing 50 vol% SiC

showed improvements after one hour at 1800°C and 1950°C but were completely oxidized after one hour at 2100°C. They concluded that additions of 35 vol% SiC to both ZrB_2 and HfB_2 provided the best protection for temperatures up to 2100°C during a furnace test, but that reasonable oxidation protection can be achieved with SiC contents as low as 15 vol% for ZrB_2 and 10 vol% for HfB_2 .[2,27] A comparison of the oxidation scale thickness as a function of temperature for pure HfB_2, SiC and HfB_2-SiC is shown in Figure 8.13. This figure clearly shows that at temperatures >2100 K the oxide scale thickness on pure HfB_2 is thinner than that on pure SiC, whose scale thickness is rapidly increasing with temperature above 2050 K. But at all temperatures >2050 K, the HfB_2-SiC materials have the thinnest oxide layers.

Fig. 8.13: Summary comparison of a 1-hour oxidation study of SiC and SiC.

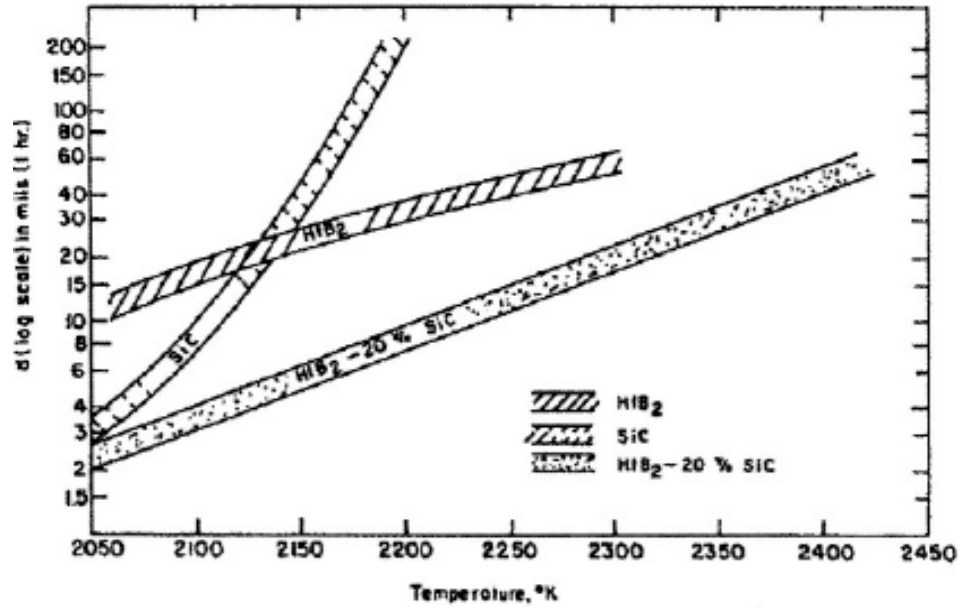

The response of the refractory UHTC materials to high temperature oxidizing conditions imposed by furnace heating has been observed to differ markedly from the behaviour observed in arc plasma facilities that provide a simulated re-entry environment.[27] Furnace evaluations are normally performed for long times at fixed temperature and slow gas flow with well defined solid/gas-reactant/product chemistry. Arc jet tests, on the other hand, are carried out under high velocity gas flow conditions in which energy flux, rather than temperature, is defined. Furthermore, furnace studies employ air at 1 atmosphere and O_2 as diatomic species. But during a typical re-entry profile for a manned space vehicle, the pressures will generally be much less than 1 atmosphere and a significant portion of the gas molecules will be dissociated into highly reactive monatomic species as they cross the bow shock formed during re-entry. The

resulting monatomic species may recombine at the surface giving up some of their energy to the material and, depending on the catalycity of the substrate, this recombination can add a significant fraction to the overall heating of the articles' surface. Arc jet testing provides the best ground based simulation of the re-entry environment, although there are a number of differences between the arc jet environment and the actual re-entry environment that must be accounted for when designing an arc jet experiment and when interpreting the data. For example, catalycity can play a more significant role during arc jet testing than in flight because a higher proportion of the air molecules are dissociated in the arc jet than in flight. Because of the differences between static or flowing air oxidation experiments and experiments in the arc jet, correlation of material responses from the two test situations is difficult -if not impossible- in many cases. For example, if material A performs better in the furnace test than material B it does not necessarily hold that the same trend will occur in the arc jet.[33]

8.6 APPLICATIONS

The need for high temperature materials that can operate with no or limited oxidation or ablation at temperatures greater than 3000K has driven the development of UHTC materials. The potential applications for UHTCs span a wide number of needs arising from future military, industrial and space based projects. Potential industrial applications for UHTCs include use in foundry or refractory processing of materials. Their chemical inertness makes them ideal for molten metal crucibles, thermowell tubes for steel refining and as parts for electrical devices such as heaters and igniters.[34]

The military and aerospace applications for UHTCs range from rocket nozzle inserts and air augmented propulsion system components to leading edges and nose caps for future hypersonic re-entry vehicles.[34,35] Early space vehicle designs, such as the space shuttle, were designed with a large radius, blunt body design to reduce aerothermodynamic heating to maintain moderate temperature limits on all parts of the vehicle. However, the larger the leading edge radii, the higher the vehicles drag, which reduces manoeuvrability and cross range during re-entry. Therefore, to improve performance, hypervelocity vehicle concepts have been proposed using slender aerodynamic shapes with sharp leading edges.[36,37] Development of sharp body vehicles increases the lift-to-drag ratio thereby improving the vehicles' re-entry cross range. A

higher lift to drag ratio also has the potential to improve the overall vehicle system safety in a number of ways. Design of a high L/D vehicle would increase the window during ascent in which a launch could be aborted and the vehicle safely recovered on land, reducing the need for crew to bail out and reducing the possibility of having to ditch the vehicle in the ocean. Secondly, as mentioned previously, the high L/D increases the vehicles cross range during descent from orbit. This provides the vehicle more opportunities to initiate descent while on orbit, and safely land the vehicle at a desirable location.

However, the temperature of the leading edge is inversely proportional to the square root of the leading edge radius, i.e. as the leading edge radius decreases the temperature increases.[37] Therefore the successful design of a sharp hypersonic vehicle requires the development of new materials with higher temperature capabilities than the current state-of-the-art materials can provide. Ultra High Temperature Ceramics are a family of materials that are promising candidates for meeting such requirements.[36,37]

Concerning carbides, hafnium carbide is, with tantalum carbide, the most refractory compound available. In spite of its excellent properties, it has only limited industrial importance, possibly because of its high cost (see Ch. 16). Some experimental applications are as follows:

- Oxidation resistant coatings for C-C composites (co-deposited with SiC)
- Production of whiskers (with nickel catalyst)
- Coating for superalloys
- Coating on cemented carbide

Then, zirconium carbide is a highly refractory compound with excellent properties but, unlike titanium carbide, it has found only limited industrial importance except as coating for nuclear-fission power plants.[5] ZrC coatings replaced SiC coatings, as the least loose their mechanical integrity at temperatures >1700°C and are chemically attacked by the fission product palladium. In contrast, ZrC coating layers have much higher temperature stability and are more resistant to Pd chemical attack.

Besides, the high hardness of the carbides, opens the possibility of production of cutting tools. Kyocera Inc. currently manifactures hot-pressed ZrC knives with sharp edges that are extremely hard, wear resistant and chemically inert.[38]

This relatively few applications for borides and carbides of Zr and Hf may be due to the high price and difficulty in obtaining them dense and free of impurities.

8.7 RECENT WORKS

Research on UHTCs slowed considerably after the works in the 1970's, until the early 1990's, when interest in the monolithic UHTC materials was renewed. The high costs of raw materials in addition to the high temperatures and pressures required to hot press UHTC powders has led many new investigations into alternate starting materials and methods of fabricating UHTCs. In addition to conventional methods, reactive hot pressing and pressureless sintering by liquid infiltration and reaction are in course of study.[28,39,40] These new reaction-based processes share the near-net shape and near-net dimension capabilities of gas-phase reaction bonding as well as reduced processing temperatures and times required for solid state sintering.

Basic property evaluation of UHTCs and UHTC composites has resumed at a number of government facilities within NASA and the military, as well as at some universities.[41-43] With this resurgence in basic research, investigations into UHTC borides, carbides and nitrides are seeing added attention as new processing techniques make the fabrication of these materials easier.

NASA Ames began working on UHTCs in the early 1990s, and in 1997 and 2000 conducted two flight experiments, SHARP-B1 and SHARP-B2 (Sharp Hypersonic Aerothermodynamic Research Probes) in collaboration with the Air Force and Sandia National Labs. These experiments briefly exposed the UHTC materials to the actual re-entry environment.[36] The nose tip was surrounded by a skirt and was instrumented with internal sensors that measured internal temperatures of 1690°C, which according to models, corresponds to an external temperature above 2760°C. The flight experiment was a success, and the materials were recovered, but due to insufficient time for materials development the materials had poor mechanical properties and a number of strake segments failed. NASA is continuing to pursue these materials and has made progress in improving the processing methodologies and resulting material properties.[44]

Aside from the work performed at NASA Ames, recent work by Levine et al., at NASA Glenn, has been conducted to improve the oxidation resistance of monolithic materials and to develop fibre reinforced UHTC materials to improve composite fracture toughness and impart a level of graceful failure in materials.[36,37,39,44] Methods to improve the environmental durability and oxidation resistance of UHTCs are also being addressed by the Navy. Work by Opeka et al., at the Naval Surface Warfare Center, and others[5,45,46] are seeking to provide an understanding of the oxidation of not only HfB_2

and ZrB_2, but of other UHTC materials, such as HfC, ZrC and HfN. Thus far, their work indicates that the oxidation resistance of HfC and HfN is improved with decreasing C and N contents, that is when the materials are substoichimetric. Studies indicate that the oxidation of HfC occurs with the formation of a compact protective interlayer of Hf-C-O.[46] In a study of the oxidation of ZrC-ZrB_2-SiC composites, Opeka et al.[5] found that ZrB_2 rich composites had the highest oxidation resistance. The oxidation of ZrC, results in the formation of a fine grained oxide that allows diffusion of O_2 to the ZrC surface, providing no oxidation protection to the composite.

Many progresses have been done with regard to understanding the behaviour of diborides and carbides- based ceramics in static oxidation as well as arc heater testing, which more accurately reproduces environments encountered during hypersonic flight and atmospheric re-entry. Although significant gains have been made, several critical areas have been identified for future research. In particular, research is needed to understand densification and oxidation mechanisms besides fundamental structure-properties relations at elevated temperatures, if these materials are to be used in hypersonic, atmospheric re-entry, or rocket propulsion applications.

On the other hand, another critical aspect of this class of materials is the low fracture toughness. Values of 3-4 $MPam^{1/2}$ are not acceptable for a wide range of applications. Considering that, most of the composites are nowadays sintered by hot pressing or spark plasma sintering, where only simple shapes can be obtained, a subsequent machining by diamond tools or electro discharge is compulsory. Hence, in view of the production of large-sized components, a high fracture toughness is a crucial issue. To this aim, a new trend of reinforced UHTCs is arising with additions of secondary toughening phases like whiskers, chopped fibres, carbonanotubes or ZrO_2 particles.

Finally, in view of application in flying missions, another crucial point is the weight; especially in the case of Hf and Ta compounds the density range is around 11-13 g/cm^3. New emerging ideas deal with the production of light structures made with UHTCs either using gradient porous multilayers or by porous foams performs soaked with opportune slurries.

References

1 L. Kaufman, E. V. Clougherty, RTD-TRD-N63-4096, Part III, ManLabs Inc., Cambridge, MA, (1966).

2 E. V. Clougherty, D. Kalish, E. T. Peters, AFML-TR-68-190, ManLabs Inc., Cambridge, MA, (1968).

3 Gangler, J. J. High Temp. High Press. **3** (1971) 487–502.

4 E. V. Clougherty, R. J. Hill, W. Rhodes, E. T. Peters, AFML-TR-68-190, Part II Vol. II, ManLabs Inc., Cambridge, MA, (1970).

5 M. M. Opeka, I. G.Talmy, E. J.Wuchina, J. A. Zaykoski, S. J.Causey, J. Europ. Ceram. Soc.**19** (1999) 2405–2414.

6 E. L.Courtright, H. C.Graham, A. P. Katz, and R. J. Kerans, AFWAL-TR-91-4061, Wright Patterson Air Force Base, Ohio (1992).

7 Cutler, R. A. ASTM Engineered Materials Handbook, Vol. 4 – Ceramics and Glasses, Schneider, S. J., technical chairman, (1991) 787–803.

8 A. F. Guillermet, G.Grimvall, Am. Inst. Phy. Conf. Proc. **231** (1991) 423–431.

9 S. Hampshire, ASTM Engineered Materials Handbook, Vol. 4 –Ceramics and Glasses, Schneider, S. J., technical chairman, (1991) 812–820.

10 P. T. B. Shaffer, ASTM Engineered Materials Handbook, Vol. 4 –Ceramics and Glasses, Schneider, S. J., technical chairman, (1991) 804–811.

11 Battelle Columbus Laboratories. "Engineering Property Data on Selected Ceramics" Vol. 2: Carbides. Metals and Ceramics Information Center, Battelle Columbus Laboratories, Report MCIC-HB-07-Vol. 2 (1979).

12 K. E. Spear, J. Less-Common Metals, **47** (1976) 195–201.

13 J. K.Burdett, E. Canadell, G. J. Miller, J. Am. Chem. Soc., **108** (1986) 6561–6568.

14 G. V. Samsonov, I. M. Vinitskii, Handbook of Refractory Compounds, Plenum Press (1980).

15 A. E. McHale, "Phase Equilibrium Diagrams – Phase Diagrams for Ceramists", National Institute of Standards and Technology, Volume X, The American Ceramic Society, (1994) 131-145.

16 R. Jenkins, Joint Committee on Powder Diffraction Standards. Powder Diffraction File: from the International Center for Diffraction Data. Swarthmore, PA (1988).

17 Schwetz, K. A., Reinmoth, K. and Lipp, A. Production and Industrial Uses of Refractory Borides, Vol. 3, Radex Rundschau, (1981) 568–585.

18 McColm, I. C. Ceramic Science for Materials Technologists, Leonard Hill, London (1983) 330–343.

19 H. E. Exner, Int. Metall. Rev. **24** (1979) 149–173.

20 L. B. Pankratz, J. M. Stuve, N. A. Gokcen, Buelletin 677, U.S. Bureau of Mines (1984) 98–102.

21 D. Kalish, E. V. Clougherty, Contract No. 426200, Summary Report (1966).

22 E. V.Clougherty, R. L. Pober, L. Kaufman, Trans. TMS-AIME, **242** (1968) 1077–1082.

23 G. V. Samsonov, T. I. Serebryakova, Sov. Powder Metall. Met. Ceram. (English Translation) **17** (1978) 116–120.

24 E. V.Clougherty, K. E. Wilkes, R. P. Tye, AFML-TR-68-190, ManLabs Inc., Cambridge, MA, (1969).

25 R. G.Munro, J. Physical and Chemical Reference Data **26** (1997) 1195–1203.

26 W. H. Rhodes, E. V. Clougherty, D. Kalish, AFML-TR-68-190, ManLabs Inc., Cambridge, MA, (1970).

27 R. Perkins, L.Kaufman, H. Nesor, AFML-TR-68-84, ManLabs Inc., Cambridge, MA, (1969).

28 L.Kaufman, E. V. Clougherty, J. B. Berkowitz-Mattuck, Trans. TMS-AIME, 239 (1967) 458–466.

29 J. B. Berkowitz-Mattuck, J. Electrochem. Soc., 113 (1966) 908–914.

30 G. H. Schiroky, R. J. Price, J. E.Sheehan, GA-A18696, General Atomics, La Jolla, CA (1986).

31 V. A. Lavrenko, A. F. Alexeev, Ceramic International 9 (1983) 80.

32 K. Upadhya, J. M. Yang, W.P. Hoffmann, Am. Ceram. Soc. Bull. **58** (1997) 51–56.

33 L. Kaufman, H.Nesor, AFML-TR-69-84, ManLabs Inc., Cambridge, MA, (1969).

34 C. Mroz, Am. Ceram. Soc. Bull. **74** (1995) 165–166.

35 I. M. Low, R. McPherson, J. Mat. Sci. Lett. **8** (1989) 1281–1283.

36 P. Kolodziej, J.Salute, D. L. Keese, NASA TM-112215 (1997).

37 D. A. Kontinos, K. Gee, D. K. Prabhu, AIAA 2001–2886 (2001).

38 ww.kyoceraadvancedceramics.com

39 S. K. Woo, C. H. Kim, E. S. Kang, J. Mat. Sci. 2 (1994) 5309–5315.

40 G. Zhang, Z.Deng, N. Kondo, J. Yang, T. Ohji, J. Am. Ceram. Soc. 83 (2002) 2330–2332.

41 S.Levine, E. Opila, M. Halbig, J. Kiser, M. Singh, J. Salem, J. Europ. Ceram. Soc. 22 (2002) 2757–2767.

42 F. Monteverde, A. Bellosi, Scripta Materialia, 46 (2002) 223–228.

43 F. Monteverde, A. Bellosi, S. Guicciardi, J. Europ. Ceram. Soc. 22 (2002) 279–288.

44 M. Gasch, D.Ellerby, E. Irby, S. Beckman, M. Gusman, S. Johnson, J. of Materials Science 22 (2003) 245-249.

45 S. Shimada, Solid State Ionics 149 (2002) 319–326.

46 C. B. Bargeron, R. C. Benson, R. W. Newman, A. N. Jette, T. E. Phillips, Johns Hopkins APL Technical Digest 14 (1993) 29–35.

CHAPTER 9

UHTCs PRODUCTIONS AND CHARACTERIZATION

9.1 MIXTURES COMPOSITION

In the present dissertation, ultra high temperature ceramics, namely ZrC, HfC, ZrB_2 and HfB_2, with $MoSi_2$ varying from 10 to 20 vol% were studied.

The materials were produced starting from the following commercial powders (wt%), whose morphology is reported in Fig. 9.1 (for $MoSi_2$ powder, see Chapter 5):

Fig. 9.1: SEM images showing the commercial powder utilized for the production of the UHTCs: ZrC, HfC, ZrB_2 and HfB_2.

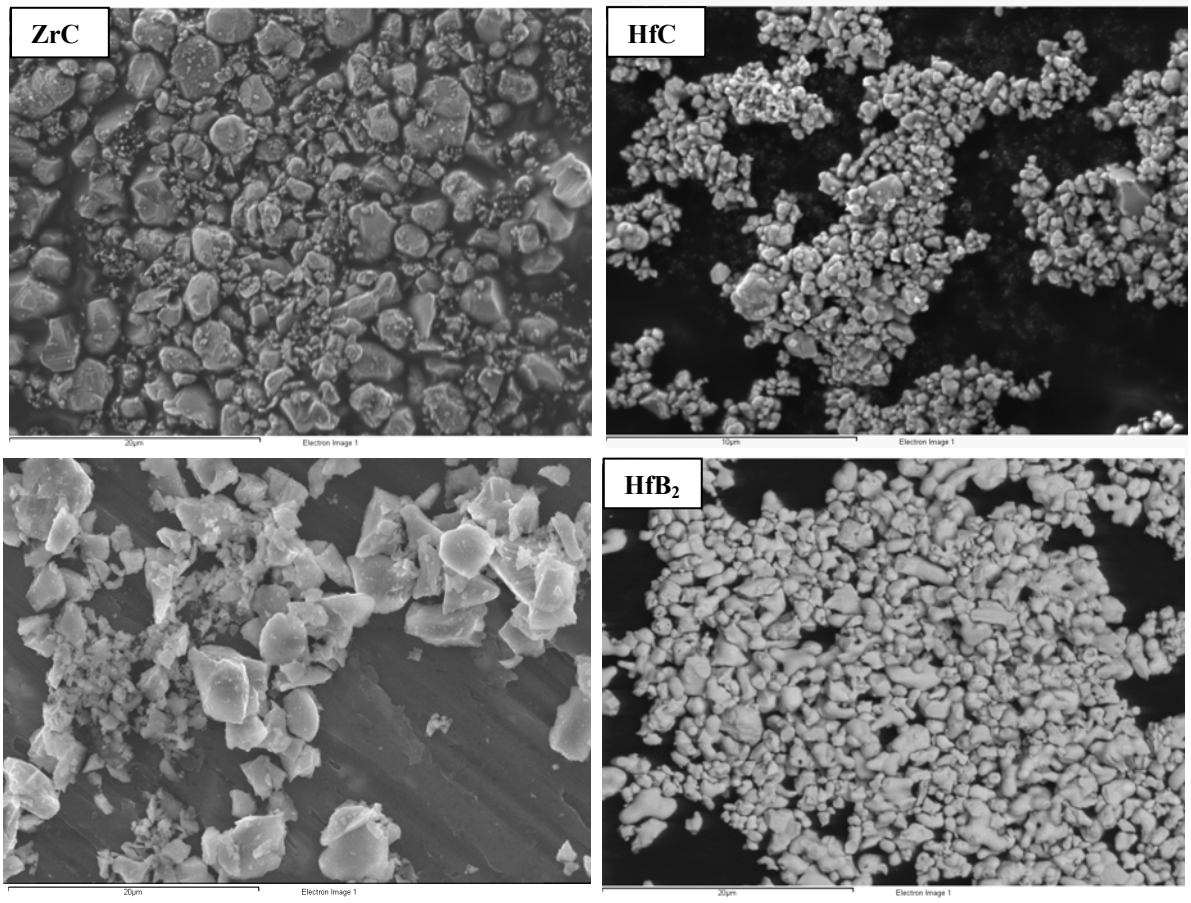

- Cubic **ZrC** (H. C. Starck, Germany): Grade B, mean particle size: 3.5 μm; particle size range 0.8-8 μm; specific surface area 3 m^2/g; impurities C 1.5, O 0.6, N 0.8, Fe 0.05, Hf 2.
- Cubic **HfC** (Cerac Incorporated, Milwaukee, USA): mean particle size 1.41 μm; particle size range 0.7-3 μm; impurities: U 0.0002, Zr<0.6.
- Hexagonal **ZrB_2** (H. C. Starck, Germany): Grade C, mean particle size 1.5 μm; particle size range 0.1-2 μm; specific surface area 1 m^2/g; impurities (max): C 0.25, O 2, N 0.25, Fe 0.1, Hf 0.2.
- Hexagonal **HfB_2** (Cerac Incorporated, Milwaukee, USA): mean particle size 2.19 μm; particle size range 0.1-6 μm; specific surface area 1.38 m^2/g; impurities: Al=0.001, Fe=0.002, Zr<0.5.
- Tetragonal **$MoSi_2$** (Aldrich, Germany): mean particle size 1 μm; particle size range 0.1-2 μm; specific surface area 1.60 m^2/g; impurities: O 1.

9.2 POWDER PROCESSING

The powder mixtures were ultrasonically treated and then ball milled for 24 h in absolute ethanol using ZrO_2 milling media; the powders were subsequently dried in a rotary evaporator and in a oven at 70°C for 24 hours and finally sieved through a 40 μm screen size.

For the sintering tests, 1 cm diameter pellets were prepared by uniaxial pressing followed by cold isostatic pressing under 350 MPa. Once identified the right sintering cycle for each composition, bigger pellets of 4 cm diameter and 1 cm height were prepared in the same conditions.

9.3 SINTERING

The pellets were pressureless sintered in a resistance-heated graphite furnace under a flowing argon atmosphere (~1 atm), to prevent the oxidation of the powders, with heating rate of 600°C/h at different temperatures ranging from 1800 to 1970 °C and holding times varying from 30 to 90 minutes. After the dwelling time free cooling was set.

9.4 CHARACTERIZATION

The final density was measured by Archimedes' method on an hydrostatic balance. The theoretical densities are calculate by the rule of mixtures following the equation (1):

$$\rho_{th} = (\Sigma_i \rho_i V_i)/V_{tot} \quad (1)$$

where ρ_i and V_i are density and volumetric fraction of the i-component respectively.

Crystalline phases were identified by X-ray diffraction (Siemens D500, Germany) using the CuK_α radiation, with 0.04 2θ-step size and 1 second scan step time.

The microstructures were analyzed using scanning electron microscopy (SEM, Cambridge S360) and energy dispersive spectroscopy (EDS, INCA Energy 300, Oxford Instruments, UK) on polished surfaces subsequently etched with colloidal silica. For this purpose, the specimens were polished with diamond paste down to 0.25 μm.

TEM samples were prepared by cutting 3 mm discs from the sintered pellets. These were mechanically ground down to about 20 μm and then further ion beam thinned until small perforation were observed by optical microscope. Carbon coating to minimize the electric charging under the irradiated electron beam was not necessary, because all the samples were electroconductive. The detailed phase analysis was performed using a transmission electron microscopy (TEM) equipped with an energy-dispersive detector system (FEI, CM120 and CM200 STEAM/EDAX, Eindhoven, The Netherlands). For the borides, EELS analyses were performed too.

Microstructural parameters, like amount of residual porosity or secondary phases, were determined through image analysis on the micrographs of polished surfaces by a commercial software.[1]

Thermodynamical calculations were performed using a commercial software[2] to study the reaction occurring during sintering at high temperature and to rebuild the mechanisms involved in the densification and the development of the microstructure.

Vickers microhardness (HV1.0) was measured on polished surfaces with a load of 9.81 N, using a Zwick 3212 tester.

Young's modulus (E) was measured either by the resonance frequency method on 28 × 8 × 0.8 mm specimens using a Hewlett Packard gain-phase analyzer, or it was evaluated from the slope of the load-displacement curves once subtracted the loading

train compliance. Measures of the same samples by the two techniques were observed to differ less than 5%.

Fracture toughness (K_{Ic}) was evaluated using the chevron-notched beam (CNB) in flexure. The test bars, 25 x 2 x 2.5 mm (length x width x thickness, respectively), were notched with a 0.08 mm diamond saw; the chevron-notch tip depth and average side length were about 0.12 and 0.80 of the bar thickness, respectively. The flexural tests were performed on a semi-articulated silicon carbide four-point jig with a lower span of 20 mm and an upper span of 10 mm on a universal screw-type testing machine (Instron mod. 6025). The specimens were deformed with a crosshead speed of 0.05 mm/min. The slice model equation of Munz et al.[3] was used to calculate K_{Ic}.

On the same machine and with the same flexural jig, the flexural strength (σ), up to 1500°C in air or Ar, was measured on chamfered bars 25 × 2.5 × 2 mm (length × width × thickness, respectively), using a crosshead speed of 0.5 mm/min. For the high-temperature tests, a soaking time of 18 min was set to reach thermal equilibrium. Five specimens were used for each temperature point. To identify the fracture origins, fractographic analysis were carried out on the surfaces of the broken bars.

Depth-sensing indentation (DSI) tests were carried out on a commercial nanoindenter (Nano Indenter XP^{TM}, MTS Systems Corporation, Oak Ridge, TN, USA) using a Berkovich diamond tip. Six peak loads were used to investigate the indentation hardness as a function of penetration depth: 1, 5, 10, 50, 100, and 200 mN. The indenter was continuously loaded up to the peak load and immediately unloaded with no holding time. For each peak load, at least twenty indentations were made. DSI hardness (H) was calculated by the data acquisition software of the nanoindenter (TestWorks^{TM} ver. 4.06A), based on the model of Oliver and Pharr.[4] The area function of the indenter tip was calibrated on a standard silica specimen for a contact depth range corresponding to that measured on the ceramic samples.

For arc-jet testing, samples with a hemispheric shape (see Fig. 9.2a) were machined through diamond tools and then exposed to sustained enthalpy flows using the arc-jet facility equipped with a 80 kW plasma torch that operates in inert gas (He, N_2, Ar and their mixtures) at mass flow rates up to 5 g/s. The specimens were located at a distance of 6 cm from the exit torch. (Fig. 9.2 b,c) The models were tested with an initial average specific total enthalpy of about 20-22 MJ/kg, that was gradually increased tuning the arc current up to 24-26 MJ/kg and then maintained for 30-240 s.

After the arc jet tests, the ceramic models were further analysed by SEM-EDS on surface and cross section.

Fig. 9.2: a) Hemispheric HfB_2 model used for arc-jet testing, curvature radius R=7.5 mm; b) Experimental setup before the test and (b) during the test.

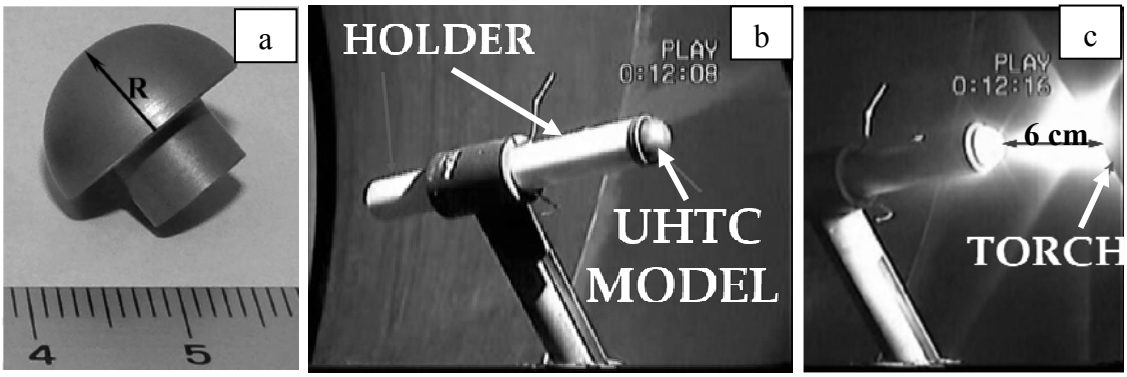

During the experiments, infrared and optical windows in the test chamber allowed visual inspection and diagnostic analyses. An automatic control system monitored the main parameters of the apparatus (voltage and current of the arc heater, water cooling temperature, mass flow rate). In particular, the specific total enthalpy (H) was evaluated through an energy balance between the energy supplied to the gas by the arc heater and the energy transferred to the cooling system (measured by the water temperature jump between inlet and outlet). The output data, processed via a dedicated software, allowed the evaluation of the surface temperature profile versus exposure time of the mode. Due to the extremely high thermal loading upon the ceramic models, surface chemical reactions like oxidation can be responsible for changes in the material's emissivity. To overcome this problem, the experiments' measurements were carried out with a radiation ratio pyrometer (Infratherm ISQ5, Impac Electronic Gmbh, Germany) which operates both in two colour and in the single colour function. In the two colour mode the instrument makes use of the ratio of two spectral radiances, measured at different wavelengths (0.9–1.05 μm), to evaluate the true temperature. This bypasses the problem of the emissivity knowledge since it is supposed to be the same at both wavelengths. Once the temperature was measured with the ratio pyrometer, its value was input to evaluate the spectral emissivity using the single colour function (λ= 0.9 μm). In combination with the pyrometer, an infrared thermo-camera (Thermacam SC 3000, FLIR Systems, USA) was used to measure the surface temperature distributions and the spectral emissivity in the long wave range of the thermograph (λ=9 μm).

References

1 Image Pro-plus 4.0, Media Cybernetics, Silver Springs, USA.
2 HSC Chemistry 5.1, Outukumpu Research Oy, Finland.
2 3 D.G. Munz, J. L. Shannon Jr., R.T. Bubsey, Int. J. Fracture 16 (1980) R137.
4 W.C. Oliver, G.M. Pharr, J. Mater. Res. 7 (1992) 1564.

CHAPTER 10

MICROSTRUCTURE AND DENSIFICATION MECHANISMS

In this work of thesis, $MoSi_2$ was selected as ceramic additive for Hf- and Zr- borides and carbides, since it was proved to be effective for the densification of ZrB_2 and HfB_2 when using pressure-assisted techniques. It will be shown that $MoSi_2$ is also helpful for the sintering of such ceramics by pressureless sintering.

Thus, in this chapter, the microstructure of pressureless sintered ZrC, HfC, ZrB_2, HfB_2 materials containing 5 to 20 vol% of $MoSi_2$ is presented and analyzed.

On the other side, transmission electron microscopy (TEM) is a powerful tool to explore microstructures on a small length scale to disclose the effective densification mechanisms. A thorough literature analysis revealed that neither detailed TEM work nor reports on densification mechanisms are available for this class of materials, which however are essential to optimize the sintering aids utilized and the processing parameters applied. Hence, the microstructure development of the compositions containing 20 vol% of $MoSi_2$ composites is carefully analyzed in order to gain a insight into the densification mechanisms during pressureless sintering.

10.1 $MoSi_2$ ADDITION TO UHTCs

Preliminary sintering tests were performed on pure HfB_2, ZrB_2, HfC and ZrC powders as reference materials in a resistance-heated graphite furnace under flowing Argon at 1950°C for 60 min. Sintering and microstructural parameters are reported in Tab. 10.I. In this case only the geometrical density was measured, due to the high amount of residual porosity which prevented Archimedes' measurements.

It can be noticed that the final relative density of the monoliths, ranging between 55 and 72.5 % of the theoretical values, nearly retained the same values of the green density after the sintering cycle. The measured values were consistent with the amount of residual porosity evaluated by SEM images on the four monoliths (Fig. 10.1). The mean grain size did not increase with respect to the starting powders; in the micrographs the

early formation of the necks between the particles is visible, but even after a permanence of 60 minutes at 1950°C it was not possible to densify these matrices by pressureless sintering.

Tab. 10.I: Green and final density and mean grain size of the monoliths prepared by pressureless sintering at 1950°C for 60 minutes holding time.

Sample	Green density (%)	Final density (%)	M. g. s. (μm)
HfB_2	54.0	55.0	1.6
ZrB_2	57.2	60.6	2.1
HfC	57.1	69.2	0.6
ZrC	63.0	72.5	3.2

Fig. 10.1: SEM fracture surfaces of monolithic ZrC. HfC, ZrB_2, HfB_2 ceramics pressureless sintered at 1950°C for 60 minutes holding time.

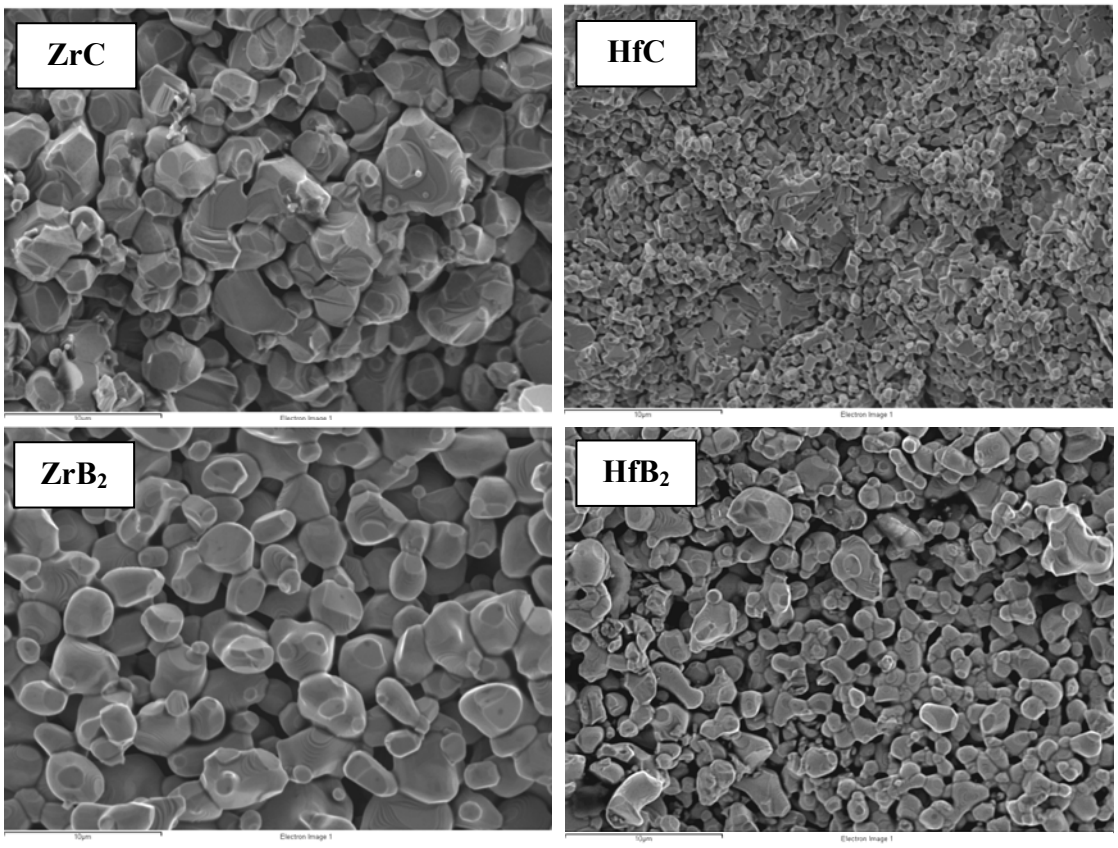

After the addition of $MoSi_2$ several sintering cycle tests were performed on 1 cm-diameter pellets for each composition in order to set the best temperature and holding time for the achievement of the maximum density. In Tab. 10.II the sintering parameters of the sintering cycles are reported. Once individuated the right parameters, a 3-4 cm diameter pellet for each composition was prepared for the mechanical testing.

If monoliths showed very poor densification, with a maximum final relative density around 70%, the composite materials showed an improved sinterability due to the addition of $MoSi_2$, with final densities in the range 96-98%. During sintering, significant weight loss occurred and it increased almost linearly with increasing the additive content, as reported in Tab. 10.II.

Table 10.II: Composition, sintering parameters, green and final relative density and weight loss occurred upon the thermal cycles. Selected material for mechanical testing are marked by *.

Label	UHTC matrix	$MoSi_2$ vol%	Th. Density g/cm^3	Sintering °C/min	Green ρ %	Final ρ %	Weight loss %
ZC5	ZrC	5	6.62	1950/60	66.4	83.2	0.8
				1950/90	67.0	88.8	1.0
				1970/60	63.3	91.4	3.4
ZC20	ZrC	20	6.57	1850/30	65.2	89.2	1.1
				1900/60	64.8	95.2	1.9
				1950/60*	63.8	96.8	2.3
HC5	HfC	5	12.37	1950/90*	54.3	98.1	0.7
HC10	HfC	10	12.05	1950/90*	56.1	97.8	1.1
HC20	HfC	20	11.41	1950/90*	55.2	96.9	1.2
ZB5	ZrB_2	5	6.11	1850/30	59.7	92.4	2.4
				1900/60*	59.2	96.4	2.4
				1950/60	59.4	94.8	2.7
ZB20	ZrB_2	20	6.14	1850/60*	55.6	99.0	2.3
HB5	HfB_2	5	10.94	1950/30	58.3	89.9	1.7
				1950/90*	56.6	96.8	1.4
HB20	HfB_2	20	10.26	1900/30	54.7	91.8	2.2
				1950/30	54.6	95.3	2.6
				1950/60	55.3	97.8	2.0
				1950/90*	54.5	98.5	3.0

10.2 ZrC-$MoSi_2$ COMPOSITES

10.2.1 Introduction

Zirconium carbide (ZrC) is a transition metal carbide characterized by excellent properties, such as high melting point (~3420°C),[1] high hardness (~25.5 GPa),[1] high electrical conductivity (78·10-6 Ω·cm) and high modulus of elasticity (~440 GPa).[1] ZrC is suitable for electronic applications (as thermoionic emitters) and nuclear ones (as diffusion barrier for fission metals in the coatings of nuclear fuels).[2,3] However, barriers to its use are the poor resistance to oxidation and a cost-effective manufacturing process for the obtainment of near-net shaped components. A brief summary of the state of the art on ZrC-based ceramics is reported in the following.

ZrC powders were densified by Barnier et al. up to 98 % of relative density by conventional hot pressing at 2300°C, 40 MPa of applied pressure and 60 min of holding time.[3] Min-Haga et al. showed that mixtures of ZrC with 20-40 wt% ZrO_2 were sintered to near theoretical density at temperatures ≥2000°C in a graphite furnace and developed a homogeneous microstructure, due to the formation of a defective oxycarbide which enhanced diffusion and densification in the carbide matrix.[4] These composites had a four-point bending strength of 220-320 MPa and a fracture toughness of 4-5.8 $MPa \cdot m^{1/2}$, thanks to the presence of tetragonal zirconia which generated toughening residual stresses.[4] Ryu et al. tried to obtain dense ZrC composites through addition of 20 wt% of Dy_2O_3, but the relative density after spark plasma sintering at 1727°C was only 68% of the theoretical value.[5] The addition of ZrB_2 was reported to enhance the densification of ZrC as composites with low residual porosity (2% to 4%) were obtained after thermal treatment at 2100°C for 2 hours.[6] Tsuchida et al. prepared a ZrB_2-ZrC composite by mechanically-activated self-propagating high-temperature synthesis of a Zr/B/C powder mixture that was subsequently consolidated by spark plasma sintering at 1800°C; the composite had a hardness of 17.8 GPa and a fracture toughness of 3.8 MPa·m1/2.[7] Kim et al. added 3 wt% of La to the eutectic composition ZrB_2:ZrC=59.9:40.1 wt% and obtained a relative density of 99% by spark plasma sintering at 1750°C.[8] Lanthanum was confirmed to accelerate mass transport mechanisms by the formation of a liquid phase. These authors also reported a fracture toughness of 2.6 $MPa \cdot m^{1/2}$.

So far, zirconium carbide has been sintered by conventional sintering at temperature higher that 2000°C, or by pressure-assisted techniques, such as hot pressing, reactive hot pressing, spark plasma sintering or.

The purpose of this work is to develop ZrC-based materials which can be consolidated by pressureless sintering at temperatures lower than 2000°C. To this aim, the studied compositions have been added with $MoSi_2$ intermetallic phase in amount of 5 and 20 vol%.

10.2.2 Sintering behaviour

Sintering cycles for the ZrC materials were carried out in the temperature range 1850-1970°C (see Tab. 10.II). The increase of either the sintering temperature or the amount of $MoSi_2$ generally led to an improvement of the final relative density. For the composite containing 5 vol% of $MoSi_2$, ZC5, despite a temperature of 1970°C, the

density retained values around 90 % of the theoretical density. Due to the low density, this composition was not mechanically characterized. On the contrary, the material containing 20 vol% of $MoSi_2$, ZC20, showed a good sinterability at 1950°C, with a final relative density of 96.8. It must be noted that, increasing the temperature, a higher weight loss occurred indicating the volatilization of species.

10. 2.3 Microstructure

The crystalline phases detected after sintering were cubic ZrC, tetragonal $MoSi_2$ and traces of β-SiC. The XRD pattern for ZC20 composite is reported in Fig. 10.2.

Fig. 10.2: X-ray diffraction pattern of the composite ZC20.

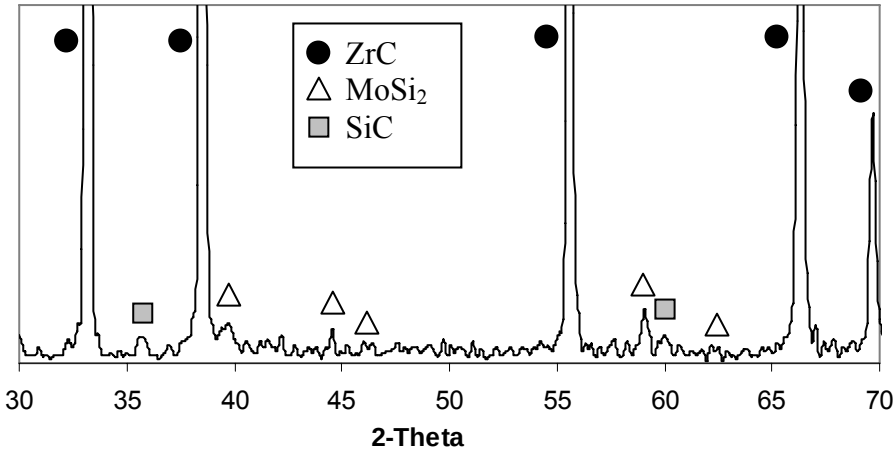

For the composite ZC20, a weight loss of 2.3% was calculated which was ascribed to the vaporization of volatile species (CO, SiO, MoO_3) and to the formation of SiC, which has a considerably lower density of 3.2 g/cm^3 than the starting phases.[9] An example of the fractured surfaces is shown in the scanning electron microscope image of Fig. 10.3a, where a transgranular mode is evident. In the polished section of Fig. 10.3b the bright phase corresponds to ZrC grains, which have a mean grain size of 6 μm and a squared shape, the grey phase with irregular shape is $MoSi_2$. Considering the mean grain size of ZrC starting powder, 4 μm, it can be deduced that a fair grain coarsening occurred during sintering. The dark agglomerates within the $MoSi_2$ phase are SiC particles; their amount was calculated to be about 1% by image analysis. The formation of SiC was attributed to the reaction between $MoSi_2$ and residual carbon present as impurity in the starting ZrC powder (1.5 wt%). Zirconium silicides with different stoichiometry were observed at the ZrC-$MoSi_2$–SiC interface (see Fig. 10.4), showing very low dihedral angles and suggesting that these silicide-based phases were liquid at the sintering

temperature. By EDS it was detected that the Zr-Si phases were also contaminated by oxygen.

Fig.10.3: BSE-SEM images of the ZC20 composite showing a) the fractured and b) the polished surface.

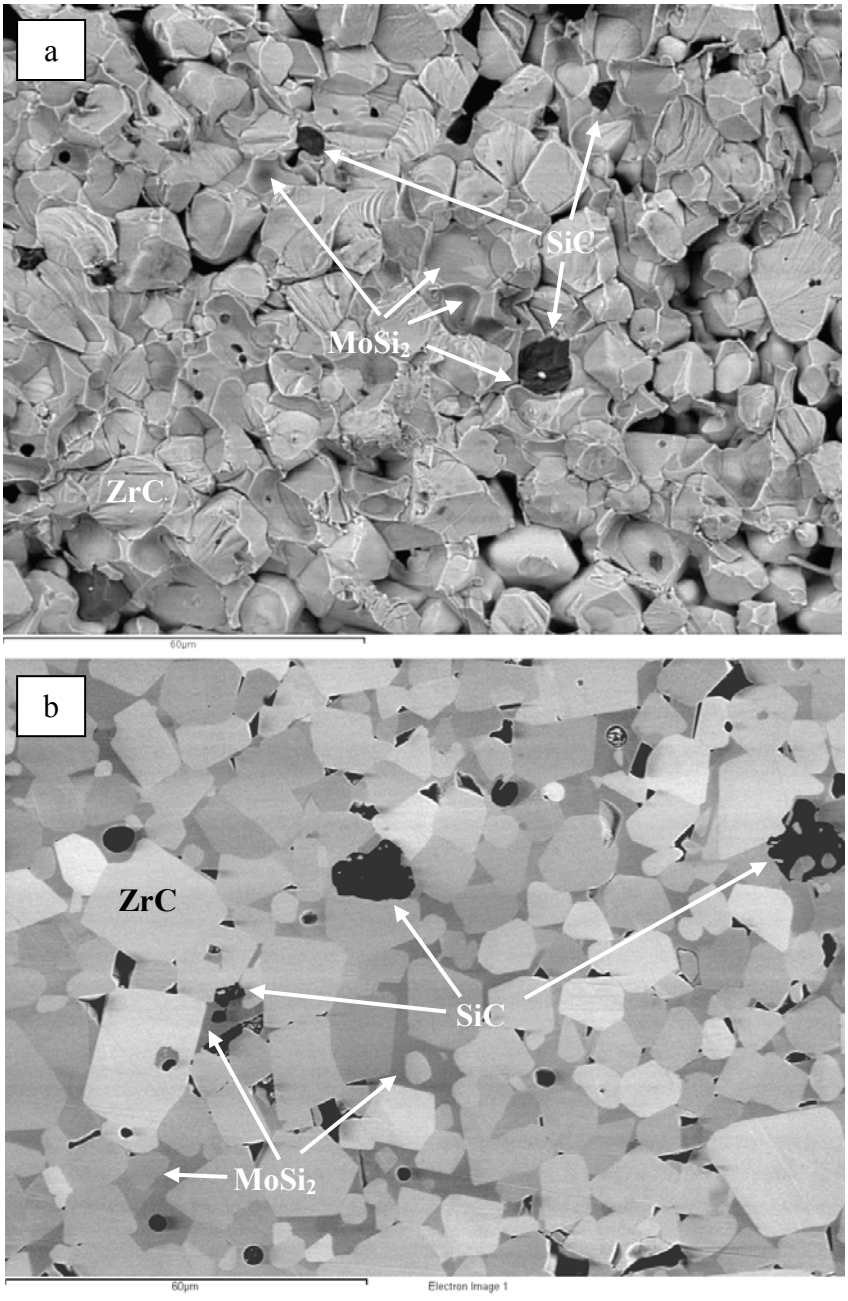

Further details on the microstructure were evidenced by TEM analyses. The bright–field image of the composite in Fig. 10.5a shows a ZrC grain and a bright SiC platelet embedded in the Zr_2Si phase. The substructure visible in the ZrC grains consists of network of dislocations. In $MoSi_2$ grains, the formation of nanoprecipitates was observed to give rise to necklaces of dislocations (Fig. 10.5b). In many cases, adjacent grains of $MoSi_2$ had the same crystallographic orientation as confirmed in Fig. 10.5c.

Fig. 10.4: SEM micrographs showing the formation of Zr-Si phases and the corresponding EDS spectra, in ZC20 composite.

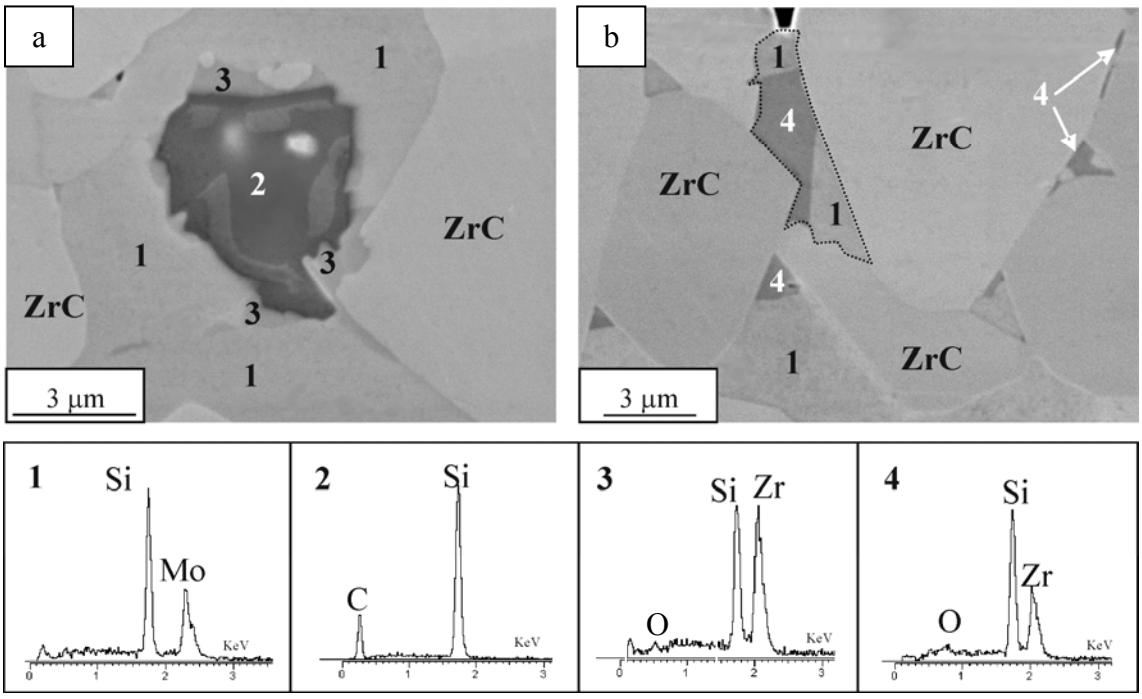

Fig. 10.5: BF-TEM images of ZC20 composite showing in a) the formation of SiC close to the Zr_2Si phase, b) dislocations in $MoSi_2$ phase, c) two adjacent grains of $MoSi_2$ with the same orientation.

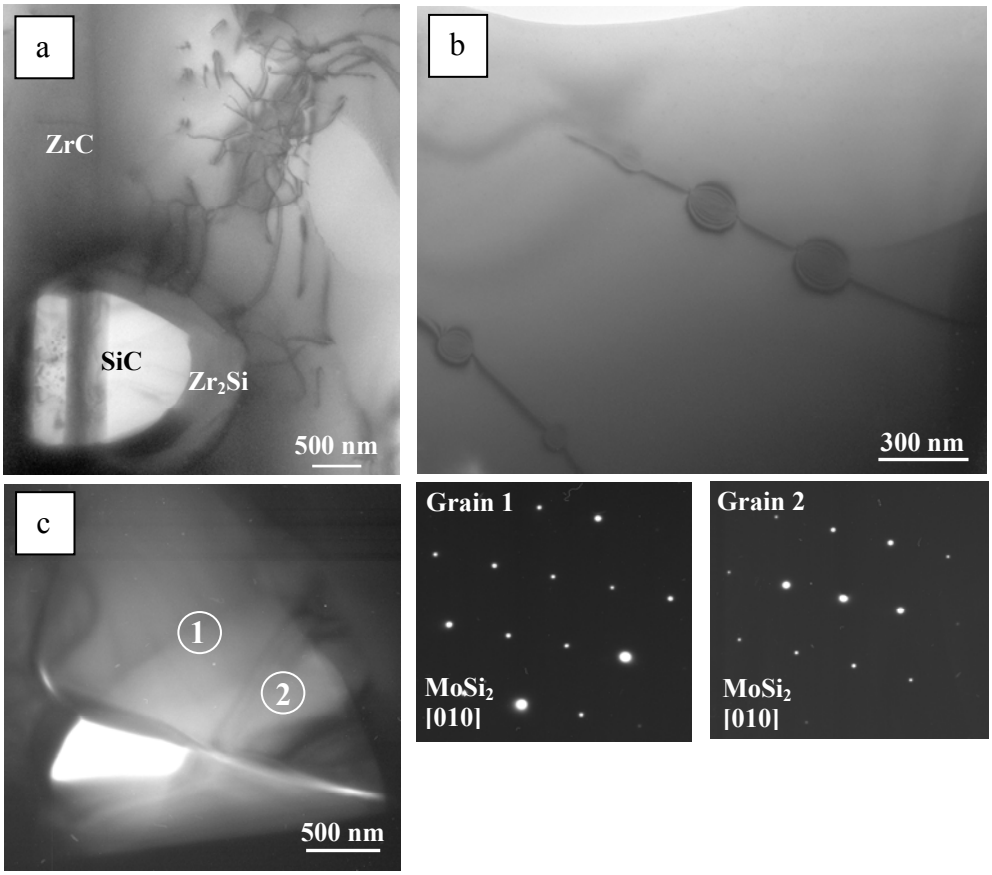

In Fig. 10.6, a mixture of reaction products is shown. TEM-EDS analyses confirmed the presence of ZrSi and $ZrSi_2$ phases with sharp boundaries. The presence of $MoSi_2$ in this area suggests that this was the original phase in which the reaction products formed. It should also be noted that, going from $MoSi_2$ towards ZrC, zirconium silicides with decreasing amount of silicon in their stoichiometry formed, hinting a diffusion process as the underlying formation mechanism.

Fig. 10.6: BF-TEM image of ZC20 material where $ZrSi_2$ and ZrSi phases coexist. A diffraction pattern for each phase is shown in the insets.

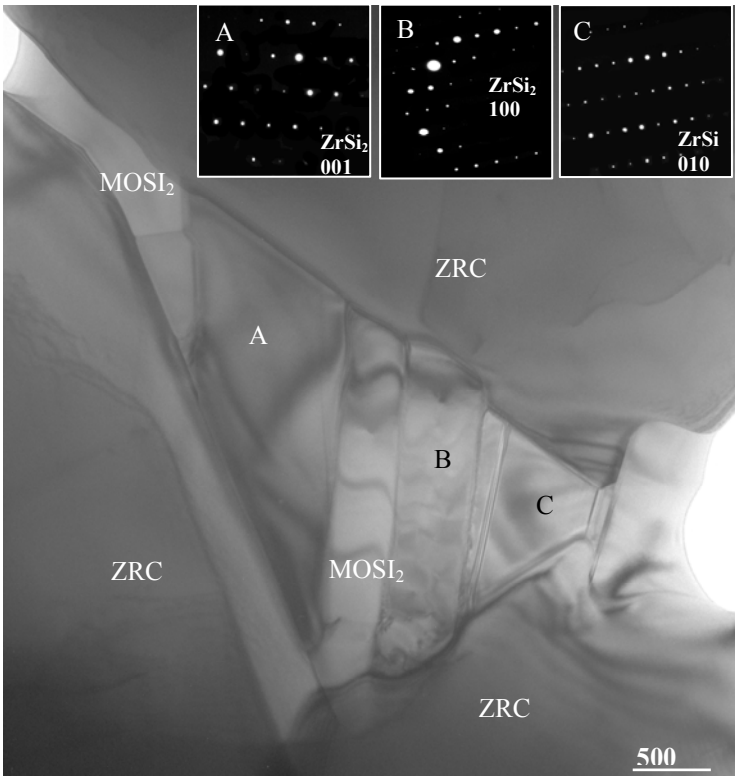

EDS spectra recorded from ZrC grains were superimposed to the theoretical ZrC spectrum and, as it can be seen in Fig. 10.7 a, the fit is not perfect. However, when Mo is included in the simulation (Fig. 10.7 b), the calculated profile nicely matches the experimental spectrum. According to quantitative analyses, the estimated amount of Mo was about 3-4 at%. Recent studies confirmed that Mo has a solubility in zirconium carbide from 1.1 to 9.4 mol%.[10] On the other hand, the presence of Zr peaks was detected in the $MoSi_2$ EDX spectra, indicating a mutual inter-diffusion of Zr and Mo into the adjacent phases.

Fig. 10.7: EDS spectra of ZrC grains and the calculated spectra superimposed including Zr-C in a) and Zr-Mo-C in b).

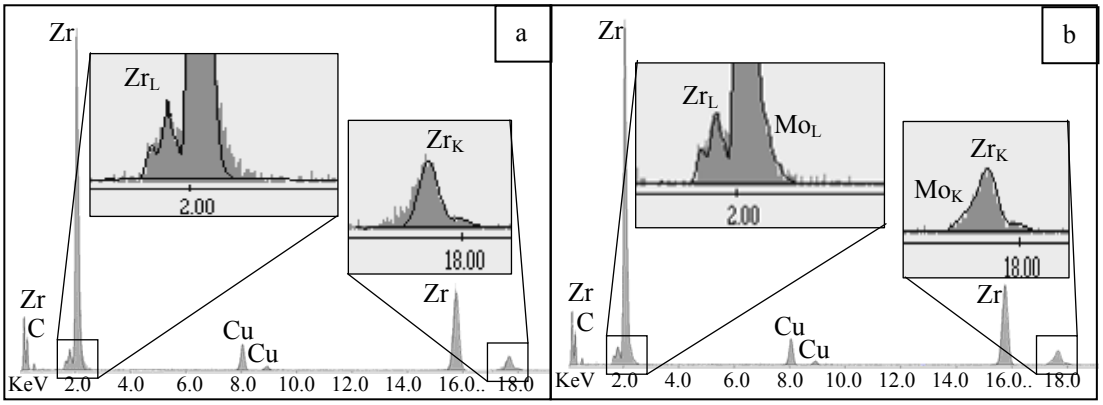

10.3 $HfC-MoSi_2$ COMPOSITES

10.3.1 Introduction

As belonging to the class of Ultra-High-Temperature-Ceramics, HfC owns high hardness, high electrical conductivity and chemical stability.[11-14] HfC is a potential candidate material for aerospace applications, because of the high melting point and low self diffusion coefficient. However, despite all the potentialities, so far it has not been developed on industrial scale due to the low sinterability and poor fracture toughness. The high melting point is the main reason for the low sinterability which does not allow HfC to be densified unless very high temperature and pressure are applied.

The literature on monolithic hafnium carbide is very scanty. Recent studies report on HfC-based coatings obtained through CVD method.[11] Other contributions are focused on hot pressed HfC_x compounds, sintered at 2500°C, with mean grain size ~40-60 μm.[12,13] The control of microstructure, i.e. grain coarsening and porosity, seems to be the main issue for this compound. In order to reduce the final mean grain size and improve the sinterability, nanosized HfC powders have been recently produced by carbothermal reduction synthesis.[14] At the moment, however, very few results on the mechanical properties of HfC-based materials are reported in literature.

In this section, the results on microstructure and densification mechanisms of HfC-based materials are presented. These compounds were pressureless sintered using $MoSi_2$ as sintering aid, in amounts of 5, 10 and 20 vol%.

10.3.2 Sintering behaviour

The densification data for HfC-based composites are presented in Tab. 10.II. Compared to the monolithic material (Fig. 10.1b), the composites showed an improved sinterability, with final densities in the range 96-98%. During sintering, significant weight loss occurred and it increased almost linearly with increasing the additive content, as reported in Tab. 10.II.

10.3.3 Microstructure

The X-ray diffraction patterns of the dense materials (Fig.10.8) showed the presence of the starting HfC and $MoSi_2$ phases and traces of a HfMoSi phase, especially in the HC20 specimen.

Fig. 10.8: X-ray diffraction pattern of HC20 sample.

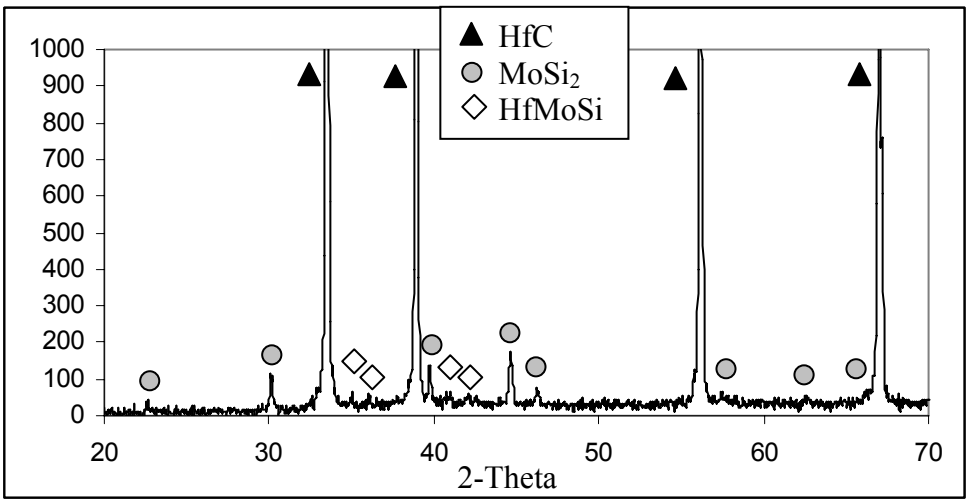

The fracture surfaces, Fig. 10.9a,c,e, are mainly intergranular for HC5 and HC10 and partially transgranular for HC20. An interesting feature of these materials is the increase of HfC grain size after sintering, in comparison with the as-received powder. The mean grain size of the composites was about 3-4 μm, with large grains up to 7-8 μm in size. Apparently, the HC20 composite had a more homogenous microstructure, compared to HC5 and HC10. Furthermore, the mean grain size slightly decreased with increasing $MoSi_2$ content (Table 10.II). The polished surfaces, shown in Fig. 10.9b,d,f, reveal bright squared HfC grains dispersed in the dark $MoSi_2$ phase, which fills the space left by the matrix grains. In these microstructures, HfC grains retained a rounded shape and reduced size, around 1 μm, in areas where the $MoSi_2$ phase was more abundant. In contrast, large faceted HfC grains up to 10 μm grew in areas where the $MoSi_2$ phase was scarce. This feature indicates that $MoSi_2$ could act as a grain growth inhibitor for HfC if the dispersion of the secondary phase is improved.

Fig: 10.9: Fracture and polished surfaces for a) and b) HC5, c) and d) HC10, e) and f) HC20.

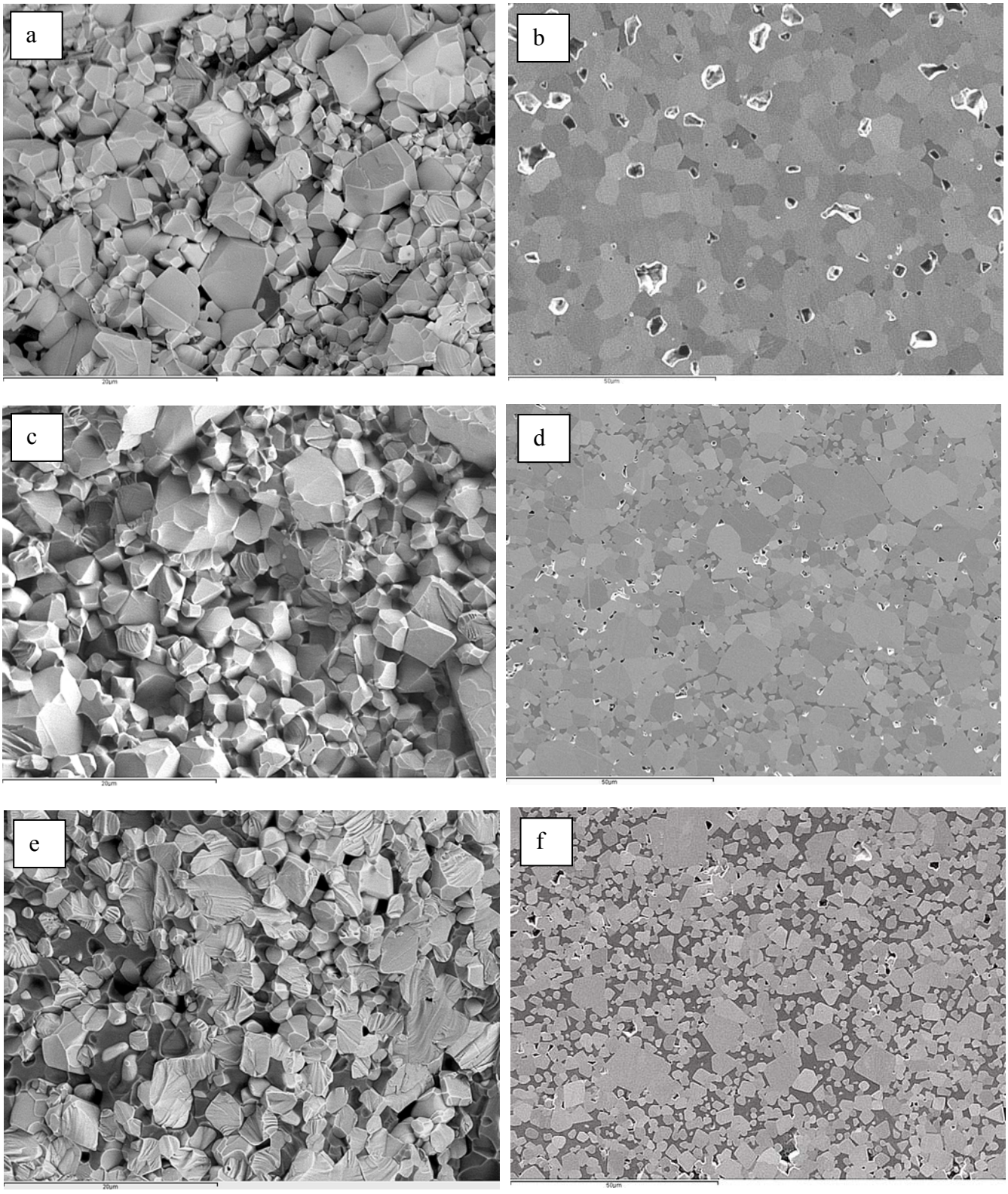

A characteristic example of the microstructure is shown in Fig. 10.10.

Analogously to ZrC-system, mixed phases based on Hf-Mo-Si-C were detected by EDS analyses, among hafnium carbide grains (Fig. 10.11). The formation of these phases suggests a mutual solubility between the two main phases and their shape, with very low dihedral angles, indicates crystallization from a liquid phase.

Fig. 10.10: SEM micrograph of HC20 sample: dark phase is $MoSi_2$, bright phase is HfC and the darker grey phase is Hf-Mo-Si.

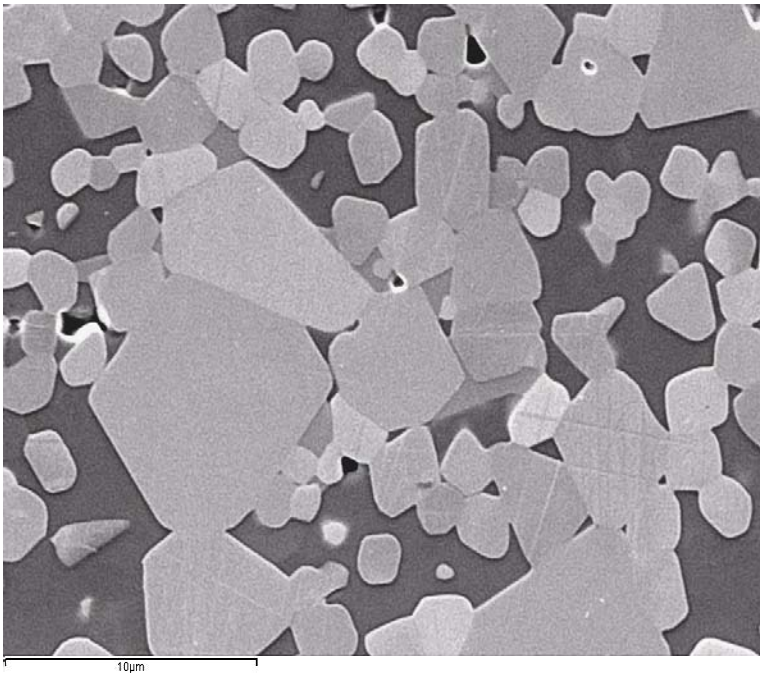

Fig. 9.11: High magnification image of HC20 sample showing the reaction phase Hf-Mo-Si and the relative EDS spectrum.

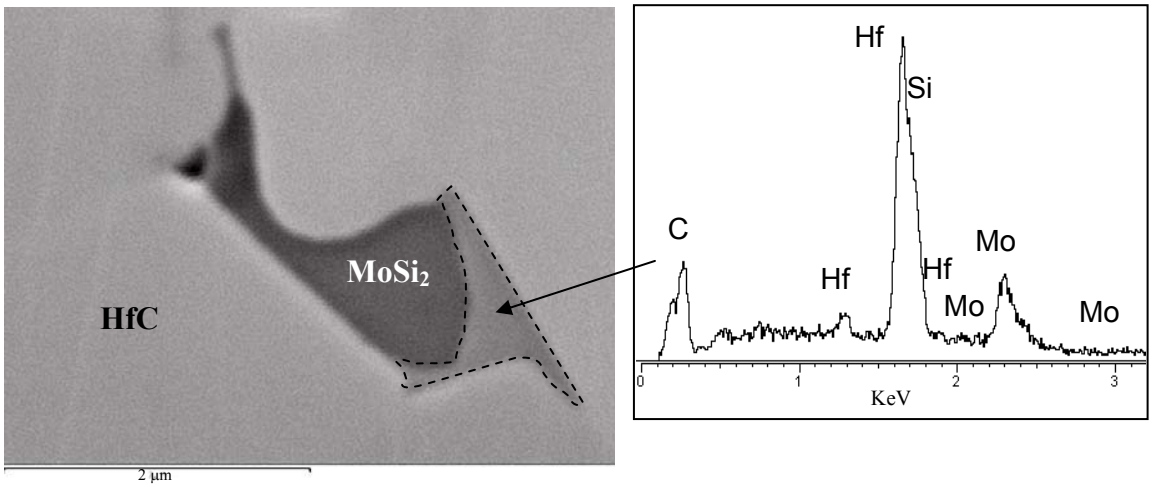

A detailed microstructural characterization by TEM did not reveal any dislocations in HfC grains, but strain contrasts were often noticed. TEM-EDX analyses confirmed the formation of a $(Hf,Mo)_xSi_y$ phase at the triple point junctions (see an example in Fig. 10.12). This aspect reveals a partial substitution of Hf into Mo sites. The interfaces of this mixed $(Hf,Mo)_xSi_y$ phase are concave towards HfC and convex towards $MoSi_2$, suggesting a wetting tendency only toward the silicide. As a matter of fact, the HfC-HfC grain boundaries were clean with plane interfaces. The size of the crystalline phase at a triple pocket varies between 150 and 200 nm. Two configurations of the triple point junction were observed: in one case at least one of the surrounding grains was $MoSi_2$, whilst in many other cases all the three adjacent grains were hafnium carbide.

The composition of the mixed phase was calculated by EDS analyses on several triple points and different stoichiometries were detected. Most of the triple points had an average composition of Mo=32, Hf=32 and Si=36 at%. If we assume that the transition metal atoms substitute Mo within the unit cell, as reported by Sakida et al.,[15] then the ratio metal/metalloid would be approximately 64/36. In addition, if we consider the phases in the system Hf-Si with a close ratio, then the possible phases are Hf_2Si (66.7/33.3) and Hf_5Si_3 (62.5/37.5). In order to identify these mixed phase, several electron diffraction patterns were taken from one single grain with different tilting angles. The analysis of the d-values calculated from the diffraction patterns, indicated that the $(Hf,Mo)_xSi_y$ phase had a structure not referable to the d-values of the known Mo-Si or Hf-Si phases. To experimentally obtain the cell constants, the parameters obtained from the diffraction patterns were checked with respect to tilting angles. The resulting unit cell has a hexagonal structure with a=7.4 Å and c=5.2 Å. Both structure and lattice constants are very close to the hexagonal Hf_5Si_3 with the space group n° $P6_3/mcm$ and lattice parameters of a=7.890 Å, c= 5.558 Å.

Fig. 10.12: Triple point junction in HC20 material, the EDS spectrum of the mixed Hf-Mo-Si phase and the corresponding diffraction patterns collected at different tilting angles.

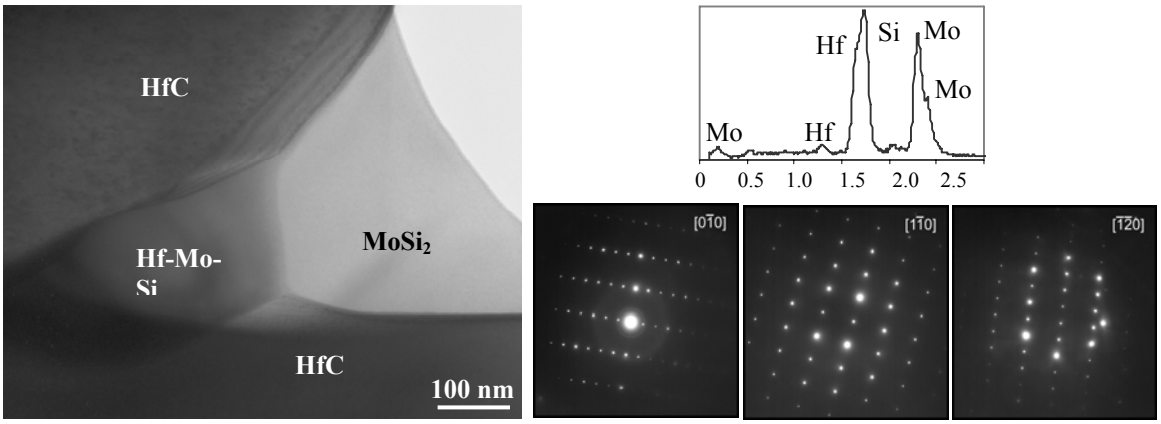

10.4 DENSIFICATION MECHANISMS OF Zr- AND Hf-CARBIDES

The most relevant data emerged from this investigation, which will be useful to understand the sintering mechanisms and the crucial role of metal silicides in the densification of these covalent compounds are the following:

- In ZrC-$MoSi_2$ material, Zr_xSi_y products were found at the interface between the two main phases and they were identified as $ZrSi_2$, ZrSi and Zr_2Si.

- ❖ Analogous to the the ZrC-$MoSi_2$ system, small amounts of the Hf-Mo-Si phase were detected besides hafnium carbide and molybdenum disilicide at triple point junctions in the HfC-$MoSi_2$ system.

From these observations we can conclude that Zr and Hf have at least a limited solubility in Mo-silicides and that Zr has a higher mobility than Hf, since pure zirconium silicides were detected compared to the mixed Hf-Mo-Si phase. Besides, the presence of only a very limited amount of secondary phases, detected at the triple point junctions, suggesting that the active species could be Mo_5Si_3 (instead of $MoSi_2$), a phase which is always present as an impurity phase.

One possible formation mechanism of these phases could be explained by the substitution of Zr or Hf at Mo sites into Mo_5Si_3, leading to the formation of Zr_5Si_3 or Hf_5Si_3. Some arguments in favour or against this hypothesis are considered.

- A necessary but not sufficient condition is the phase stability criterion with respect to the size factor, which refers to the 15% Hume-Rothery rule.[16] If we consider the atomic radius of Mo equal to 130 pm,[17] then the range of atomic radius which can be accommodated in the silicide at Mo sites is compatible with the atomic radius of Zr and Hf with 145 and 144 pm respectively.[17]
- Another favourable factor is the crystal structure. Like many other silicides, Mo_5Si_3 typically crystallizes in either a tetragonal or a hexagonal structure.[18] The body-centered tetragonal structure has the space group I4/mcm and lattice parameters equal to a= 9.59 Å, c= 4.87 Å (PDF #34-0371). Minimum addition of carbon destabilizes the tetragonal structure and results in the formation of a carbon stabilized hexagonal Nowtotny phase.[19] The hexagonal phase is characterized by the space group $P6_3/mcm$ and lattice parameters equal to a= 7.29 Å, c= 5.00 Å.[20] Both Zr_5Si_3 and Hf_5Si_3 have a hexagonal structure with space group $P6_3/mcm$ and lattice parameters a= 7.885 Å, c=5.558 Å (PDF #06-0582) and a=7.890 Å, c= 5.558 Å (PDF #12-0468), respectively. The shift from tetragonal to hexagonal structure would imply a distortion of the cell from 90-90° to 60-120°, but if we consider a transition from the Nowotny phase to Zr_5Si_3 or Hf_5Si_3, then the same hexagonal crystal structure is preserved. In both cases, the orientation of the crystal with an elongated c-axis is maintained.
- Calculations of the covalent and molecular volumes favour a Transition Metal/Mo substitution, since both $MoSi_2$ and tetragonal Mo_5Si_3 have a molecular volume lower than the covalent volume (-2% and -12% respectively), which implies a cell

with free space available for atoms with larger steric hindrance, such as Zr and Hf. On the other side, the hexagonal Mo_5Si_3 shows the opposite tendency, the covalent volume exceeds the molecular volume of about 5% and consequently it shouldn't be prone to the substitution.

- The last consideration relates to the mixed Hf-Mo-Si phase observed in the HfC-$MoSi_2$ material. Since the parameters calculated for this phase are very close to the Hf_5Si_3 lattice, the substitution of Mo by Hf in Mo_5Si_3 is highly probable.

The hypotheses of cation transfer, diffusion and change in crystal structure are strongly promoted by the presence of liquid phase. Hence, it is worthy to point out the possible origin of liquid formation based on phase diagram considerations.

From the Mo-Si phase diagram in Fig. 10.13a, redrawn from [19], we can see that below the sintering temperature, if the actual composition slightly differs from the peritectic composition of either $MoSi_2$ or Mo_5Si_3, we have compresence of liquid phase and, at a composition of 55 at% of Si, a eutectic liquid is predicted at 1910°C between $MoSi_2$ and Mo_5Si_3. Since the sintering temperature is 1950°C, we see that there is a high probability to form a liquid phase during sintering.

Another useful diagram is the one reported by Fan et al.[20] where $MoSi_2$ and C are considered (compare Fig. 10.13b). Above 1700°C, SiC formation and the presence of a liquid phase is predicted at any C/$MoSi_2$ ratio.

Melting points and onset temperatures of liquid phase formation in the Zr-Si and Hf-Si systems are summarized in Tab. III.[21, 22] These temperatures were inferred, for clarity, from the corresponding phase diagrams reported in Fig. 10.14.

Fig. 10.13: In a) the Mo-Si phase diagram redrawn from [19] and in b) the $MoSi_2$-C pseudo binary phase diagram redrawn from [20]. This pseudo-binary phase diagram was observed by section through the C-Si-Mo ternary system along the C-$MoSi_2$ tie line at different temperatures, resulting in phase fields where three phases are in equilibrium.

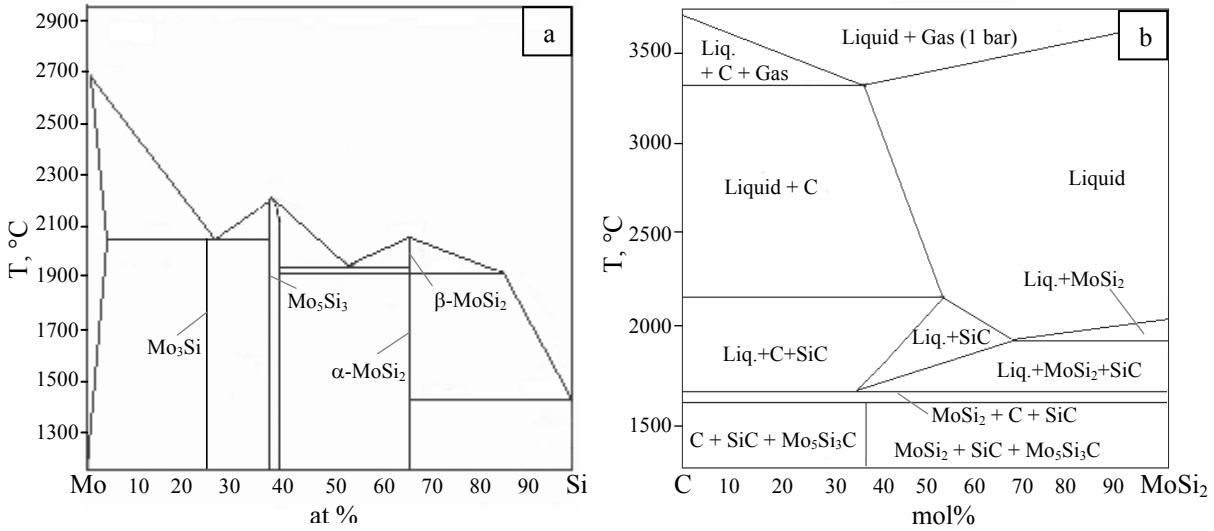

Tab. III: Melting or decomposition temperatures and corresponding eutectic or peritectic temperatures (liquid formation) in the systems Zr-Si and Hf-Si.[21,22]

System	Phase	Melting/ decomp. T (°C)	Eutectic/ peritectic T (°C)
Zr-Si	Zr_3Si	1650	1570
	Zr_2Si	1925	1650
	Zr_5Si_3	2180	1925
	Zr_3Si_2	2215	2215
	Zr_5Si_4	2250	2215
	ZrSi	2215	1620
	$ZrSi_2$	1620	1370
Hf-Si	Hf_2Si	2083	1828
	Hf_5Si_3	2357	2083
	Hf_3Si_2	2480	2320
	Hf_5Si_4	2313	2133
	HfSi	2133	1546
	$HfSi_2$	1546	1325

Fig. 10.14: In a) the Zr-Si phase diagram[21] and in b) the Hf-Si binary phase diagram.[22]

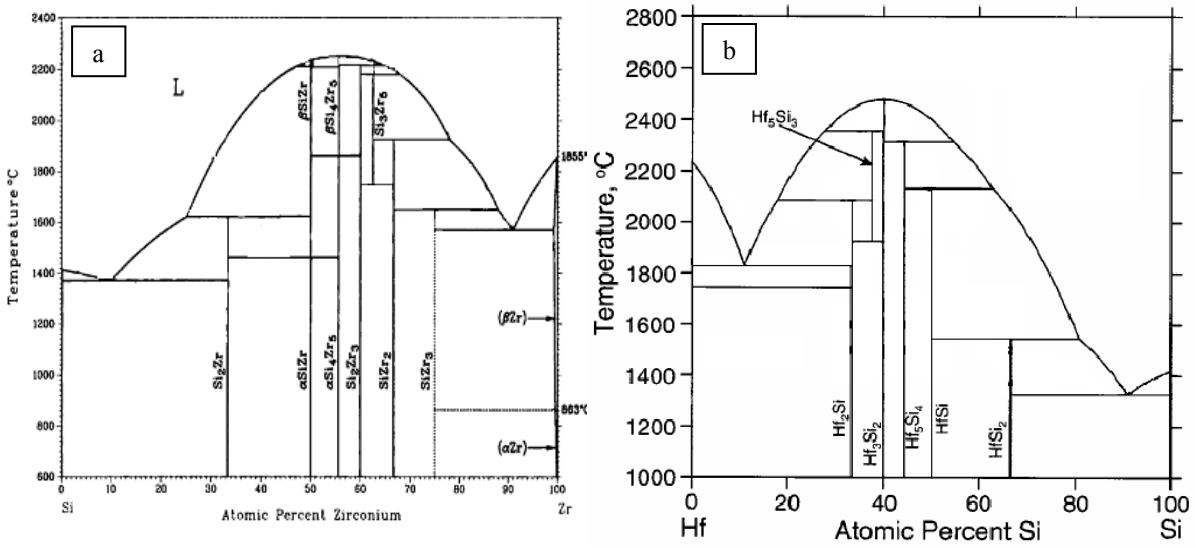

The eutectic temperature of a number of compositions is below the sintering temperature (1950°C) and hence a liquid phase must be present during densification. Thus, microstructural features in combination with the phase diagrams strongly suggest that densification of ZrC-$MoSi_2$ and HfC-$MoSi_2$ composites is promoted by a liquid phase, involving rearrangement of grains and matter transfer via the transient liquid.

However, the reaction path leading to the formation of the observed phases remains to be determined. To this purpose the thermodynamics of these systems are considered. For lack of data on HfC-$MoSi_2$ interactions, only the ZrC-$MoSi_2$ system will be discussed in light of thermodynamical calculations performed with a commercial software.[23] The starting hypotheses are atmospheric pressure, C-rich environment and

interdiffusion of the cations. The changes in Gibbs free energy values as a function of temperature for the reactions considered are plotted in Fig. 10.15.

Fig. 10.15: Plot of the possible reactions in the system ZrC-$MoSi_2$ calculated at ambient pressure. The Gibbs free energy as a function of the temperature.

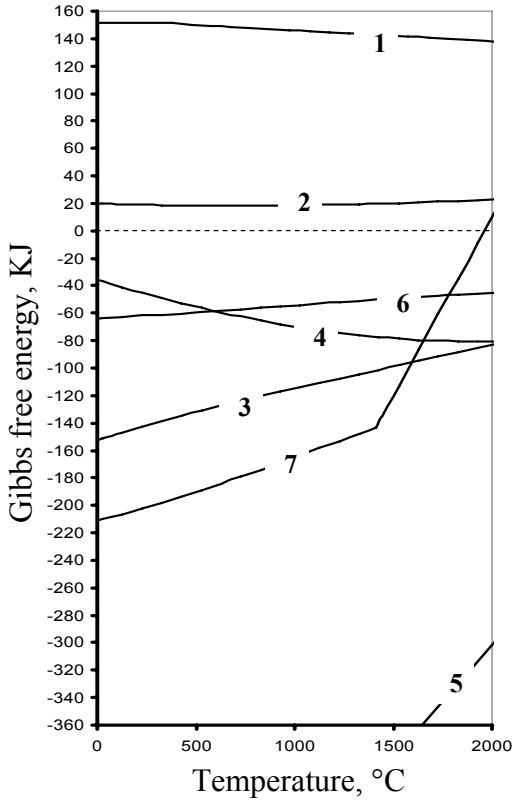

N°	Reaction
1	$ZrC + MoSi_2 = ZrSi_2 + MoC$
2	$Zr + MoSi_2 = ZrSi_2 + Mo$
3	$5\ MoSi_2 + 7\ C = Mo_5Si_3 + 7\ SiC$
4	$5\ Zr + Mo_5Si_3 = Zr_5Si_3 + 5\ Mo$
5	$2\ Zr_5Si_3 + C = 5\ Zr_2Si + SiC$
6	$Zr_5Si_3 + MoSi_2 = 5\ ZrSi + Mo$
7	$Zr_5Si_3 + 7\ Si = 5\ ZrSi_2$

The free energy calculation for the reaction between ZrC and $MoSi_2$ (Reaction 1) which leads to $ZrSi_2$, indicates a positive free energy at the sintering temperature of 1950°C; hence it is not favourable.

$ZrC + MoSi_2 = ZrSi_2 + MoC$ (1)

Similarly, the diffusion of Zr into $MoSi_2$ (Reaction 2), which leads to $ZrSi_2$ and Mo, is not thermodynamically allowed at and below 1950°C, but since Zr_xSi_y species were observed in the final microstructure at the interface between ZrC and $MoSi_2$, other reaction paths have to be figured out.

$Zr + MoSi_2 = ZrSi_2 + Mo$ (2)

Due to the highly reducing environment of the furnace[14] and the presence of pure carbon in the raw powders, the formation of Mo_5Si_3 and SiC is favourable through Reaction 3.

$5\ MoSi_2 + 7\ C = Mo_5Si_3 + 7\ SiC$ (3)

As the Mo_5Si_3 phase was never observed in the microstructure of the ZrC-based composite, it is likely that Mo is replaced by Zr to give Zr_5Si_3, as indicated by Reaction 4 ($\Delta G<0$ at all temperatures).

$$5\ Zr + Mo_5Si_3 = Zr_5Si_3 + 5\ Mo \quad (4)$$

The Zr-Si phase diagram[21] indicates that Zr_5Si_3 is liquid at the sintering temperature. Hence, it can flow into the microstructure filling voids among matrix grains favouring matter transport. When this phase gets in contact with a carbon source (Reaction 5), the formation of Zr_2Si and SiC is predicted from thermodynamical calculation and the overall free energy for this reaction at 1950°C is estimated to be –313.7 kJ.

$$2\ Zr_5Si_3 + C = 5\ Zr_2Si + SiC \quad (5)$$

If instead a source of silicium is close to Zr_5Si_3, it will react to form ZrSi and $ZrSi_2$ according to Reactions 6 and 7.

$$Zr_5Si_3 + MoSi_2 = 5\ ZrSi + Mo \quad (6)$$

$$Zr_5Si_3 + 7\ Si = 5\ ZrSi_2 \quad (7)$$

Excess molybdenum, as derived from Reactions 4 and 6, can oxidize to volatile MoO_3 or can be incorporated into the ZrC lattice, forming solid solutions as confirmed by EDS analysis (see Fig. 10.7). As shown in Fig. 10.15, the reactions discussed above are feasible and the products, according to the Zr-Si binary phase diagram, are liquid at the sintering temperature applied (see Tab. III).

Concerning the HfC-$MoSi_2$ system, an analogous behaviour is assumed, activated by the formation of Mo_5Si_3 followed by a partial substitution of Hf on Mo sites. Moreover, Hf-Si compounds are liquid below the sintering temperature.

It could also be possible that Zr or Hf_xSi_y could have formed due to solid-state reaction during heating of the powder compact at lower temperature. Considering the binary phase diagrams of system based on Mo, Si, Hf, Zr, C[21-24] it is evident that the transition metal silicides, even if formed in the solid state, would melt (melting temperatures ranging between 1390 and 2000 °C) and form a liquid at 1950°C. TEM investigations revealed that these phases were present at triple pockets in the sintered microstructure, due to the migration of the liquid phase to those pockets during sintering. The segregation of all the silicides in the solid-state to the triple points is rather unlikely due to the sluggish solid state diffusion.

All the aforementioned observations led to a new picture regarding the effective role of $MoSi_2$ upon densification of ultra high temperature ceramics, involving liquid formation, chemical reactions and cations diffusion at sintering temperature.

10.5 ZrB_2-$MoSi_2$ COMPOSITES

10.5.1 Introduction

Being a member of UHTCs, ZrB_2 possesses high refractoriness, high electrical and thermal conductivity, chemical inertness against molten metals or non-basic slags, and good oxidation resistance.[24] All these properties make it an attractive candidate for applications where corrosion, wear and oxidation resistance are active processes. Potential applications of zirconium diboride have been recently considered for aerospace manufacturing as, for example, the leading edge parts on hypersonic re-entry spacecrafts.[25] Owing to the high melting point, the densification of ZrB_2 powders requires very high temperatures (2100–2300°C) and pressure-assisted sintering procedures.[26] Generally, the final microstructures are coarse and an amount of residual porosity is present. Recent research has shown that high-density ZrB_2- based materials can be obtained by hot pressing at temperatures lower than 2000°C, thanks to the addition of metal sintering aids such as Ni and Fe,[27,28] and ceramic additives like Si_3N_4.[29] However, the formation of grain boundary phases deriving from the sintering aids often deteriorates the high-temperature properties. Hot-pressed ZrB_2–$MoSi_2$ ceramics were previously studied, and it was found that the addition of 10–30 vol% $MoSi_2$ improved both room-temperature mechanical properties[30] and oxidation resistance[30,31] compared with monolithic ZrB_2 materials.

In this section, the microstructure of pressureless-sintered ZrB_2–$MoSi_2$ composites is presented.

10.5.2 Sintering behaviour

The densification data are summarized in Tab. II. Experimental densities were compared to theoretical densities calculated with the rule of mixtures on the basis of the starting nominal compositions assuming no impurities and no reactions during processing. Several tests were carried out by varying the temperature, from 1800 to 1900°C, and the holding time, ranging from 30 to 60 min, to investigate the possibility to obtain dense composites by pressureless sintering. Preliminary experiments with 5–15 vol% $MoSi_2$ resulted in samples with residual porosity (~5%).[31] An improvement in

the final density up to 99% was obtained by increasing the $MoSi_2$ content to 20 vol%. The best sintering conditions for this composition was found to be 1850°C with 30 min of holding time (Tab. 10.II).

10.5.3 Microstructure

The X-ray diffraction patterns for the composite ZB20 are reported in Fig. 10.16.

Besides the presence of hexagonal ZrB_2 and tetragonal $MoSi_2$ (Fig. 10.16a), backscattered X-ray diffraction carried out at diffraction angles >100, evidenced the presence of additional ZrB_2 peaks, very close to those of pure ZrB_2 phase but shifted slightly towards higher angles (Fig. 10.16b). These peaks testify the formation of a ZrB_2-based solid solution with contracted cell parameters.

Fig: 10.16: X-Ray diffraction pattern for ZB20 sample: a) carried out at conventional angles (2θ: 20-70), b) carried out at high angles (2θ: 130-160) showing the presence of a $(Zr\text{-}Mo)B_2$ solid solution.

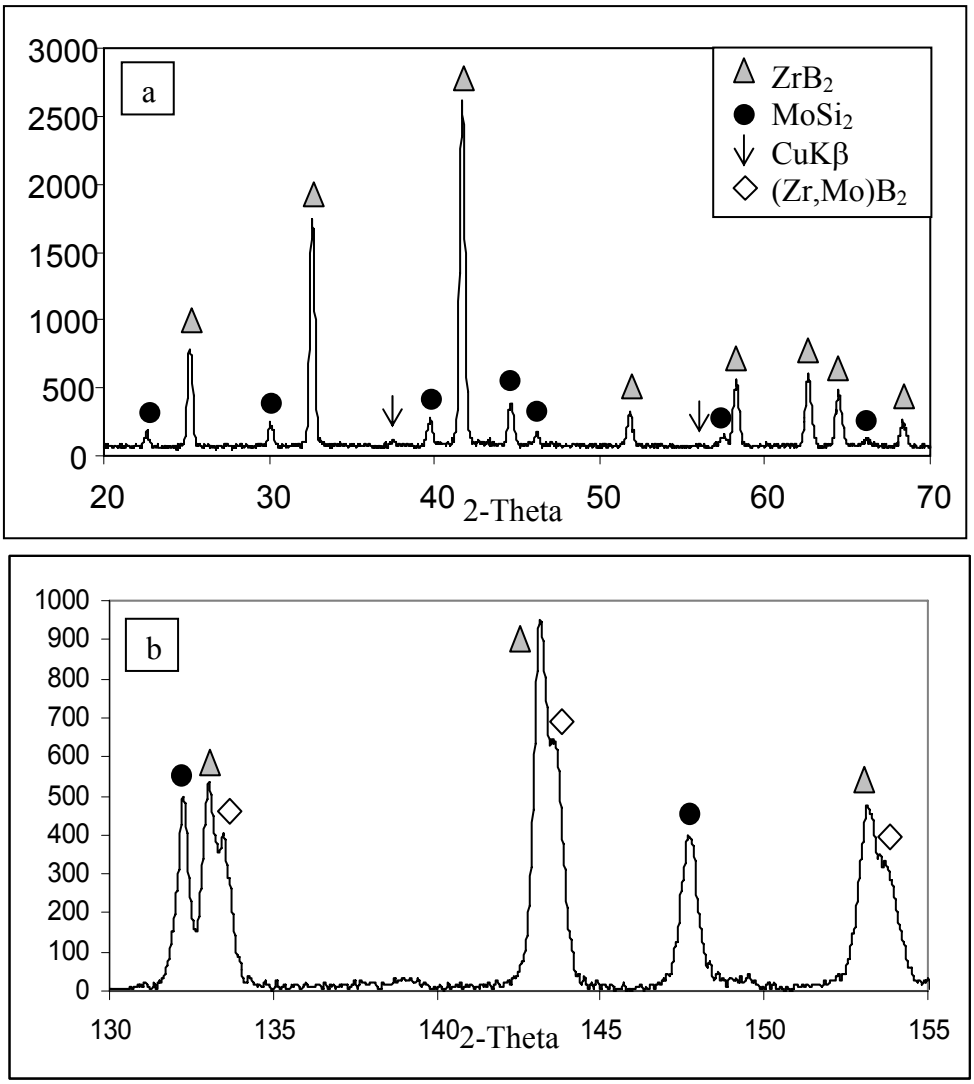

As most of borides, ZrB_2-based composites showed a transgranular fracture as shown in Fig. 10.17a,b. The 5 vol% $MoSi_2$-containing sample showed a higher level of residual porosity compared with the 20 vol% $MoSi_2$-containing one (Fig. 10.17 c-d).

Fig: 10.17: Fracture surfaces for a) ZB5 and b) ZB20; polished surfaces for c) ZB5 and d) ZB20 showing homogeneous microstructure and some residual porosity in ZB5; typical microstructure for e) ZB5 and f) ZB20 showing the secondary phases. Legend: 1 ZrB_2, 2 $MoSi_2$, 3 MoB.

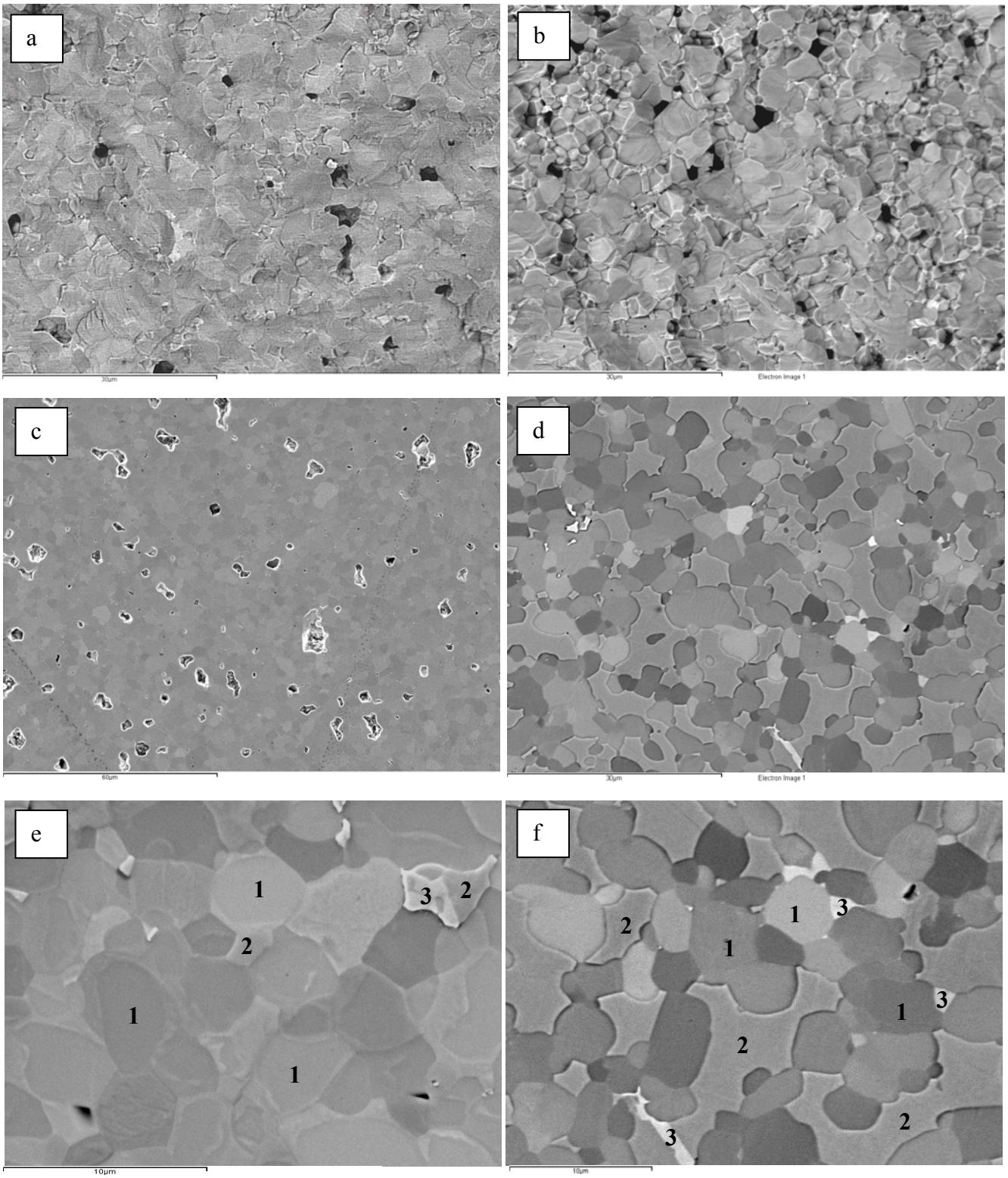

On the polished sections (Fig. 10.17c-f), ZrB_2 exhibits rounded grains, whilst $MoSi_2$ is characterized by an irregular shape with low dihedral angles. The mean grain size of the ZrB_2 grains was about 2.5 μm, for all the compositions. A low amount of secondary phases was detected by EDS analysis and included products deriving from ZrB_2 and $MoSi_2$ reactions, such as MoB, which appears as bright contrast, often located at the tips of $MoSi_2$, ZrO_2, ZrC, and Zr-C-O (Fig. 10.17e,f). The presence of ZrO_2 is imputed to both oxygen contamination of the starting powders and oxygen take-up during the milling procedure. The presence of ZrC/ZrCO may be due to carbon contamination deriving from powder impurities, graphite crucible and supports, as explained in section 10.7.

In Fig. 10.18 a detailed view of the matrix grains is shown. ZrB_2 grains have a substructure, resembling a core-shell type. By EDS analysis, carried out with reduced energy in order to limit the beam lateral spread, pure ZrB_2 phase was recognized in the cores, while Zr, B and small amounts of Mo were detected in the shell. However, since Zr and Mo K and L lines are nearly superimposed, the effective presence of Mo in ZrB_2 grains is difficult to be ascertained. On the other side, it must be mentioned that the formation of (Zr,Mo)–B solid solutions has been already reported for pressureless sintered ZrB_2–SiC composites containing Mo as the sintering additive.[32] Furthermore, formation of a discrete solid solution between ZrB_2 and Mo up to 10 mol% was previously mentioned by Kislyi and co-authors, who noticed the dissolution of molybdenum in zirconium diboride at 1600-1700°C.[33]

Fig: 10.18: Polished surfaces for ZB20 sample showing the core-rim structure and the relative EDS spectra.

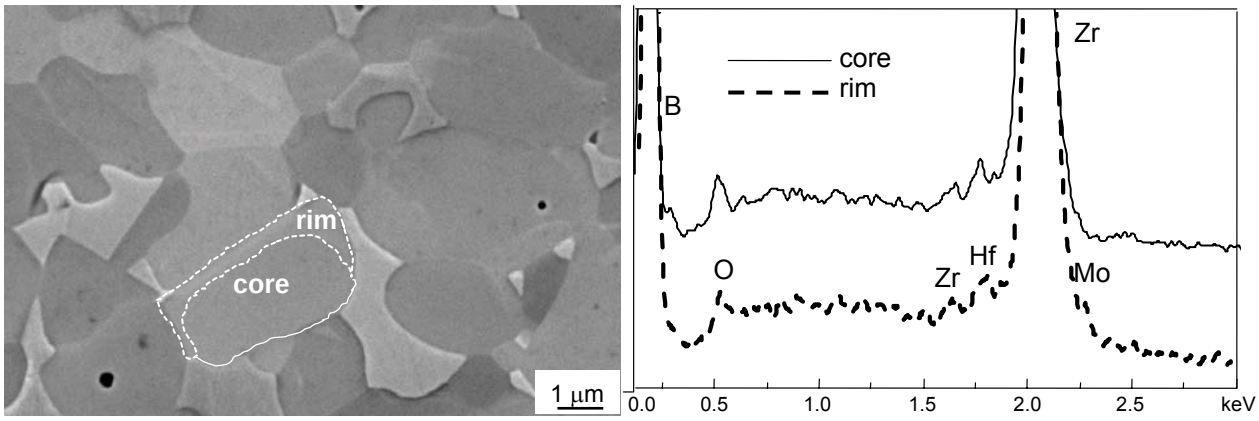

By detailed TEM investigations further phases were detected (Fig. 10.19). A part from large pools of MoB-phase, Mo_5Si_3 and Mo_5SiB_2 containing Zr and O impurities

were detected at the triple junctions (Fig. 10.20). Although electron diffraction patterns were recorded on these latter phases, it was not possible to appreciate the lattice distortion of the cell provoked by the introduction of Zr, as Zr and Mo possess very close atomic numbers, 40 and 42, respectively. Deeper investigations were performed on the core-rim structure suggested by SEM analyses. The presence of oxygen and molybdenum, besides boron and zirconium, was confirmed by nanoprobe by EDS and EELS as shown in Fig. 10.21. Moreover, electron diffraction and high resolution imaging revealed clean interfaces between inner and external zone and an epitaxial orientation between the same (Fig. 10.22). This morphology induces to suppose a partial solubilization of Zr in a Mo-rich liquid phase and reprecipitation on ZrB_2 grains. As confirmation of the mutual solubility between Zr and Mo, Zr was detected in $MoSi_2$ grains, as shown in the EDS of Fig. 10.20.

Fig. 10.19: Bright field TEM images showing a) MoB phase and b) and c) the formation of Mo_5Si_3 and Mo_5SiB_2 at the triple points with the corresponding diffraction patterns.

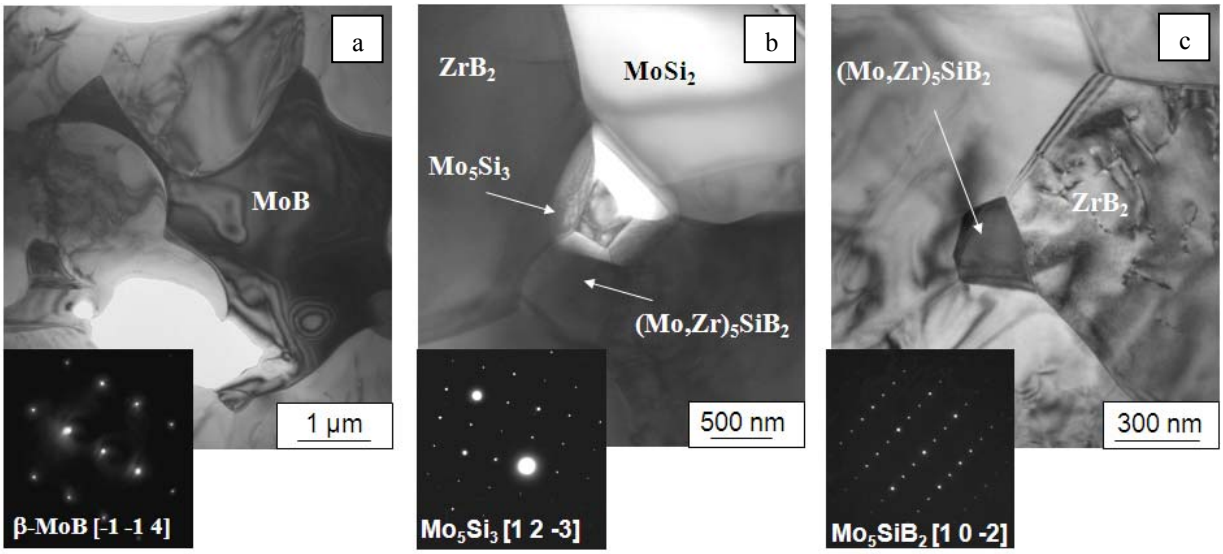

Fig. 10.20: $MoSi_2$, Mo_5Si_3 and Mo_5SiB_2 EDS spectra recorded by TEM showing the presence of Zr and O peaks, too.

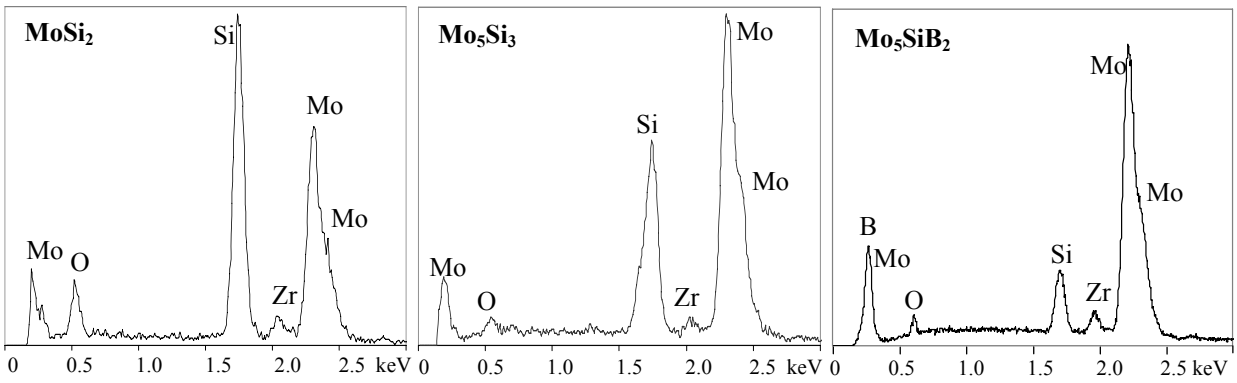

Fig. 10.21: BF-TEM image showing the morphology of ZrB_2 grains. The elemental composition of core and rim is reported in the EDS and EELS spectra.

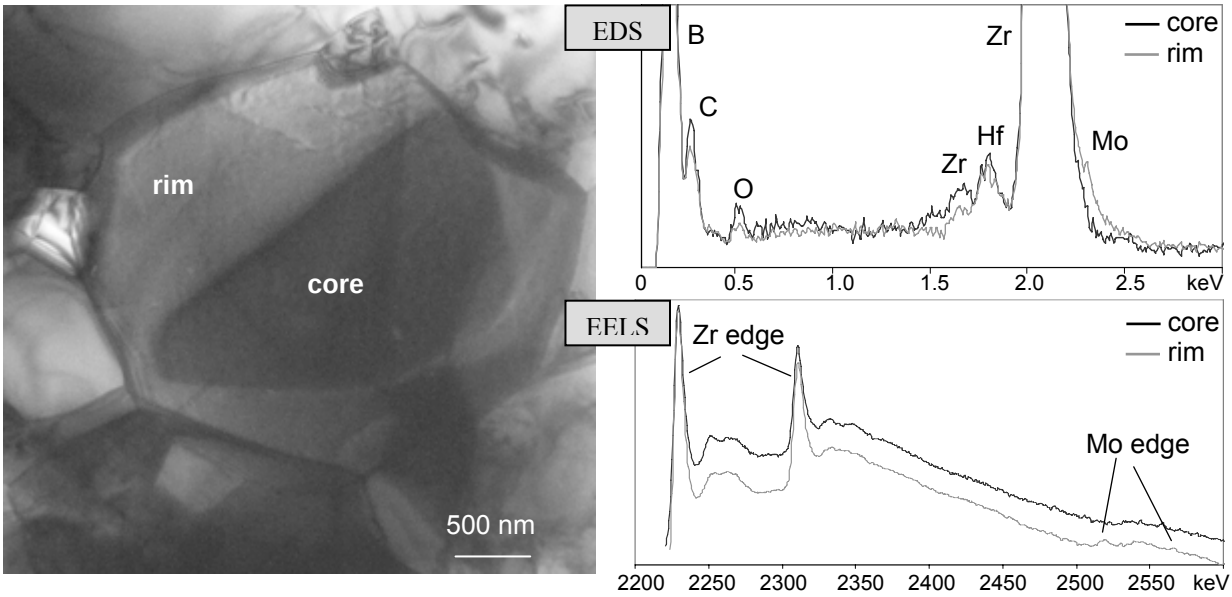

Fig. 10.22: HRTEM image showing the epitaxy between core and rim in ZrB_2 grains.

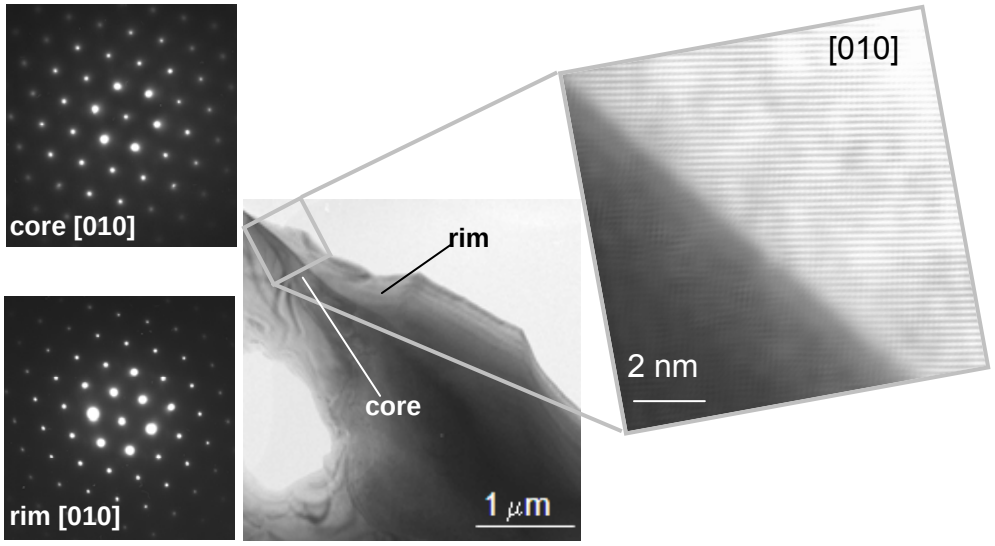

10.6 HfB_2-$MoSi_2$ COMPOSITES

10.6.1 Introduction

Hafnium diboride-based ceramics are materials of high interest for ultrahigh temperature applications because of their combination of engineering properties such as high melting point, solid state stability and good thermochemical and thermomechanical properties. Other desirable properties are high hardness, wear resistance, high emissivity, low electrical resistivity, excellent corrosion resistance against molten iron and slags and superb thermal shock resistance. They constitute a class of promising materials for high temperature applications in several industrial sectors, like foundry or

refractory industries. Applications are also found in aerospace industry: leading edges and nose caps in hypersonic re-entry space vehicles, rocket nozzle inserts and air-augmented propulsion system components.[31,34-37]

To ensure that favourable properties are attained, control of densification and microstructure is necessary, because strength and corrosion resistance, for instance, are adversely dependent on porosity in sintered bodies. Due to the high melting point, the sintering of HfB_2 needs pressure-assisted sintering procedures at temperatures higher than 2000°C.[36,37] Generally, the final microstructures are coarse and a considerably amount of residual porosity is present.[12] Recent works on HfB_2-based materials showed that high density samples with refined microstructure and improved room temperature mechanical properties can be obtained at temperatures lower than 2000°C, using ceramic additives like Si_3N_4, HfN.[38,39] However, the type and amount of grain boundary phases deriving from the sintering aids often deteriorate the high temperature properties.[38,39]

In this section, $MoSi_2$ was selected as ceramic additive for HfB_2, due to the promising results obtained with other ZrC, HfC and ZrB_2 matrices, both on the sintering behaviour and on the mechanical properties.

10.6.2 Sintering behaviour

The sintering tests performed on HfB_2-based composites are summarized in Tab. 10.II. In order to achieve high density bodies, the sintering cycle was set at 1950°C/60 min, irrespective of the additive content. Tests at 1900°C revealed that even with 20 vol% additive, the final density remained as low as 92%. For these compositions a higher sintering temperature was necessary to obtain a fully dense material, 1950°C compared to 1850°C required by ZrB_2-based material, confirming the higher refractoriness of HfB_2.

10.6.3 Microstructure

By x-ray diffraction only hexagonal HfB_2, tetragonal $MoSi_2$ and traces of HfO_2 were detected in the 2θ angles range 20-70, as shown in Fig. 10.23a. In opposition to the former composite, in back scattered reflection XRD in Fig. 10.23b, there was no evidence of extra peaks due to the formation of solid solutions. Although a tiny shoulder was detected adjacent to HfB_2 peaks on the right, it was not possible to distinguish if it was a residue of Cuk_β filtering or a new phase.

The fracture surface of the HfB_2-$MoSi_2$ composites showed a transgranular fracture mode (as reported in Fig. 10.24a,b). In Fig. 10.24c-f, the polished sections of compositions HB5 and HB20 show a very regular microstructure, with little residual porosity. In agreement with density measurements, a higher level of porosity was observed for the composition with lower content of the intermetallic phase. HfB_2 grains have a rounded shape while the $MoSi_2$ phase has an irregular morphology with concave shapes. This peculiar characteristic indicates that $MoSi_2$ was very ductile at the sintering temperature and could fill the void left by the matrix. This phenomenon is not surprising since the sintering temperature, 1950°C, was very close to the melting point of $MoSi_2$ (2020°C).[19] The HfB_2 mean grain size retained the dimensions of the starting powder, about 1.5 μm. Analogously to ZrB_2-$MoSi_2$ system, the analysis of secondary phases by EDS confirmed the presence of HfO_2, which appears as rounded bright contrasting particles, HfC and traces of Mo–B phase (Fig. 10.24e,f).

Fig: 10.23: X-Ray diffraction pattern for HB20 sample: a) carried out at conventional angles (2θ: 20-70), b) carried out at high angles (2θ: 110-150). Indicated by "?" the peaks presumably belonging to a $(Hf,Mo)B_2$ solid solution.

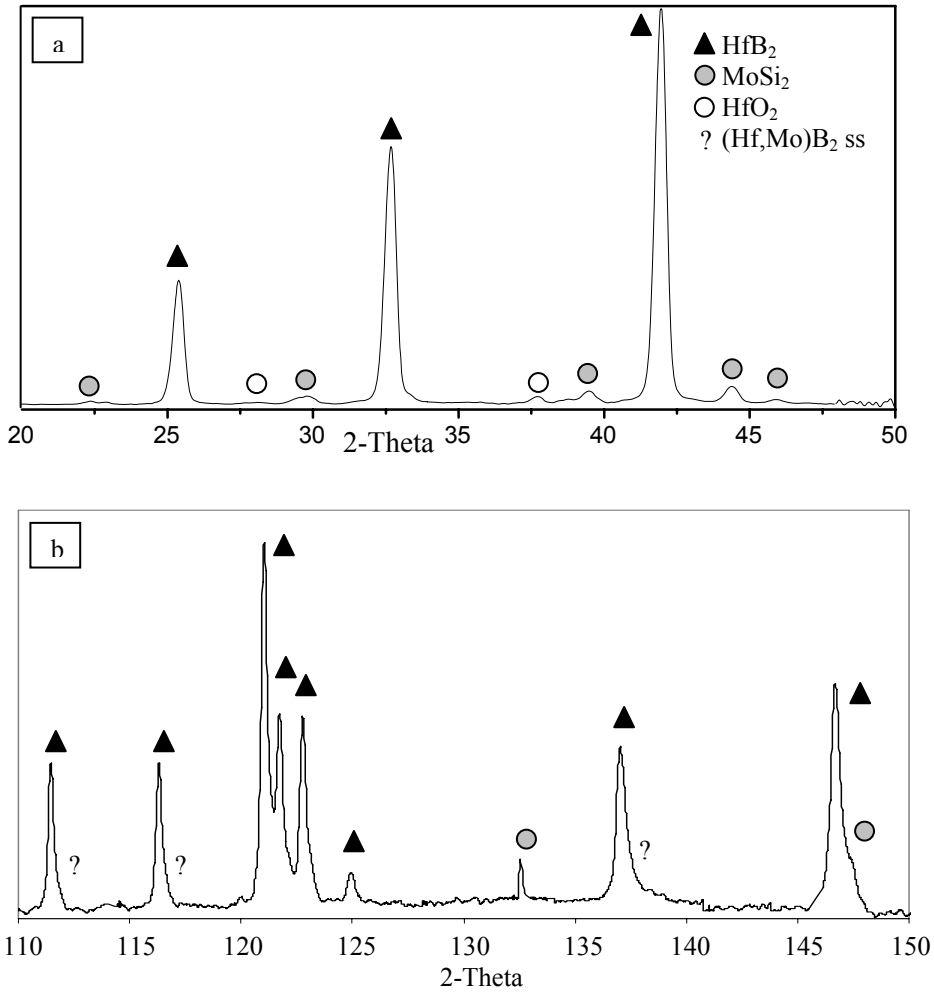

Fig: 10.24: Fracture surfaces for a) HB5 and b) HB20; polished surfaces for c) HB5 and d) HB20 showing homogeneous microstructure and some residual porosity; typical microstructure for e) HB5 and f) HB20 showing the secondary phases. Legend: 1 HfB_2, 2 $MoSi_2$, 3 MoB, 4 HfO_2, 5 HfC.

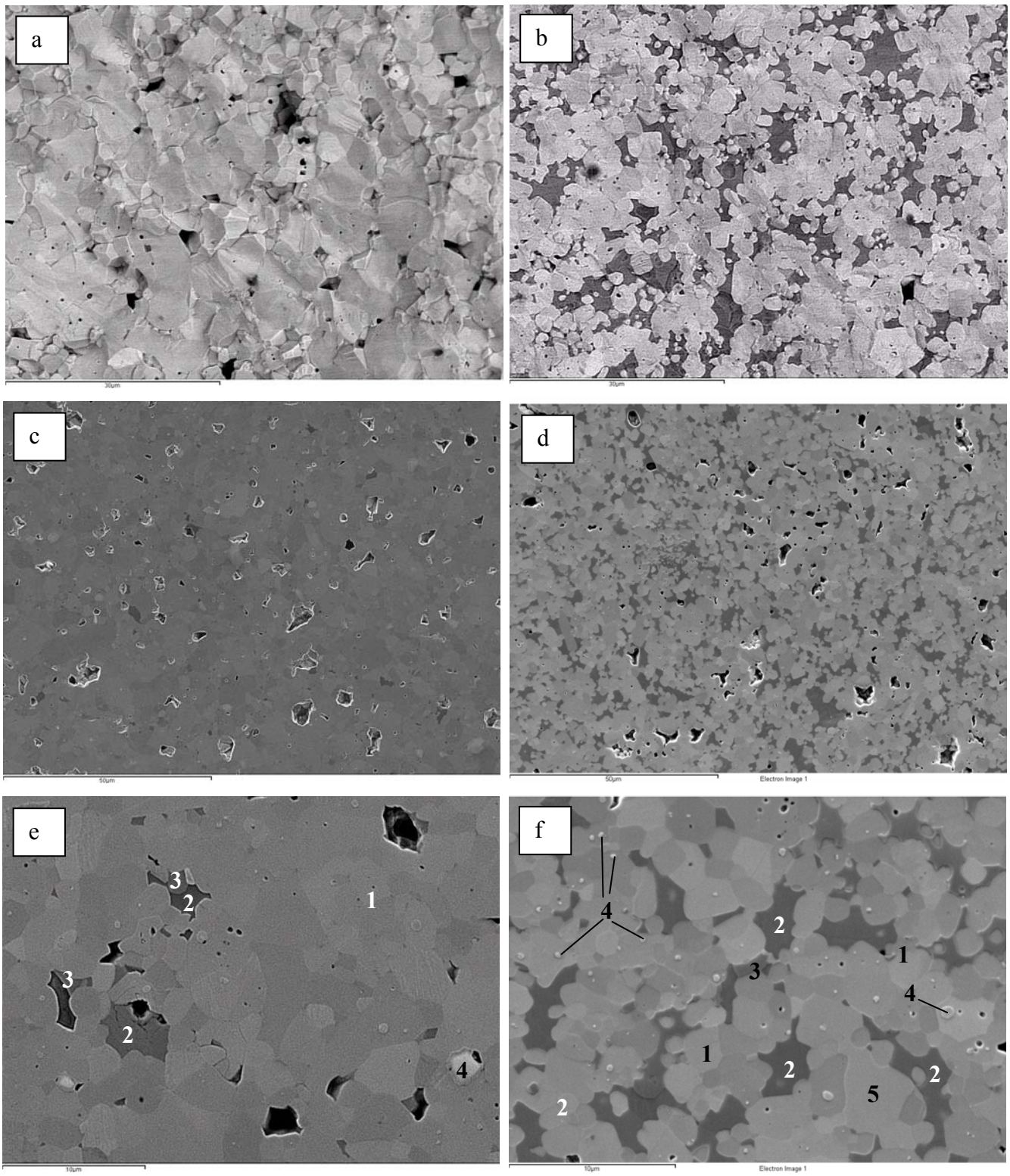

Much attention was devoted to search a Hf-Mo-B substructure surrounding HfB_2 grains, analogous to the ZrB_2-$MoSi_2$ system. Yet, only a bare contrast was occasionally observed, see Fig. 10.25, but even in this case, due to the small volume of the outer phase and the low amount of Mo which is supposed to enter in solid solution, the EDS analysis can not be conclusive.

By transmission electron microscopy, HfO_2 nanoparticles with twinned structure were observed on HfB_2 grains, as shown in Fig. 10.26. Also for this composite, Mo_5Si_3 and Mo_5SiB_2 containing Hf impurities were detected at the triple points showing partial wetting tendency, as illustrated in Figs. 10.27. Regarding the morphology of HfB_2 grains in the composite, a Mo-containing substructure surrounding HfB_2 grains was sporadically observed (Fig. 10.28), but its presence is strongly suggested by analogy with the former system and the indications from x-ray diffractometry or microscopy. These less marked features in the HfB_2-$MoSi_2$ system compared to ZrB_2-$MoSi_2$ system could be explained with a lower solubility of Mo in HfB_2 or Hf in Mo-silicides.

Fig. 10.25: SEM image of polished HB20 surface showing the sluggish core-shell substructure of HfB_2 grains with the corresponding EDS spectra.

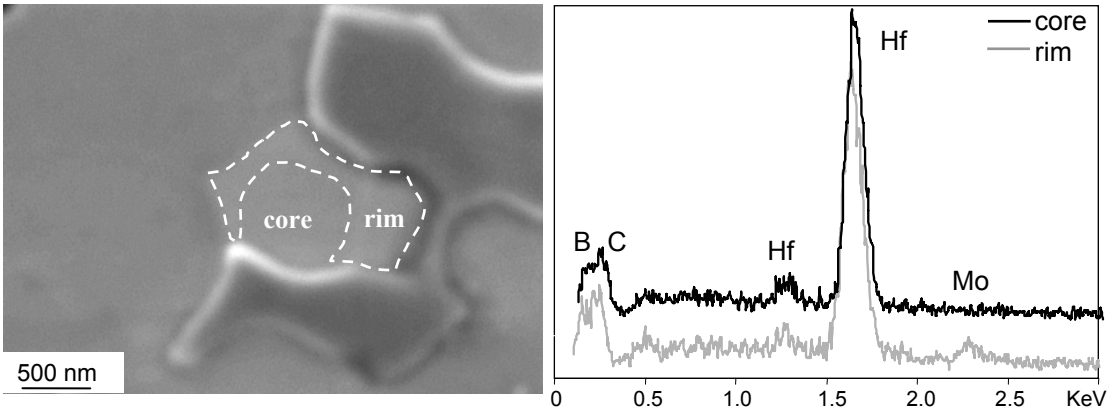

Fig. 10.26: HfO_2 nanoparticles showing a twinned structure.

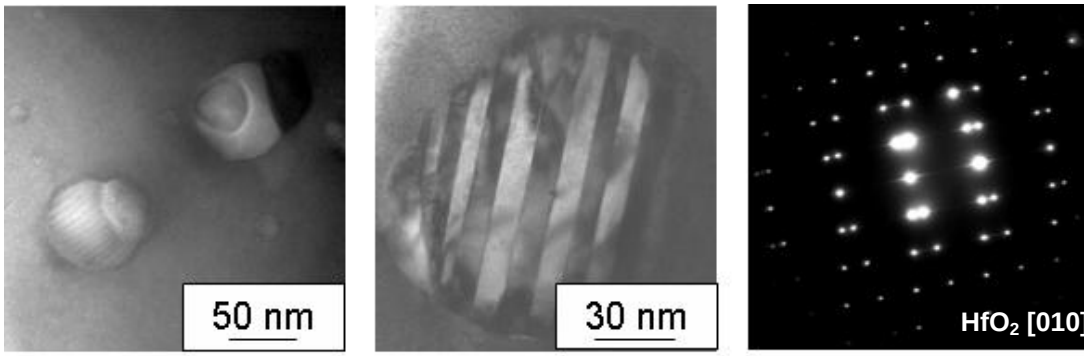

Fig. 10.27: Triple point junction in HB20 sample showing a) wet and b) clean grain boundaries.

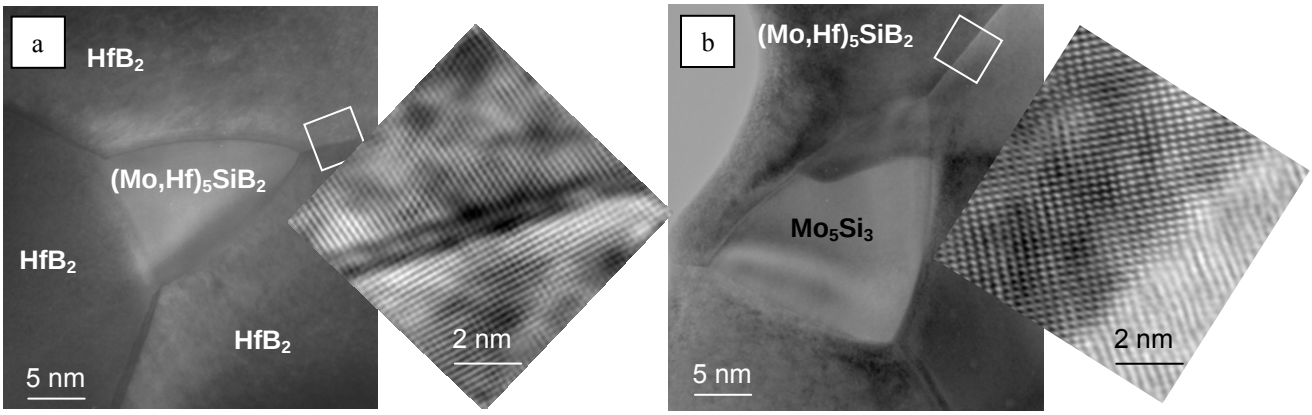

Fig. 10.28: BF-TEM image where the presence of (Hf, Mo)B_2 is indicated by arrow. On the right the corresponding EDS spectra.

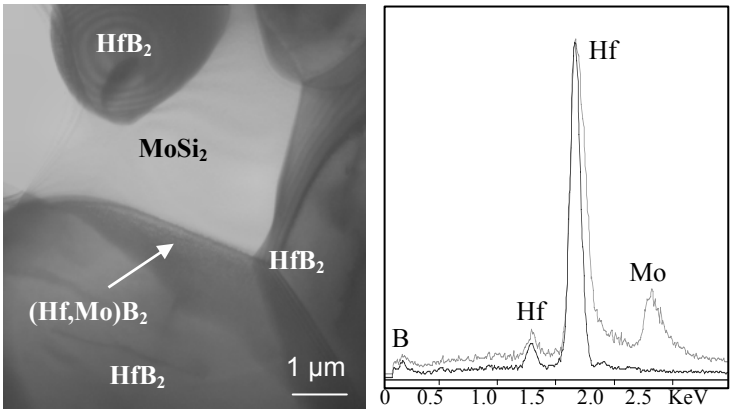

10.7 DENSIFICATION MECHANISMS OF Zr- AND Hf-BORIDES

For both the compositions, the addition of $MoSi_2$ was proved to be beneficial for the densification and the achievement of homogeneous microstructures. Actually, the comparison with typical grain sizes of monolithic zirconium and hafnium diboride, for which dimension of 10-20 µm are reported,[40] highlights that $MoSi_2$ particles hindered the matrices grain growth. Moreover, due to its transition brittle-ductile at temperatures over 1000 C,[41] it favoured the formation of porosity-free materials.

In order to understand the mechanisms of densification of borides doped with $MoSi_2$, it can be useful to resume the most significant findings.

- Firstly, the presence of secondary phases and solid solutions, as detected by SEM and TEM techniques, testifies that the constituent species are not that stable as widespread thought.

- In particular, the formation of Hf and Zr carbides suggests that the carbon-rich sintering environment is highly reactive
- The formation of (Zr or Hf, Mo)$_5SiB_2$ mixed phases indicates that diffusion of Zr, Hf and B occurs in molybdenum silicides.
- The development of (Zr,Mo)B_2 solid solutions, confirms a partial solubility of Mo into ZrB_2 and, on the other side, the detection of Mo traces into HfB_2 grains suggests that molybdenum is also partially soluble in hafnium boride matrix phase, even if to a lower extent compared to the other system.

Concerning the chemistry of the systems, the formation of MoB species during sintering is an indication of the interaction between residual B_2O_3, present as surface oxide, and the silicide. A possible reaction which can take place is

$$2\ MoSi_2 + 5/2\ O_2 + B_2O_3 \rightarrow 2\ MoB + 4\ SiO_2 \quad (8)$$

favourable in the whole temperature range.

Similarly, Mo_5Si_3, beside to be present in small amounts in the starting $MoSi_2$ powder, can also derive from interaction of $MoSi_2$ with oxygen-bearing species according to:

$$5\ MoSi_2 + 7/2\ O_2 \rightarrow Mo_5Si_3 + 7\ SiO_2 \quad (9)$$

Mo_5Si_3, in presence of boron-species, either B_2O_3, or B diffused from the matrix, could originate the Mo_5SiB_2 phase according to the following:

$$Mo_5Si_3 + B_2O_3 + C \rightarrow Mo_5SiB_2 + 2\ SiO + CO \quad (10)$$

Note that the inhibition of sintering in non-oxide ceramics is generally attributed to the presence of oxide impurities on the powder particle surface;[38] while the above mentioned reactions helps the removal of surface oxides, like B_2O_3, from the borides particle surfaces.

Actually, SiO_2 resulting from reactions 1-3 was hardly observed in the pressureless sintered ZrB_2-based materials. On the contrary silica species were quite abundant in the same system sintered by hot pressing or spark plasma sintering.[35,40] It was hypothesized that the highly reducing atmosphere of the furnace, due to C and or CO species, along with the slow sintering rate favoured the dissociation or carbothermal reduction of silica, owing to a late closure of open pores. Thus, the most probable reaction is:

$$SiO_2 + C = SiO(g) + CO(g) \quad (11)$$

for which a negative ΔG is calculated all along the temperature range and is also confirmed by previous specific studies on the reduction of silica by carbon,[42] which reports that this reaction proceeds via intermediate gaseous products.

The presence of a reducing atmosphere is also proved by the formation of Zr and Hf carbides which derive from the corresponding oxides:

$ZrO_2 + 3\ C \rightarrow ZrC + 2\ CO(g)$ (12)

$HfO_2 + 3\ C \rightarrow HfC + 2\ CO(g)$ (13)

For which a negative ΔG is reported starting from 1700°C.

Matter transfer mechanisms are strongly enhanced by the presence of liquid phases, whose formation is suggested by the irregular shapes of the new-formed phases, the wet interfaces and is foreseen by the phase diagram of the involved species.

The formation of a first eutectic temperature between SiO_2 and B_2O_3 is predicted to take place at 372°C,[43] but since in the final microstructure no Si-B-O phases were detected, it has to be supposed that a carbo-reduction occurred with formation of gaseous species as previously stated. If we consider silica to play a key part in the formation of liquid phases, eutectics are expected to occur at around 1680°C with ZrO_2 or HfO_2.[44,45] Nevertheless, also in this case, Si peak was not detected in either ZrO_2 or HfO_2 particles, so this reaction has to be ruled out and it can be confirmed that the oxides found in the final microstructure are due to pre-sintering oxygen impurities, with any further formation.

Considering the Mo-Si system,[19] if the actual composition slightly differs from the peritectic composition of either $MoSi_2$ or Mo_5Si_3, we have compresence of liquid phase and, at a composition of 55 at% of Si, an eutectic liquid is predicted at 1910°C between $MoSi_2$ and Mo_5Si_3. This temperature was achieved only in the system HfB_2-$MoSi_2$ sintered at 1950°C. Since the composite ZrB_2-$MoSi_2$ was sintered at 1850°C, lower eutectic temperatures have to be considered. To this purpose, the C-$MoSi_2$ pseudo binary phase diagram[20] reports the formation of an eutectic at around 1630°C.

Moreover, the Mo-Si-B ternary phase diagram, reported in Fig.10.29, redrawn after[46] shows the formation of three eutectic points. The first at 1350°C between $MoSi_2$-MoB-B-Si, the second at 1802°C between MoB-Mo_5Si_3-$MoSi_2$ and the third at 1885°C between Mo-MoB-Mo_5Si_3-Mo_5SiB_2. It is then clear that the formation of small amounts of such liquid is very probable.

However, it has to be considered that the just mentioned phase diagrams are calculated in standard conditions, that differs from the experimental environment. So the eutectic temperatures give just an indication of the temperatures at which a liquid phase could form.

The Mo-Si-B liquid phase formed allowed the dissolution, at least partial, of the boride matrix, followed by epitaxial reprecipitation of the $(M,Mo)B_2$ solid solution on the former MB_2 grains during cooling.

Fig. 10.29: Mo-Si-B ternary phase diagram redrawn after [46].

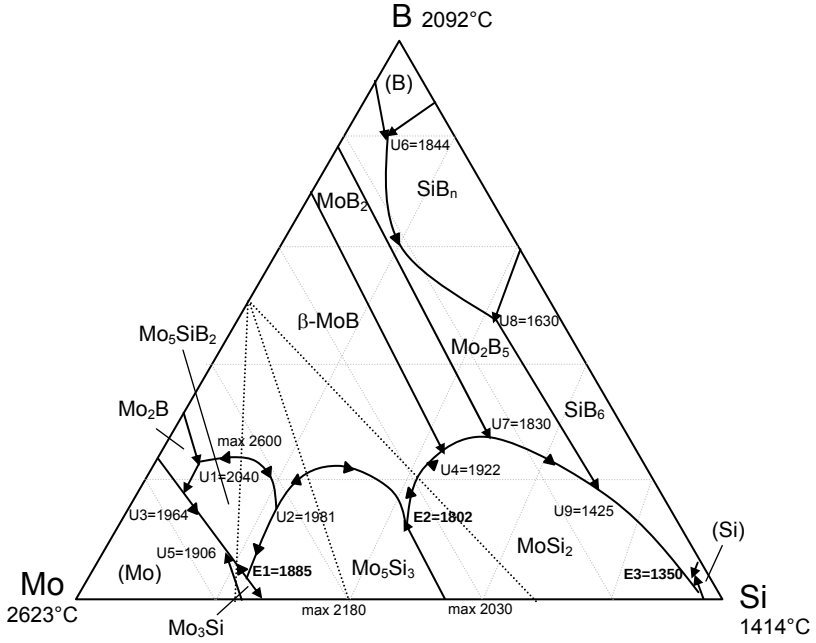

The matrix mean grain size further proves that in the ZrB_2-$MoSi_2$ system, these mechanisms are more active, leading to a coarser microstructure, i.e. 2.5 μm for ZrB_2-based composite, compared to 1.5 μm for HfB_2-based composite. For the HfB_2-$MoSi_2$ system the dissolution and reprecipitation occurred in lower extent, as the mean grain size of the sintered specimen is very similar to the dimension of the starting powder.

As demonstrated, the densification of Zr and Hf-B_2 doped with $MoSi_2$ took place mainly through a Mo-Si-B-O liquid phase, since all the conditions necessary for the occurrence of liquid phase sintering were satisfied:

- the presence of liquid phase at the sintering temperature was guaranteed, due to the formation of eutectic points below the sintering temperature;
- the mechanisms of solution of the matrix in the liquid and reprecipitation was proved by the presence of mixed phases in the sintered specimen, such as $(M,Mo)_5SiB_2$ and $(M,Mo)B_2$ solid solutions;

- the wetting of the matrix by means of the liquid was also confirmed by the wet grain boundaries.

10.8 CONCLUSIONS

Based on the discussion concerning the carbides it is concluded that:

I. Densification of Hf and Zr carbides doped with $MoSi_2$ does occur via liquid phase sintering which is constituted by transition metals silicides.

II. Mo_5Si_3 is likely to be the starting phase for the formation of Zr-Si or Hf-Si species as it has a larger solubility for IV Group transition metals carbides than $MoSi_2$.

III. Local Mo_5Si_3 formation may occur through different mechanisms: it is already present in the starting powder due to $MoSi_2$ oxidation or could form due to a carbon-rich environment.

IV. Zr completely substitutes Mo in Mo_5Si_3 and forms Zr_5Si_3, which in turn is transformed into Zr_2Si (if next to C sources) or ZrSi and $ZrSi_2$ (if next to Si sources). Therefore neither Mo_5Si_3 nor Zr_5Si_3 were found in the final microstructure.

V. Hf has a lower mobility than Zr and only partially substitutes Mo sites in the Mo_5Si_3 structure and hence $(Hf,Mo)_5Si_3$ was observed in the final microstructure

Based on the discussion concerning the borides it is concluded that:

I. Oxygen species are removed from the borides by effect $MoSi_2$, giving rise to MoB and SiO_2. This last is then carbo-reduced thanks to the favourable sintering environment.

II. The crucial presence of Mo_5Si_3, coming from $MoSi_2$ powder as oxidation product, allows the diffusion of B leading to the formation of Mo_5SiB_2. This last compound, together with $MoSi_2$, MoB and Mo_5Si_3, is expected to form liquid phases from 1350 to 1927°C in which Zr and Hf are partially soluble.

III. During cooling, epitaxial reprecipitation of the liquid on the matrix occurs with formation of a $(M,Mo)B_2$ solid solution surrounding the borides grains. This effect is more pronounced in the ZrB_2-based composite, due to a higher reciprocal solubility of Zr in the Mo-Si-B liquid and of Mo in the ZrB_2 grains.

References

1 H. O. Pierson: Handbook of refractory carbides and nitrides, (William Andrew Publishing/Noyes, Westwood, New Jersey, USA, (1996) 68.

2 T. Ogawa, K. Ikawa, J. Nucl. Mater. 105 (1982) 331.

3]P. Barnier, C. Brodhag, F. Thevenot, J. Mater. Sci. 21 (1986) 2547.

4 E. Min-Haga, W. D. Scott, J. Mater. Sci. 23 (1988) 2865.

5 H. J. Ryu, Y. W. Lee, S. I. Cha, S. H. Hong, J. Nuclear Appl. 352 (2006) 341.

6 W. B. Johnson, A. S. Nagelberg, E. Breval, J. Am. Soc. 74 (1991) 2093.

7 T. Tsuchida, S. Yamamoto, Solid State Ionics 172 (2004) 215.

8 K. H. Kim, K. B. Shim, Materials Characterization 50 (2003) 31.

9 A. Krajewski, L. D'Alessio, G. De Maria, Cryst. Res. Technol. 33 (1998) 341.

10 N. Nomura, T. Suzuki, S. Nakatani, K. Yoshimi, S. Hanada, Intermetallics 11 (2003) 51.

11 A. Sayir, J. Mat. Sci. Lett., 39 (2004) 5995.

12 M.M. Opeka, I. G. Talmy, E. J. Wuchina, J. A. Zaykoski, S. J. Causey, J. Eur. Ceram. Soc., 19 (1999) 2405.

13 E. Wuchina, M.Opeka, S. Causey, J. Spain, A. Cull, J. Routbort, F. Guitierrez-Mora, J. Mat. Sci., 39, (2004) 5939.

14 M.D. Sacks, C-A Wang, Z.Yang, A. Jain, J. Mat. Sci. 39 (2004) 6057.

15 R. Sakida, J. H. Perepezko, Metall. and Mater. Trans. A, 36 (2005) 507.

16 W. Hume-Rothery, “Atomic Theory for Students of Metallurgy,” Monograph and Report Series No. 3, The Institute of Metals, London (1969).

17 P. Silvestroni, “Fondamenti di Chimica”, Veschi Editore, Roma (1980) 532.

18 Concise Encyclopedia of the Structure of Materials, Ed. J.W. Martin, Elsevier (2006) 237.

19 A.B. Gokhale, G. J. Abbaschian, J. Phase Equilib. 12 (1991) 493.

20 X. Fan, K. Kack, T. Ishigawi, Mat. Sci. Eng. A 278 (2000) 46.

21 H. Okamoto, Bull. Alloy Phase Diag. 11 (1990) 513.

22 J. –C Zhao, B. P. Bewlay, M. R. Jackson, Q. Chen, J. Phase Equilib. 21 (2000) 40.

23 F*A*C*T, Facility for the Analysis of Chemical Thermodynamics, www.crct.polymtl.ca/fact/.

24 C. Mroz, Am. Ceram. Soc. Bull. 73 (1994) 141.

25 M. M. Opeka, I. G. Talmy, and J. A. Zaykoski, J. Mater. Sci. 39 (2004) 5887–904.

26 M. Pastor, Boron and Refractory Borides, Edited by V. I. Matkovich. Springer, New York (1977) 457–93.

27 S.-K. Woo, I.-S. Han, H.-S. Kim, E.-S. Kang, J.-H. Yang, and C.-H. Kim, J. Korean Ceram. Soc. 33 (1996) 259.

28 Monteverde, A. Bellosi, and S. Guicciardi, J. Eur. Ceram. Soc. 22 (2002) 279.

29 Monteverde, S. Guicciardi, and A. Bellosi, Mater. Sci. Eng. A346 (2003) 310.

30 A. L. Chamberlain, W. G. Fahrenholtz, and G. E. Hilmas, Advances in Ceramic Matrix Composites IX, Ceramic Transactions, Vol. 153, Edited by N. P. Bansal, J. P. Singh, W. M. Kriven, and H. Schneider, The American Ceramic Society, Westerville, OH (2003) 299–308.

31 D. Sciti, M. Brach, and A. Bellosi, J. Mater. Res. 20 (2005) 922.

32 Y. Yan, Z. Huang, S. Dong, D. Jiang, J. Am. Ceram. Soc. 89 (2006) 3589.

33 P.S. Kislyi, M. A. Kuzenkova, Powder Metallurgy and Metal Ceramics, 4 (1965) 23.

34 D. Sciti, M. Brach, A. Bellosi, Scripta Mater. 53 (2005) 1297.

35 D. Sciti, L. Silvestroni, A. Bellosi, J. Mater. Res. 21 (2006) 1460.

36 R.A. Cutler, S. J. Schneider Jr. (Ed.), Ceramics and Glasses, Engineered Materials Handbook, Vol. 4., ASM International, Materials Park, OH (1991) 787-803.

37 M. Gasch, D. Elleby, E.I. Irby, S. Beckam, M.Gusman, S. Johnson, J. Mat. Sci. 39 (2004) 5925.

38 F. Monteverde, S. Guicciardi, A. Bellosi, Mat Sci Eng A346 (2003) 310.

39 F. Monteverde, A. Bellosi, J. Mat. Res. 19 (2004) 3576.

40 D. Sciti, L. Silvestroni, M. Nygren, J. Europ. Ceram. Soc. 28 (2008)1287.

41 Y.-L. Jeng, E.J. Lavernia, J. Mater. Sci. 29 (1994) 2557.

42 J.-G. Lee and I.B. Cutler, Ceram. Bull. 54 (1975) 195.

43 P. Doerner, L. J. Gauckler, N. Krieg, N. L. Lukas, G. Petzow, J. Weiss, CALPHAD: Comput. Coupling Phase Diagrams Thermochem., 3 (1979) 241.

44 U. N. Parfenkov, R.G. Grebenshchikov, N. A. Toropov, Dokl. Akad. Nauk. SSSR, 185 (1969) 840.

45 N. A. Toropov, F. Ya, Galakov, Uch. Zap. Kazan. Goa. UNiv., 2 (1965) 158-161.

46 S. Katrych, A. Grytsiv, A. Bondar,P. Rogl, T. Velikanova, M. Bohn, J. Alloy and Comp. 347 (2002) 94.

CHAPTER 11

MECHANICAL PROPERTIES AND OXIDATION

In the first part of this chapter the mechanical properties of carbides and borides of Zr and Hf containing 5-20 vol% of $MoSi_2$ are presented and discussed. In the second part, the results relative to oxidation tests in arc-jet device of two specific compositions are treated. The composites characterized by this method are HfB_2 and HfC containing 5 vol% of $MoSi_2$

The mechanical properties for selected samples are reported in Tab. 11.I. In the first two columns microstructure details are reported too, in order to correlate the mechanical behaviour to the morphological features of each sample. Due to the high level of porosity, the mechanical characterization of monolithics and ZC5 composite was not carried out.

Tab. 11.I: Relative density (ρ), Mean grain size (M.g.s), Vickers Hardness (HV 1.0), Young' modulus (E), flexural strength (σ) room temperature, 1200 and 1500°C of selected samples.

Sample	ρ	M.g.s.	HV1.0	E	K_{Ic}	σ_{RT}	$\sigma_{1200°C}$	$\sigma_{1500°C}$
	%	μm	GPa	GPa	MPa·m$^{1/2}$	MPa	MPa	MPa
ZC20	**95.2**	**5.75**	12.7±1.6	346±4	3.4±0.2	272±12	156±6*	-
HC5	**98.1**	**3.9**	15.2±1.0	434±4	3.6±0.1	465±45	408±31*	241±112*
HC10	**97.8**	**2.9**	16.1±0.4	415±4	3.5±0.3	452±90	357±21*	306±18*
HC20	**96.5**	**2.9**	15.5±0.9	385±4	3.4±0.3	383±74	350±78*	299±71*
ZB5	**96.0**	**2.6**	15.2±1.0	516±4	2.9±0.1	569±54	533±87	488±46
ZB20	**99.4**	**2.5**	16.0±0.4	489±4	4.0±0.6	531±46	655±17	500±58
HB5	**96.8**	**1.6**	19.1±0.5	442±4	4.0±0.3	472±10	501±89	486±19
HB20	**97.8**	**1.5**	18.8±0.3	482±4	4.1±0.4	405±72	548±56	577±39

*tests carried out in Ar protective environment

11.1 MECHANICAL PROPERTIES

11.1.1 ZrC-based composites

The hardness of ZC20 sample, ~13 GPa, was well below the values reported in literature for monolithic zirconium carbide (~25 GPa) and various ZrC-based

composites (15-17 GPa).[1-3] This property was certainly affected by the presence of soft secondary phases, as $MoSi_2$ and Zr-silicides, as well as by residual porosity and the relatively coarse microstructure.

Young's modulus was 346 GPa, slightly below the 400 GPa reported for the monolithic material.[4] The reasons for this low value find origins in a discrete amount of porosity and presence of secondary phases, such as Zr_xSi_y which are expected to be softer (E ~200 GPa).[5]

Fracture toughness was in the range of the values reported in the literature for ZrC-based composites (2.6-5.8 $MPa \cdot m^{1/2}$),[2,3,6] despite different compositions and densification techniques. No evidence of toughening mechanisms like thermal residual stress, crack deflection or crack pinning was observed.

The flexural strength tested at room temperature was around 270 MPa. As the fractographic analysis did not evidence any critical flaw, such as large inclusions or coarsened grains, it can be concluded that the strength was mainly affected by the low fracture toughness, the presence of residual porosity and the coarse microstructure. It must be pointed out that the value obtained is in the range, or even higher, than those reported in the literature for other ZrC-based materials (220-320 MPa).[2]

Concerning the high temperature properties for ZrC, to the best of the authors' knowledge there is no data available in the literature. For the high temperature strength test, ZrC-$MoSi_2$ composite was preliminarily subjected to a conventional test in air at 1200°C. However, despite the short permanence at this temperature, the bar was reduced to a whitish powder as a consequence of catastrophic oxidation already before the bending test. According to the literature, monolithic ZrC suffers from pest oxidation in the temperature range 1100-1600°C.[7] The addition of $MoSi_2$ was expected to improve the oxidation resistance by way of a silica layer formation. The well known oxidation reaction of $MoSi_2$ is:[20]

$$MoSi_2 + 7/2\ O_2(g) = 2SiO_2 + MoO_3(g) \quad (1)$$

At T≥1200°C, the formation of silica should be therefore fast enough to protect the sample[8,9]. Although the oxidation mechanisms of this composition deserve deeper investigations, the analysis of the powdered sample revealed instead that no silica formed during heating. This feature was observed for other carbide-$MoSi_2$ compositions and led to the conclusion that, in presence of a carbide matrix, an active oxidation of $MoSi_2$ occurs, with production of volatile SiO instead of protective SiO_2.

Accordingly, for the subsequent high temperature bending tests the chamber was flushed with Argon in order to minimize contact of the samples with oxygen. Nonetheless, for composition ZC20 the flexural strength values at 1200°C decreased to about 43% of the room temperature value and the samples were covered by a whitish layer implying that they reacted with residual oxygen present in the test chamber. It is likely that the decrease of strength is mostly due to new defects introduced by oxidation. An examples of the fracture surfaces after tests at 1200°C is shown in Fig. 11.1. At 1500°C, despite the Ar flux, the bars were broken apart by the rapid oxidation already before the bending tests.

When the bending tests were carried out, the load-displacement curves were linear up to fracture.

Fig. 11.1: Fracture surface of ZC20 sample after bending test at 1200°C in Ar. Any trace of silica protective phase was detected by EDS analysis.

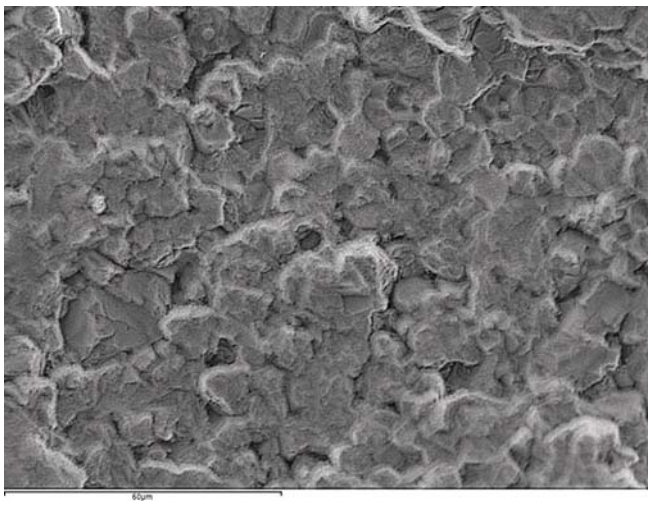

11.1.2 HfC-based composites

The properties of the composites are summarized in Tab. 11.I.

The hardness was very close among the samples tested, in the range 14-16 GPa and substantially lower than values reported for monolithic HfC (22-23 GPa).[4]

The reason for this difference are the lower hardness of the $MoSi_2$ phase, (9-11 GPa) and the presence of some residual porosity.

Young's modulus showed an almost linear decrease with increasing the $MoSi_2$ content, probably due to increasing content of the lower stiffness phase, i.e. $MoSi_2$, and the presence of residual mixed phases, such as the Hf-Mo -Si phase. As a reference, a value of about 420 GPa is reported in literature for a hot pressed HfC monolithic material.[10]

The fracture toughness of the composites can be considered equivalent from the statistical point of view, even if a slight decrease of the mean value with increasing the $MoSi_2$ content is apparent from data in Tab. 11.I.

The room temperature flexural strength is very close for HC5 and HC10, whilst HC20 showed a lower value. Typical critical flaws observed after strength tests were large $MoSi_2$ agglomerates, shown in Fig. 11.2, which had the tendency to form in the $MoSi_2$ richer compositions, i.e. HC10 and HC20.

Fig. 11.2: Critical defect on the fracture surface of HC10 sample after bending test at room temperature.

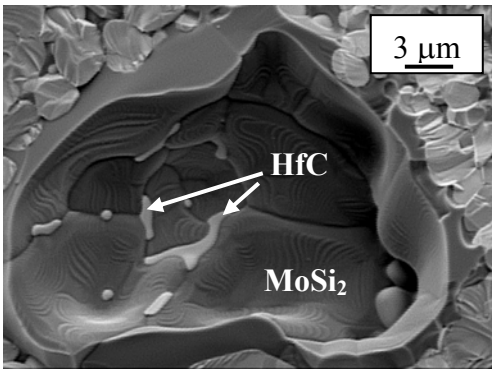

Therefore, the factors inducing the strength decrease with increasing additive content could be basically the slight decrease of toughness, the increasing of $MoSi_2$ agglomerates size and the exaggerated grain growth of HfC. Prismatic HfC grains of dimensions around 20 μm were in fact observed to act as critical defects, as indicated in Fig. 11.3. The presence of such triangular grains was due to preferential growth along the {111} planes, which are the most densely populated and favored to grow during thermal treatment. Introducing an ultrasonication step in the powder treatment, it was obtained the double effect of improved dispersion of the two powders and rounding off of HfC grains. The microstructure of the composite produced with ultrasonication is reported in Fig.11.4b next to the analogous produced by only conventional milling in Fig. 11.4a. The mean grain size passed from 2.9 to 1.8 μm and, as a consequence, the flexural strength raised up to 538±22 MPa, compared to the 452±90 MPa. Beside the increase of room temperature strength of about 100 MPa (16%), the standard deviation decreased of 75% due to a more homogeneous microstructure and the elimination of larger grains.

Fig. 11.3: Large HfC prismatic grains, which acted as critical defects during the fracture of HC10. The two images on the right represent the positive and negative side of the same defect observed in the two broken pieces of a bar.

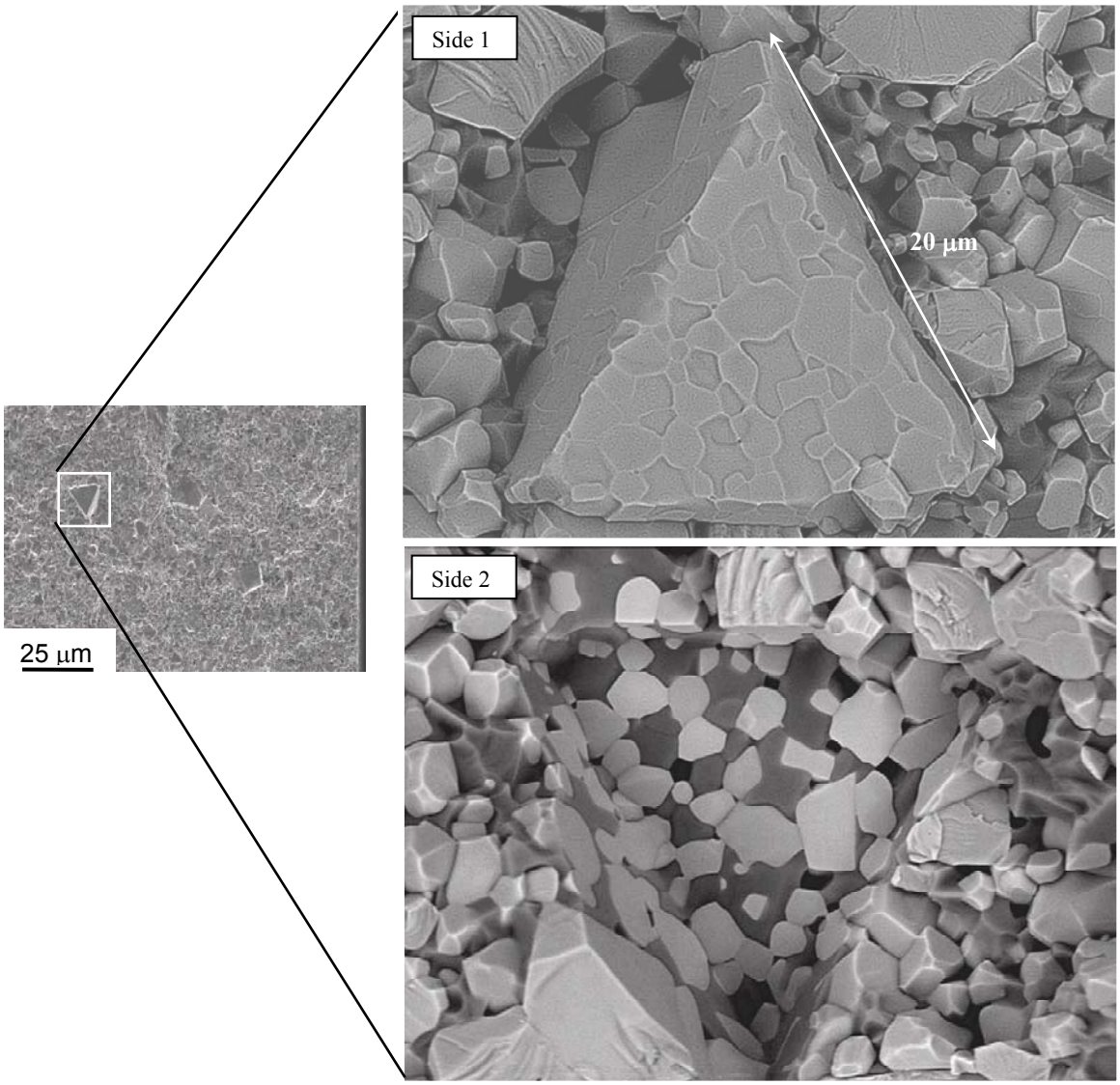

Fig. 11.4: Microstructure of HC10 sample a) without and b) with the ultrasonication of the powders before ball milling. Note the rounded and homogeneous microstructure and the absence of exaggerated grain growth in b).

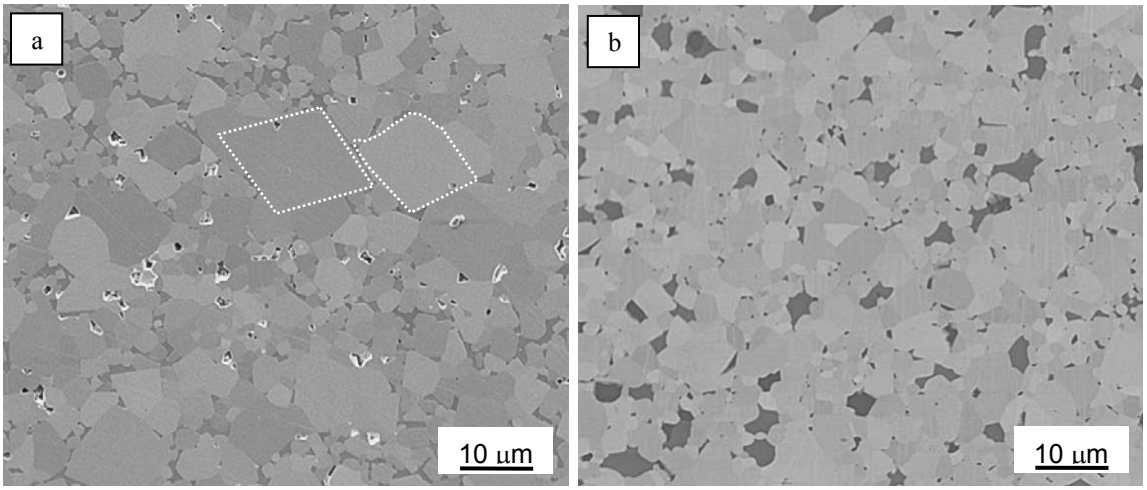

Fig. 11.5: Fracture analysis after high temperature bending tests of HfC-based ceramic composites. On the left, appearance of the bars and on the right, fracture surface after exposure at 1200 and 1500°C. a) and b) HC5 tested at 1200°C, c) and d) HC5 tested at 1500°C, e) and f) HC20 tested at 1200°C, g) and h) HC20 tested at 1500°C.

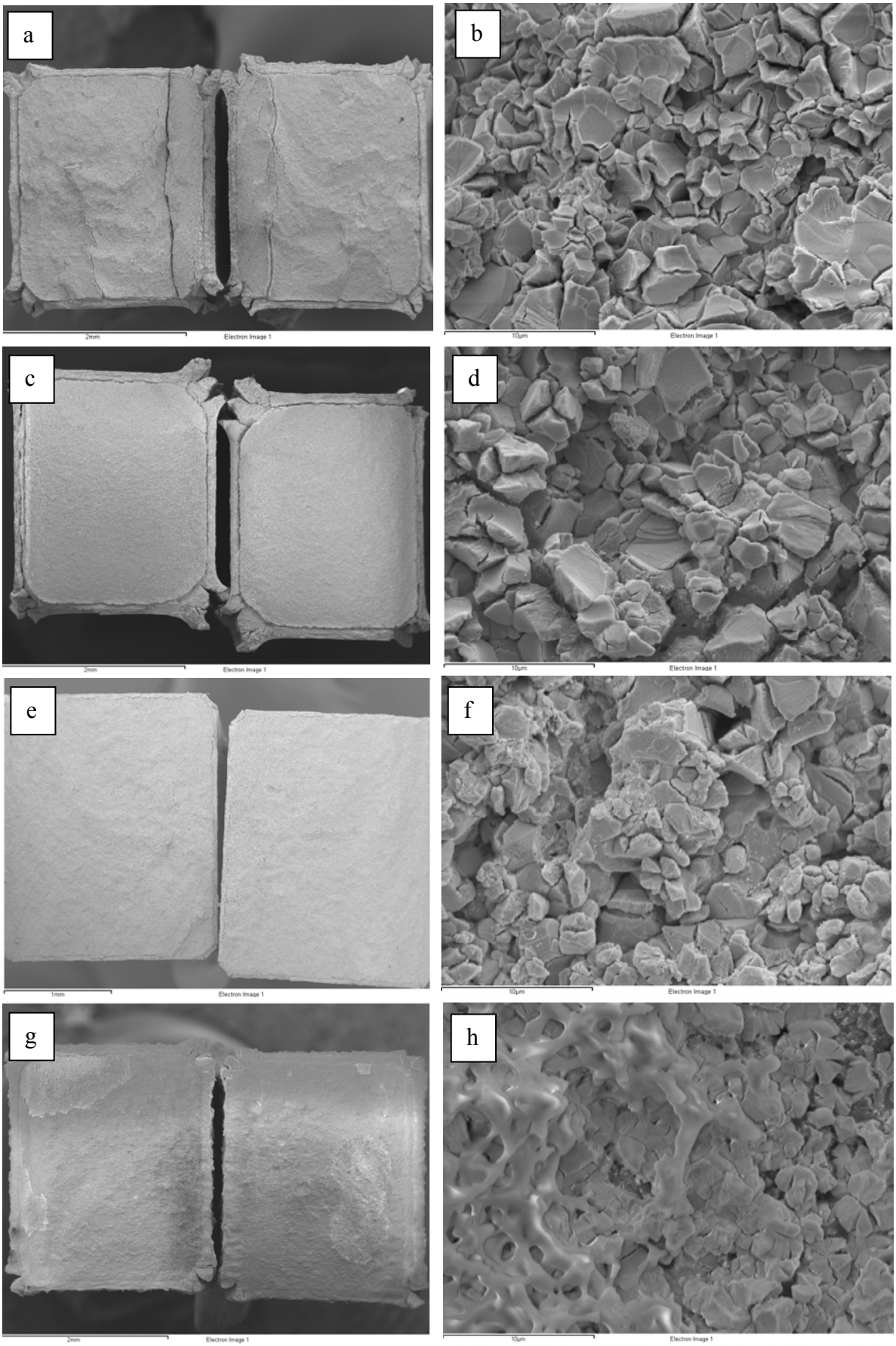

Previous strength tests at 1200°C in air revealed that these composites, as the ZrC-based, were strongly damaged by oxidation, as observed for ZrC-composites. For this reason, the tests presented in Tab. 11.I at 1200 and 1500°C were carried out in partially protective Ar atmosphere. For all the samples there was a decrease of the strength values both at 1200°C, and at 1500°C, a decrease which was more pronounced for HC5 sample.

As a comparison, examples of broken specimen after high temperature flexural strength are reported in Fig. 11.5. It can be noticed that for the sample HC5, in Fig. 11.5a-d, cracking at the corners of the bars occurred. It is probable that the good adherence of the external oxidized layer to the unreacted bulk did not allow stress relaxation by spalling, leading to the opening of the cube edges and formation of the Maltese cross. This phenomenon was also previously reported for the oxidation of TaC-based materials and other HfC-based ceramics.[11,12] The Maltese cross was less pronounced in the external scale of HC20, in Fig. 11.5e-f, because of the presence of SiO_2-glassy phase that favoured the stress relaxation associated to the phase transformation from HfC to HfO_2. The fractured surface of the oxidized samples testified the presence of glassy phase in HC20, which provides a smooth and gluey appearance compared to the rough aspect of HC5.

For all the samples and for each tested temperature, the load displacement curves were linear up to fracture.

11.1.2.1 Nanoindentation

Depth-sensing indentation (DSI) technique allows to measure mechanical properties such as hardness and Young's modulus in very small volumes. In the case of composite microstructures which are not too coarse, varying the peak load should permit to extract the mechanical properties of the constituent phases and to test also the composite mechanical behaviour as a whole. In this section, the hardness behaviour of two HfC-based composites, HC10 and HC20, is studied by nanoindentation. On these HfC-$MoSi_2$ composites, depth-sensing indentation (DSI) tests were carried out with the aim to get the hardness of the constituent phases. By applying simple composite hardness rules, the expected composite hardness was then compared to the experimental results.

The values extracted for $MoSi_2$ phase from the composites were also compared to the values extracted from monolithic $MoSi_2$ (details on this material can be found in Chapters 5 and 6).

An example of low-load indentations grid in composite HC20 is shown in Fig. 11.6a. By SEM scrutiny, the indentations on the composites were selected according to the indented phases. For peak load ≥50 mN, most of the indentations included both HfC and $MoSi_2$ phases, see Fig. 11.6b. Even if it was not possible to estimate the volume fractions of the indented phases, these indentations were taken as representative of the DSI hardness of the composites as a whole. For peak load<50 mN, the indentations were small enough to be mainly confined into the two phases, so that, after selection of well-positioned indentations, the hardness of HfC and $MoSi_2$ could be extracted, see Fig. 11.6c.

Fig. 11.6: Indentation tests on HC20 sample. a) An example of 5 mN grid, b) a 200 mN indentation which deformed both the phases, c) example of 5 mN indentations which interested one single phase, $MoSi_2$ (dark) or HfC (bright).

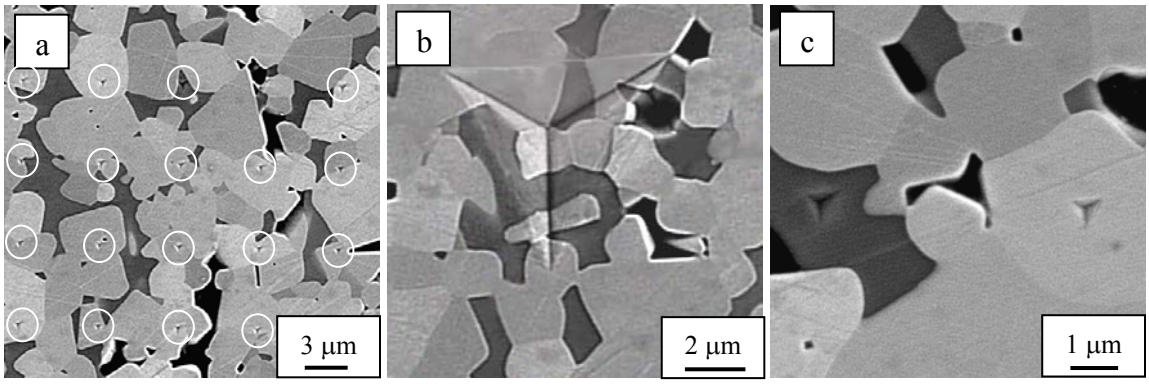

In Fig. 11.7, the DSI hardness results as obtained on composites HC10 and HC20 are shown as a function of peak load, composite and indented phase. As already stated, for peak load ≥50 mN the DSI hardness refers to the macroscopic hardness of the composites. As can be seen in the plot of Fig. 11.7, composite HC10 was harder than composite HC20 due to its lower content of $MoSi_2$ phase. The DSI hardness of both composites significantly decreased when the peak load was increased, a phenomenon known as indentation size effect (ISE).[13] For peak loads <50 mN, the hardness values refer to each single constituent phase. Regarding the HfC phase, the mean values of the DSI hardness were in the range 30-35 GPa. The HfC hardness was statistically independent on the composite, but affected by ISE. The indentation size effect and the high density of our materials can give reasons for the high HfC hardness we measured with respect to the published Vickers results for this phase: from 20 to 29 GPa for bulk materials[4,14] and from 20 to 30 GPa for deposited film.[15] The hardness of the $MoSi_2$

phase was in the range 19-24 GPa and independent on the tested composite. The indentation size effect was statistically assessed for the $MoSi_2$ phase in HC10 but not confirmed in HC20. The DSI hardness of the $MoSi_2$ phase was higher than that reported for a monolithic $MoSi_2$ ceramics.[16]

In order to evaluate the overall effect of residual stress and of the eventual $MoSi_2$ confinement by effect of HfC, nanoindentation tests were performed also on monolithic $MoSi_2$; the results are reported in Fig. 11.8 and the indentation size effect is well evident.

Fig. 11.7: Hardness measurements as a function of applied load, material and interested phase, as incated by the legend. The grey rectangle indicates Vickers hardness measured on the two composites HC10 and HC20.

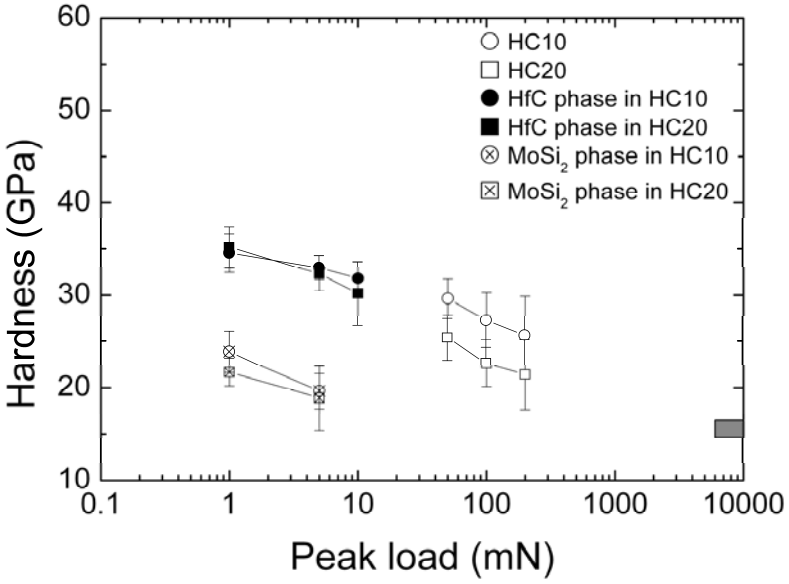

Fig. 11.8: $MoSi_2$ Nanohardness as a function of the applied load and tested material. The grey rectangle indicates Vickers hardness measured on the monolithic $MoSi_2$. (mean value ± standard deviation).

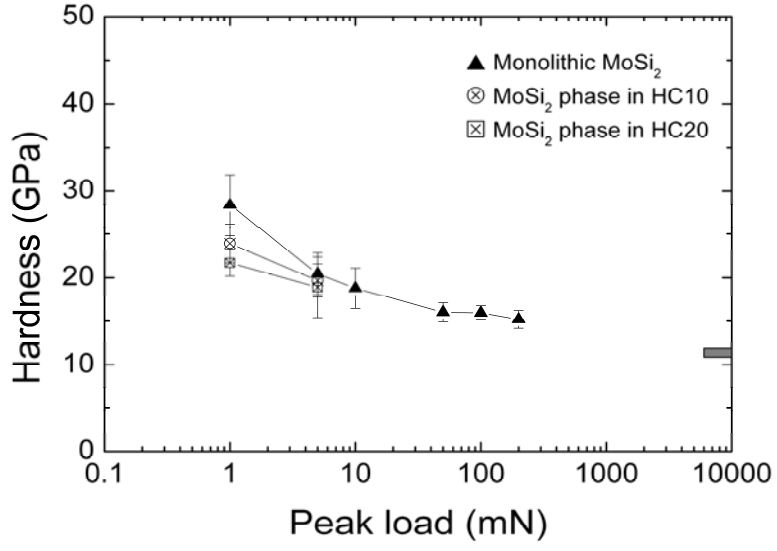

Comparing the values obtained from monolithic $MoSi_2$ and those extracted by the two composites, it can be deduced that they agree in the three materials at 5 mN, whilst at 1 mN some discrepancy can be observed. In the composites lower values were obtained, probably due to residual stress or to a different surface finishing, which is a critical parameters when such small volumes are investigated (300-600 nm). No confinement effect was observed because, if this was the case, the hardness of the $MoSi_2$ phase in the composites should have been higher due to surrounding harder HfC phase. For the monolithic material, the Vickers hardness was 11.4±0.3 GPa, compatible to the values reported in the literature.

As shown, DSI tests allowed to measure the hardness of the constituent phases and, by increasing the peak load, also the hardness of the composites as a whole. Theoretically, the hardness bounds of a composite (H_c) can be calculated starting from the hardness of the constituent phases (H_{HfC}, H_{MoSi2}) according to simple "series" and "parallel" models:[17]

$$H_c = v_{HfC} H_{HfC} + v_{MoSi2} H_{MoSi2} \quad (2)$$

$$\frac{1}{H_c} = \frac{v_{HfC}}{H_{HfC}} + \frac{v_{MoSi2}}{H_{MoSi2}} \quad (3)$$

where v_{HfC} and v_{MoSi2} are the volumetric fractions of the phases. In order to account for the indentation size effect, the model of Nix and Gao[18] was applied to the hardness of the HfC and $MoSi_2$ phase. According to this model, the hardness (H) of a material varies with the penetration depth (h_c) as:

$$H = H_0 \sqrt{1 + \frac{h^*}{h_c}} \quad (4)$$

where H_0 is the intrinsic hardness and h^* a characteristic length. The fitting equations obtained applying eq. (3) to the hardness data of the HfC and $MoSi_2$ phases were then inserted in eqs. (2) and (3) to obtain the composite hardness bounds as a function penetration depth. To compare these bounds with the experimental results, the effect of the small amount of porosity (p) of the composites had to be taken into account. The experimental hardness results were therefore corrected to obtain the hardness of the full-density materials (H_0) according to:[13]

$$H = H_0(1-p)^2 e^{-bp} \quad (5)$$

where *b* is a constant depending on the pore's shape, which was taken as 0.35.[13]

The comparison between the calculated bounds and the experimental results is shown in Fig. 11.9. Considering all the hypotheses which were made, the agreement should regarded as quite good, particularly for HC10 (Fig. 11.9). DSI tests combined with the composite theory seem therefore to be suitable tools for measuring, forecasting and verifying composite properties starting from the measured properties of the constituent phases.

Fig. 11.9: Experimental composite hardness as a function of penetration depth for composite HC10. The solid lines represent the upper, eq. (1), and lower bounds, eq. (2), for composite hardness. Points and error bars represent mean±1 standard deviation.

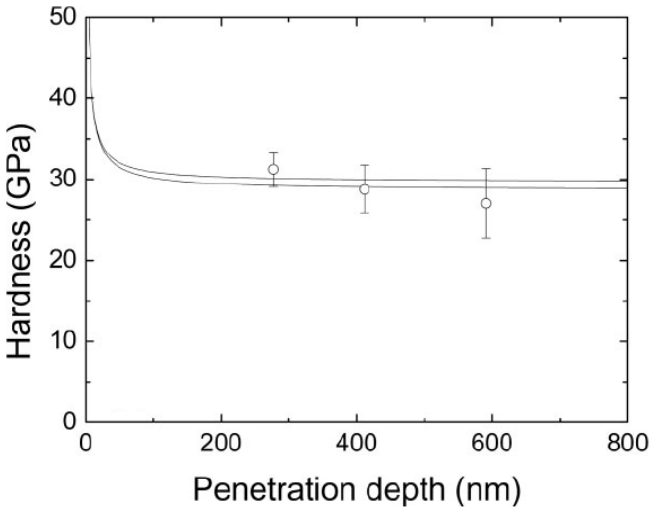

Concluding, $MoSi_2$-containing HfC composites were characterized by depth-sensing indentation tests to evaluate the hardness behavior of the composites and of the constituent phases. For the composites hardness, it was shown that a higher $MoSi_2$ content lowered the hardness of the composite. Moreover, each composite showed an indentation size effect, which was further confirmed by the Vickers hardness whose values were much lower that those measured by DSI tests. By SEM examination, selected indentations allowed to separately extract the hardness of HfC and $MoSi_2$. It was shown that the HfC hardness exhibited an evident ISE with values ranging from 30 to 35 GPa. The hardness as measured by DSI tests in the $MoSi_2$ phase were compared with those measured in the same way on a monolithic $MoSi_2$ material. At the smallest peak load, a difference was observed between the hardness of the monolithic $MoSi_2$ and the same phase in the composites. This difference could be due to residual thermal stresses but further investigations are required to confirm this

hypothesis. The experimental hardness results on the composites were compared with the composite bounds calculated starting from the values of the constituent phases and the agreement was found to be very good.

11.1.3 ZrB_2- based composites

The thermo-mechanical properties of the tested materials are reported in Tab. 11.I.

As in the previous cases, the microhardness was mainly affected by the presence of a relatively soft phase as $MoSi_2$ (9–11 GPa). The expected decrease of hardness with increasing the $MoSi_2$ contents was counterbalanced by an increase of the final density, therefore hardness values were not significantly different for $MoSi_2$ content between 5 and 20 vol%.

The Young's modulus values were quite high as a result of the high stiffness of the constituent phases, with the highest value measured on the ZB5 sample. The values found for the composites are comparable to those reported for monolithic hot pressed ZrB_2.[19]

The fracture toughness data have to be compared with a value of 2.8 MPa $m^{1/2}$,[20] of a monolithic ZrB_2, and indicate that only in ZB20, which achieved a value of 4 MPa·$m^{1/2}$, the addition of $MoSi_2$ particles activated some significant toughening mechanisms such as crack deflection, residual stresses, and so on. This was likely due to the difference in the CTEs between the ZrB_2 matrix[21] and the $MoSi_2$ particles[22] combined with a sufficient volumetric fraction of the $MoSi_2$ phase.

The room-temperature strength was 569 and 531 MPa for ZB5 and ZB20, respectively. There are few or no reports on strength results of pressureless sintered Zr-borides. A values of 444±30 MPa has been recently reported for a pressureless sintered ZrB_2 monolithic sample,[20] which is close to the results presented in this work. Despite the higher mean grain size, the ZrB_2-based composites were generally stronger than HfB_2-ones, at room temperature. Furthermore, it can be observed that, at room temperature, the increase of $MoSi_2$ content caused a decrease of strength for both the borides. This features was already found for HfC-$MoSi_2$ composites and, as for that case, it was attributed to the formation of large agglomerates of the $MoSi_2$ phase, which acted as critical defects.

The beneficial effect of $MoSi_2$ was disclosed at high temperature. Strength values measured at 1200°C were close to, or even higher, than those found at room temperature. At 1200°C, the specimens showed an increase in strength and a decrease

in dispersion. These effects were attributed to partial healing of surface defects from silica glass formed during the test, as confirmed by the fractographic study of the fractured bars (not shown). At this temperature, the formation of silica was a consequence of $MoSi_2$ oxidation.[23] At 1500°C, the strength values were in the range of 450-500 MPa. After the test, all the sample surfaces were found to be coated by a silica layer, likewise for the materials tested at 1200°C. The load-displacement curves, shown in Fig. 11.10, were linear up to fracture both at 1200 and at 1500°C, confirming the high refractoriness of the constituent phases.

Fig. 11.10: Typical load–displacement curves of ZB20 for 1200 and 1500°C strength tests in air.

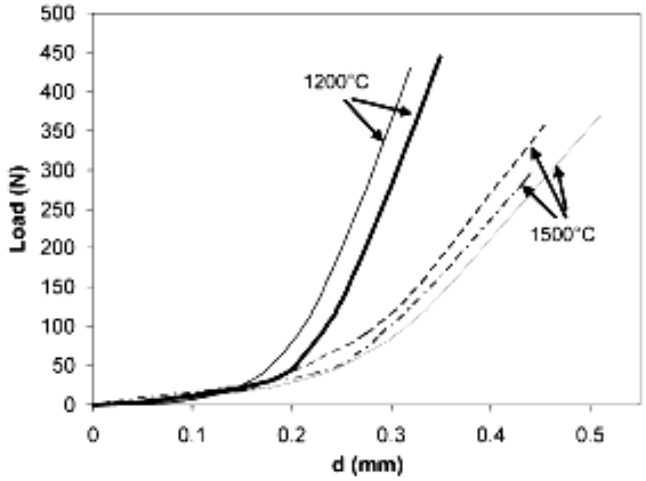

Fig. 11.11: Comparison of flexural strength values from room temperature to high temperature among different ZrB_2 materials sintered with various sintering additives or techniques.

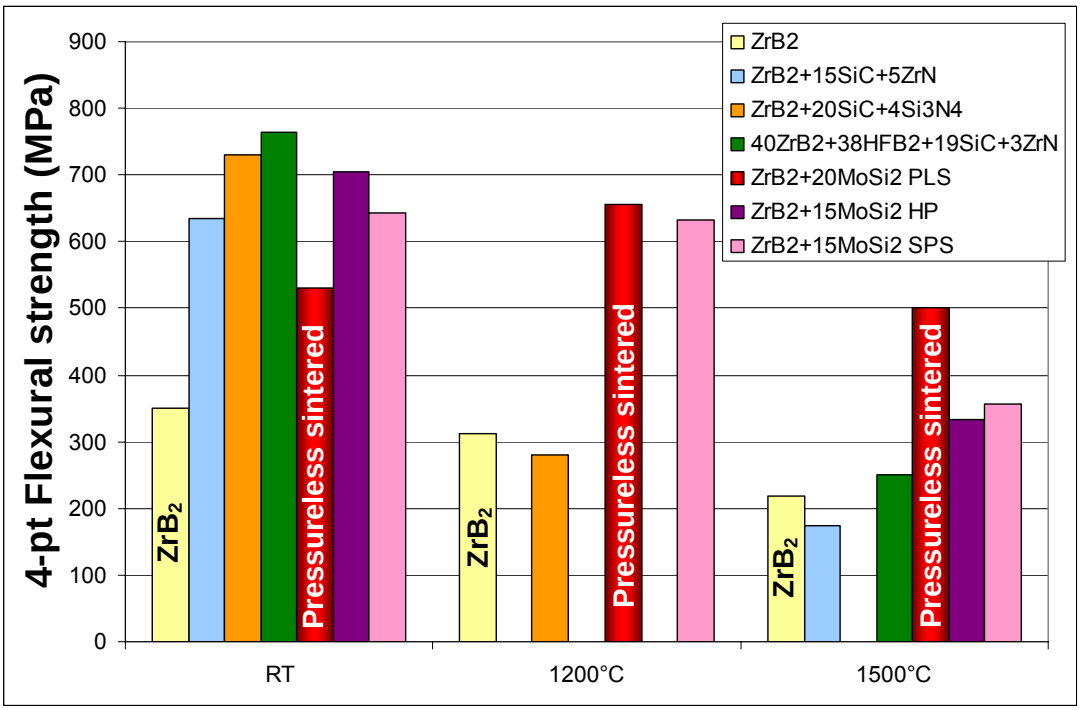

It is worth noting that high temperature strength values of ZrB_2-$MoSi_2$ composites were superior to those of ZrB_2-based materials added with Si_3N_4, Ni, SiC, or other ceramic additives,[24-27] independently from the sintering method (hot pressing or spark plasma). In Fig. 11.11 the flexural strength of ZrB_2-based materials are plotted. It can be observed that, if at room temperature composites containing SiC, ZrN or Si_3N_4 are stronger, at high temperature the pressureless sintered ZrB_2-$MoSi_2$ materials possess a superior strength resistance.

11.1.4 HfB_2- based composites

Mechanical properties for HfB_2-based ceramics are summarized in Tab. 11.I, for the compositions of interest.

The microhardness of the composites was negatively affected by the addition of $MoSi_2$ and some residual porosity. The expected decrease of hardness with increasing the $MoSi_2$ contents was counterbalanced by an increase of the final density, therefore hardness values were not significantly different for $MoSi_2$ doping level of 5 and 20 vol%. HfB_2-based composites were harder (~18 GPa) than the corresponding ZrB_2-based composites (~16 GPa), probably due to the lower mean grain size and the higher hardness of the hafnium boride matrix compared to the zirconium boride one.

Concerning Young's modulus, values for the tested materials were quite high (442-489 GPa, Table 11.I), thanks to the high stiffness of the constituent phases. The values found for all the samples are comparable to those reported for monolithic hot pressed HfB_2.[19,28,29]

The measured values of fracture toughness (3-4 $MPa \cdot m^{1/2}$) are in agreement with those reported in the literature for these materials, even if obtained with different sintering technique and sintering aids.[26,30] As transgranular fracture was observed for all the compositions, it can be concluded that the addition of $MoSi_2$ did not have any significant effect on the crack propagation behaviour of these specimens.

To study the crack front interactions with the microstructure, a 98 N Vickers indentation was introduced onto the polished surface of the material. As can be noticed in Fig. 11.12, the crack propagated mainly transgranularly and only sporadically crack bridging phenomena were observed.

Fig. 11.12: Crack path generated by a 98 N Vickers indentation on HB20 sample. Arrows indicate crack bridging. Crack propagation from right to left.

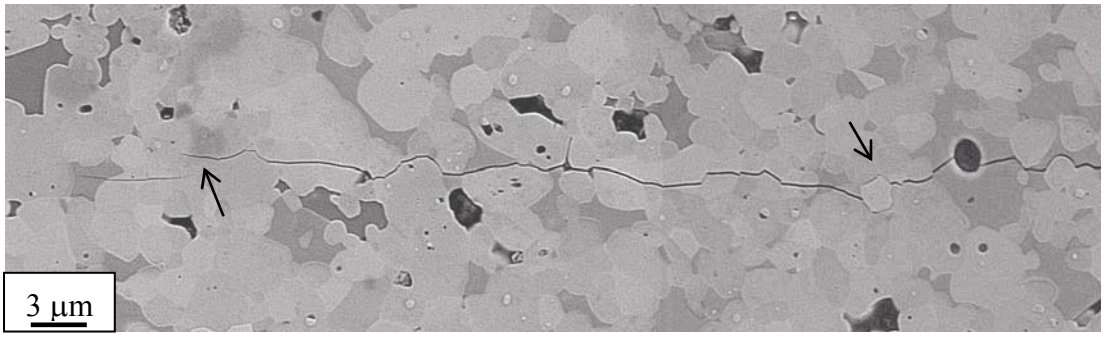

There are very few reports on strength results for pressureless sintered Hf-borides. As mentioned in the previous section, the ZrB_2-based composites were generally stronger than HfB_2-ones at room temperature. HfB_2-based compositions were in fact more prone to formation of voids and large $MoSi_2$ agglomerates (Fig. 11.13a), during the forming stage, probably due to a different density of the two phases (6.31 g/cm^3 for $MoSi_2$ and 11.18 g/cm^3 for HfB_2) which led to phase segregation. As a matter of fact, it can be observed that at room temperature the increase of $MoSi_2$ content caused a decrease of strength for both the borides due to the higher probability to have agglomerates which act as critical defects.

For Hf-borides (HB5 and HB20), a monotonic increase of strength was observed with increasing the test temperature. At 1500°C, the strength values were in the range of 500-580 MPa (Tab. 11.I). Possible causes are crack healing and/or compressive stresses generated by formation of a surface silica layer, due to $MoSi_2$ oxidation. Fractographic study of the fractured bars (see Fig. 11.13b) confirmed that at these temperatures (1200 -1500°C), significant formation of silica occurred as a consequence of $MoSi_2$ oxidation.[23] Moreover, the strength increase could also be due to an increase of the fracture toughness with respect to the test temperature. Previous studies conducted on a HfB_2-15 vol% $MoSi_2$ composition[30] revealed an increase of fracture toughness from 3.8 to 4.4 MPa·m$^{1/2}$ (+16%) from room temperature to 1500°C Finally, The load-displacement curves were linear up to fracture both at 1200 and at 1500°C, confirming the high refractoriness of the constituent phases. Finally, at high temperature, an increase of strength with increasing the $MoSi_2$ content was found, confirming the protective action exerted by this intermetallic phase.

The plot in Fig. 11.14 evidences the excellent refractoriness of presureless HB20. If at room temperature hot pressed materials are more competitive, at 1500°C HB20 shows

the highest strength. It is worthy to notice that composites containing SiC and Si_3N_4 as sintering additives suffer of a dramatic collapse at 1500°C. Nevertheless, the UHTC baseline materials are considered those containing SiC, since they show better oxidation and abrasion resistance and thus are potentially more prone to bear re-entry extreme conditions. Further explanation will be given in section 11.5.

Fig. 11.13: Fracture surface after 4-pt bending test at a) room temperature, b) 1200°C. At room temperature is well visible a critical flaw, at 1200°C flaws are sealed by an amorphous boron-silicate layer.

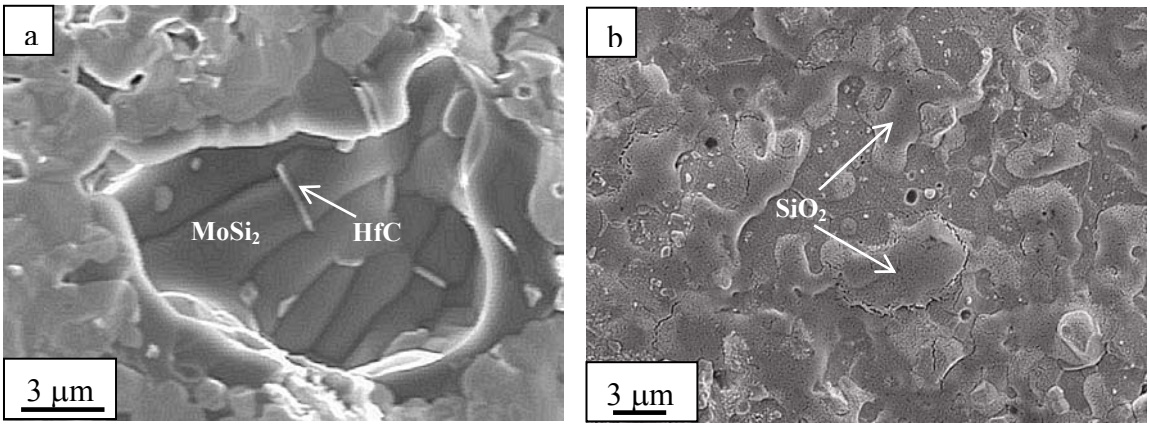

Fig. 11.14: Comparison of flexural strength values from room temperature to high temperature among different HfB_2 materials sintered with different sintering additives or techniques.

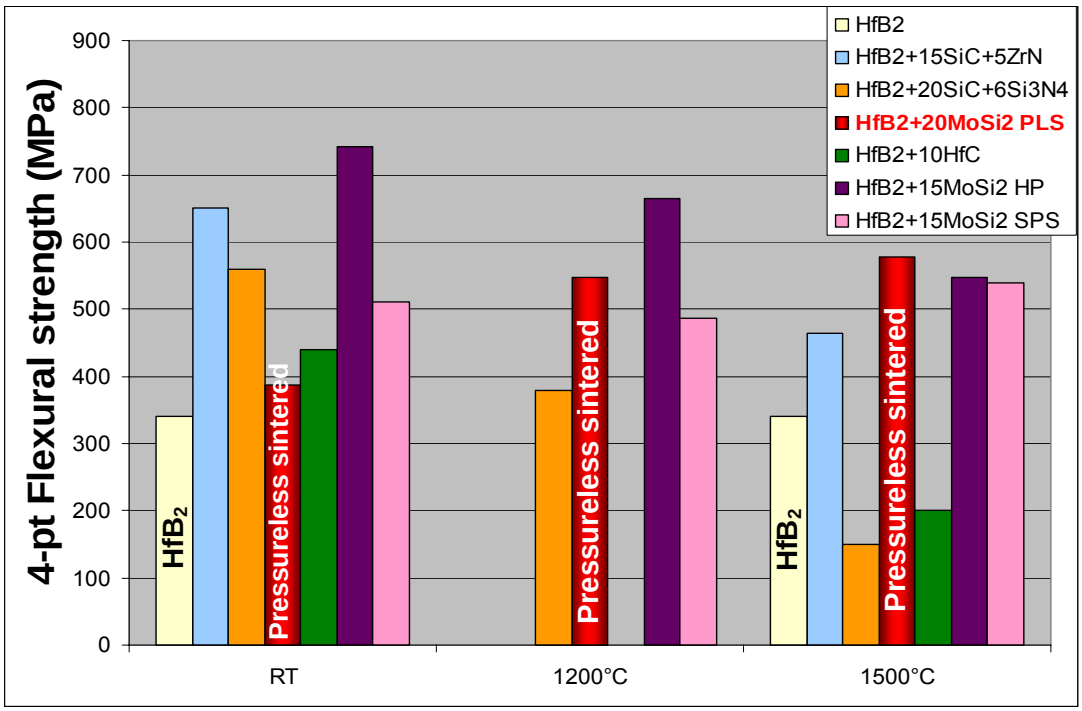

An overall comparison between the mechanical properties of carbides and borides tested in the present work is reported in Fig. 11.15.

Fig. 11.15: Comparison of mechanical properties among ZrC, HfC, ZrB_2 and HfB_2-based composites, object of the present work.

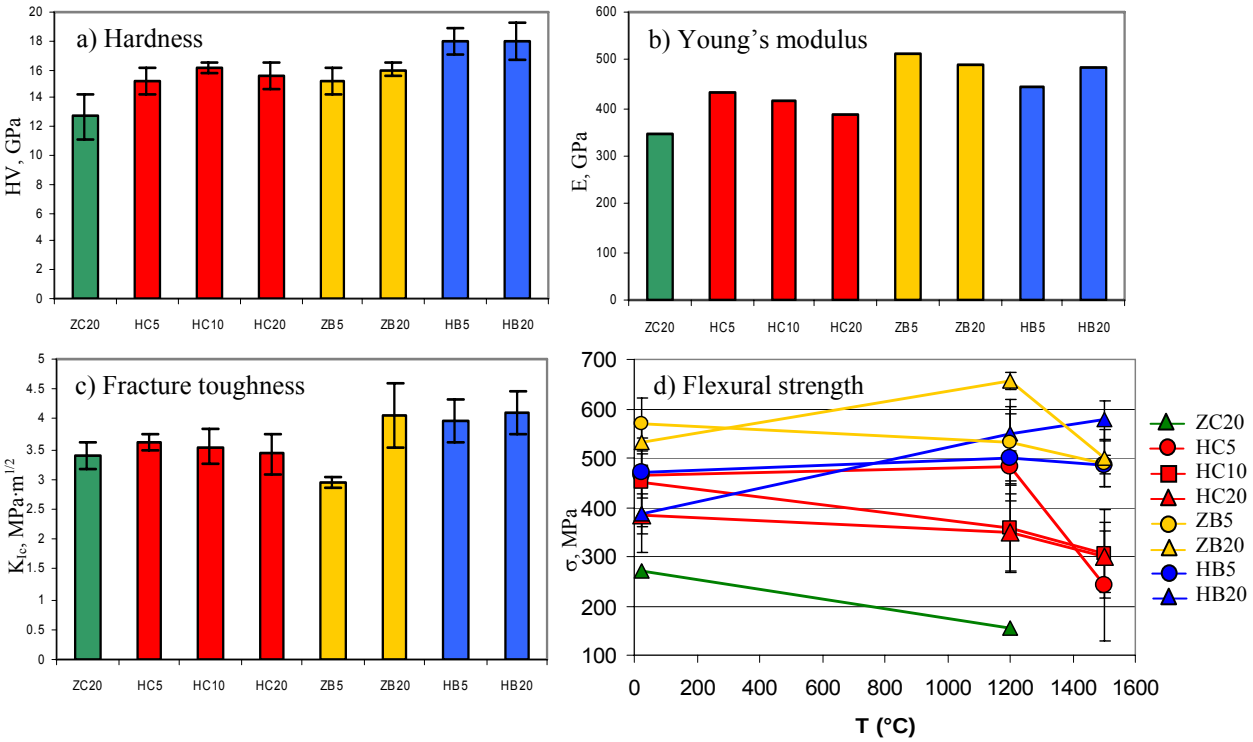

Concerning hardness (Fig. 11.15a), the highest values are those of HfB_2-based composites, around 19 GPa. HfC and ZrB_2 composites are around 15-16 GPa, while ZrC-$MoSi_2$ possesses lower hardness, around 12 GPa, because of the coarse microstructure and some residual porosity.

Young's modulus highest values belong to the borides, 450-520 GPa, whilst for the carbides the stiffness retains values ranging from 350 to 450 GPa (Fig. 11.7b).

The generally low fracture toughness values (see Fig. 11.15c) reflect a typical feature of UHTC materials and this aspect strongly limits their widespread use. Measured values range between 3 to 4 $MPa \cdot m^{1/2}$, with borides slightly tougher than carbides. Transgranular fracture and absence of toughening mechanisms are the main factors that weigh upon the low values of K_{Ic}.

Flexural strength, reported for all the tested materials in Fig. 11.7d, clearly show the excellent high temperatures capabilities of the borides. Regarding the carbides, good values were obtained for HfC-based composites up to 1200°C, whilst a decrease of 50-100 MPa occurred at 1500°C. For the ZrC-based material all the values were negatively affected by the coarse microstructure and the sensitivity to residual oxidizing species at 1200°C.

11.2 ARC JET OXIDATION

11.2.1 Introduction

Ultra-high temperature ceramics (UHTCs) are currently considered as emerging materials for aerospace applications.[31–34] The increasing attention is driven by the demand of developing re-usable hot structures as thermal protection systems (TPS) of re-entry vehicles characterized by sharp leading edges and therefore by larger aerothermal heating than blunt edges, such as those on the Space Shuttle, able to withstand temperatures that may exceed 2000°C during re-entry. As available materials can not survive such extreme temperatures, new ones are required for advanced thermal protection systems.[31,34,35]. The use of UHTCs for sharp leading edges would also imply lower aerodynamic drag, improved flight performances and crew safety, due to the larger cross range and manoeuvrability along with more gentle re-entry trajectories.[33,363,7]

Hafnium boride and hafnium carbide, belonging to the class of the UHTCs, are candidates for thermal protection materials in both re-entry and hypersonic vehicles because of their high melting points (~3900°C) and excellent chemical stability.[10,29,38-41] Besides, the addition of $MoSi_2$ is also expected to improve the oxidation resistance thanks to the development of a silica protective coating.[23]

In this section, arc-jet testing at temperatures between 1950°C and 2400°C is carried out on the pressureless sintered HfB_2- and HfC-based materials doped with 5 vol% of $MoSi_2$. HB5 and HC5 arc-jet testing represents the best ground-based simulation of a re-entry environment, in different ways. On one hand, it provides the possibility to explore the oxidation behaviour of these materials under extreme conditions. On the other hand, the materials response to large heat fluxes is evaluated through the determination of two important parameters, i.e. emissivity and catalicity. High values of emissivity and low values of surface catalycity are desired for the above mentioned applications as they reduce temperature gradients and thermal stresses in the structure, thus enabling the vehicle to operate under relatively high enthalpy flow conditions. So far, only ZrB_2-SiC and HfB_2-SiC composites were the predecessor materials analysed by arc-jet testing in the literature of UHTCs.[33,42]

Microstructural modifications induced by high thermal loading are investigated and discussed. In addition, fluid dynamic numerical simulations are carried out in order to rebuild, through Computational Fluid Dynamic (CFD) modelling, the

experimental tests and to evaluate an average catalytic efficiency of the different materials with respect to oxygen and nitrogen surface recombination reactions.

11.2.2 Plasma flow characterization

The results herein presented refer to a 75% argon-25% nitrogen mixture plasma jet with mass flow rate of 1.45 g/s, for an average specific total enthalpy of the flow at the torch exit varying from 20 to 28 MJ/kg, at atmospheric pressure. At the exit of the torch the plasma containing argon, nitrogen and atomic nitrogen expands through a nozzle (5 mm in diameter), comes into contact with the surrounding air at ambient conditions, so that atmospheric oxygen dissociates and a reacting mixture composed of Ar, O_2, N_2, NO, O and N is formed. Fig. 11.16 shows the computation results of the plasma composition and average specific total enthalpy as a function of the distance from the torch exit performed for the case of an average specific total enthalpy of 26 MJ/kg at the torch exit. According to the calculations, the average specific total enthalpy at about in proximity of the specimen is drastically reduced to about 6-8 MJ/kg.

Fig. 11.16: Computed mass fractions of the different species along the torch axis. At the bottom, specific total enthalpy contours with the relative legend. Total enthalpy at the torch exit=26 MJ/kg.

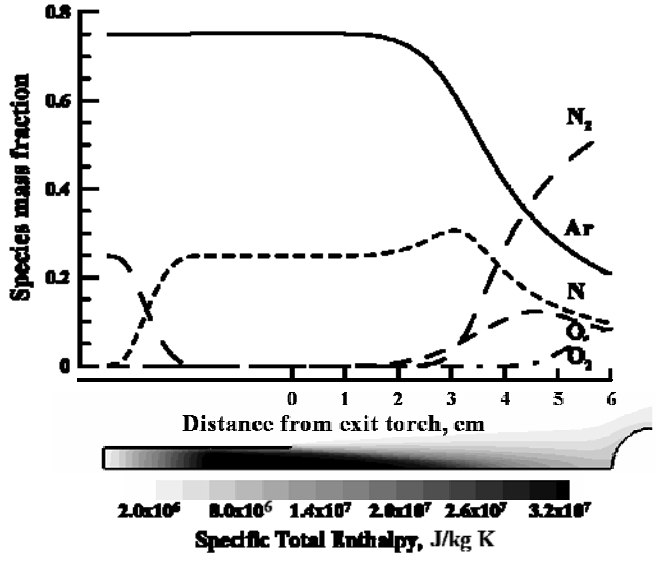

Tab. 11.II summarizes the experimental conditions and the computed flow characteristics for the different experiments. Correspondingly, Fig. 11.17 shows the increase of the surface temperature as a function of the exposition time for HfB_2 and HfC samples, respectively.

Tab. 11.II: Test conditions.

Arc Power / Flow conditions	38.0 kW	42.5 kW	46.0 kW	51.0 kW
Exit Torch conditions				
Average Specific Total Enthalpy, MJ/kg	20	22	24	26
Temperature, °C	17500	19300	21000	23000
Flow conditions at model location				
Specific Total Enthalpy, MJ/kg	5.8	6.5	7.1	8.0
Temperature, °C	2900	3200	3400	3800
Ar mass fraction	0.21	0.21	0.21	0.21
N_2 mass fraction	0.55	0.55	0.53	0.52
N mass fraction	0.076	0.08	0.09	0.10
O_2 mass fraction	0.12	0.11	0.1	0.08
O mass fraction	0.046	0.05	0.07	0.08
NO mass fraction	0	0	0	0
Stagnation point				
Pressure, Pa	114000	116000	119000	122000
Non catalytic Heat Flux, MW/m^2	5	6	7	8

Fig. 11.17: Temperature profiles vs. time during arc-jet testing of the (a) HB5 and (b) HC5-I and HC5-II samples corresponding to specific total enthalpies during the test.

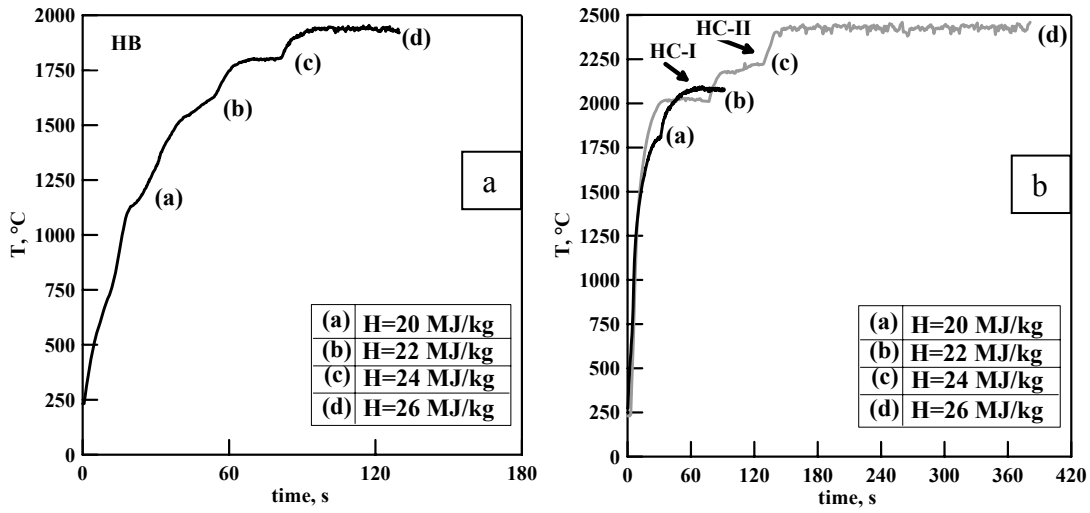

It must be mentioned that the temperature reached at the sample surface depends on the ability of the material to reject the heat by radiation, i.e. on its emissivity ($\varepsilon = 1$ for an ideal black body, $\varepsilon < 1$ for a real material surface). The higher is the emissivity, the greater is the emitted radiation. However, the temperature of the sample also depends on its thermal conductivity, since a high thermal conductivity allows heat to be conducted from the leading edge to colder zones and from there to be radiated away.

The maximum temperature reached on the surface of HfB_2 sample was 1950°C, Fig. 11.17a. The corresponding stagnation point heat flux, computed by numerical

simulation was in the range 5-8 MW/m^2. A value of about 0.9 was estimated for the emissivity at the highest temperature.

During the first test on HfC (HC5-I), the surface temperature achieved by the sample was 2050°C (Fig. 11.17b). During the second test (HC5-II) the surface temperature reached the value of 2400°C that was maintained for about four minutes. The corresponding computed surface heat flux were of the order of 10 MW/m^2. In both tests a value of about 0.7 was measured for the emissivity at the highest temperatures. The emissivity values of the samples, tested at different conditions, were found to be independent of the test temperature and conditions. These values were similar to those found for other ZrB_2-SiC ultrahigh temperature ceramics tested in similar conditions.[42,43]

Both the boride and carbide materials showed an excellent stability during the tests, despite the unavoidable microstructural changes occurring on their surface, as described below.

11.2.3 Microstructural modifications

HfB_2-$MoSi_2$ sample - Due to high thermal loading and the presence of oxidizing species, oxidation of the constituent phases occurred. The increment of the specimen weight was of the order of 1-2%. However, this can not be considered a fully indicative parameter of the extent of oxidation, as concurrent leakage of volatile species can cause weight loss. The sample surface was covered by a compact silica-based scale (15-20 μm thick), which embedded HfO_2 crystals (Fig. 11.18a,b). Bubble formation accounts for evolution of gaseous products. The analysis of the cross section (Fig. 11.18c-e), revealed that the overall scale thickness was about 70 μm and well adherent to the bulk, i.e. no micro/macrospallation of the oxide was observed. Underneath the silica oxide layer (I), the scale was mainly constituted by large HfO_2 grains and silica (II). In the innermost layer (III), the formation of MoB, SiO_2 and HfO_2 was also observed.

The chemistry of the experiment carried out on HfB_2-based material was governed by the oxidation reaction of the two constituent phases. Hafnium boride oxidises according to:[7]

$$HfB_2(s) + 5/2\ O_2(g) = HfO_2(s) + B_2O_3(l) \quad (6)$$

$$B_2O_3(l) = B_2O_3(g) \quad (7)$$

Hafnia is a very stable phase in oxidizing atmosphere above 2000°C. It has a melting point of 2900°C and relatively low vapour pressure.[44] Boron oxide has a low melting point and high vapour pressure, therefore at T>1100°C, it starts to evaporate, according to reaction (2).

Fig. 11.18: HfB_2 sample after arc-jet test (a), (b) surface, (c) cross section, (d) enlarged view of layers I, II, (e) enlarged view of layer III

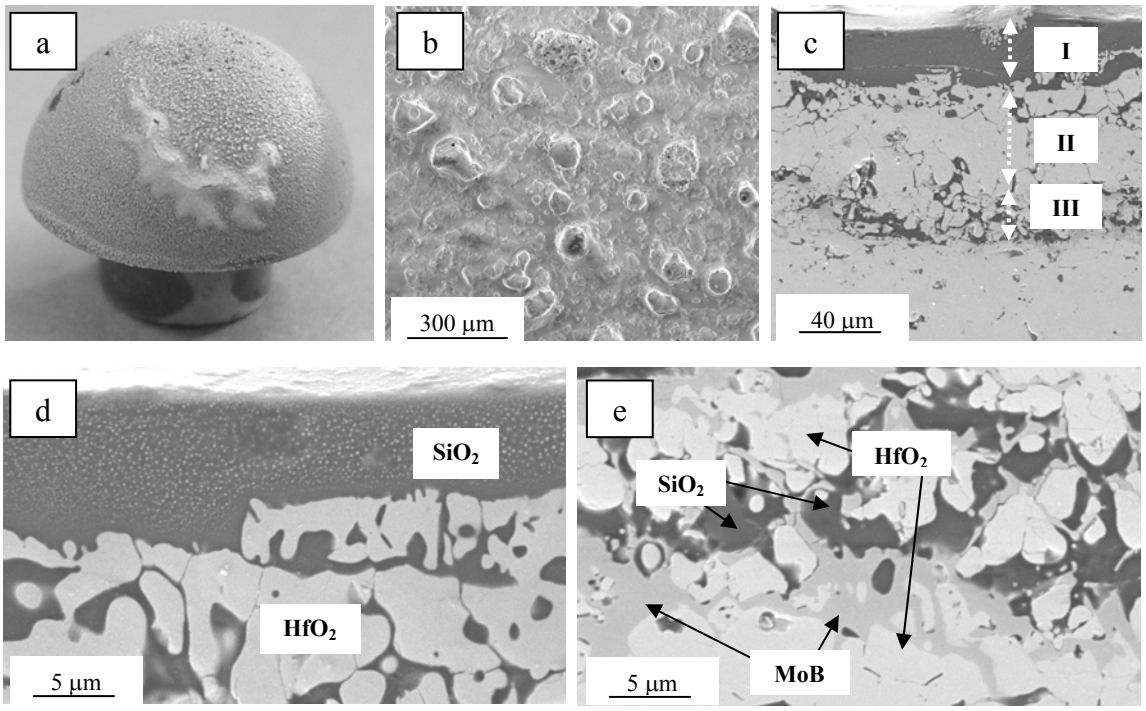

On the other hand, at temperatures >1000°C, $MoSi_2$ is known to form a stable silica layer according to:[45]

$$MoSi_2 + 3.5\ O_2(g) = MoO_3(g) + SiO_2 \quad (8)$$

The nature of the oxide observed suggests that during the plasma torch tests the silica production, according to reaction (3), was fast enough to protect the material. The formation of bubbles was produced by the leak of gaseous by-products, such as MoO_3 and B_2O_3. In the innermost layer(III), the formation of molybdenum boride suggests that, beside reactions (1-3), the following reaction occurred:

$$HfB_2 + 2\ MoSi_2 + 5\ O_2(g) = 2\ MoB + HfO_2 + 4\ SiO_2 \quad (9)$$

According to thermodynamical calculation,[46], reaction (4) is strongly favoured. In spite of that, no molybdenum boride was detected in the proximity of the sample surface, implying that on the surface the evaporation of MoO_3 and B_2O_3 species was favoured over the formation of MoB.

HfC-$MoSi_2$ sample - The increment of the specimen weight after the HFC-I test was of the order of 1%. No significant variation of the sample size and shape was observed, implying that the extent of ablation was very low. The surface turned from dark grey to a whitish colour (in Fig. 11.19a,b) and was covered by a thick oxide scale mainly constituted by monoclinic hafnium oxide. The specimen section displayed in Fig. 11.19c-f, showed the formation of a compact scale, with thickness of about 70 μm, well adherent to the unreacted bulk, i.e. no micro/macrospallation of the oxide was observed. The outer layer (I) was only partially porous, since porosity was filled by silica (Fig. 11.19d). The intermediate layer (II) was dense and contained hafnia and molybdenum oxide (Fig. 11.19e). The innermost layer (III) contained SiC and Mo_5Si_3C, beside partially oxidised HfC (Fig. 11.19f). Similar features were displayed by the specimen tested at 2400°C (test HfC-II), even if the oxide scale (~300 μm thick) was found to be partially detached from the unreacted bulk.

Fig. 11.19: HfC sample after arc-jet test (a),(b) surface, (c) cross section, (d) enlarged view of layer I, (e) enlarged view of layer II, (f) enlarged view of layer III

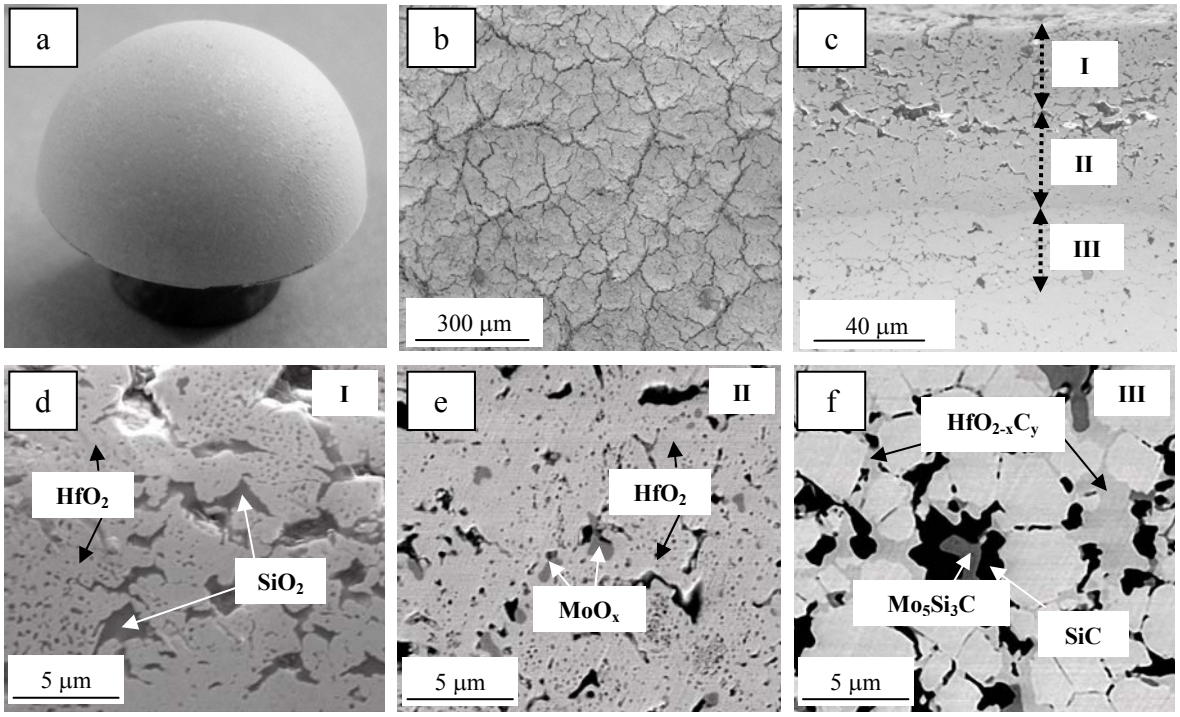

Despite the presence of $MoSi_2$ as a SiO_2-forming phase, no silica was found on the surface of HfC, in contrast with the results obtained for HfB_2. This finding can not be imputed to the fact that the test temperature for HfC was higher than 2000°C. The same compositions, HB5 and HC5, were in fact previously oxidised in static air (i.e. in absence of significant ablation) at 1650°C, in a conventional furnace. Even under these

milder conditions, HfB_2 displayed the formation of a compact layer of silica, whilst the surface of HfC was mainly covered by an HfO_2 scale with few discontinuous pockets of silica. This simple experiment suggests that the presence of a carbide matrix rather than a boride one favoured the active oxidation of $MoSi_2$, with the formation of volatile SiO. According to themodynamical calculations,[46], on the surface of the sample, the following reaction could have occurred:

$$MoSi_2 + HfC + 3O_2(g) = HfO_2 + 2SiO(g) + MoO(g) + CO(g) \quad (10)$$

In the cross section, the layered structure of the oxide (Fig. 11.19c) resembled the results presented in the literature on the oxidation behaviour of monolithic HfC.[44,47] These studies reported the formation of a layered scale, which comprised a porous outer layer, a dense interlayer and an oxycarbide layer, $HfO_{2-x}C_y$.[44,47] The addition of $MoSi_2$ in the composites of the present work resulted in formation of silica which partially filled the inner porosity of the HfO_2 scale, a feature which improved its oxidation resistance.

In the outermost layer underneath the surface (I), the following reaction was likely to occur:

$$MoSi_2 + HfC + 4\ O_2(g) = 2\ SiO_2 + HfO_2 + MoO(g) + CO(g) \quad (11)$$

Accordingly, in the intermediate layer (II), the following reactions can be hypothesized:

$$MoSi_2 + HfC + 3.5\ O_2(g) = HfO_2 + MoO_2 + 2\ SiO(g) + CO(g) \quad (12)$$

$$MoSi_2 + HfC + 4.5\ O_2(g) = 2\ SiO_2 + HfO_2 + MoO_2 + CO(g) \quad (13)$$

Finally in the innermost layer (III), the formation of SiC and Mo_5Si_3 can be explained in terms of the following reaction:

$$5MoSi_2 + 7HfC + 7O_2(g) = 7SiC + 7HfO_2 + Mo_5Si_3 \quad (14)$$

11.2.4 Catalicity evaluation

Numerical computations were carried out using the model described in section 11.2.2, under different assumptions about the catalytic properties of the specimen surface with reference to catalytic efficiency of atomic nitrogen and oxygen. The simulations refers to the plasma torch test conditions reported in Tab. 11.II. Based on the computed heat flux distributions, a thermal analysis was carried out to evaluate the catalicity efficiency value, γ, needed to fit the experimental temperature data. The

catalytic efficiency is defined as the ratio of the number of dissociating atoms that recombine at the wall to the total number of the colliding atoms with the wall. For a non-catalytic wall this value is 0, while for a fully catalytic wall this is 1. Fig. 11.20 shows the steady state results computed under the two assumptions of fully catalytic and non catalytic wall and the experimental data obtained with the pyrometer for both material samples.

Fig. 11.20: Experimental results and numerical solutions corresponding to the different assumption of fully catalytic (FC) and non catalytic (NC) wall for (a) HfB_2 and (b) HfC.

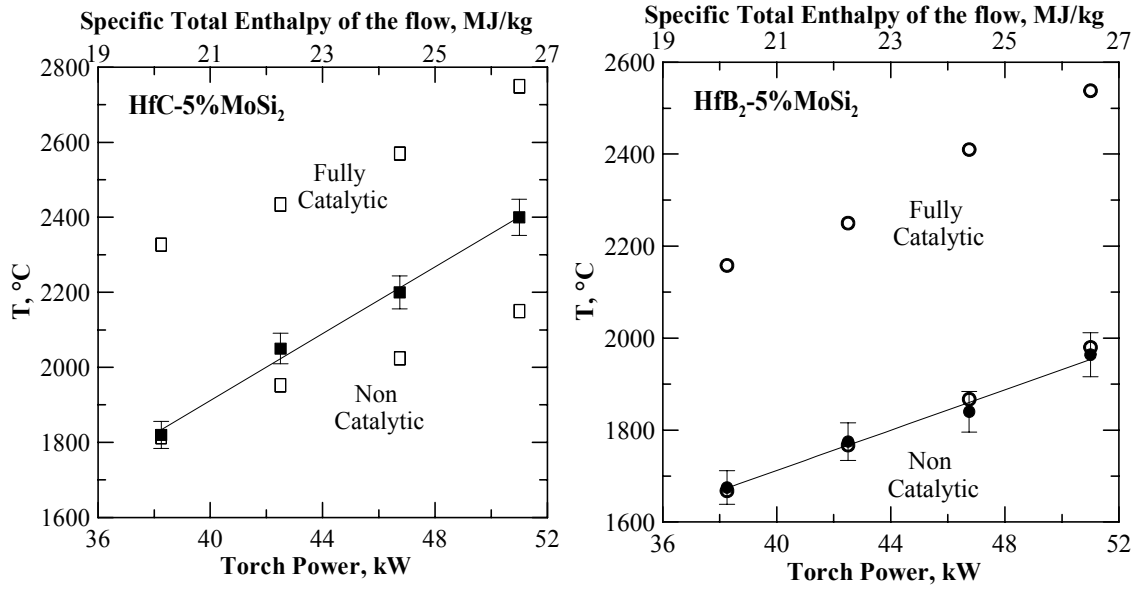

For this thermal analysis, input values of specific heat and thermal conductivity are necessary. As a first approximation, the values of monolithic HfC and HfB_2 were considered for the composites, as follows: 200 J/kg K and 22 W/ mK for specific heat and thermal conductivity of HfC,[4] 300 J/kg K and 80 W/ mK for specific heat and thermal conductivity of HfB_2 [48] The data displayed in Fig. 11.20, at the same plasma torch conditions, i.e. the same free stream conditions, highlight that the heating behaviour of the two materials was rather different. The experimental results of HfB_2 sample matched very well the numerical values corresponding to the non catalytic wall condition. This points out that the material herein tested exhibits a non catalytic behaviour at very high temperatures. This behaviour can be explained by the formation of a silica surface layer (Fig. 11.18) which is known to possess very low catalytic recombination behaviour.[49,50] The presence of such a surface layer also justifies the high values of the surface emissivity, according to the literature data.

The experimental results for HfC suggested a partially catalytic behaviour which varies with the temperature. In order to identify such a dependence of surface

temperature with catalicity, different values of catalicity efficiency were considered for each test conditions until the calculated temperatures matched the experimental ones. Figure 11.21 shows the results of such computations. As can be seen, at 1800°C HfC exhibited an almost non catalytic behaviour ($\gamma \sim 2 \cdot 10^{-5}$). In order to match the experimental temperatures at increasing total enthalpy, the catalytic efficiency had to be increased up to a value of $2 \cdot 10^{-3}$ at 2400°C which is still far from a fully catalytic wall condition ($\gamma=1$) and of the same order of other low catalytic materials such as those of the Space Shuttle tiles.[51]

Fig. 11.21: Numerical evaluation of surface temperature as a function of the coefficient of catalytic recombination and total enthalpy for the HfC-5%$MoSi_2$ sample.

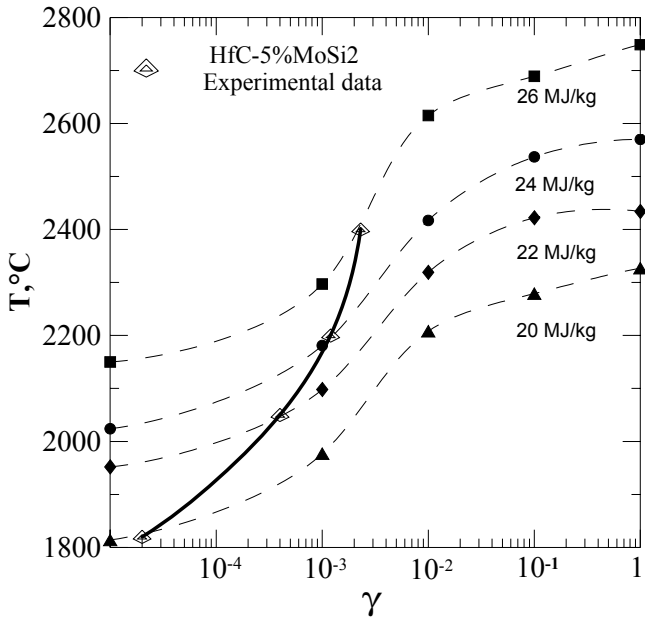

It should be pointed out that the present tests have been carried out at atmospheric pressure conditions. Experimental and theoretical works on the catalytic activity of silica-based materials under simulated re-entry conditions[52] showed that at constant temperature the catalytic atomic recombination coefficients are decreasing functions of the pressure. Therefore the catalytic properties of the material, in respect to the recombination of oxygen atoms, may be larger at lower pressures, as found for instance in arc-jet experiments with ZrB_2/SiC and HfB_2/SiC ceramic materials.[32]

11.2.5 Conclusions

Two different ultra-high temperature ceramics, HfB_2+5%$MoSi_2$ and HfC+5%$MoSi_2$ were exposed to ground simulated atmospheric re-entry conditions using arc-jet

testing, with an average specific total enthalpy of the flow around the body of the order of 5-10 MJ/kg and at atmospheric pressure.

The HfB_2+5%$MoSi_2$ sample surface reached a peak temperature of 1950°C for H approaching 8MJ/kg. SEM-EDS analysis of the cross-section after exposure showed the formation of a compact silica oxide (about 15 μm thick) which sealed the underlying HfO_2 scale.

The HfC+5%$MoSi_2$ sample surface reached peak temperatures of 2100 and 2400°C in two repeated tests. Cross-section analysis showed a layered structure, constituted of an outer layer of porous HfO_2 and an inner layer mainly constituted of HfO_2 and silica.

Numerical calculations, which simulated the chemical non-equilibrium flow around the hemispheric model, correlated well with the experimental results assuming an almost non catalytic surface behaviour for HfB_2 and a low catalytic behaviour, which slightly increased with temperature, for HfC.

Although more testing is necessary to improve the understanding of the oxidation mechanisms under extreme conditions, the composites presently tested showed an excellent resistance to high enthalpy hot flows. No spallation or cracking were observed and just the first 80-90 μm of the surface underwent microstructural modifications. This stability at temperature around 2000°C opens up new developments in several fields of application, including nuclear applications and industries where extreme conditions are involved.

Finally, to remark the very good behaviour of the above presented materials, in Fig. 11.22 a similarly tested material is reported: AlN + 15 vol% SiC + 30 vol% $MoSi_2$. It was exposed to a maximum enthalpy of 20 MJ/kg and, despite the highest achieved temperature on the tip was 1900°C, held for 1 minute, it appears strongly damaged by the heat flux.

Fig. 11.22: Example of a candidate material for ultra high temperature applications after arc jet testing. Max enthalpy: 20 MJ/kg, 1 minute holding time.

References

47 H. O. Pierson: Handbook of refractory carbides and nitrides, (William Andrew Publishing/Noyes, Westwood, New Jersey, USA, 1996), 68.

48 E. Min-Haga, W. D. Scott, J. Mater. Sci. 23 (1988) 2865-2870.

49 T. Tsuchida, S. Yamamoto, Solid State Ionics 172 (2004) 215-216.

50 A. Krajewski, L. D'Alessio, G. De Maria, Cryst. Res. Technol. 33 (1998) 341-374.

51 E. Ryshkewitch, J. Am. Ceram. Soc. 34 (1951) 322-326.

52 K. H. Kim, K. B. Shim, Materials Characterization 50 (2003) 31-37.

53 J.B. Berkowitz-Mattuck, J. Electrochem. Soc. 114 (1967) 1030-33.

54 D. Sciti, M. Brach, A. Bellosi, J. Mat. Res. 20 (2005) 922-930.

55 Y.T. Zhu, L. Shu, F. P. Butt, J. Am. Ceram. Soc. 85 (2002) 507-509.

56 M.M. Opeka, I. G. Talmy, E. J. Wuchina, J. A. Zaykoski, S. J. Causey, J. Eur. Ceram. Soc., 19 (1999) 2405-2414.

57 D.Brut, N. Alexandre, J. Desmaison, J. Europ. Ceram. Soc. 17 (1997) 1325.

58 D. Sciti, L. Silvestroni, S. Guicciardi, D. Dalle Fabbriche, A. Bellosi, to be published in J. Mater. Res.

59 I. J. McColm, Ceramic Hardness, Plenum Press, New York, USA (1990).

60 Engineering property data on selected ceramics, Vol. II, Carbides, Metals and Ceramics Information Center, Battelle, Columbus Lab., Columbus, OH (1979).

61 D. Ferro, R. Teghil, S.M. Barinov, L. D'Alessio, G. De Maria, Mater. Chem. Phys. 87 (2004) 233.

62 A. Newman, T. Jewett, S. Sampath, C. Berndt, H. Herman, J. Mater. Res. 13 (1998) 2662.

63 H.S. Kim, Mater. Sci. Eng. A 289 (2000) 30.

64 W. D. Nix, H. Gao, J. Mech. Phys. Sol. 46 (1998) 411.

65 R.A. Cutler, in: S. J. Schneider Jr. (Ed.), Ceramics and Glasses, Engineered Materials Handbook, Vol. 4., ASM International, Materials Park, OH (1991) 787-803.

66 A.L. Chamberlain, W.G. Fahrenholtz, G.E. Hilmas, J. Am. Ceram. Soc., 450 (2006) 89.

67 R.A. Cutler In: S.J. Schneider, Editor, Engineered Materials Handbook, Ceramic and Glasses vol. 4, ASM International, The Materials Information Society, Materials Park, OH (1991). 787

68 J.F. Shackelford and W. Alexander, Editors, CRC Materials Science and Engineering Handbook, CRC Press, Boca Raton, Fl (2001).

69 Y.-L. Jeng, E.J. Lavernia, J. Mat. Sci. 29 (1994) 2557.

70 F. Monteverde, S. Guicciardi, A. Bellosi, Mat Sci Eng A346 (2003) 310.

71 F. Monteverde, A. Bellosi, J. Mat. Res. 19 (2004) 3576.

72 F. Monteverde, A. Bellosi, Adv. Eng. Mater. 6 (2004) 331.

73 A.L. Chamberlain, W.G. Fahrenholtz, G.E. Hilmas, in: N.P.Bansal, J.P. Singh, W.M. Kriven, H. Schneider (Eds.), Advances in Ceramic Matrix Composites IX, Am. Cer. Soc., Westerville (2003) 299-308.

74 A.L. Chamberlain, W.G. Fahrenholtz, G.E. Hilmas, J. Am. Ceram. Soc., 89 (2006) 450.

75 E. Wuchina, M. Opeka, S. Causey, K. Buesking, J. Spain, A. Cull, J. Routbort, F. Guitierrez-Mora, J. Mat. Sci. 39 (2004) 5939.

76 D. Sciti, L. Silvestroni, A. Bellosi, J. Mater. Res. 21 (2006) 1460.

77 K. Upadhya, J.M. Yang, W. Hoffman, Am. Ceram. Soc. Bull., , 76 (1997) 51–56.

78 J. Marschall, A. Chamberlain, D. Crunkleton B. Rogers, J. Spacecraft Rockets 41 (2004) 576–581.

79 M. Gasch, D. Ellerby, E. Irby, S. Beckman, M. Gusman S. Johnson, J. Mater. Sci. 39 (2004) 5925–5937.

80 A. Bongiorno, C. J. Forst, R. K. Kalia, J. Li, J. Marschall, A. Nakano, MRS Bull. 31 (2006) 410–418.

81 N. Richet, P. Lespade, P. Goursat, E.Laborde, Key Eng. Mater. 264–268 (2004) 1047–1050.

82 R. Janowski, M. Tauche, M. Scheper, R. Monti, R.Savino, Proceedings of the 1st Inter- national ARA Days, Atmospheric Reentry Systems, Missions and Vehicles. Session 15-System Design, (2006).

83 R. Monti, M. De Stefano Fumo, R. Savino, J. Thermophys. Heat Transfer 20 (2006) 500–506.

84 I.E. Campbell, E. M. Sherwood (Eds.), "High-Temperature Materials and Technology", Wiley, New York (1967).

85 E.V. Clougherty, L. Kaufman, RTD-TDR-63-4096, ManLabs, Inc., Cambridge, MA (1963).

86 S.R. Levine, J. Europ. Ceram. Soc. 22 (2002) 2757-67.

87 W. G. Fahrenholtz, G. E. Hilmas, NSF-AFOSR Joint Workshop on Future Ultra-High Temperature Materials, National Science Foundation Workshop, Arlington, VA, 13-14 (2004).

88 F. Monteverde, R. Savino, J. Eur. Ceram. Soc. 27 (2007) 4797.

89 L. Scatteia, R. Borrelli, G. Casentino, E. Beche, J.L. Sans, M. Balat-Pichelin, J. of Spacecrafts and Rockets 43 (2006) 1004-12.

90 C. R. Wang, J.M. Yan, Mat. Chem. Phys. 74 (2002) 272-281.

91 S. Lohfeld, M. Schütze, Materials and Corrosion 56 (2005) 23-26.

92 C. B. Bargernon, R. C. Bendon, A.N. Jette, T.E. Phillips, J. Am. Ceram. Soc. 76 (1993) 1040-46.

93 R. Loehman, E. Corral, H. P. Dumm, P. Kotula, R. Tandon, SANDIA REPORT 2006-2925, Sandia National Laboratories, Albuquerque, New Mexico, USA (2006).

94 J. C. Greaves, J. W. Linnett, Trans. Faraday Soc. 55 (1959) 1346.

95 P. G. Dickens, M. B. Sutcliffe, Trans. Faraday Soc. 60 (1964) 1272.

96 P.A. Gnoffo, G.R. Inger, AIAA 96 (1996) 4589.

97 A. F. Kolesnikov, A. N. Gordeev, S. A. Vasilevskii, J. L. Verant, Proceedings of the 1st European Conference for Aerospace Sciences EUCASS (2005).

98 A. F. Kolesnikov, M. I. Yakushin, I. S. Pershin, S. A. Vasilevskii, O. Chaot, B.Vancrayenest, Proceedings of the 4th Europ. Symp. Aerothermodynamics for Space Applications, ESA SP-487 (2001) 481–486.

CHAPTER 12

TERNARY COMPOSITES

The design of three-phase composites came from the need to lower the sintering temperature or to improve the oxidation resistance of HfB_2 and ZrC, respectively. To this scope, the first part of this chapter is dedicated to the microstructure and mechanical properties of HfB_2-based ternary composites, whilst the second part presents the microstructure and mechanical properties of ZrC-based ternary composites.

12.1 HfB_2-BASED TERNARY COMPOSITES

12.1.1 Introduction

In this section, HfB_2 is combined with either ZrB_2 or HfC with the aim of further improvements in sintering, microstructure and properties. 20 vol% $MoSi_2$ is used as sintering aid, similar to previous experiments.[1-3] The development of the microstructures and mechanical properties are studied and compared with the reference HfB_2-, ZrB_2- and HfC-based composites doped with the same amount of $MoSi_2$.[1,3]
The compositions prepared are shown in Tab. 12.I.

Tab. 12.I: Composition, sintering conditions and final densities of tested compositions**.**

Sample	Composition	Sintering	Relative density
	Vol %	°C, min	%
HZBM	40 HfB_2-40 ZrB_2-20 $MoSi_2$	1850, 60	96
		1900, 60	98
		1950, 60	98
HHM	40 HfB_2-40 HfC-20 $MoSi_2$	1950, 60	96
		1950, 90	96

12.1.2 Densification behaviour

Sintering conditions were chosen in accordance with the sintering temperature and holding time of previous studies on compositions HfB_2-$MoSi_2$, ZrB_2-$MoSi_2$, and HfC-$MoSi_2$. Pressureless sintering tests were carried out in the temperature range 1850-1950°C for HfB_2-ZrB_2-$MoSi_2$ material (HZBM) and at 1950°C for 60-90 minutes of

holding time for HfB_2-HfC-$MoSi_2$ material (HHM), as reported in Tab. 12.I. The sintering cycle for HZBM material was finally set at 1900°C/60 min as it led to a relative density of 98%. Tests at 1850°C on this composition revealed that the final density remained as low as 96%. For HHM material, the sintering cycle was set at 1950°C/60 min, to achieve a relative density of 96% as no significant variation of density was obtained for longer holding times.

12.1.3 Microstructure

The X-ray diffraction patterns, fracture and polished surfaces for the dense HfB2-based composites are shown in Figs. 12.1-12.6.

HfB_2-ZrB_2-$MoSi_2$ composite (HZBM) - According to the X-ray diffraction spectrum collected in the (20-50°) 2θ range, the diffraction peaks detected were compatible with an $Hf_xZr_{1-x}B_2$ solid solution. The peaks of the solid solution were found to be shifted to higher θ angles compared to stoichiometric ZrB_2 and shifted to lower θ angles compared to stoichiometric HfB_2 (Fig. 12.1).

Fig. 12.1: X-ray diffraction pattern for HZBM sample.

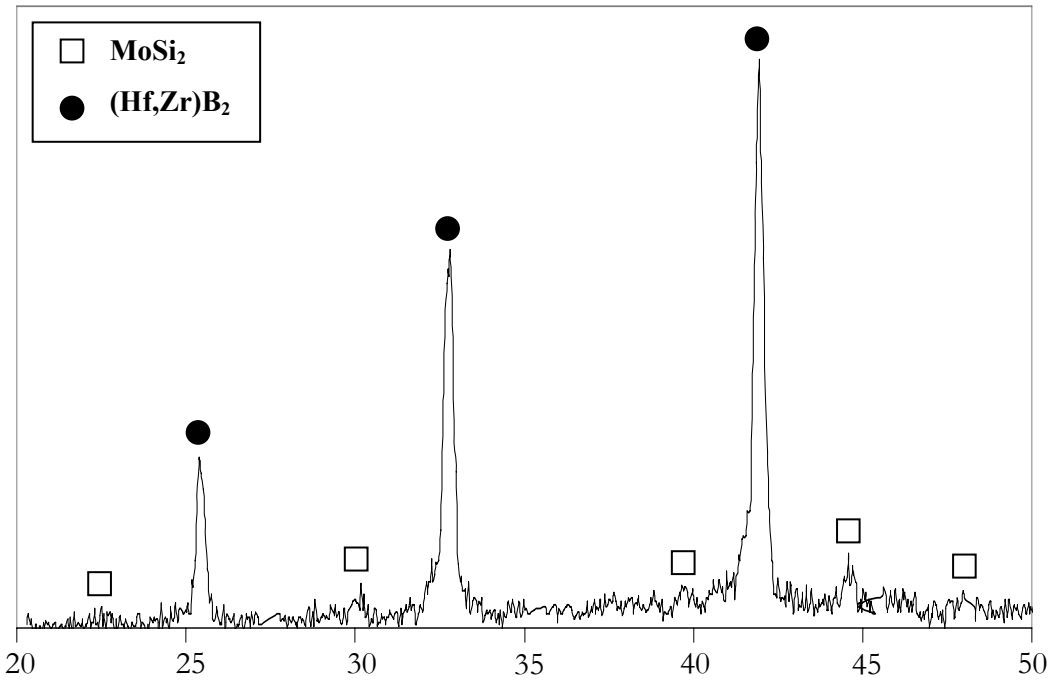

All the necessary conditions for the formation of a solid solution between ZrB_2 and HfB_2 were satisfied: same electronic charge, difference between atomic radii lower than 15% (Zr:1.60 Å, Hf:1.58 Å), same crystal lattice and high processing temperatures. Additionally, low-intensity peaks belonging to tetragonal $MoSi_2$ were also recognized.

The material was found to be nearly full dense with no residual porosity. One example of a fractured and a polished section is reported in Fig. 12.2.

Fig. 12.2: Scanning electron micrograph of a) fractured surface and b) polished surface for HfB_2-ZrB_2 composite. Dark phase is $MoSi_2$, bright core is HfB_2, dark grey core is ZrB_2 and the grey rim is the $(Hf,Zr)B_2$ solid solution. In the inset on the right, the EDS spectrum of the solid solution.

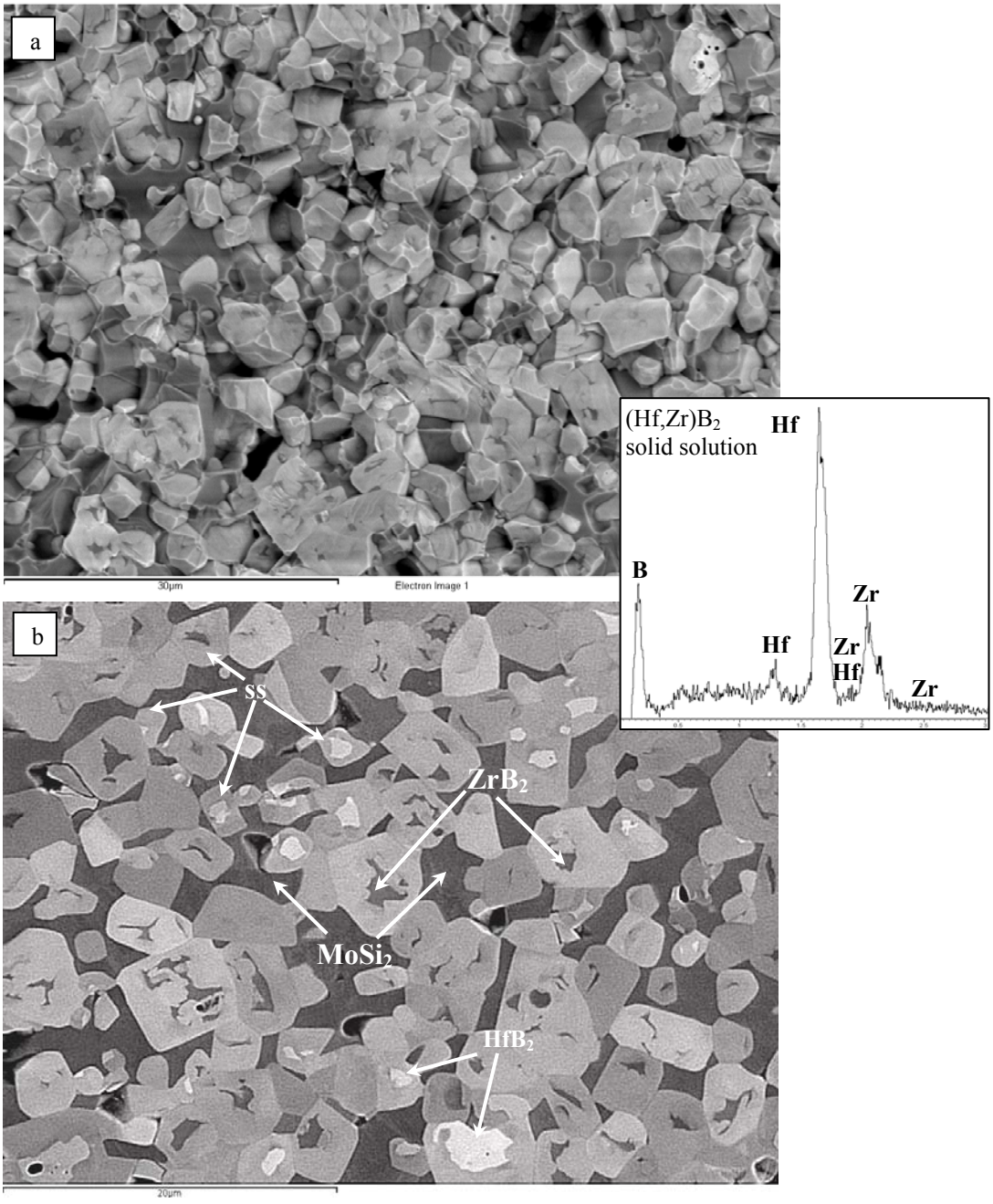

As can be seen in the polished section (Fig. 12.2b), the $Hf_xZr_{1-x}B_2$ solid solution grew onto original cores of either HfB_2 or ZrB_2 grains. HfB_2 core appeared brighter than the solid solution, while ZrB_2 core appeared darker. This means that solid solution formation could originate either by incorporation of Hf atoms into the ZrB_2 structure, or by Zr incorporation into the HfB_2 structure. Quantitative EDS analyses were carried out

in order to determine the compositions of the solid solution. To limit lateral spreading of the beam, the accelerating voltage was set at 6 keV. It was found that the stoichiometry of the solid solution was very close to a $(Zr_{0.5}Hf_{0.5})B_2$ composition. The formation of solid solutions led to a notable coarsening of the microstructure compared to the starting powders' dimensions, with mean grain size of the boride grains being about 6 μm (Tab. 12.II); the grains had a faceted morphology, unlike HfB_2-$MoSi_2$ composites,[13] whilst the original cores had an irregular shape.

Tab. 12.II: Mean grain size and mechanical properties of selected materials. For comparison, reference composites are reported too. HV1.0=Vickers Hardness, E=Young's modulus, K_{Ic}=fracture toughness, σ=flexural strength. * test carried out in a partially protective Ar atmosphere.

Sample	M.g.s.	HV	E	K_{Ic}	σ_{RT}	σ_{1200}	σ_{1500}
Vol %	μm	GPa	GPa	$MPam^{1/2}$	MPa	MPa	MPa
ZrB_2+20 $MoSi_2$	2.5	16.0±0.4	489±4	4.1±0.6	531±47	656±17	500±58
HZBM	HB:6, ZB:6	14.2±1.0	453±4	3.5±0.2	453±100	464±8	449±20
HfB_2+20 $MoSi_2$	1.5	18.8±0.3	482±4	4.1±0.4	388±40	548±56	577±39
HHM	HB:1.7, HC:2.7	16.9±0.9	372±4	3.1±0.3	470±38	330±21*	362±8*
HfC+20 $MoSi_2$	2.8	15.5±0.9	385±4	3.4±0.3	383±74	350±78*	299±71*

In the proximity of $MoSi_2$ agglomerates, a brighter Mo-Zr-Hf-Si phase formed (Fig. 12.3). Due to close similarity of atomic radius it is very likely that Zr/Hf atoms replaced the Mo sites in agreement with studies reported in literature.[4,5] The boundaries between this Mo-rich phase and the boride grains were flat (atomically smooth interface), indicating that interface reaction is expected to control the coarsening. Carbide phases with compositions similar to $Hf_{0.8}Zr_{0.2}C_{0.9}$ were also detected. Carbon, provided by the graphite-rich environment of the furnace most probably caused carbothermal reduction of the hafnium and zirconium oxides.

The complex chemistry of this system demonstrates that densification was aided both by the addition of $MoSi_2$, as found for other compositions, and by the mutual solid solubility between the borides. The formation of solid solutions lowered the sintering temperature from 1950°C, which is typical of HfB_2-based composite,[3] to 1850-1900°C, which is typical of ZrB_2-based composites.[3] However, the sintering cycle and starting compositions have to be adjusted in order to prevent grain coarsening.

Fig. 12.3: Backscattered electron micrograph of HZBM sample and EDS spectra of (1) $MoSi_2$, continuous line, and (2) Mo-Zr-Hf-Si phase, dotted line.

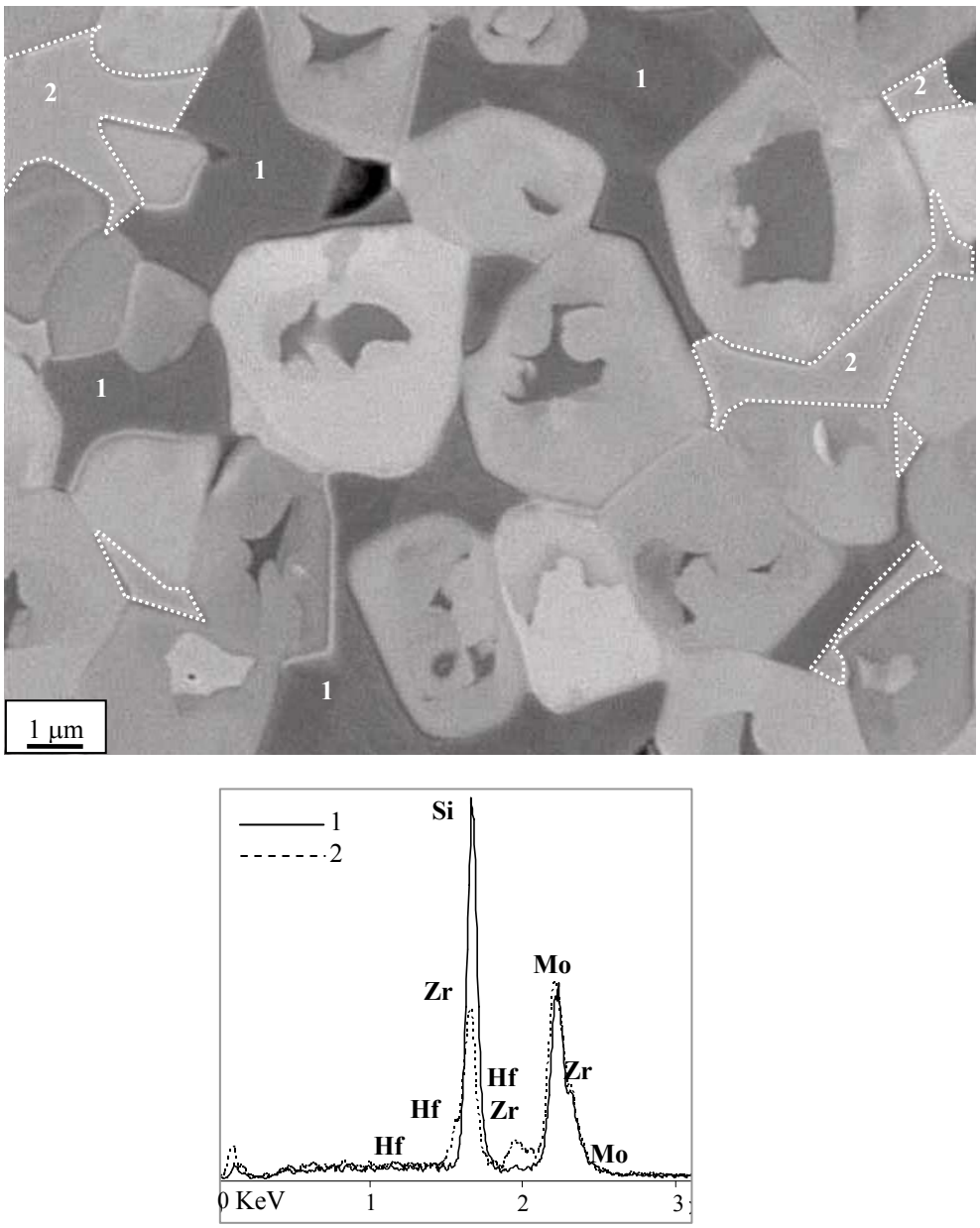

HfB_2-HfC-$MoSi_2$ composite (HHM) - According to the X-ray diffraction pattern shown in Fig. 12.4, no solid solution was formed between HfB_2 and HfC, thus confirming the insolubility between cubic carbides and hexagonal diborides.

This sample showed very little residual porosity, as can be seen from the surfaces in Fig. 12.5. A prevalence of transgranular fracture was observed for both the boride and the carbide phases. The boride grains had a mean grain size of ~1.5 μm, while the carbide grains coarsened to ~2.7 μm. Good adhesion was found between the boride and the carbide and, up to the SEM resolution, the boundary interfaces were clean. During densification, agglomerates of HfC particles formed necks, coalesced and entrapped

HfB_2 grains. Since the carbide powder was finer than the boride powder, the HfC particles could fill the spaces among bigger HfB_2 particles, as shown in Fig. 12.5b.

Fig. 12.4: X-ray diffraction pattern of HHM sample.

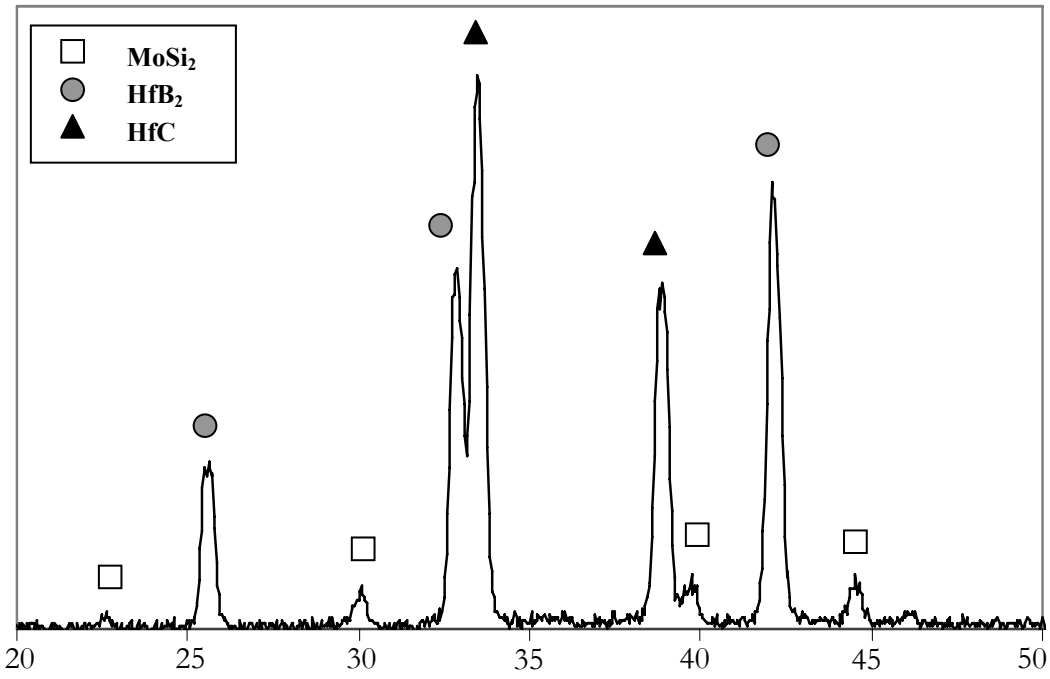

Although HfB_2 starting powder was notably contaminated by oxygen, HfO_2 was detected occasionally in the form of rounded particles embedded into HfB_2 grains (Fig. 12.6). It is believed that when surface HfO_2 came into contact with HfC or into the presence of carbon provided by the graphite-rich environment, HfO_2 was partially or totally reduced to HfC. Among the HfC grains and $MoSi_2$, reaction products were detected by EDS analysis (Fig. 12.6), containing Hf, Si, Mo, and C, indicating the possibility of mutual solubility between the $MoSi_2$ and HfC compounds. This feature suggests that sintering of HfC grains was aided by an Mo-Si-based liquid phase, acting as medium for matter transport by diffusion between near neighbour grains and hence favouring their coarsening. By SEM observation, next to $MoSi_2$, an MoB phase was detected, too (Fig. 12.6), deriving from the reaction between B_2O_3 present on the surface of HfB_2 powder and $MoSi_2$ Again, $MoSi_2$ played a key role in the densification of these systems thanks to its ductility at temperatures over 1000°C,[6] so that it could settle among the hard HfB_2, ZrB_2, HfC particles, and its tendency to form solid solution with Zr and Hf borides, thus yielding to the formation of high-density materials.

Fig. 12.5: Scanning electron micrograph of a) fractured surface and b) polished surface for HfB_2-HfC-$MoSi_2$ composite.

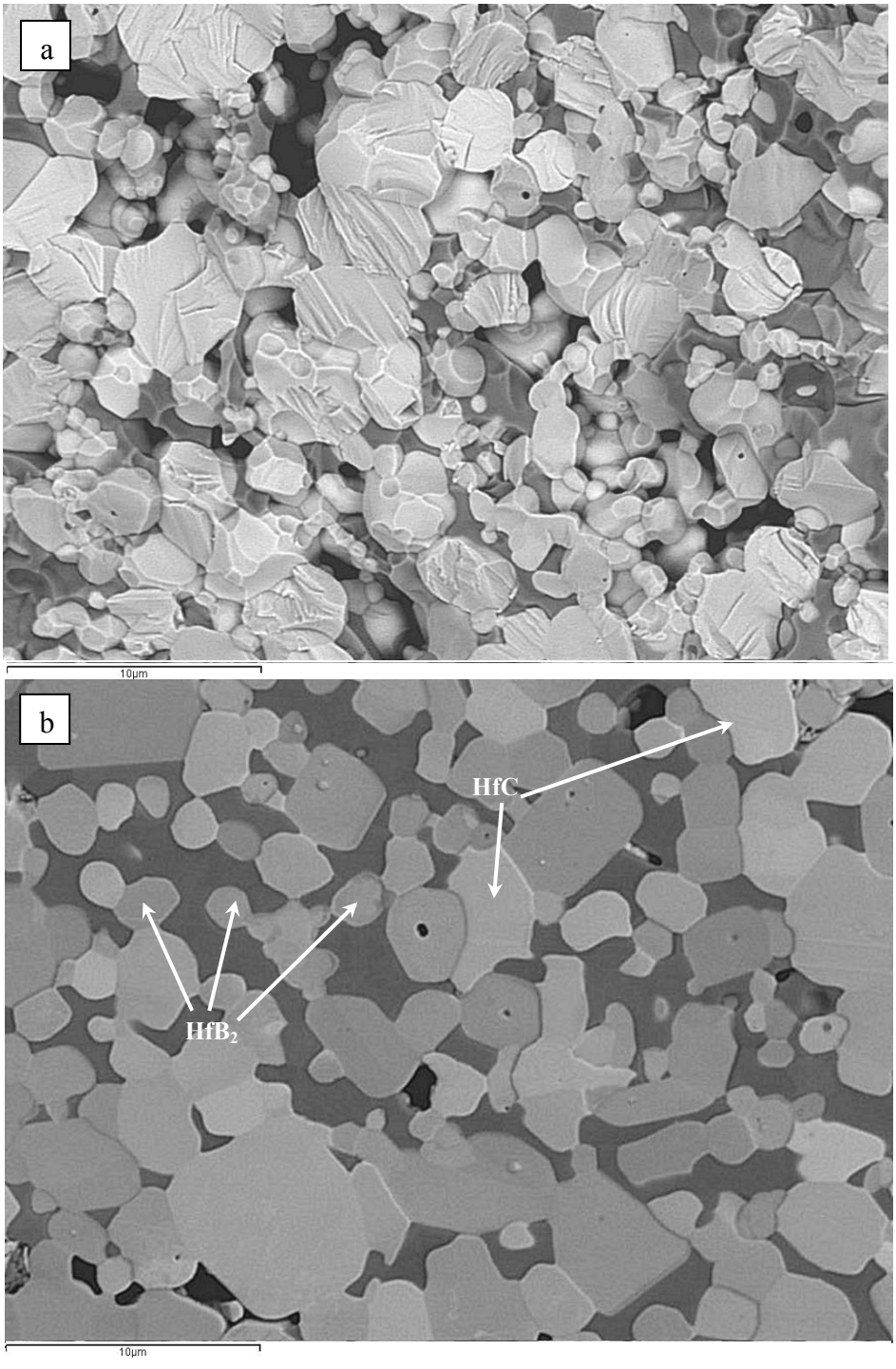

Fig. 12.6: Backscattered image of HHM sample and EDS spectra of the secondary phases MoB and Hf-Si-Mo-C.

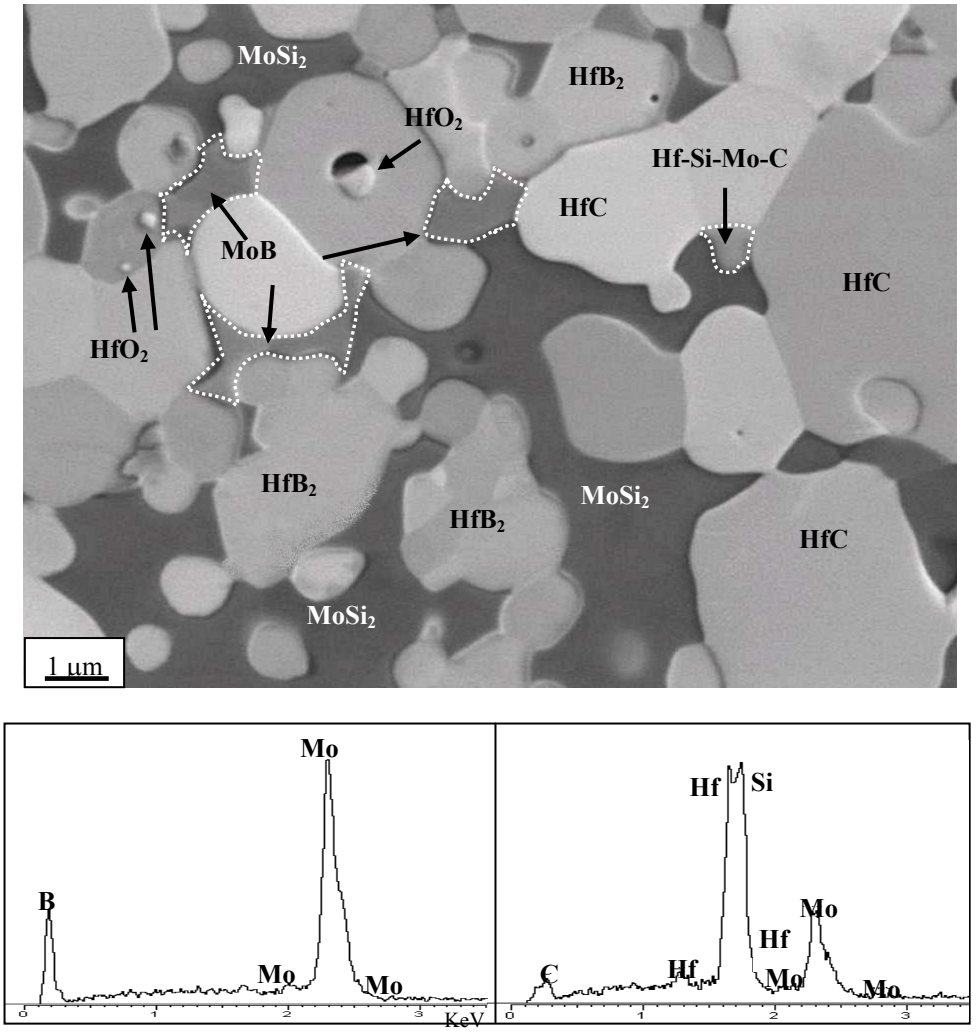

12.1.4 Mechanical properties

The measured properties are summarised in Tab. 12.II. For the sake of comparison, the mechanical properties of HfB_2-, ZrB_2-, HfC-20 vol% $MoSi_2$[1,3] are also reported.

Because of microstructural coarsening occurred in the HZBM sample, the microhardness value is lower than the reference materials' values (HfB_2-20 vol%$MoSi_2$ and ZrB_2-20 vol%$MoSi_2$), which are 18.8 and 16.0 GPa respectively.[3] In contrast, for HHM sample, the hardness value lies between the values of the HfB_2 and HfC reference materials: in this case, the mean grain size is comparable with that of the HfB_2-20 vol% $MoSi_2$ and HfC-20 vol%$MoSi_2$ materials, being 1.5 and 2.8 μm respectively.[1,3]

For both the composites, the Young's modulus values were lower than those of their reference materials (Tab. 12.II). Residual porosity is likely the main factor negatively affecting this property.

The measured values of fracture toughness are in agreement with those reported in the literature for these materials, despite the use of different sintering techniques and

sintering aids.[7-10] These values indicate that toughness is a major concern for potential use of these compounds. Apparently, the addition of $MoSi_2$ does not improve this property. Analysis of the crack paths (not shown) obtained by 10 kg indents showed that the silicide phase was not effective in deviating the advancing crack.

Flexural strength tests carried out at room temperature showed that for HZBM composition the experimental value (453±100 MPa) was in the range between the reference materials. Critical flaws detected by SEM on fracture surfaces were $MoSi_2$ agglomerates with dimensions of about 30 μm. Comparison with the microstructure of HfB_2- and ZrB_2-based composites demonstrates that grain coarsening and $MoSi_2$ agglomerations were the key factors affecting room temperature strength. For HHM sample, the measured value (470±38 MPa) is even higher than those reported for HfB_2- and HfC-based materials (388±40 and 383±74 MPa respectively). This increase was attributed to improvement of secondary phase dispersion through ultrasonication of the starting powders. Actually, further studies on $MoSi_2$ dispersion are needed, because 30-μm wide agglomerates of $MoSi_2$ were still found to be the critical flaws. An example of such critical defects is shown in Fig. 12.7. Interestingly, HZBM material held the same value of flexural strength from room temperature up to 1500°C. Strength retention at high temperature was attributed to the sealing of surface defects by means of silica glass formed during the test, as confirmed by the fractographic study of the fractured bars tested in air reported in Fig. 12.8a. Even at 1200°C, significant formation of silica occurred as a consequence of $MoSi_2$ oxidation.[11]

Fig. 12.7: A $MoSi_2$ agglomerate which acted as critical flaw in HHM sample.

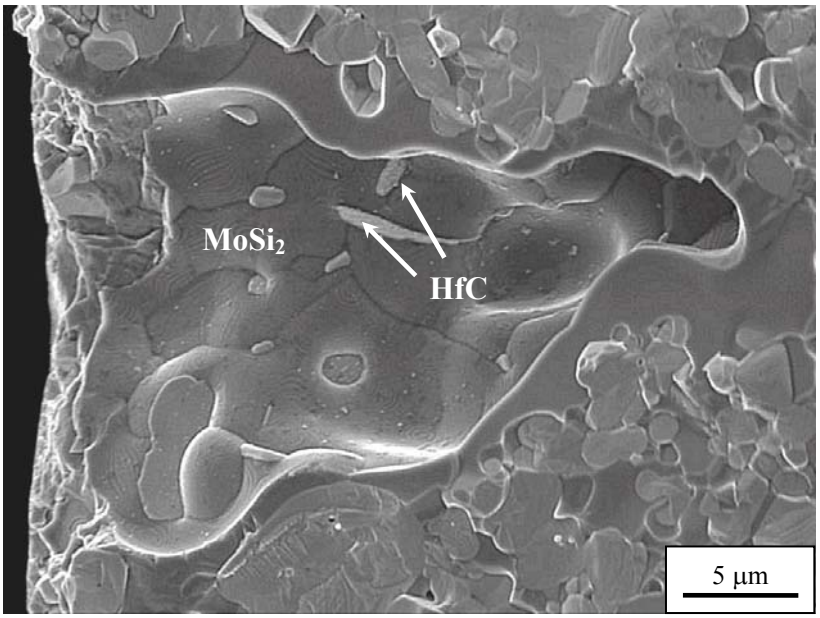

For materials with HHM composition, high-temperature tests were carried out in a partially protective Ar atmosphere because of the presence of hafnium carbide, which is sensitive to oxygen and tends to form a non-protective HfO_2 scale. At 1200°C a decrease of 30% in respect with the room temperature value was observed, but this value (~330 MPa) remained unchanged up to 1500 °C. An example of fractured surface is shown in Fig. 12.8b.

Fig. 12.8: Fracture surface for a) HZBM and b) HHM samples after the flexural strength test at 1500°C.

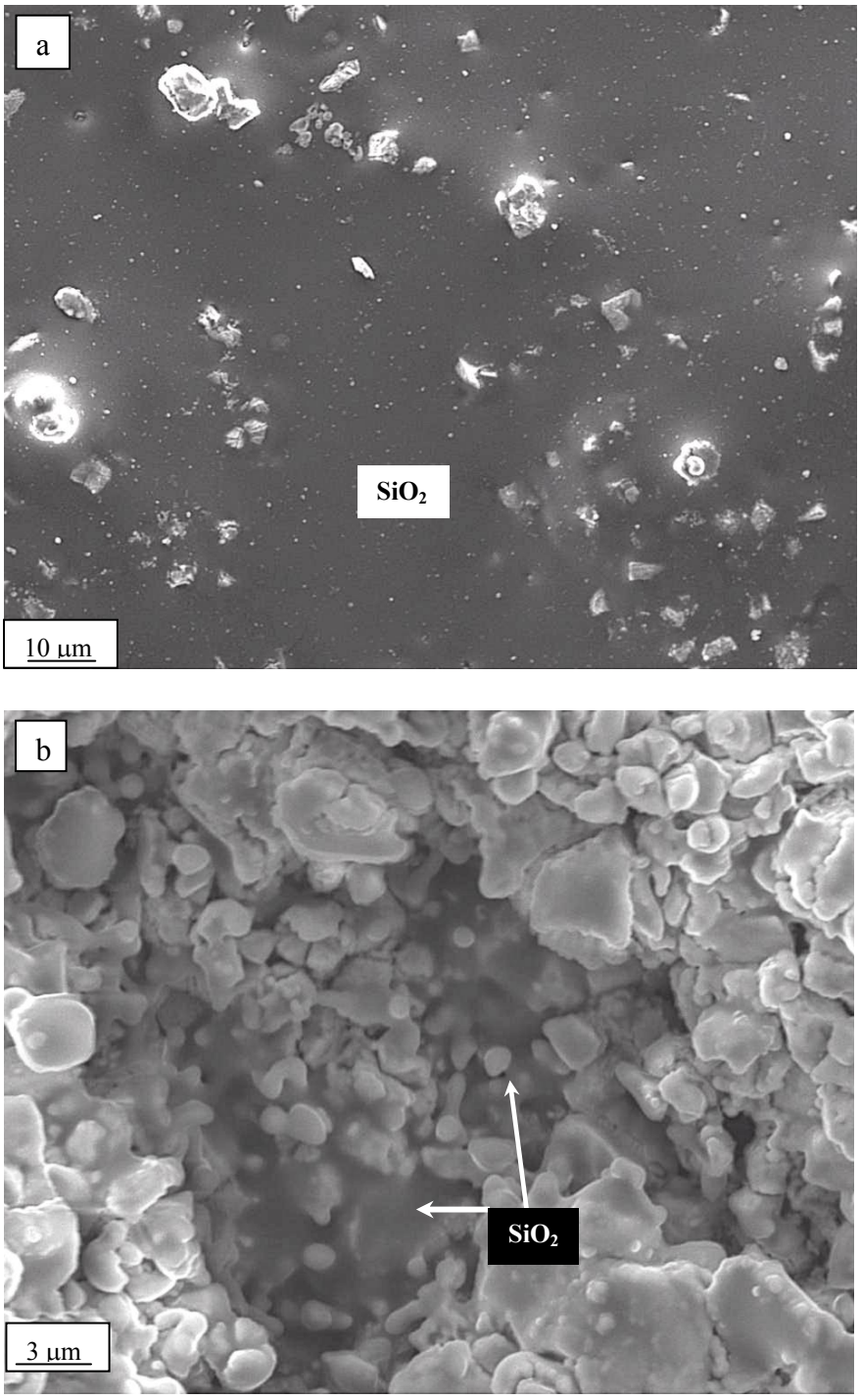

Despite the partially protective Ar environment, the formation of hafnia and silica was noticed on the surface, accounting for the presence of residual oxygen in the furnace chamber. One interesting feature of these composites is the linearity of the load-displacement curves up to fracture even at 1500°C (not shown), confirming the high refractoriness of the present phases.

12.1.5 Conclusions

HfB_2-based composites with additions of either ZrB_2 or HfC were densified to 96-98% of the relative density by pressureless sintering at 1900-1950°C with 20 vol% $MoSi_2$ as sintering aid.

The dominant feature of the HfB_2-ZrB_2-$MoSi_2$ composite was the formation of a (Hf, Zr)B_2 solid solution which enhanced the densification of the composite. As a drawback, a slight coarsening of the microstructure occurred (mean grain size ~6 μm). The flexural strength at 1500°C was 450 MPa and the high temperature stability of this composite is believed to originate from the silica coating provided by the $MoSi_2$ phase.

The microstructure of the HfB_2-HfC-$MoSi_2$ composite was finer (1-3 μm) and homogeneous and no reaction occurred between boride and carbide. The 4-pt flexural strength at 1500°C was still 77% of the room temperature value (470 MPa).

12.2 ZrC-BASED COMPOSITES

12.2.1 Introduction

The purpose of this work is to develop ZrC-based materials which can be consolidated by pressureless sintering at temperatures lower than 2000°C. To this aim, two ternary compositions in the systems ZrC-HfC-$MoSi_2$ and ZrC-ZrB_2-$MoSi_2$ were studied. Densification, microstructure and mechanical properties are presented and discussed.

12.2.2 Densification behaviour

Sintering cycles of the ZrC-based materials were carried out in the temperature range 1850-1950°C (see Tab. 12.III). The increase of the sintering temperature generally led to an improvement of the final relative density. For ZrC-20 vol% $MoSi_2$ composition (ZCM), a relative density of 96.8% was obtained at 1950°C, see also Chapter 10, section 10.5. Similar results were obtained for the ZrC-HfC-$MoSi_2$ sample (ZHCM), which achieved a relative density of 96% at 1950°C. For the ZrC-ZrB_2-$MoSi_2$

mixed composite (ZZM), a temperature of 1900°C was sufficient to obtain a relative density of 97%. By increasing the temperature to 1950°C no further improvement of the density was achieved.

Tab. 12.III: Compositions, theoretical densities, sintering temperatures, green and final relative densities of the prepared ceramics. For all the samples a soaking time of 60 minutes was set.

Sample	Composition (vol%)	Th. density (g/cm^3)	Sintering T (°C)	Green density (%)	Final density (%)
ZCM	80 ZrC+20 $MoSi_2$	6.57	1850	65.2	89.2
			1900	64.9	95.2
			1950	63.8	96.8*
ZHCM	40 ZrC+40 HfC+20 $MoSi_2$	8.99	1850	65.5	91.6
			1900	69.0	92.6
			1950	68.2	95.7*
ZZM	40 ZrC+40 ZrB_2+20 $MoSi_2$	6.35	1850	62.7	94.8
			1900	62.5	97.4*
			1950	62.5	97.6

* compositions selected for characterization

12.2.3 Microstructure

As a reference, the X-ray diffraction pattern for the material ZCM is shown, along with the ternary compounds in Fig. 12.9.

ZrC-HfC-$MoSi_2$ composite (ZHCM) - According to X-ray diffraction pattern in Fig. 12.9b, the reflections fall between ZrC and HfC peaks and the phenomenon becomes more evident at higher diffraction angles (not shown). This indicates the formation of a solid solution between the two carbides. Studies reported in the literature[12] confirm a complete solubility between group IV carbides. Furthermore, traces of silicon carbide were detected when the analysis was carried out with longer acquisition time, 10 seconds per degree, (see insert in Fig. 12.9b).

According to Fig. 12.10a the fracture is mainly transgranular and little porosity is retained in the microstructure (about 3.5%). ZrC grains are no longer distinguishable from HfC grains because of the solid solution formation (Fig. 12.10b). The carbide grains have a faceted shape and a mean grain size of about 5.5 μm, indicating that grain coarsening occurred during densification. By EDS analysis, the composition of the solid solution was found to be close to $Hf_{0.5}Zr_{0.5}C$, Fig. 12.10c. Residual unreacted HfC particles were occasionally recognized in the microstructure. Beside the faceted $Hf_{0.5}Zr_{0.5}C$ grains, carbide grains with irregular morphologies were also observed. An example is given in Fig. 12.10d. According to EDS analysis the composition of these phases is close to $Hf_{0.25}Zr_{0.75}C$.

Fig. 12.9: X-ray diffraction spectra of a) ZCM, b) ZHCM, c) ZZM materials.

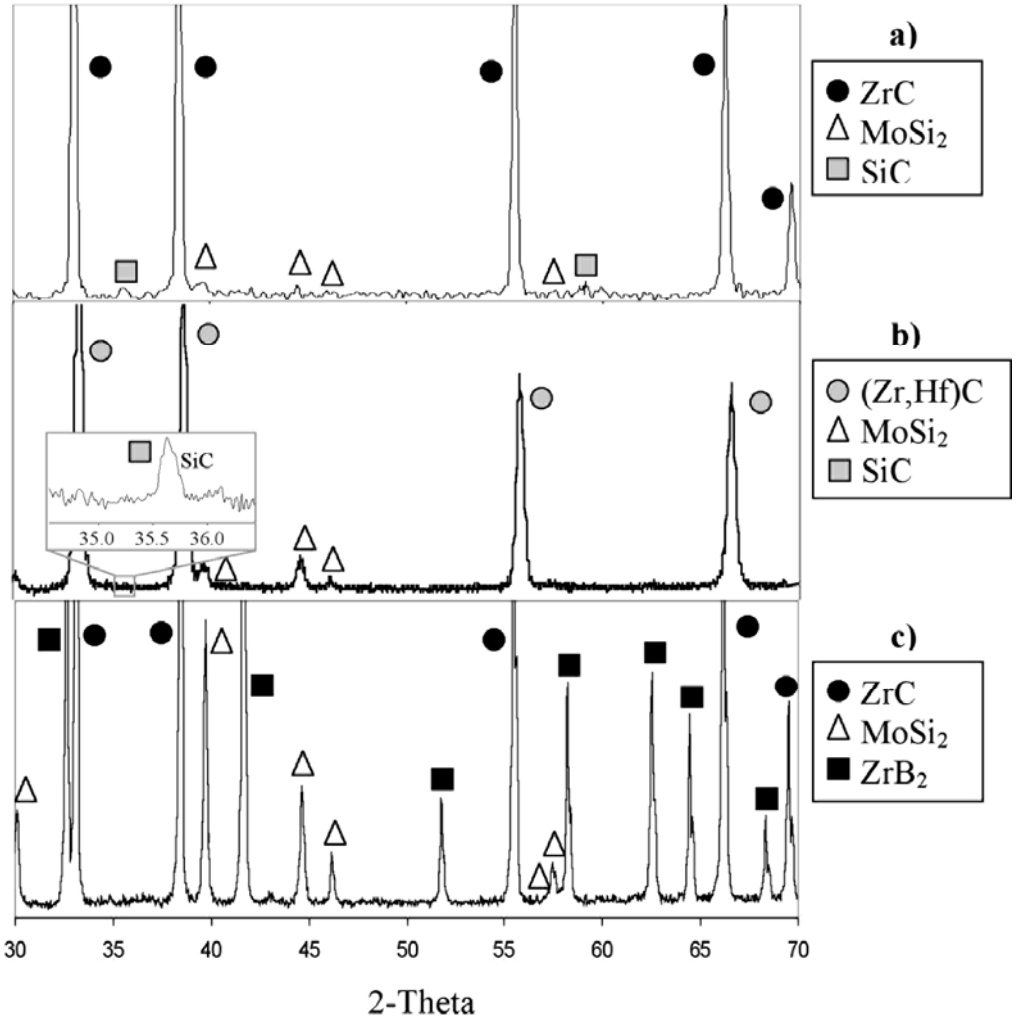

Fig. 12.10: Backscattered images of ZHCM sample: a) fracture surface, b) polished section and c) EDS spectrum of the (Zr,Hf)C solid solution formed. SE imaging mode showing d) SiC formation and ductile morphologies of carbides (indicated by arrows). e) and f) micrograph and related spectrum of Si-O- based intergranular phases (EHT=5KeV).

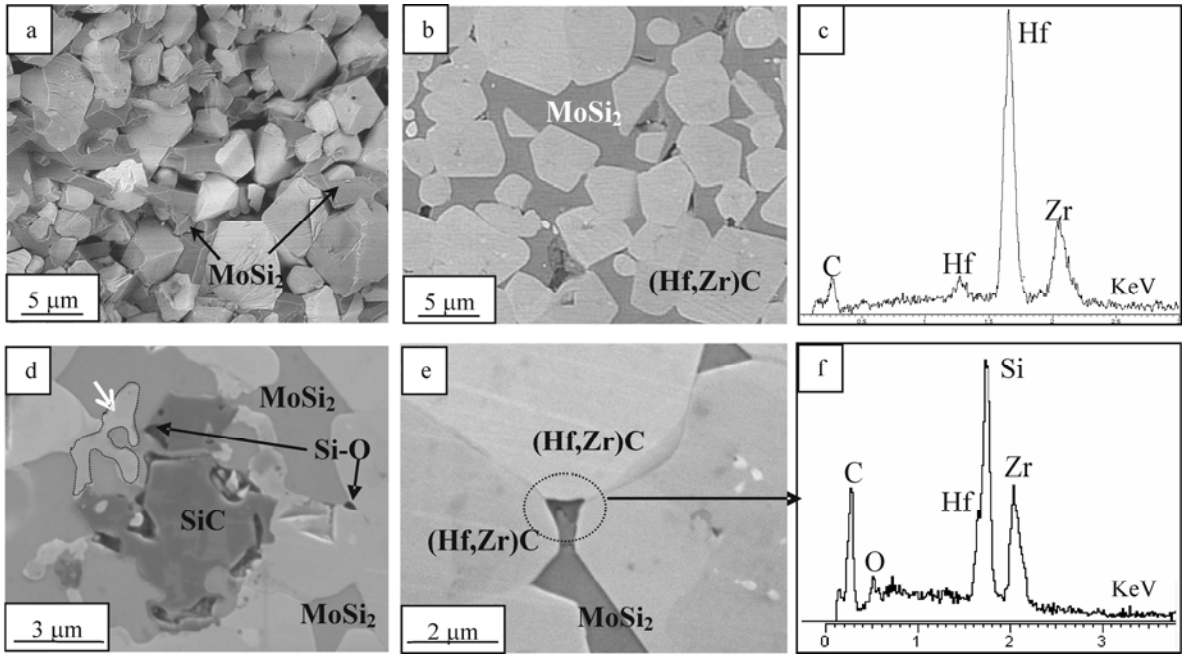

As for the ZrC-$MoSi_2$ composite, low amounts of SiC were detected in the microstructure, Fig. 12.10d. The irregular morphology and the presence of residual Si-O phases suggests that SiC formed from a Si-based liquid phase. Additionally, Si-O or Si-O-C intergranular phases were also detected at triple points as shown in Fig.12.10d-f.

ZrC-ZrB_2-$MoSi_2$ composite (ZZM) - Cubic ZrC, hexagonal ZrB_2 and tetragonal $MoSi_2$ were the main crystalline phases identified by X-ray diffraction, as displayed in Fig. 12.9c. As for the previous compositions, traces of silicon carbide were detected. According to SEM analysis, the composite resulted quite dense, with a residual porosity of about 3%. The fracture in Fig. 12.11a is transgranular for ZrC grains and mainly intergranular for ZrB_2 grains. Examples of polished surfaces are shown in Fig. 12.11b-c.

Fig. 12.11: BSE images of ZZM sample a) fracture surface and b) low magnification polished section c) enlarged view of the polished section and EDS spectra of Zr-Mo-Si phases with different compositions, (1) Mo-rich and (2) Zr-rich.

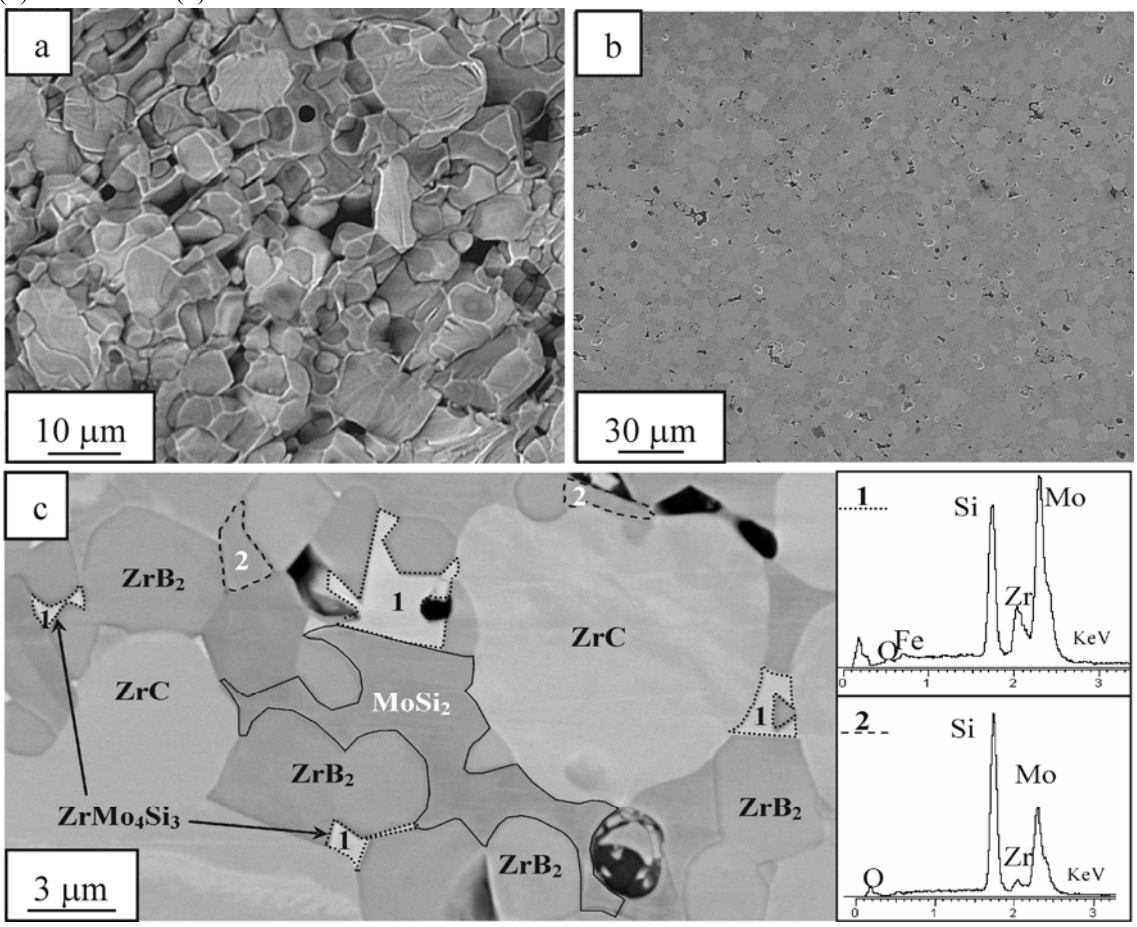

ZrC grains have a mean size of 9 μm, whilst ZrB_2 particles have a mean size of 2 μm, indicating that the carbide grains underwent grain coarsening whilst the boride grains retained their original grain size. At the ZrC/$MoSi_2$ interface, reaction phases containing Zr-Mo-Si, Zr-Si-B, Zr-Si-C were detected by EDS analysis (Fig. 12.11c). Zr-Mo-Si

phases were found to have a variable stoichiometry, as shown in the EDS spectra of Fig. 12.11c. About 1% of silicon carbide was calculated by image analysis carried out on SEM micrographs of polished section. SiC appeared as a dark contrasting phase with a morphology which suggests a solidification from a liquid phase (Fig.12.12).

Fig. 12.12: SiC phase formation at the interface between ZrC and $MoSi_2$ in ZZM sample.

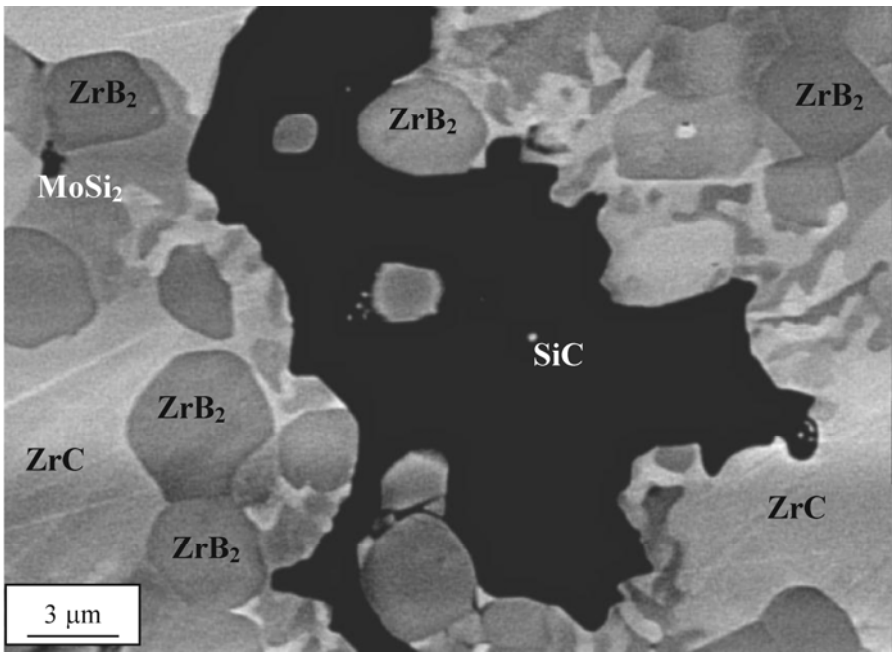

The microstructural features of the composites indicate that the sintering of ZrC-based composites is a combination of several phenomena, including formation of new reaction phases, solid solutions, local melting phenomena. However, the most important factor affecting the densification is the formation of high wetting liquid phases, based on Si or Mo-Si. The nominal melting point of $MoSi_2$ is 2020°C, i.e. higher than the temperature of the sintering cycles, 1950°C. According to the Mo-Si phase diagram,[13] for temperatures<1950°C, there are two eutectic compositions: a MoSi2+Si eutectic occurring at 1400°C, (Si 98.3 at%) and a Mo_5Si_3+$MoSi_2$ eutectic occurring at 1900°C (Si: 54 at%). The 1400°C eutectic is improbable to occur as it requires a strongly unbalanced Mo-Si ratio. On the other hand, it is also unlikely that the formation of liquid phase is due to the 1900°C eutectic. Indeed, the composition ZrC-20 $MoSi_2$ reaches a relative density of 90% at 1850°C, implying that the densification starts at a temperature well below. Microstructural features suggest that C could play a key role in the chemistry of these systems. Fan et al.[14] calculated the C-$MoSi_2$ pseudo-binary phase diagram. According to their studies, above 1700°C, a liquid phase forms at any C/$MoSi_2$ concentration. In the present system, as $MoSi_2$ is more abundant than C, a

mixture containing liquid phase+$MoSi_2$+SiC is predicted. Sources of Carbon are easy to identify in the compositions investigated. As previously mentioned, an amount of free C is present in the starting ZrC powder. Further contamination may occur during sintering which is conducted in a graphite-rich environment. SiC formation is a clear indication of the interaction between C and $MoSi_2$ and this phase is frequently found at the interface between $MoSi_2$ and ZrC. As Fan et al. observed, silicon carbide probably forms in-situ inside the solidifying $MoSi_2$ phase assuming an irregular shape.[14]

In addition, high wetting phases in the Zr-Mo-Si system were also detected in these compositions. Although the Zr-Mo-Si phase diagram is not easy to track in the literature, microstructural features indicate that formation of liquid phases in this system is also possible. Nomura et al.[15] studied the joining between Mo-ZrC materials and a Mo-Si-B alloy and reported the formation of Zr-Mo-Si phases at the interface, implying that at least interdiffusion of metal cations should be relatively easy for these compounds.

Hence, it can be concluded that the densification of ZrC-based composition is favored by high wetting liquid phases in the systems Mo-Si-C and Zr-Si-Mo, which start to form presumably at T>1700°C.

12.2.4 Mechanical properties

The values of the mechanical properties are summarized in Tab. 12.IV for the compositions of interest. Mechanical properties of ZrC-20 vol% $MoSi_2$ (ZC20) are also reported for comparison.

Tab. 12.IV: Mean grain size and mechanical properties of selected materials. HV1.0=Vickers Hardness, E=Young's modulus, K_{Ic}=fracture toughness, σ=flexural strength. * partially protective Ar atmosphere.

Sample	Composition vol%	M. g. s. μm	HV GPa	E GPa	K_{Ic} MPa·m$^{1/2}$	σ_{RT} MPa	$\sigma_{1200°C}$ MPa	$\sigma_{1500°C}$ MPa
ZC20	ZrC+20$MoSi_2$	ZrC:6.0	12.7±1.0	346±4	3.5±0.2	272±12	156±6*	-
ZHCM	40ZrC+40HfC +20$MoSi_2$	(Zr,Hf)C: 5.5	12.4±1.1	361±4	3.6±0.2	290±6	164±2*	-
ZZM	40ZrC+40ZrB_2 +20$MoSi_2$	ZrC:9.0 ZrB_2:2.0	12.5±0.9	390±4	4.0±0.9	363±31	256±119*	163±5*

Hardness values are very similar (~12 GPa) for the samples under investigation and they are well below the values reported in literature for monolithic zirconium carbide (~25 GPa).[12] This property is certainly affected by the presence of a secondary soft phase as $MoSi_2$, as well as by residual porosity of the samples and the relatively coarse microstructure. Moreover, our experimental values of hardness are slightly lower

than those found in the literature for various ZrC-based composites (ranging between 15 and 17 GPa).[16,17]

Young's modulus ranges from 346 to 390 GPa, the lowest value is for the ZrC-$MoSi_2$ composite, the highest for ZrC-ZrB_2-$MoSi_2$ ternary material. As the materials are affected by similar amounts of porosity, it can be concluded that the variations are mainly due to the stiffness of the constituent phases. The elastic modulus of ZrC is reported to be around 400 GPa,[18] while higher values are reported for HfC (425-430 GPa)[18,19] and ZrB_2 (~500 GPa).[20] Therefore, additions of either ZrB_2 or HfC may result in an increase of the composites stiffness.

Fracture toughness values are of the order of 3.5-4 $MPa \cdot m^{1/2}$ and are in the range of the values reported in the literature for ZrC-based composites, despite different compositions and densification techniques (2.6-5.8 $MPa \cdot m^{1/2}$).[16,17,21] No evidence of toughening mechanisms like thermal residual stress, crack deflection or crack pinning was observed.

The flexural strength of the materials tested at room temperature is in the range of 270-360 MPa. As for other properties, the highest value was found for the ternary composition containing ZrB_2. As the fractographic analysis did not evidence any critical flaw such as large inclusions or coarsened grains, it can be concluded that the strength is mainly affected by low fracture toughness, coarse grains and presence of residual porosity. It must be pointed out that the values obtained are in the range or even higher than those reported in the literature for other ZrC-based materials (220-320 MPa).[16]

As mentioned in the previous chapter, the high temperature strength tests were performed in flowing Ar, since preliminary test in air at 1200°C turned the bars into a whitish powder, due to the catastrophic oxidation of the bulk. Also in this case and despite the short permanence in temperature, for the compositions ZCM and ZHM, the flexural strength values at 1200°C decreased to about 43% of the room temperature value and the samples were covered by a whitish layer implying that they reacted with residual oxygen present in the test chamber. It is likely that the decrease of strength is mostly due to new defects introduced by oxidation. Examples of the fracture surfaces after tests at 1200°C are shown in Fig. 12.13. During tests at 1500°C, despite the Ar flux, the bars were broken apart by oxidation.

The flexural strength of ZrB_2-containing composite (ZZM) decreased to about 30% of the room temperature value after the test at 1200°C. A further decrease (55% of the room temperature value) was recorded at 1500°C, but no pest oxidation occurred. In

Fig. 12.13b the surface of the ZZM sample after the bending test at 1200°C is shown. The EDS analysis carried out on the surface revealed that, different from samples ZCM20 and ZHCM, a glassy silica-based phase partially embedded the matrix grains. This different behavior compared to pure carbide composition suggests that an addition of ZrB_2 could be a strategy for the improvement of high temperature properties for ZrC-based composition.

For the compositions which survived the high temperature tests, the load-displacement curves were linear up to fracture even at 1500°C, which rules out that softening of secondary phases can be responsible for the strength decrease.

Fig. 12.13: Fracture surface for a) ZHCM and b) ZZM samples after bending test at 1200°C.

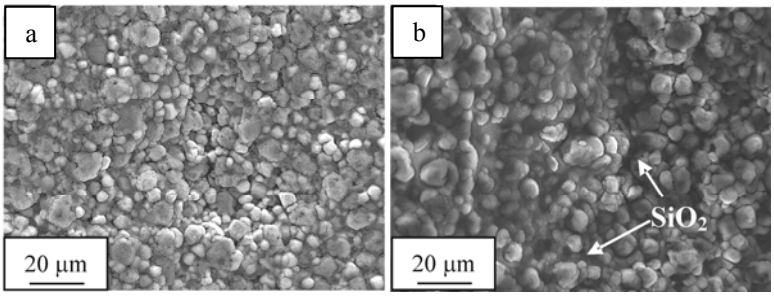

12.2.5 Conclusions

ZrC-based ternary composites in the systems ZrC-HfC-$MoSi_2$, ZrC-ZrB_2-$MoSi_2$ were densified to 97% of the relative density by pressureless sintering at 1900-1950°C.

The dominant feature of the ZrC-HfC-$MoSi_2$ composite was the formation of a (Hf, Zr)C solid solution which confirmed the complete mutual solubility of the carbides of the fourth group. SiC or Si-O-C phases were detected in the microstructure.

The microstructure of the ZrC-ZrB_2-$MoSi_2$ composite had a bimodal grain size distribution: ZrC grains coarsened up to 9 μm, whilst ZrB_2 grains retained their original size. SiC and Zr-Mo-Si secondary phases were detected.

On the basis of the morphologies of the secondary phases detected, a liquid-phase sintering is supposed to occur during densification of these materials, mainly driven by the reaction between $MoSi_2$ and C.

For all the produced materials the room temperature mechanical properties are similar to those of ZrC materials produced with pressure-assisted technique. For the first time, high temperature flexural strength results are reported. Despite the addition of a silica-forming phase, the composites only containing carbide phases were strongly damaged by oxidation. The addition of ZrB_2 was beneficial for improving both room temperature and high temperature properties of these composites.

References

1 D. Sciti, L. Silvestroni, A. Bellosi, J. Am. Ceram. Soc. 89 (2006) 2668.

2 D. Sciti, M. Brach, A. Bellosi, J. Mat. Res. 20 (2005) 922.

3 L. Silvestroni, D. Sciti, Scripta Materialia 57 (2007) 165.

4 Y. Yan, Z. Huang, S. Dong, D. Jiang, J. Am. Ceram. Soc. 89 (2006) 3589.

5 Y. Harada, Y. Murata, M. Morinaga, Intermet. 6 (1998) 529.

6 Y.-L. Jeng, E.J. Lavernia, J. Mat. Sci. 29 (1994) 2557.

7 M.Gasch, D.Elleby, E.I. Irby, S. Beckam, M.Gusman, S. Johnson, J. Mat. Sci. 39 (2004) 5925.

8 D. Sciti, L. Silvestroni, A. Bellosi, J. Mat. Res., 21 (2006) 1460.

9 A. Bellosi, F. Monteverde, D. Sciti, Int. J. Appl. Ceram. Technol. 3 (2006) 32.

10 F. Monteverde and A. Bellosi, Adv. Eng. Mater. 6 (2004) 331.

11 Y.T. Zhu, M. Stan, S.D. Conzone, D.P.Butt, J. Am. Ceram. Soc. 82 (1999) 2785.

12 H. O. Pierson: Handbook of refractory carbides and nitrides, (William Andrew Publishing/Noyes, Westwood, New Jersey, USA, 1996), 68.

13 A.B. Gokhale, G.J. Abbaschian, J. of Phase Equilibria 12 (1991) 493-498.

14 X. Fan, K. Kack, T. Ishigawi, Mat. Sci. Eng. A278 (2000) 46-53

15 N. Nomura, T. Suzuki, S. Nakatani, K. Yoshimi, S. Hanada, Intermetallics 11 (2003) 51-56.

16 E. Min-Haga, W. D. Scott, J. Mater. Sci. 23 (1988) 2865-2870.

17 T. Tsuchida, S. Yamamoto. Solid State Ionics 172 (2004) 215-216.

18 A. Krajewski, L. D'Alessio, G. De Maria, Cryst. Res. Technol. 33 (1998) 341-374.

19 James F. Shackelford, William Alexander (Eds.): Materials Science and Engineering Handbook, 3rd edition, (CRC Press, Boca Raton, FL, USA, 2001), 762

20 D.E. Wiley, W.R. Manning, O. Hunter, J. of the Less-Common Metals 18 (1969) 149-157.

21 K. H. Kim, K. B. Shim, Materials Characterization 50 (2003) 31-37.

CHAPTER 13

CONCLUSIONS II

The second part of this thesis deals with the production and characterization of Ultra High Temperature Ceramics (UHTCs), namely borides and carbides of the fourth group of transition metals. These materials posses very high melting point, above 3000°C and are candidates for applications in aerospace engineering due to their extraordinary chemical-physical properties. The main obstacle to their production is the sintering process, as pressure assisted techniques and temperature exceeding 2000°C are usually required to obtain full dense materials.

The goal of this work was to find out the most suitable sintering additive which allowed the densification of UHTCs by conventional pressureless sintering without negatively affecting the mechanical properties from room temperature up to 1500°C and the oxidation behaviour up to 2000°C.

To this scope, **Chapter 9** concerns the production of borides and carbides of Zr and Hf with addition of $MoSi_2$. This intermetallic was chosen as sintering additive due to its high melting point, compatible with the working temperature for which these materials are planed, its high stiffness and its good oxidation resistance, thanks to the formation of a protective silica layer which hinders the bulk degradation. The amount of $MoSi_2$ added to ZrC, HfC, ZrB_2 and HfB_2 matrices ranged between 5 and 20 vol% and the optimized thermal treatments were set at temperature between 1850 and 1950°C for 60 minutes holding time under flowing Ar.

In **Chapter 10** the microstructural characterization for the composites is described and, in the light of the observed features, the densification mechanisms are proposed.

The comparison between doped and undoped materials evidenced the beneficial effect of $MoSi_2$ additions: the relative density of ZrB_2-, HfB_2-, HfC-based materials containing 5-20vol % $MoSi_2$ increased indeed from 70% to 99% at temperatures ranging from 1850 to 1950°C. The only exception regarded ZrC-based composites, for which the addition of 5 vol% of $MoSi_2$ resulted in a maximum density of about 90%. All the dense bodies displayed a homogeneous microstructure with minimal grain

growth and very low amounts of residual porosity. The carbides presented a slight grain coarsening, the mean grain size was 6 μm for ZrC-based and 2-3 μm for HfC-based, whilst the borides retained a finer microstructure with mean grain size around 1-2 μm.

Scanning electron micropscopy (SEM) studies on the carbides evidenced the presence of secondary phases, like SiC and, at the interface between matrix and $MoSi_2$, transition metals silicides. The subsequent analyses by Transmission electron microscopy (TEM) allowed to identify the stoichiometry of the transition metals-silicides. Pure Zr_xSi_y were observed in the ZrC-based materials, whilst $(Hf,Mo)_xSi_y$ mixed phases with a ratio metals/silicon equal to 5/3 were detected at the triple points in the HfC-based composites.

On the basis of on the microstructural features, crystallographic considerations and the thermodynamics of the systems, it was concluded that the densification of Hf and Zr carbides doped with $MoSi_2$ does occur via liquid phase, which is constituted by transition metals silicides. Mo_5Si_3 was identified to be the starting phase for the formation of Zr-Si or Hf-Si species as it has a larger solubility for the IV Group transition metals carbides than $MoSi_2$. The local formation of Mo_5Si_3 may occur through different mechanisms: it could be already present in the starting $MoSi_2$ powder or could form through reaction with C impurities. Then, Zr completely substitutes Mo in Mo_5Si_3 and forms the Zr-silicides, more or less Si-rich depending on the local environment. On the other hand, since Hf has a lower mobility than Zr, it substitutes Mo sites in the Mo_5Si_3 structure only partially, giving rise to a $(Hf,Mo)_5Si_3$ phase in the final microstructure.

In the borides-based composites, beside the two main compounds, further phases were identified by SEM, like MoB and oxides and carbides of the corresponding Zr or Hf. At the triple point junctions auxiliary analyses by TEM revealed the presence of Mo_5Si_3 and Mo_5SiB_2 which contained Zr or Hf impurities. Moreover an epitaxial substructure was noticed surrounding the matrices' grains: the inner part was pure Zr- or HfB_2, whilst the outer part also contained Mo and O.

Concerning the densification mechanisms of the borides, the "cleaning effect" of $MoSi_2$, i.e. the removal of oxygen species from the matrices, was identified as the key step. Actually, due to oxygen impurities, the formation of MoB and SiO_2 was favourable, but no silica species was observed in the final microstructure because of the carbo-reducing environment. The crucial presence of Mo_5Si_3, coming from $MoSi_2$

powder as oxidation product, allowed the diffusion of B leading to the formation of Mo_5SiB_2. This last compound, along with $MoSi_2$, MoB and Mo_5Si_3, is expected to form liquid phases from 1350 to 1927°C in which Zr and Hf are partially soluble. In the final step, during cooling, epitaxial reprecipitation of the liquid onto the matrix grains occurred with the formation of a $(M,Mo)B_2$ solid solution surrounding the borides grains. This effect was more pronounced in the ZrB_2-based composite, due to a higher reciprocal solubility of Zr in the Mo-Si-B liquid and of Mo in the ZrB_2 grains. An important finding of this work is that, in presence of $MoSi_2$, the borides and carbides are not that stable as generally believed.

Moving to **Chapter 11**, the mechanical properties and arc-jet tests are presented for compositions of interest. The mechanical properties of dense ZrC-, HfC-ZrB_2-, HfB_2- based materials containing 5-20vol % $MoSi_2$ are discussed in relationship with the content of the silicide. The experimental values are compared to the values reported in the literature for the same class of materials. Relationships between process, microstructure and properties are discussed for each system.

Concerning hardness, the highest values were those of HfB_2-based composites, around 19 GPa. HfC and ZrB_2 composites were around 15-16 GPa, while ZrC-$MoSi_2$ exhibited the lowest hardness, around 13 GPa, due to a coarser microstructure and some residual porosity.

The highest Young's modulus values were measured on the borides, 450-520 GPa, whilst for the carbides the stiffness retained values ranging from 350 to 450 GPa.

The generally low fracture toughness values reflected the typical feature of UHTCs and pointed out the pressing need to effectively reinforce these materials to widen their applications spectrum. Measured values ranged between 3 to 4 $MPa \cdot m^{1/2}$, with borides being slightly tougher than carbides.

Flexural strength tests clearly showed the excellent high temperatures capabilities of the borides, which maintained values of 500-580 MPa from room temperature to 1500°C. This behaviour was attributed to the formation of a boron-silicate glassy layer which sealed the defects and prevented further oxidation of the bulk. Regarding the carbides, good values were obtained for HfC-based composites up to 1200°C, whilst a decrease of 50-100 MPa occurred at 1500°C. For the ZrC-based material all the values were negatively affected by the coarse microstructure and the sensitivity to residual oxidizing species at 1200°C. Furthermore, it has to be underlined that, for the carbides, it was necessary to carry out the high-temperature bending tests in a protective Ar

environment in order to avoid an excessive oxidation damage of the specimens. Generally speaking the performance of the present composites was analogous or even superior to the results presented in the literature, especially for what concerns the high temperature properties.

Nanoindentation tests were performed on HfC-based materials containing 10 and 20 vol% of $MoSi_2$ to extract the property values of the single phases. HfC hardness ranged from 30 to 35 GPa, that of $MoSi_2$ from 19 to 24 GPa depending on the applied load. All the composites under examination presented in fact the "indentation size effect", which means the hardness increased as the applied load decreased, due to a smaller volume interested by the deformation and hence due to a lower probability to find flaws or unhomogeneities.

Since these ceramics are potential candidates for space applications, such as scramjets, nosecones and sharp leading edges, arc jet tests simulating the re-entry conditions could not be missing. HfB_2 and HfC composites containing 5 vol% of $MoSi_2$ were subjected to heat fluxes at rising enthalpy up to 26 MJ/kg. The maximum temperature achieved by the two composites was 1950 and 2100°C, with a total duration of 2 and 6 minutes, respectively. The specimens after oxidation did not present any trace of spallation and just a surface layer of 80-90 μm showed microstructural modifications. This high temperature stability opens up new developments in several fields of application, including nuclear and industrial applications where extreme conditions are involved.

Finally, **Chapter 12** tackles the preparation and characterization of ternary composites obtained from the combination of carbides and/or borides, as follows: HfB_2-ZrB_2, HfB_2-HfC, ZrC-ZrB_2, ZrC-HfC; they all contain 20 vol% of $MoSi_2$. Microstrucutre and properties are compared with those of the binary composites described in the previous chapters. The design of three-phase composites came from the need to lower the sintering temperature or to improve the oxidation resistance of HfB_2 and ZrC, respectively.

HfB_2-based composites with additions of either ZrB_2 or HfC were densified to 96-98% of the relative density by pressureless sintering at 1900-1950°C with 20 vol% $MoSi_2$ as sintering aid.

The dominant feature of the HfB_2-ZrB_2-$MoSi_2$ composite was the formation of a (Hf, Zr)B_2 solid solution which enhanced the densification of the composite. As a drawback, a slight coarsening of the microstructure occurred (mean grain size ~6 μm).

The flexural strength at 1500°C was 450 MPa and the high temperature stability of this composite was believed to originate from the silica coating provided by the $MoSi_2$ phase.

The microstructure of the HfB_2-HfC-$MoSi_2$ composite was fine (1-3 μm) and homogeneous without any reaction between the boride and carbide phase.

The 4-pt flexural strength at 1500°C was still 77% of the room temperature value, this being 470 MPa.

ZrC-based ternary composites in the systems ZrC-HfC-$MoSi_2$, ZrC-ZrB_2-$MoSi_2$ were densified to 97% of the relative density by pressureless sintering at 1900-1950°C.

The foremost feature of the ZrC-HfC-$MoSi_2$ composite was the formation of a (Hf, Zr)C solid solution which confirmed the complete mutual solubility of the carbides of the fourth group. SiC or Si-O-C phases were also detected in the microstructure.

The microstructure of the ZrC-ZrB_2-$MoSi_2$ composite had a bimodal grain size distribution: ZrC grains coarsened up to 9 μm, whilst ZrB_2 grains retained their original size. In addition, SiC and Zr-Mo-Si secondary phases were detected.

On the basis of the morphologies of the secondary phases detected, a liquid-phase sintering was supposed to occur during densification of these composites, mainly driven by the reaction between $MoSi_2$ and C.

For the two ZrC-based ternary materials the room temperature mechanical properties were similar to those of ZrC materials produced with pressure-assisted techniques. As far as concerns the high temperature properties, despite the addition of a silica-forming phase, the composites containing only carbide phases were strongly damaged by oxidation. The addition of ZrB_2 was beneficial for improving both room and high temperature properties of these composites.

In conclusion, the addition of $MoSi_2$ has been proved to be very effective for the densification of UHTC ceramics, as the sintering temperatures are up to 500-600°C lower than those normally required for the densification of monolithic materials. The drastic decrease of the sintering temperature allows the achievement of materials with refined microstructure, which in turn causes a marked increase of the mechanical properties. As a matter of fact, some of the materials studied in the present work perform even better than those produced with more expensive pressure-assisted

technique such as ZrB_2/SiC and HfB_2/SiC, especially at high temperature and under extremely oxidising conditions.

For the first time, thorough studies have been conducted on the microstructure by transmission electron microscopy, leading to the identification of the most important mechanisms which cause the densification of these systems.

In the light of the results herein presented, new paths of research will be addressed to the combination/substitution of $MoSi_2$ with lower amounts of Mo_5Si_3, which was identified as the essential phase enhancing the densification of these systems.

Another challenge will be the toughening of UHTCs by reinforcing phases, such as whiskers or fibres, in order to improve the resistance to crack propagation and to facilitate the machining of complex shapes.

Finally, of course, to better understand the oxidation behaviour under extreme conditions of high temperature and heat flux, further oxidation tests need to be performed in the arc jet device.

AKNOWLEDGEMENTS

Ora che si conclude anche questo percorso, vorrei ringraziare alcune persone che hanno reso possibile la realizzazione di questa tesi e mi hanno supportato e incoraggiato durante i miei 3 anni di dottorato così densi di esperienze e vissuto.

In primo luogo ringrazio Gian Nicola Babini e Goffredo de Portu per avermi dato la possibilità di svolgere l'attività di ricerca presso l'ISTEC-CNR.

Ringrazio inoltre il Coordinatore Luigi Angiolini, il mio relatore Giuseppe Palombarini e il Collegio docenti per avermi permesso di realizzare questa tesi di dottorato.

Un grande ringraziamento va subito a Diletta Sciti, che in questi anni è stata una guida ammirevole, mi ha fatto appassionare alla ricerca, pur non risparmiandosi in "frasi sagge" e in sagaci consigli su uomini, uncinetto e piatti pronti in 2 minuti (a lei devo anche la riscoperta di prosciutto e melone). La ringrazio tanto anche per essere riuscita a prendersi cura di me e del mio lavoro senza mai farmi sentire abbandonata a me stessa, nonostante la maternità e un'Elenina vivace.

Grazie a Stefano Guicciardi, che dalla sua mansarda si è sempre interessato e preso a cuore le mie attività, si è battuto per farmi andare in Germania ed è sempre stato un saldo punto di riferimento per tutti questi anni. Grazie per le sue competenze scientifiche, la sua diplomazia e le sue lezioni di vita.

Un grande riconoscimento va certo ad Alida Bellosi, per il supporto tecnico e morale, la fiducia e il calore umano dimostratomi e per avermi dato inoltre la possibilità di affrontare esperienze non da tutti i giorni.

Grazie a Laura Esposito, che così schietta e ed estrosa, mi fa dimenticare di lavorare su un progetto che non mi piace. Grazie per il suo parlare in modo asciutto, mirato… e ovviamente pungente.

Grazie a Ciccio, che nonostante i primi disaccordi, mi ha permesso di sfiorare l'Olimpo del laboratorio di proprietà meccaniche e alla fine gli è anche un po' dispiaciuto che me ne sia andata… oppure no, forse è più contento che non faccia più dispendiosi danni ai suoi supporti di allumina, ma mi limiti a chiedergli se ha imparato a nuotare.

Grazie a Daniele che, oltre a prendersi carico delle cotture meticolosamente, mi ricorda ogni giorno i principi della carità cristiana, del perdono e della benevolenza fraterna… facendomi però notare che anche la cura del corpo è importante.

Grazie a Celotti per la bramosia con cui si è occupato dei miei XRD e per gli aneddoti quotidiani sull'origine del nome degli elementi della tavola periodica, sulla politica dei paesi sovietici e sulla criminalità in Brasile.

Grazie anche al suo compare Silvano, per aver dato la priorità ai raggi X di quelli che vengono da Russi e per gli strabilianti racconti durante i passaggi a casa.

Grazie a Micio per i giorni che ha passato a contemplare un rullo di allumina in movimento, ma molto di più per i peperoncini, i libri e la genialità pazzoide.

Grazie anche a Fréderic per i preziosi segreti su SEM e preparativa che sono riuscita a strappargli di bocca.

Grazie a Magda, per i consigli, l'affetto e i pranzi a crakers da 23 anni (grazie a dio, per i crackers, solo 3 anni). La ringrazio per essermi stata sempre vicina dandomi lezioni quotidiane di positivismo supportate da bizzarre teorie di macchine gialle, Mulino Bianco e tirolesi con le guance paffute, e soprattutto per aver vissuto insieme i momenti più belli e più brutti delle nostre vite.

Grazie a Selanna per la compagnia in ufficio e le chiacchierate a cuore aperto durante le pause pranzo.

Un grazie va anche alla Sanson, che ha sempre una parola di conforto e di incoraggiamento e soprattutto per l'esempio di lavoratore statale non-convenzionale che dà a tutti.

Grazie anche a Stefania Albonetti per le notizie di straforo e la disponibilità anche verso i suoi non-dottorandi.

Grazie a Valentina e Mauro per avere sopportato i miei attacchi di arterio nella lotta per finestre e condizionatori.

Da Darmstadt….

Ringrazio immensamente il Prof. Achim Kleebe, per avermi accolto nel suo gruppo nel modo più caloroso e avermi dato la possibilità di lavorare sotto la guida di uno dei massimi esperti di TEM su ceramici. Grazie per avermi aperto l'affascinante

nano-mondo dei pallini (ahimè, più righe che pallini) e per avermi fatto capire che i PZT proprio non mi piacciono.

Un grazie di cuore anche a Stefan Lauterbach per la sua infinita pazienza e disponibilità, per i rifornimenti di cioccolata e carne secca di antilope (che ho pagato con 6 kg di abbondanza!) e per quella volta che ha rimediato al mio dramma del campione sperduto nella colonna. Grazie anche per le birre consolatorie delle 20.00 che seguivano frustranti sessioni al microscopio.

Ringrazio Mathis per la sua pazienza ed estrema abilità nel preparare i campioni, per i passaggi sulla sua Trabi vibrante e per il silenzio complice.

Ringrazio inoltre Betina, che mi ha assistito nei primi tempi traducendomi documenti incomprensibili sia in tedesco che in italiano, e tutto il gruppo di Microscopia Elettronica di Geologia e Scienza dei Materiali, TUD.

Un grazie sentito va poi ai miei sudici vicini di tugurio, che per 9 mesi mi hanno arricchito con le loro personalità singolari e lasciato ricordi esilaranti. Grazie al gruppo sovietico (Slawa, Mitja e Vanja) per la musica, l'immancabile vodka e il pesce secco con la birra; grazie agli Indians (Gereesh, Badri, Pratap, Mohanish e Roy) per gli odori e le lenticchie speziate; grazie al cinese Meng per le lezioni di salute e germanistica, grazie ai Marocchini (nessuno saprà mai in quanti vivessero in quella stanza) e a tutti gli altri che non parlavano molto, ma sporcavano assai.

Inoltre ringrazio Beatriz, Nora e Donald per il loro affetto e la continua presenza e le mie baci Ebru e kanka Agnes per tutte le elettrizzanti esperienze che abbiamo condiviso.

Grazie anche a Skype che mi ha fatto sentire a casa e permesso di badare i miei nipoti anche a 1000 km di distanza.

Tornando in Italia, vorrei ringraziare i miei amici intellettuali del Clandestino il sabato sera, gli psicanalisti on-line e i gatti da divano che mi sono stati vicino facendomi ridere col loro cinismo, pensare con le loro riflessioni e rilassare con la loro pacatezza.

Ringrazio poi i nonni Bruno e Lidia per avermi foraggiato durante i miei soggiorni a Bologna e fatto sbellicare con i loro spassosi siparietti da ottantenni pseudo-innamorati.

Ringrazio anche la nonna Luisa per le torte di riso, il suo scetticismo verso gli UHTC e la sua eterna convinzione che io facessi cocci di ceramica e per avermi lasciato in eredità la sua forza d'animo e la sua prontezza nelle risposte.

Ringrazio poi mia sorella e Christian perché mi permettono di invadere il loro spazio TG per costruire rumorose navicelle spaziali, "ssattolini", o ingombranti zattere a Ciro e Vito che mi mettono sempre di buonumore.

Grazie a mia mamma per la sua forza e il suo sarcasmo, nonostante tutto. E grazie anche perché mi lascia andare in giro per il mondo… a patto che poi torni a casa.

Grazie infine a mio babbo, che sarebbe stato fiero del mio percorso scientifico in una famiglia di "donne di lettere", per avermi sempre supportato nelle mie scelte professionali. Grazie per tutto quello che mi ha insegnato nonostante fossi già nata "imparata", dall'uso del trapano a colonna e della sega a filo, alla saldatura con lo stagno, fino al buonumore e all'ironia. Grazie anche per aver insistito per l'ultimo piatto di cappelletti dai Dentoni e perché so che ha un ruolo nelle fortune che ho e che ho avuto.